Universidade do Minho
Escola de Ciências

Sergey Vladimirovich Pyrlin

Modelling the physical properties of nanostructures and composites

fevereiro de 2016

Modelling the physical properties of nanostructures and composites

Sergey Vladimirovich Pyrlin

UMinho | 2016

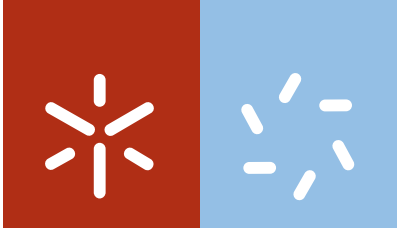

Universidade do Minho
Escola de Ciências

Sergey Vladimirovich Pyrlin

Modelling the physical properties of nanostructures and composites

Tese de Doutoramento em Ciências
Especialidade em Física

Trabalho efetuado sob orientação da
Prof. Dr. Marta Maria Duarte Ramos

fevereiro de 2016

STATEMENT OF INTEGRITY

I hereby declare having conducted my thesis with integrity. I confirm that I have not used plagiarism or any form of falsification of results in the process of the thesis elaboration.
I further declare that I have fully acknowledged the Code of Ethical Conduct of the University of Minho.

University of Minho, 25 de fevereiro de 2016

Full name: Sergey Vladimirovich Pyrlin

Signature: Pyrlin S.V.

Acknowledgments

Writing of this thesis would not be possible without the financial support of:

1. Marie Curie Initial Training Network "CONTACT" for the tailored supply-chain development of CNT-filled composites with improved mechanical and electrical properties, funded by European Community's Seventh Framework Program (FP7-PEOPLE-ITN2008-238363) http://www.contactproject.eu/.
2. Portuguese Foundation of Science and Technology (Fundação para a Ciência e a Tecnologia, FCT) through the PhD grant with the reference SFRH/BD/88995/2012.

The Center of Physics of University of Minho research is sponsored by FEDER funds through the program COMPETE- Programa Operacional Factores de Competitividade and by national funds through FCT under the project PEst-C-FIS/UI607/2011-2012.

Apart from this I would like to express my deep gratitude to Professor Dr. Marta Ramos for being my scientific advisor. I am deeply grateful to the members of GFCT group and the CONTACT project research and management team for creating the atmosphere of friendship and support. Especially I would like to note Dr. Anna Y. Matveeva for being my closest colleague in this project and friend sharing with me good and bad days during these years in Portugal. I want to thank Dr. Gustavo Zelada-Guillen and Dr. Arjan Kleij for giving me pass into the world of self-assembly and Dr. Nicholas Hine and the rest of ONETEP developers team for invaluable help. As well, I am grateful to Dr. Olga Erkovitch and other members of Physics Department of Bauman University and to Antonina Vardanyan, my school physics teacher, for giving me the perfect start in science.

Last, but most important, this text would never be written without the help, support and understanding of my family to whom I address my love and gratitude.

Abstract

This thesis investigates the possibility to design novel composite materials by addition of carbon nanotubes to polymer matrix. Despite the extensive research in this field the problem of achieving stable electrical conduction, anticipated by early theoretical studies, still constitutes a significant challenge. One approach to circumvent this problem is apply the recently synthesized tetrakis-Schiff zinc-complexes as a guiding agents for nanotubes. The remarkable ability of such complexes to self-assemble in molecular networks, incorporating nanotubes, opens a promising possibility to achieve good conductivity at extremely low concentrations.

In order to understand the scattered electrical properties obtained from the experiments, this thesis studies the effects of agglomeration and alignment of carbon nanotubes in polymer matrix as the possible sources of high deviations in experimentally measured direct current resistivities. It is shown with Monte Carlo simulations that, with the contemporary methods of industrial processing, the nanotube agglomerates can be reduced to the limit where their impact on composite's conductivity is negligible. Thus, the alignment of nanotubes must be viewed as the main source of electrical properties deviation. It was also shown using molecular dynamics simulations that bending of nanotubes, expected at high concentrations, results in diminishing of their benefits for composite's mechanical properties.

Using the simple Monte Carlo approach it is shown in this thesis that employment of self-assembling tetrakis-Schiff zinc-complexes as guiding agents allows the formation of connected networks at extremely low nanotube concentration. This thesis also reports the extensive molecular dynamics studies of the of tetrakis-Schiff complexes behaviour in solvent environment and suggests a possible mechanism, explaining all the experimental findings concerning the formation of molecular networks of connected rings available so far. The suggested mechanism is supported by free energy calculations for association of tetrakis-Schiff molecular chains in solvent.

The findings reported in this thesis support the emerging direction in polymeric composites design, within which composite morphology is controlled via molecular self-assembly.

Resumo

Esta tese investiga a possibilidade de serem desenvolvidos novos materiais compósitos através da adição de nanotubos de carbono a matrizes poliméricas. Apesar da extensa investigação nesta área, a dificuldade em obter condução elétrica estável, prevista em estudos teóricos iniciais, continua a ser um desafio maior. Uma nova abordagem para ultrapassar este problema é a aplicação a estes compósitos das moléculas de "tetrakis-Schiff zinc-complexes", com capacidades de auto-organização, para servirem como agentes orientadores para os nanotubos de carbono no interior da matriz polimérica, abrindo a possibilidade de se obter boa condutibilidade elétrica para concentrações de nanotubos extremamente baixas.

Através de simulações de Monte Carlo mostrou-se que, com os métodos atuais de processamento industrial, os aglomerados de nanotubos são reduzido a um limite onde o seu impacto na condutividade do compósito é insignificante. Assim, o alinhamento de nanotubos deve ser tido em conta como a principal fonte de variação nas propriedades elétricas. Através de simulações de dinâmica molecular demonstrou-se que a flexão de nanotubos, esperada a concentrações elevadas, resulta numa diminuição dos seus benefícios para as propriedades mecânicas do compósito.

Usando o método de Monte Carlo, é mostrado nesta tese que o uso das moléculas de "tetrakis-Schiff zinc-complexes", com capacidades de auto-organização, em compósitos poliméricos com nanotubos de carbono, permite a formação de redes de nanotubos para concentrações extremamente baixas. Esta tese também apresenta um estudo detalhado sobre o comportamento de complexos tertakis-Schiffe em solvente, usando o método de dinâmica molecular, e sugere um mecanismo possível para a formação de redes moleculares de anéis interligados nestas moléculas, explicando todos os resultados experimentais disponíveis até à data. O mecanismo sugerido tem por base cálculos de energia livre da associação de cadeias moleculares de tetrakis-Schiff no solvente.

Os resultados apresentados nesta tese sugerem que a direção a ser seguida no desenvolvimento de novos compósitos poliméricos com propriedades elétricas

estáveis, deverá ser aquela em que a morfologia do compósito é controlada através de auto-organização molecular.

Contents

Nomenclature

Acronyms

GCD	greatest common divisor
B3LYP	Becke 3-parameter Lee-Yang-Parr hybrid exchange and correlation functional
BAR	Bennet acceptance ratio method
BPA	bisphenol-A
BSSE	basis set superposition error
CNT	carbon nanotube
DC	direct current
DCM	dichloromethane
DFT	density functional theory
DLS	dynamic light scattering
DNA	deoxyribonucleic acid
DZP	double zeta plus polarization basis for quantum chemical calculations
ESP	electrostatic potential
FEM	finite element method
FEP	free energy perturbation
GAFF	generalized AMBER force field
GGA	generalized gradient approximation for exchange and correlation functional

GPGPU	general purpose graphics processing unit
HF	Hartree-Fock method
LCAO	linear combination of atomic orbitals
LDA	local density approximation for exchange and correlation functional
MC	Monte Carlo method
MD	molecular dynamics method
MWCNT	multiwalled carbon nanotube
NBO	natural bond orbital analysis
NEB	nudged elastic band method
NGWF	non-orthogonal generalized Wannier function
NPT	isothermal-isobaric ensemble: constant number of particles, pressure and temperature
NVE	microcanonical ensemble: constant number of particles, volume and energy
NVT	canonical ensemble: constant number of particles, volume and temperature
PBE	Perdew-Burke-Ernzerhof generalized gradient approximation for exchange and correlation functional
PC	polycarbonate
PMF	potential of mean force
PtP	porphyrin platinum dichloride
QC	Quantum chemical
RESP	restricted electristatic potential method
RMSD	root mean square deviation
SMD	steered molecular dynamics

SWCNT	single walled carbon nanotube
TC	thiacyanine
THF	tetrahydrofuran
TOL	toluene
US	umbrella sampling
WHAM	weighted histogram analysis method

Greek symbols

(ϕ, θ)	when speaking of MC simulation, directional angles
α	aspect ratio, for CNT model - ratio of length to diameter
α, β, γ	when speaking of crystall structure, angles between lattice vectors
α_i	when speaking of self-assembled rings-and-rods molecular network, sector angle between connection point of two rods to one ring
β	Boltzmann factor
χ	when speaking of quantum calcultions, atomic basis wavefunction
Δ	difference
δ	percolation exponent
δ_{ij}	Kronecker delta
ϵ	when speaking of MD simulation, potential well depth
ϵ	when speaking of mechanical properties, elastic stress
ϵ	when speaking of quantum calculations, single electron energy
η	when speaking of self-assembled rings-and-rods molecular network, scaling parameter, characterising the sparsity of network
η_C	when speaking of self-assembled rings-and-rods molecular network, percolation threshold in terms of scaling parameter

γ	when speaking of Langevin thermostat, dampung factor
λ	coupling parameter in free energy perturbation method
ω	when speaking of CNT shape, curviness (or wavyness) parameter
Φ	when speaking of tatrakis-Schiff molecule, angle, definig the position of side group
ϕ	when speaking of quantum calcultions, single electron wavefunction
ϕ_w	weight fraction
$\phi_{3D(2D)}$	when speaking of percolation, bulk (or surface) percolation threshold
ϕ_{vol}	when speaking of MC simulation, filler volume fraction
π	when speaking of electronic orbitals, pi-orbital
Ψ	multielectron wavefunction
ρ	when speaking of composite content, density
ρ	when speaking of electric properties, electric resistivity
R, R'	when speaking of chemical formulas, any radical
σ	when speaking of MC simulation, standard deviation
σ	when speaking of MD simulation, distance at which pair interaction potential is zero
σ	when speaking of electrical properties, electric conductance
$\sigma_{\mathcal{R}\theta}$	when speaking of self-assembled rings-and-rods molecular network, width of Gaussian-type distribution of the angles between z-axis and rings' axis
Θ	when speaking of tatrakis-Schiff molecule, central angle
ε	electric constant
ε	when speaking of MD simulation, dielectric permittivity of solvent
ξ_b	when speaking of MD simulation, bond length or angle

ζ	reaction coordinate

Roman Symbols

(n, m)	pair of indexes, characterizing SWCNT atomic structure
$\boldsymbol{A}$	when speaking of MC simulation, matrix of normalized conductances
$\boldsymbol{B}$	when speaking of MC simulation, matrix of normalized conductances to the right electrode
$\boldsymbol{I}$	when speaking of MC simulation, set of inclusion indexes, unity matrix
δt	when speaking of MD simulation, timestep
δU	variation of interaction potential in free energy perturbation method
$\hat{H}$	Hamilton operator
$\hbar$	reduced Plank constant
$\langle ... \rangle$	average value
$\mathbb{L}(\mathbb{R})$	when speaking of MC simulation, set of inclusion indexes, belonging to the left (right) electrode
$\mathbb{N}$	when speaking of MC simulation, set of inclusion indexes, belonging to connected network
$\mathbf{r}_i$	when speaking of quantum calculations, extended coordinates of electron, including real coordinates and spin
$\vec{\mathcal{X}}$	when speaking of MC simulation, generalized coordinates of a spherocylinder model, including the cartesian coordinates of the model's center, the directional cosines of the cylinde's axis vector, length and diameter of the particle.
$\mathcal{N}_{r/\mathcal{R}}$	when speaking of self-assembled rings-and-rods molecular network, average number of connections per ring
$\mathcal{N}^{C}_{r/\mathcal{R}}$	when speaking of self-assembled rings-and-rods molecular network, number of rods per ring achieved in simulation

$\mathcal{N}_{r/\mathcal{R}}^{T}$	when speaking of self-assembled rings-and-rods molecular network, desired number of rods per ring
$\mathcal{P}$	microscopic distribution of a molecular system
$\mathcal{S}_{\mathcal{R}}$	when speaking of self-assembled rings-and-rods molecular network, average surface per ring in 2D
$\mathcal{S}$	bulk electric conductivity
$\mathcal{V}_{\mathcal{R}}$	when speaking of self-assembled rings-and-rods molecular network, average volume per ring
$\vec{a}, \vec{b}, \vec{c}$	when speaking of crystall structure, lattice vectors
$\vec{a}_{1,2}$	hexagonal lattice vectors
$\vec{C}$	chiral vector of carbon nanotube
$\vec{F}_{ij}$	when speaking of MD simulation, force acting on atom i from atom j
$\vec{p}, p$	when speaking of tetrakis-Schiff molecule, the vector of electric dipole moment and it's absolute value
$\vec{R}(t)$	when speaking of Langevin thermostat, random vector
$\vec{r}_i$	when speaking of MD simulation, coordinates of atom or particle
$\vec{V}$	when speaking of MC simulation, Cartesian coordinates of particle's orientation vector.
$\vec{v}_i$	speed of atom i
$\vec{X}$	when speaking of MC simulation, vector of Cartesian coordinates of particle center.
A	when speaking of CNT shape, amplitude of CNT profile deviation form central axis
A	when speaking of thermodynamic quantities, Helmholtz free energy
A, B, C	when speaking of MD simulation, parameters of Morse potential
a_{CC}	carbon-carbon bond length of graphitic hexagonal lattice

$a_{i,j}$	when speaking of MC simulation, elements of conductance matrix
A_{slv}	surface area of molecular chain in solvent
B	when speaking of MC simulation, length of simulation box side
c_{CNT}	circumference of SWCNT
C_{kl}	when speaking of quantum calcultions, basis expantion coefficient
D	when speaking of MC simulation, diameter of agglomerate
d	when speaking of MC simulation,diameter of inclusion model
d	when speaking of diffusion, molecular displacement from the initial position.
d_{CNT}	diameter of SWCNT
D_{diff}	diffusion coefficient
E	when speaking of MD simulation, total energy
E	when speaking of mechanical properties, Young's elasticity modulus
e^-	electron charge
f_A	when speaking of MC simulation, fraction of fillers belonging to agglomerate
G	when speaking of thermodynamic quantities, Gibbs free energy
g	when speaking of Nose-Hoover thermostat/barostat, number of degrees of freedom
$g(r)$	radial pair distribution function
G_0	conductance quantum
h	when speaking of CNT shape, sine-wave period or step of helix
h_{film}	when speaking of self-assembled rings-and-rods molecular network, thickness of a thin film composite

K	when speaking of MD simulation, kinetic energy
K_b	when speaking of MD simulation, spring constant of harmonic bond
k_B	Boltzmann constant
k_{NEB}	spring constant in nudged elastic band method
L	when speaking of self-assembled rings-and-rods molecular network, rod length
l	when speaking of MC simulation, length of inclusion model
L_X	when speaking of mechanical properties, sample lenght in X direction
N	when speaking of percolation, number of CNTs per surface area, otherwise - any integer number
N_{CNT}	number of atoms in unit cell of SWCNT
P	when speaking of MD simulation in solvent, pressure
p	when speaking of MC simulation, probability density
p	when speaking of MD simulation, impulse
$P(\eta)$	when speaking of self-assembled rings-and-rods molecular network, probability to obtain connected network of desired sparsity
$P(\Theta, \Phi)$	when speaking of tatrakis-Schiff molecule, probability to find the molecule in the desired conformation
Q	mass associated with Nose-Hoover thermostat/barostat
q	when speaking of MD simulation, atomic charge
Q_{Zn}	when speaking of MD simulation, zinc cation charge in the fixed point carge molecular model
$R(\eta)$	when speaking of self-assembled rings-and-rods molecular network, resistance of the simulated network with desired sparcity
r^{min}	when speaking of MD simulation, distance at which pair interaction potential reaches minimum value

$R_{\mathcal{R}}$	when speaking of self-assembled rings-and-rods molecular network, ring's radius
r_B	Bohr radius
r_{ij}	when speaking of MD simulation, distance between atoms i and j
S	when speaking of self-assembled rings-and-rods molecular network, surface area of symulation box
s	when speaking of Nose-Hoover thermostat/barostat, additional dergee of freedom
s_i	when speaking of quantum calculations, electron spin
T	temperature
t	when speaking of MD simulation, time
$t_{\mathcal{R}}$	when speaking of self-assembled rings-and-rods molecular network, rim thickness (the diameter of the ring's rim)
T_{CNT}	period of SWCNT unit cell
$t_{i,j}$	when speaking of MD simulation, atom type index
U	when speaking of MD simulation, potential energy
U_b^{bond}	potential energy of covalently bonded interaction of bond or angle number b
U^{ext}	potential energy of external field
U^{nb}	potential energy of covalently bonded interaction of bond or angle number b
U_R	when speaking of umbrella sampling, restraining potential
$u_{1,2}$	when speaking of MC simulation, random numbers
V	volume
V	when speaking of self-assembled rings-and-rods molecular network, simulation box volume

$V(^*)$	when speaking of quantum calculations, electrostatic (pseudo)potential
V_{ex}	excluded volume
V_{XC}	exchange-correlation functional
W	thermodynamic work
w_I	weighting coefficients in WHAM
$W_{i,j}$	when speaking of self-assembled rings-and-rods molecular network, weight associated with the rod, connecting rings i and j
$x_i.y_i, z_i$	point or particle coordinate
m_i	when speaking of MD simulation, mass of atom i
N_C	when speaking of percolation, percolation threshold in terms of number of CNTs per surface area

Units

Å	angstrem
Ω/□	Ohm per square
Ω	Ohm
cm^2/Vs	centimeter squared per volt per second
S/m	Siemence per meter
S	Siemence
a.u.	arbitrary unit
atm	atmospheric pressure
B	byte
eV	electron volt
flops	float operations per second
g	gramm
K	Kelvin

m	meter
N	Newton
s	second
surf.%	surface percent
vol.%	volume percent
wt.%	weight percent

List of Figures

List of Tables

Chapter 1

Introduction

1.1 Motivation

Possibility to design novel materials by addition of nano-sized inclusions to polymer matrix attracts increasing attention in the last decades as a potential way to prepare functional composites, the properties of which could be fine-tuned by varying the nanoadditives' concentration and alignment inside polymer. Carbon nanotubes (CNT) and graphene nanoribbons are widely used as highly promising additives when high mechanical strength and good electrical conductivity are desired. However, development of such hybrid materials with predefined properties constitutes a hard challenge due to significant properties' variations depending on inclusion's distribution and interaction. The poor interaction of nanotubes with surrounding matrix and tendency to form agglomerates lead to decline of material properties' improvement with increasing concentration [1]. This problem is further complicated by high deviation of measured resistivities of nanotube-based microelectronic devices, depending on the nanotube types and geometry of the contact.

One approach to circumvent this problem is to use an additional component as a guiding agent for filler particles. The recently discovered ability of tetrakis-Schiff zinc-complexes to self-assemble into extended networks, composed of micrometer-sized rings, connected with thin rods, and to incorporate carbon nanotubes, present in solution in this self-assembled structure [2] opens the possibility of increasing control over CNT distribution and alignment inside polymer matrix and reduce the filler content require to achieve the stable properties. In turn, this approach replaces the problem of the optimal way to mix CNTs with polymer properly, by the challenge of molecular self-assembly studies inside polymer and in combination with the nanotubes.

In this thesis these challenges are approached using modern computer simulation techniques. To understand structure-property relations in pure CNT-polymer materials optical image analysis and numeric modelling are widely used, however matching such data with properties' measurements for industrial nanocomposites requires a link to be established between experimental and modelling length scales. In this work a software tool was developed to create a model composite structure with a predefined distribution probability of inclusions using NVIDIA CUDA GPGPU approach. The code is capable of randomly populating and analysing samples of the typical size of microphotographs used for experimental characterization and typical nanoinclusions' concentrations avoiding unphysical intersections and, thus, allowing to correlate the results of both optical characterization and statistical computer modelling. The initial probability distribution can be taken from experimental samples and further varied to investigate the effect of distribution on a desired property. In this thesis the tool is applied to study the effect of nanotube agglomerates on the polycarbonate samples' electrical resistivity.

A number of ways to deposit filler particles in a patterned way are known by present moment. This includes application of patterned matrices, thermodynamic effects, leading to formation of circular structures in evaporating solvents, as well as targeted self-assembly of ring-like macrocycles. The possibility of self-assembled networks of tertakis-Schiff zinc-complexes to surpass the limitations for the pure CNT-polymer composites is studied in this thesis using a simple Monte Carlo approach, using the available results of flat networks characterization. This study is followed by abinitial and molecular dynamics studies of such molecules behaviour in solvent environment to show. These studies are aimed to show that the formation of "rings-and-rods" like networks indeed occurs due to peculiar character of intermolecular interactions in such systems and could be explained without addressing to the aforementioned macroscopic effects. The significance of this fact is that the morphology of the networks (and, hence, of the carbon nanotubes containing composites and films) is determined by the chemical structure of the molecular complexes and, thus, could be controlled by synthesizing novel compounds with the structure optimized for the targeted self-assembly parameters.

1.2 Objectives

The main research objective of this thesis is to study the potential to obtain CNT-polymer composites with stable electric properties via application of tetrakis-Schiff zinc-complexes as guiding agents for nanotubes. To achieve this goal, the following intermediate objectives are outlined:

- Investigate the effect of CNT agglomeration and alignment on the polymer composites, processed with contemporary methods;
- Evaluate the potential of self-assembled "rings-and-rods" like molecular networks to serve as the CNT guiding agents for production of transparent films and polymer composites;
- Study the detailed behaviour of the tetrakis-Schiff zinc complexes in solvent environment and to suggest an explanation for the experimentally observed formation of self-assembled networks only from phenyl-functionalized complexes in dichloromethane out of other attempted structures and solvents.

1.3 Thesis outline

The thesis is structured as follows.

Chapter 2 summarizes the current state of the art in the field of carbon nanotubes (CNT) and materials, including them, with the special focus on their electrical properties and the sources of resistance. This chapter also introduces the methods currently used to form ring-like structures and names several examples, where such methods were used in combination with CNTs. Concluding this chapter is the brief overview on the development of Schiff-based metal-organic compounds and their self-assembling properties.

The literature review chapter is followed by chapter 3, which describes the theoretical foundations of the three simulation methods, used in this thesis: Monte Carlo (MC), molecular dynamics (MD) and abinitial quantum chemistry (QC) calculations. As several different implementations of these methods are used throughout this thesis, each of the following three chapters begins with a short methods section, naming the software tools and the details of the simulation procedure used in that chapter.

Chapter 4 describes computer simulations using simple Monte Carlo approach, augmented with non-uniform distribution of CNTs, derived from the data obtained by our colleagues from microscopic studies of experimental samples.

Chapter 5 describes Monte Carlo studies of the percolation characteristics of flat "rings-and-rods" like networks, basing on the statistical parameters re-

ported for experimentally observed tetrakis-Schiff networks [2]. With caution, the same procedure was extended to 3D case, where the self-assembled networks were also observed, but for which no reliable statistics could be measured so far. Predictions on the percolation threshold values of the CNT content in films and composites, where the self-assembled networks used as a guiding agent, are given in this chapter, showing the high potential of such complex structures for this application.

Chapter 6 describes the extensive studies of the tetrakis-Schiff zinc-complex molecules using modern molecular dynamics techniques. Basing on these studies a mechanism of self-assembling process is suggested and supported with free energy calculations for multi-molecular associates, serving the essential blocks of thus assembled molecular networks.

The key findings of this research are summarized in concluding chapter 7. Several directions for the future work are also outlined there as well as approbation of the research results via peer-reviewed publications and international conferences.

Chapter 2

Literature review

As was stated in the motivation section, the focus of this review is the application of the recently discovered tetrakis-Schiff molecules, capable of self-assembling into networks of interconnected rings, to guide carbon nanotubes in transparent and conducting films and novel composites. The aim of this chapter is to explain the benefits of such guiding as well as the specific character of this material among the vast variety of other self-assembling molecular structures. For this purpose a concise summary is provided here, reviewing the current state of the art in the field of carbon nanotubes in material design, with the special attention to their electric properties, and different approaches leading to formation of ring-like structures. It also introduces the reader to the field of Schiff-base complexes, especially salphen derivatives, and the recent advances in controlling their self-assembling properties.

2.1 Carbon nanotubes in polymer composites

Although evidences exist that the first electron microscopy images of tubular carbon nanofilaments were published as early as 1952 by Radushkevich and Lukyanovich in Russian Journal of Physical Chemistry [3], it was the observation of "helical microtubules of graphitic carbon" by Sumio Iijima in 1991 [4] that ignited the active research of this phenomenon throughout the international scientific community and became a turning point in several branches of modern science and technology, including chemistry, electronics and material design. Subsequent studies have clarified the growth mechanism [5] of so-called carbon nanotubes (CNT) and have shown that they can be up to 1 layer thick [6, 7], such nanotubes are called "single-walled" (SWCNT), and can withstand significant deformation without damage to their lattice structure [8]. Typically closed at both ends with

fullerene- like "caps" [5] they can be opened with thermal treatment and filled to transform into fibers with various properties [9].

It was also shown that CNT can have a variety of possible structures, depending on the direction in which the graphitic hexagonal lattice is rolled up to form the tube [10]. The tube's structure is commonly characterized by a pair of indexes (n, m) representing the direction of the vector $\vec{C}$, the endpoints of which are joined to form nanotube's circumference, in the terms of hexagonal lattice vectors $\vec{a}_1$ and $\vec{a}_2$: $\vec{C} = n\vec{a}_1 + m\vec{a}_2$, - as shown on the figure 2.1. Basing on the values of n and m an SWCNT can be of "armchair" $(n - m)$, "zigzag" $(m = 0)$ or chiral type $(n \neq m \neq 0)$.

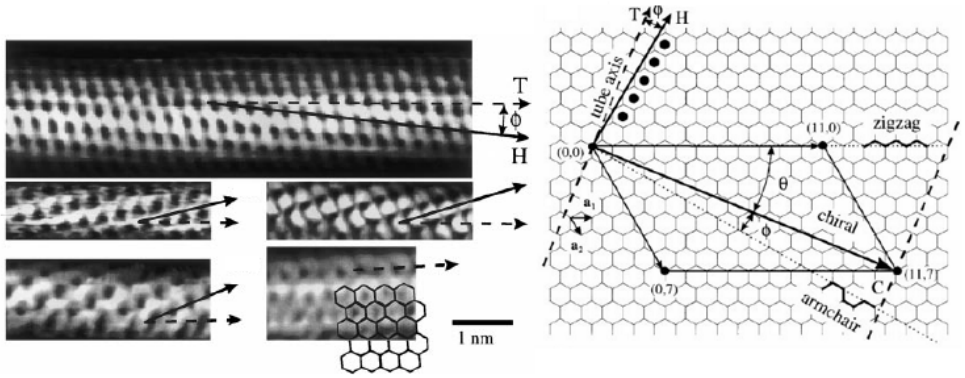

Figure 2.1: Atomically resolved electron microscopy image of CNT structure (left) and its representation as the stripe of a single graphite layer [10] (right)

Using these indexes and the length of graphitic average bond length $a_{CC} = 1.42\,\text{Å}$, other CNT geometry characteristics can be expressed, such as diameter (d_{CNT}, eq. 2.1.1), circumference ($c_{CNT} = |\vec{C}|$, eq. 2.1.2), lattice period in the direction of tube axis (T_{CNT}, eq. 2.1.3) and the number of atoms in such lattice (N_{CNT}, eq. 2.1.4) [11]:

$$d_{CNT} = \frac{a_{CC}\sqrt{3}}{\pi}\sqrt{n^2 + nm + m^2}; \tag{2.1.1}$$

$$c_{CNT} = a_0\sqrt{3(n^2 + nm + m)}; \tag{2.1.2}$$

$$T_{CNT} = 3a_0\frac{\sqrt{n^2 + nm + m^2}}{GCD(2n + m, n + 2m)}; \tag{2.1.3}$$

$$N_{CNT} = \frac{4(n^2 + nm + m^2)}{GCD(2n + m, n + 2m)}; \tag{2.1.4}$$

where $GCD(I, J)$ - is the greatest common divisor of the two integers I and J.

The electric properties of CNT also strongly depend on (n, m): if the difference of the two indexes is the multiple of 3, the CNT's electronic structure has a crossing of bands at the Fermi level and, therefore, has conductivity of a metallic type, in the opposite case the nanotube is semiconductor with a bans gap of ~ 0.5 eV [10]. Furthermore, being an exceptional example of long extended π-conjugated system, CNTs possess a specific conduction mechanism - ballistic conduction, due to which the minimal resistance of a single SWCNT in the absence of defects and thermal noise can be as low as $1/2G_0 \sim 6.5\,\mathrm{k}\Omega$, where $G_0 = |e^-|^2/\pi\hbar = 77.5\,\mu\mathrm{S}$ is the conductance quantum - the conductance of a single channel in the absence of scattering (multiplied by 2 to account for electron spin), e^- being the charge of electron and $\hbar$ - reduced Plank constant, which was proved by experimental measurements under ultra-low temperatures [12, 13].

In a number of studies the unique properties of CNTs were employed to design single-molecule transistors [14–17]. The field effect transistor properties were demonstrated for individual semiconducting SWCNT under room temperature conditions in [14]. In [15] Shea, Martel and their co-workers have fabricated ta number of multiwalled carbon nanotube (MWCNT) three terminal devices that proved to have metallic type conductivity with the full device resistance of $\sim 100\,\mathrm{k}\Omega$ as was expected for this kind of tubes. This behavior was altered if the CNT contact points were pressed to collapse into almost flat layers: the resistance was found to vary from 76 to 120 kΩ. Attributing all conductivity only to the outer shell the single wall conductivity was estimated to be $\sim 32\,\mathrm{k}\Omega$. In [17] single CNTs were folded into ring-like coils, held by strong van der Waals attraction between the segments, without loss of metallic conductivity with the resistance $\sim 10 - 15\,\mathrm{k}\Omega$. Transistor properties were also observed for "intramolecular" junctions: for fused silicon nanowire-CNT [18] and metallic-semiconducting CNTs [19] junctions. In the former case the resistance across the junction was measured to be 608 kΩ, while the resistances of the tubes were 56 and 101 kΩ. In general, the properties of such junctions strongly depend on the band structure details of the parts of junction, so one has to employ quantum level calculations to describe each individual junction type [20].

As it follows from the experimental observations, the single metallic CNTs generally has resistances of the order $\sim 100\,\mathrm{k}\Omega$, so the contact resistance become non-negligible. In [16] for a SWCNT-bundle transistor with the golden electrodes Lui and co-workers estimated the tube-electrode contact resistance of $\sim 3.3\,\mathrm{M}\Omega$. In the previously mentioned work [15] Shea and Martel also report a contact resistance as high as $\sim 1.1\,\mathrm{M}\Omega$ for a SWCNT device (although for MWCNT

in the same paper the contact resistance was estimated to be only $\sim 23\,\mathrm{k}\Omega$). So high contact resistances may originate from the presence of impurities or charge transfer between CNT and metal with different work function: electrons redistribute between the tube and electrode in the contact region until Fermi levels are aligned, creating a Schottky barrier [21].

The problem of contact resistance becomes even more important for CNT intermolecular junctions. Fuhrer and co-workers have measured the contact resistances for a number of crossed SWCNT of different types [22]. Their setup represented a 4-terminal device where each of the crossing CNTs was attached to a pair of electrodes forming almost 90° angle between the tubes. The contact resistances measured by them for junctions of two metallic CNTs varied in the range of 90-360 kΩ (corresponding to conductance of 0.04-0.14 G_0), while for junctions of semiconducting SWCNTs the resistance up to 1.3 MΩ (0.01 G_0). The conductance of metallic-semiconductor type junctions were two orders of magnitude smaller indicating the formation of a Schottky barrier. In [23] the resistance over crossover points of individual CNTs and their bundles were studied using conductive atomic force microscope. It was shown that such junction resistance can vary from 98 kΩ for individual metallic SWCNT junctions and 230 kΩ for single SWCNT-small diameter bundle to 2.7 MΩ for the crossings of large diameter bundles.

In [24] the authors studied the contact between individual nanotube and graphite sheet depending on the angle of rotation and report contact resistance oscillations from 1 to 45 kΩ with the period of 60°. The minimal resistance was found for so-called "in registry" mutual orientations, for which the two hexagonal lattices are stacked as the two layers of graphite, so the Fermi wave vectors are parallel and, therefore, the electron moment is preserved upon crossing of the contact. The same problem of lattice matching was also studied theoretically for the contact between the two metallic nanotubes in [25]. In agreement with the aforementioned experimental works, oscillations of conductivity with the lattices mismatch angle was found. The "in registry" contact resistance for the crossed CNTs was evaluated as 2 MΩ for the rigid nanotubes, but decreased to 682 kΩ when the atomic geometries were relaxed and to 121 kΩ if additional forces were applied to simulate the effect of substrate surface adhesion. The "out of registry" resistance was found to be 3.36, 3.21 and 1.66 MΩ under the same assumptions. Furthermore, the effect of the contact length was studied for the two parallel semi-infinite CNTs. For the two armchair nanotubes oscillations of the conductance from almost 0 to 0.3-0.4 G_0 with the period equal to half of Fermi wavelength.

For zigzag type tubes the oscillations had the period of hexagonal lattice and were related to the overlap of atomic positions. It was also reported that the contact resistance increases with the tubes diameter as the weight of the contact region decreases for the conducting channel, spread over larger circumference.

An interesting approach to the contact resistance problem was suggested in [26]: by passing electric current through junction of two CNTs the authors were able to locally decompose metal-containing precursor vapor by the heat generated in the junction and "solder" it with Pb or HfB_2. This resulted in ~ 6 times increase of direct current.

Even more sophisticated the question of electrical conductivity becomes for flat and bulk materials, containing CNTs. In the aforementioned [23] the direct current (DC) conductivity $\sigma_{DC} = 6 \cdot 10^5\,\mathrm{S/m}$ for acid treated films of CNTs that decreased to $\sigma_{DC} = 9 \cdot 10^4\,\mathrm{S/m}$ after thermal annealing (corresponding to sheet resistance 110 and 285 $\Omega/\square$[1]) with transmittance ~78-79 %. This is 1-2 orders of magnitude lower than the conductivity of individual CNTs measured in the same work: $\sigma_{DC} = (4.4 \pm 1.6) \cdot 10^7\,\mathrm{S/m}$ for SWCNT and $\sigma_{DC} = 8 \cdot 10^6\,\mathrm{S/m}$ for MW-CNT. The authors of [27] have studied the conductivity of SWCNT films as the function of the films' thickness and temperature. They have observed that the very thin (thickness of the order of one CNT bundle, transmittance in range 30-95 %) have semiconducting type of conductivity, for which the resistance decreases with temperature. Conductivity of a thick film ($\sim 35\,\mu\mathrm{m}$) was found to have a large metallic component, staying finite even at very low temperatures and possessing a maximum at room temperature, after which the resistance increases due to thermal scattering or CNT expansion. This occurs because of SWCNTs with different conductivity type are mixed in such networks: for the thinnest films the conductivity is dominated by Schottky barriers in metallic-semiconducting CNT junctions; in the same time in the thick film contacts between highly conductive metallic CNTs dominate the film performance. The non-linear character of resistivity with temperature was explained by electron tunneling between metallic CNTs, at the temperature ~ 230 K electron-phonon scattering starts to dominate the resistance and, thus, its temperature dependence changes to metallic type.

In [28] the decrease of film conductivity as temperature decreased was also observed for a 100 nm thick SWCNT network. As in the previously reported work, the authors employ the "fluctuation induced tunneling" mechanism to explain this behavior. This mechanism describes the current through the CNT-CNT junction

[1] "Ohm per square", the unit used to characterize resistivity of flat conductors originating from the fact that a square film of any size would have the constant resistance.

via electron tunneling, additionally introducing the change of voltage between the conducting sides due to thermal fluctuations, it follows then that the conductance of such tunneling junction has the following temperature dependence [29]:

$$\sigma = \sigma_0 \exp\left(-\frac{T_1}{T + T_0}\right); \tag{2.1.5}$$

where σ - is the electrical conductivity, T - temperature, σ_0, T_1 and T_0 are used as fitting parameters. The authors of [28] estimated T_1 as $289 \pm 79\,\mathrm{K}$ and T_0/T_1 as 0.3 ± 0.19, thus at room temperature the increase of conductivity due to thermal fluctuations is small and metallic type resistivity dependence is restored. In contrast, the authors of [30] prepared a bulk material of densely packed MWCNT and graphite particles and studied its conductivity over wide range of high temperatures: from 328 to 958 K. They have shown that for such material even at high temperatures the conductivity maintains a weak growth from 1.02 to 1.38 S/m, unexpected for metallic systems. The authors explained this in terms of fluctuation induced tunneling between CNTs and electron hopping between graphite particles. However, thermal expansion of CNT diameters, suggested of one of the possible sources of conductivity temperature dependence in [27], was completely neglected, although at high temperatures in such dense bulk materials it can lead to an increased contact area, unlike the thin film case.

As the flat films of CNTs are viewed as a perspective conducting transparent electrode material various groups have studied so-called "percolation" behavior of such films' conductivity [31, 32]. The term "percolation" is used to describe the transport processes in random media. Applied to materials, where electric conductivity is created by randomly distributed conductive particles, it speaks of the formation of "culsters" of connected particles, i.e. a collection of particles through which the charge can travel due to pairwise electric contacts between them [33]. Modelling CNTs as the sticks of infinitely small thickness, the authors of [31] have shown that the experimental measurements for transparent CNT networks are well described by the percolation law:

$$\sigma \sim (N - N_C)^{\delta}; \tag{2.1.6}$$

where δ - is the parameter called "percolation exponent" and dependent on the particle geometry and dimensionality of space, N - is the number of CNTs per surface area, N_C - the percolation threshold, according to theory, the value of N, for which an infinite conducting cluster appears, i.e. the threshold after which a macroscopic sample becomes conductive. The later quantity was estimated using

the formula for a collection of randomly dispersed sticks of equal length [34] :

$$l\sqrt{\pi N_c} = 4.236; \tag{2.1.7}$$

where l - is the length of a stick (CNT). In [31] found $N_C \sim 1.2$ CNTs per μm in close agreement with 1.43, predicted by equation 2.1.7. The best fit was achieved for the value of percolation exponent $\delta = 1.5$ compared to 1.33 as was predicted theoretically. In [32] the equation 2.1.7 was rewritten in terms of CNT volume fraction - the ratio of the CNT volume to the film volume. The authors found the percolation exponent to be 1.65 and the volume fraction of metallic CNTs at percolation threshold $\sim 5.5 \cdot 10^{-3}$. This is 1/3 of the CNT content as only about the third of all CNTs are metallic. Below this value the films conductivity type changed to semiconducting up to the CNT fraction of $\sim 9 \cdot 10^{-4}$, where the films represent non-connected networks.

An important contribution to the understanding of CNT films conduction was done by an international group of researchers in [35]. The authors compared the morphologies and properties of the CNT networks, deposited from vapor by four different methods: electrostatic or thermal precipitation, filtration with either subsequent press transfer or dissolving the filter, and inspected the networks characteristics for optoelectronic application: charge mobility (directly related to network conductivity) and electric current change as the function of gate electrode voltage (ON/OFF ratio). Although the CNTs were produced the same way and all networks consisted of single SWCNTs and bundles of 2-7 CNTs, the deposition technique strongly affected network density and morphology and thus electrical properties.

Electrostatic precipitation resulted in dense deposition and high amount of bended CNTs, causing band-gap opening and, hence, change of metallic conductivity type to semiconducting. Such networks had the highest ON/OFF current ratio $\sim 5 \cdot 10^5$, but low charge mobility ($\sim 2-13$ cm^2/Vs). The networks obtained via thermal precipitation had the lowest density of CNTs with preferred orientation, tuning deposition time allowed to achieve ON/OFF ratio up to 10^5-10^6 while keeping carrier mobility at 20 cm^2/Vs. It is interesting that the networks produced via filter dissolution exhibited the highest carrier mobility (40-50 cm^2/Vs), but lowest ON/OFF current ratio (2-8). This attributed to large number of Y-junctions, formed by solvent, having lower resistance due to larger contact area.

The same challenges of the contact resistance, percolation and morphology emerge in the area of polymer composites. The number of works in this field over the past years has increased exponentially due to advances in research methods

on the one hand and high industrial potential of such engineered materials on the other. The detailed review of these works can be found in outstanding overviews [36, 37]. Here only the key issues and approaches will be mentioned.

One moment needs to be cleared here to prevent confusion. There are two ways to characterize the CNT content in such composites: the fraction of filler volume (vol.%) and the fraction of filler weight (wt.%) in the final composite. The former is commonly used in theoretical estimations, where only geometrical parameters matter. However, experimental studies usually report the results in the terms of weight fraction as, unlike the volume fraction, this property can be directly measured.

From theoretical point of view the conductivity of such composites is described by percolation of conductive CNTs. This was especially convincingly demonstrated in [38] by straining the stripes of CNT-polyethylene oxide composite, where the nonlinear conductivity curve, characteristic for percolation type behavior, was clearly observed. However, in contrast with the case of flat films, in bulk composites the percolation threshold must take into account finite thickness of CNTs as they are not allowed to intersect. This is taken into account by the excluded volume theory [39]. Within it the estimate of percolation threshold for randomly distributed "sticks" or rod-like particles in a 3-dimentional space (ϕ_{3D}) is given by inequality:

$$1 - exp\left(-\frac{1.4V}{\langle V_{ex}\rangle}\right) \leq \phi_{3D} \leq 1 - exp\left(-\frac{2.8V}{\langle V_{ex}\rangle}\right); \tag{2.1.8}$$

where V is the volume of a stick (equal length and thickness are assumed for all particles) and $\langle V_{ex}\rangle$ is the "excluded volume" - volume of the space around particle's center, in which the center of another particle cannot be found, averaged by angle between the stick's axises. For a cylindrical filler particle the length of which is 1000 times larger than its diameter (typical CNT aspect ratio) the estimated percolation threshold is of the order of 0.1 vol. %.

Despite quite promising estimates form the equation 2.1.8, the main problem standing between laboratory studies and commercial production is the stability of the results. As can be seen from the tables in [36, 37], the composites of the same polymer matrix with CNT of similar type may have from several times to order of magnitude difference in final mechanical and electric properties due to details of the composite processing. For example, for MWCNTs with aspect ratio $\sim 10^3$ in epoxy the percolation thresholds achieved by several groups varied from 0.011 to 0.03 wt.% and maximum conductivity of the composite - from 0.01 to 0.4 S/m.

A number of experimental studies of thermal and concentration dependencies of such composites' electrical properties have shown that their conductivity is dominated by tunneling in CNT-CNT contacts, rather than CNT resistance itself [40,41]. However, tuning the CNT distribution morphology inside the polymer matrix to enable good electrical contacts is yet more sophisticated task then for the case of thin films. The main problem here arises from the fact that CNTs, being extended conductors, attract each other via quite strong van der Waals forces, but interact poorly with the surrounding polymer. As the result the nanotubes, embedded into polymer matrix, aggregate into micron-sized agglomerates [42].

To improve exploitation of CNTs properties different approaches exist. One of them is pre-processing of CNT material using sonication [42] or treatment with dispersing agents [43] to break the agglomerates, initially present in the CNT powder. Intensive stirring in also used to break the remaining agglomerates with shear forces on the mixing stage [44]. The effect of polymer matrix composition on the percolation characteristics of the dispersed CNTs was also studied in [45]. Chemical functionalization of CNTs was also used to improve the CNT-polymer interaction [46, 47]. In [48] an interesting approach was demonstrated: the short fragments of CNTs were connected "end-to-end" with linker chains to create a dendrite structure. However, chemical treatment damages the outer shell of CNTs, the most responsible for conductance, so non-bonding or wrapping functionalization is actively studied for the applications where the best conductivity is required [49].

However, the influence of CNT agglomeration on the composites' electric conduction is not strictly negative. It was shown in [50] that, besides reducing the effective fraction of CNTs, employed in electric conduction, the agglomerates also increase the CNT-CNT contact surface, therefore improving overall conductivity.

Furthermore, it was demonstrated in [51] that CNT alignment by post-fabrication stretching of composites can enhance the conductivity by the factor of 2. This phenomenon was also studied theoretically in [52]. It was shown that conductivity-alignment dependence is not linear: although alignment can increase the anisotropic conductivity by creating the paths for current with fewer junctions in the preferred direction, it also decreases the probability of intertube contact, increasing percolation threshold beyond certain point.

2.2 Formation of the ring-like structures

Ring-like structures and their networks of different molecules were observed by various groups for more than 15 years. To show how the "ring-and-rods" networks of tetrakis-Schiff molecules are different from those studied before, a concise summary of the main ring forming mechanisms studied by far is given here. This includes the dewetting processes, where the ring shape is "inherited" by the solute molecules from the circular rim of the evaporating solvent, toroid globule formation in semi-flexible polymers and self-assembly of nanometer-sized ring-like molecules.

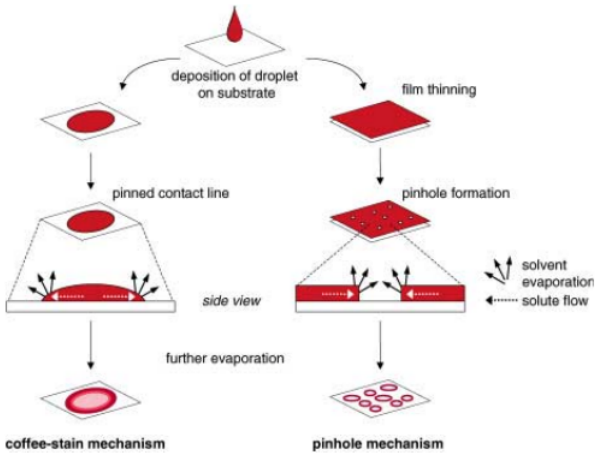

Figure 2.2: Schematic explanation of the "coffee-ring" and "pinhole opening" effects [53]

One of the most studied and controllable ways to produce ring-like structures is the so called "coffee-ring" or "coffee-stain" effect (figure 2.2). It borrows the name from a well known observation that a spot after a drying coffee drop would have the rim colored more intensively than its middle part. This occurs because the higher the curvature of the liquid's surface the faster its molecules evaporate. This difference between the curvature on the sharp edge of droplet and its almost flat central part creates the gradient of evaporation speed that results in the lateral flows of solvent molecules from the droplet center to its periphery, bringing the solute molecules to the rim [54]. In general, this effect represents a problem, when the uniform deposition is required [55]. However, it can also be a convenient tool to form the standalone rings of the solute material with well defined diameter and position. Ring-like structures of amorphous carbon were produced this way in [56]. Rings of metal-organic compounds were also reported in [57]. Combined with ink-jet printing technique this mechanism was successfully employed to produce networks of CNTs with 80% transparency and sheet

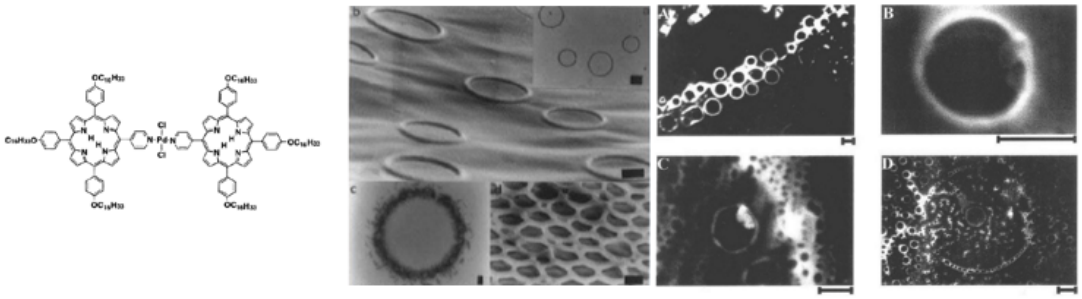

Figure 2.3: PtP molecule structure (left) and their self-assembled rings observed by transmission electron [60] (center, scale bars equal to 1 μm for *a*, *b* and *d* and 30 nm for *c*) and confocal fluorescence [61] (right, all scale bars represent 10 μm) microscopy

resistance as low as $\sim 150\,\Omega/\square$ [58]. The CNT rings obtained with this method are 100s of μm in diameter and about 300 nm in height, so their rims are formed with dense bundles of CNTs. To achieve such results a complex equipment was required to deposit several layers of drops precisely displacing the next layer to create overlapping rings. Furthermore, the transmittance of 80%, although being a great achievement for the field, speaks of a quite significant surface fraction of CNTs that is quite far from the theoretical predictions for random distribution of CNTs on surface.

The so called pinhole mechanism, observed in flat evaporating films, is tightly linked to the "coffee-ring" effect being, in certain sense, complementary to it (figure 2.2). It has the same driving force - the lateral flows induced by the difference of evaporation speed that drags the solute molecules closer to the circular rim. However in this case the liquid occupies the surface around the opening hole, hence the name of the effect. The surface of the thin liquid film exist in an unstable equilibrium so the hole formation can be triggered by any irregularity, for example by a particle or drop of non-mixing liquid, accidentally "punching" the film and initiating a growing 2D "bubble" (figure 2.2) [59]. Unlike the previously mentioned "coffee-ring effect" it can be used to create wast connected networks on a substrate. Furthermore, it is possible to control the concentration and size of the such formed rings by controlling the concentration of "seeds" - the particles or droplets, used to initiate pinholes.

Pinhole mechanism was used to explain the formation of self-assembled micrometer sized porphyrin platinum dichloride (PtP) rings, observed after solvent evaporation in [60, 61] (figure 2.3). Schenning *at al.* studied the effect of concentration on the forming structure: it was reported that at PtP concentration of 10^{-6} M separate, well defined rings could be observed, while at higher concentrations ($\sim 10^{-2}$ M) ta honeycomb lattice is formed. The same paper also reports

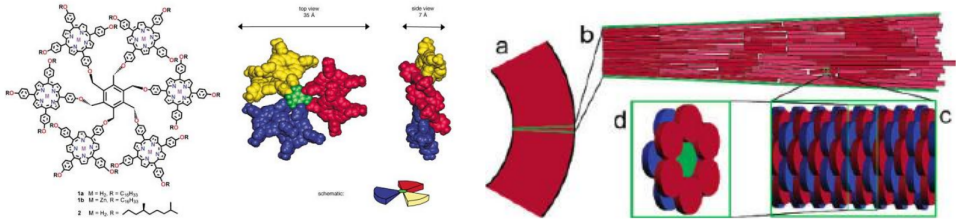

Figure 2.4: Porphirin disk-shaped molecule [53] (left) and the suggested hierarchical structure of the micrometer scale self-assembled from it [62] (right)

the effect of solvent and found that the most ideal rings could be obtained from carbon tetrachloride (CCl_4). Replacing it with chloroform ($CHCl_3$) or dichloromethane (DCM, CH_2Cl_2) led to less perfect structures. This was linked to the increasing speed of evaporation as the formation of the perfect ring requires more time. When tetrahydrofuran (THF) or toluene (TOL) were used as solvents, no rings were observed. The authors specifically outlined that, in general, the PtP must be present as standalone monomers in solvent to form the rings. Comparing the possible explanation of the rings' formation, the authors also considered the formation of aggregated porphirin domains that undergo a circule-torus transition, but rejected this possibility on the grounds that such mechanism is concentration dependent, while the porphyrin "wheels" were observed in a wide range of concentrations.

Hofkens *at al.* has also observed PtP rings with an irregular structure [61]. Using confocal fluorescence microscopy they showed that the large rim of the ring in turn consists of smaller rings. It was suggested that smaller rings arrange around small gas bubbles that then fuse together in a larger ring due to a pinhole dewetting.

Self-assembled rings were also observed by [53] and [62] for aggregates of porphirin hexamer and dodecamer molecules (figure 2.4). Lensen and co-workers suggest that such molecules, having almost flat disk-shape, assemble into columnar stacks. These columns aggregate in hexagonal packs and align around pinhole by solvent flow, oriented perpendicularly to it. The resulting ring has the rim thickness equal to the stack height ($\sim$ 200 nm) and height of the ring is equal to the diameter of agglomerate of stacks (15-20 nm). Such model was supported by fluorescence microscopy study by [62], indicating uniform symmetric distribution of the molecule dipoles along the ring. Jeukens *et al.* also studied intensively the effect of a various substrates on the formation of rings by pinhole mechanism. They report that the well defined rings were formed both on hydrophilic and hydrophobic glass, however, untreated glass, mica or pyrolytic graphite results

into no rings or network of merged rings. Furthermore, high humidity ($\geq 60\%$) is required for the formation well defined and uniform in size rings. These observations speak in favor of pinhole mechanism as it requires slow evaporation and uniform substrate surface.

Takazawa *et al.* produced 5-30 μm rings of thiacyanine (TC) molecules with wave-guiding properties from evaporating chloroform solutions as reported in [63]. Again, high humidity was needed to enable the rings formation. Takazawa and co-workers were able to control the rings quality by tuning solute molecules interactions. This was achieved by changing the length of the functional group, connected to TC base. "Short-tailed" TC molecules (with 2 monomer long side group) strongly bind to each other by $\pi - \pi$ interactions are capable of self-assembling into $\sim 100\,\mu$m long fibers under normal conditions. Such molecules begin to stack early and, in humid environment, formed rings with irregular outer rim. Increasing the length of the side groups (4 and 8 monomer long) reduced TC molecules "stackability", allowing the aggregation only in the highly concentrated region around the pinhole. Thus smooth regular rings were formed from such molecules. In contrast with the porhyrin rings, where the fluorescence imaging showed the radial orientation of molecular stacks around the pinhole, TC molecules were divided into regions with uniform dipole orientation. To explain this Takazawa and co-workers suggested that the domains are formed in solvent yet before the pinhole opening and remain during the dewetting stage.

The ultimate application of the hydrostatic forces to produce arrays of micrometer-sized rings or connected honeycomb lattices controllable way is the method of "breath-figures": the solvent film, containing polymer chains, evaporates under the flow of humid air, as the solvent temrepeture decreases below the dew point, droplets of water condense on the liquid surface, arranged in a hexagonal lattice by the capillary forces and convection of raising solvent vapor, as the solvent evaporates and the droplets cool down, they dip into the solution, serving as the seeds initializing pore formation in the solvated polymer [64].

Nanosized rings of symmetrical phthalocyanine nickel-complexes with irregular outer rim were observed in [65]. Although the authors suggest that the same solvent evaporation-driven mechanism as for the aforementioned porphyrin rings is behind the ring shape formation here, in this study aggregation of solute molecules occurs not due to their deposition on a solid substrate, but on the air-solvent interface. Due to this the rings in this study were smaller compared to those observed by the groups of Schenning and Hofkens (inner and outer diameters of 50 nm and 70-150 nm correspondingly). A striking difference here, is

that the formation of the rings of phthalocyanine molecules was observed even at very small initial concentrations, which indicates that aggregation occurs due to the strong intermolecular forces between the complexes and not only due to the pinhole opening. Change of the functional groups an decrease of the temperature hindered the formation of the rings. In case of the lower temperatures nanocrystals formed instead of the rings.

The authors of [66] report a successful self-assembling of sparse networks with circular pores or honeycomb lattices formed by protoporphyrin molecules. In contrast with the "porphyrin wheels", observed by Schenning *at al.*, in this case the networks could be deposited from the polar solvent (dimethyl sulfoxide), while no assembly was observed in non-polar chloroform. To explain this Bhosale and co-workers suggest that polar solvent does not interact strongly with the molecules due to hydrophobic chains, thus protoporphyrin self-assemble into long fibers that form network or lattice structure. The circular shape of pores in this case, most probably, is still induced by hydrostatic effect, however, unlike the aforementioned results of Jeukens and Takazawa, molecular aggregation occurs in liquid phase rather then in the pinhole rim region, thus the long fibers are wrapping the holes and not aggregate radially or in some preferred domain orientation like the shorter columnar stacks reported in [62, 63].

Carrol *et al.* have reported the deposition of toroids of poly(n-hexyl isocyanate) from evaporating solvent film on mica surface [67]. The polymer was functionalized with chiral photochromic side chains to induce helical structure of backbone. The toroids were 40-60 nm high and had an external diameter $\sim 2\,\mu$m and internal - in the range of 400-900 nm. This behaviour was observed in chloroform, tetrahydrofuran and toluene without significant changes. Although not completely excluding the possibility of pinhole mechanism, the authors still point out that in this case the deposited polymer most likely would collapse into a droplets, rather then stay in ring form as observed here. Also no toroidal structures were observed without the aforementioned functionalization. Instead it is suggested that the polymer, having a preferred helical shape, folds into a coil, oriented perpendicularly to the surface, as the solvent evaporate.

Chains of certain polymers can assume toroidal shape upon condensation even without special groups due to specific elastic properties [68]: on the short range such chains are quite rigid, however, on the larger scale small rotations adds up and the chain behaves as a flexible string, different parts of which can move independently. This behaviour is called "semi-flexibility". Elasticity of such polymers is characterized by "persistence length": the distance along the chain at which

movement of two monomers can be considered independent. Due to this property, when the chain condensates upon changing the solvent conditions (solvent evaporation or replacement with incompatible solvent), segments shorter then persistence length cannot bend freely and align parallel to each other, however the segments that were further away along the chain can come in contact with the former and became the part of the same packing with them. Thus if the initial metastable loop is created, the chain folds upon it to form a stable donut-like structure [69]. Formation of a number of rod- and ring-like structures according to this mechanism was observed for xanthan complexes in [70] and the stability of torus shape was demonstrated with thermal annealing. Although the chains much longer then the persistence length of the polymer should, theoretically, be flexible enough to form spherical globules, it was shown in [71] that even in such case the stage of toroidal globule can exist as a metastable intermediate state between extended coil and compacted spherical globule, thus the chains can be kinetically "arrested" in this state by freezing or if the solvent evaporates too fast.

One of the most intensively studied examples of such behaviour is the formation of rod-like and toroidal structures by DNA molecules [72]: in solvent environment DNA is charged and residues of the same charge repel, forcing the molecule to unfold into a coil, however, if the oppositely charged ions are present in solution, the electrostatic repulsion is shielded and DNA folds back into a rod-like or toroidal globule. Using transmission electron microscopy it was shown in [73] that the shape of toroid cross-section can also be controlled by the choice of the condensation agent. The typical size of such toroids is $\sim$ 100 nm [74] that can be explained by the competition between the surface energy, entropy and impact of topological defects [75]. The shape of such globule can be varied from rod to toroid by using different condensing agents [76]. Although initially partially folded globules were thought to be unstable [77] such structures were observed in the form of "necklace" [78] and "rings-on-string" [79] globules (figure 2.5) and explained as the result of balance between electrostatic and entropic effects [80].

Bazler *et al.* also observed rings of self-assembled fibers in [83]. However unlike previous examples, where the change of the solvent conditions caused the ring-like structure formation, here the nanostructures were formed by deposition of p-phenilene directly from gas state in vacuum chamber. In this case, supporting surface determined the type of nanostructure that was assembled on it: on hydrophilic mica surface needle-like rods of p-phenilene grew directly on mica surface and were oriented by strong surface dipole fields, however, if treated with

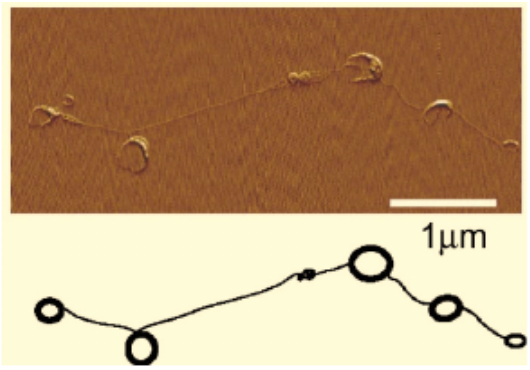

Figure 2.5: "Rings-on-a-string" globule of compacted DNA [81]

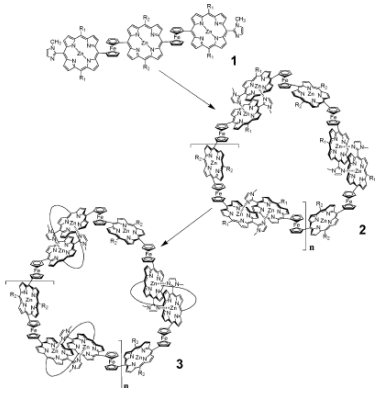

Figure 2.6: Formation of nanorings by self-assembly of Zn-substituted porphyrin trimers [82]

water or methanol, the mica surface became hydrophobic and the molecules deposited parallel to the surface and self-assembled into curved strings or closed rings 2-6 μm in diameter.

Finally, microcycles of several zinc-substituted porphyrin dimers and trimers were synthesized by [82, 84, 85]. In this assemblies the porphyrin bases are connected by $\pi - \pi$ and cation-π interactions between imidazole residue and zinc ion or ferrocene bridges resulting in formation of a stable nanosized ring-like association (figure 2.6). It is reported that such coordination interaction can be formed in non-polar solvents and decomposes in polar. Although such macromolecular cycles are a few nm in size and not suitable for network formation or CNT guidance, these works represent an important examples of ring-like structures formed only due to the molecule shape and non-bonding interactions, rather than due to external hydrostatic effect.

2.3 Metal-organic complexes of Schiff bases

Schiff base is a common name for chemical compounds with the general formula $R_2C{=}NR'$, where $R' \neq H$ [86]. Schiff-base compounds where R contains a hydroxyl group are well known for the ability to bind metal ions with negatively charged N and O atoms, which gives them valuable catalytic properties [87]. To improve the later significant scientific effort was devoted to study the influence of molecular structure on chemical and electronic properties of such compounds.

Benefiting from their ability to form nanoscale supramolecular aggregates due to hydrogen bonds or oxygen-metal ion interaction between adjacent molecules a

number of multi-metal center clusters were synthesised [88, 89]. Since such molecular agglomerates are connected only with non-covalent bonds, their structure and properties are strongly affected by interactions with solvent molecules. In several papers acetate ion was reported to act as a binding agent bridging two Zn-salphen complexes together [90, 91]. Using XRD analysis it was shown [90] that Zn ion is displaced from its original position in N_2O_2 plane due to interaction with anion. Zn-O bond length was measured to be 2.0269(8) Å, compared to 1.9590(9) and 1.9733(10) Å for Zn-O(salphen). Varying the solvent in which the reaction between ligand and copper salt occurs, the authors of [87] obtained the four different compounds, representing a ligand dimer stabilized by additional Cu ions and solvent molecules. Methanol, ethanol and n-butanol produced partially deprotonated complexes with two Cu ions each enclosed in N_2O_2 cite of each ligand and additionally coordinated by oxygen of solvent molecules. Yet another Cu ion was found to bond the two ligands together interacting with four oxygen atoms, two from each ligand. However, a different structure was found for n-propanol: this time ligands were completely deprotonated and bonded by a pair of additional Cu ions, while the ions, enclosed in N_2O_2 cites were additionally coordinated by water molecules. Another intriguing feature of that last compound is that hydroxyl groups of propanol molecules participate in hydrogen bonds with one of the ligand's deprotonated oxygens and with hydrogen of the coordinated water molecule. Thus a molecular bridge is created binding Cu-ligand dimers into potentially infinite supramolecular structure.

Due to $\pi - \pi$ interaction between aromatic side groups such molecular aggregates can further assemble into crystal structures in solid state. As an interesting indication of relative strength of the interactions involved, in the work [92] photoluminescence spectra were compared for zinc-substituted complexes of tridentate[2] Schiff based ligands in different solvents. It was noted that the two distinct dimeric assemblies could be obtained from the same ligand by reaction with $Zn_2(ClO_4)_2$ and $Zn(NO_3)_2$. In solid state both have a crystalline structure stabilised by $\pi - \pi$ interactions, which is easily dissolved. However, in the former case the the two Zn ions of the adjacent complexes are well separated and molecular dimer holds due to hydrogen bonds that remains in DCM, but decomposes in THF. In the later Zn and oxygen ions interact directly and complexes remain dimerized in both solvents.

An experimental observation of Schiff-base zinc compounds dimerization effect on the compound's electronic properties was reported in [93]. Five bis-Schiff

[2]i.e. binding metal ion with 3 negatively charged atoms.

base Zn complexes with different side-groups were produced two estimate their performance as OLED materials. For those three out of them, which had a planar geometry, a red shift of solid-state photoluminescence spectre peak was observed with respect to liquid-state. In the same time the two non-planar complexes showed a blue shift. The authors explained this with strong inter-molecular interactions, appearing from Zn-O attraction in dimeric aggregates.

A special type of Schiff compounds are symmetric salen and salphen ligands (figure 2.7), obtained by adding 2 equivalents of salicylaldehyde (C_6H_4CHO-2-OH) to 1 equivalent of ethylenediamine ($C_2H_4(NH_2)_2$) or ortho-phenylenediamine ($C_6H_4(NH_2)_2$) respectively [94].

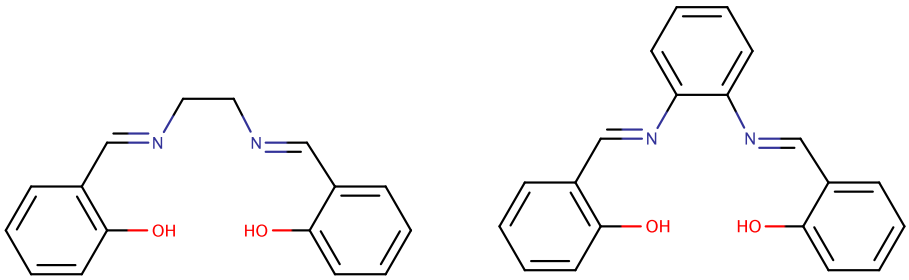

Figure 2.7: Salen (left) and salphen (right) ligands.

Salen/salphen-based complexes were thoroughly studied by several groups as potential building blocks for molecular self-assembly [95]. The reason for this is that in case of symmetric and almost planar salen/salphen ligands Zn ion binds an oxygen atom of the adjacent monomer in axial position, i.e. in the direction perpendicular to the ligand's plane [96]. Due to this binding anisotropy, supramolecular assembly of zinc-salphen complexes into microscale fibrils and gels was demonstrated by the group of MacLachlan in [97]. The formation of continuous assembly was attributed to consequent binding of zinc and oxygen ions of adjacent monomers rather than to commonly expected pi-pi interactions or hydrogen bonds, as complexes containing Ni centers produces poorly defined complexes compared to Zn based complexes, while Cu or vanadyl based complexes showed no fiber assembly. It was also shown that fibrils parameters could be controlled by addition of functional groups. Soluble groups (such as glucose and galactose for methanol) narrowed the fiber diameter down to 5-7 nm, compared to tens of nm before. In the same time functionalization with tert-butyl groups was shown to prevent aggregation, which was attributed to high steric stress induced by them. Self-assembled gels were produced by condensation of metal-salphen complexes from aromatic solvents such as benzene, toluene and o-xylene. In the

same time pyridine was shown to disrupt gelation.

Thorough study of a number of zinc-salphen based compounds was conducted in [98]. It was reported that dimerized compounds were the dominant form both in solid state and in solution for most of the studied compounds except for the compound, functionalized with two tert-butyl groups, preventing association. It was also reported that at high concentrations (10:1) pyridine can suppress zinc-salphen dimerization by coordinating zinc cation.

By joining several salphen ligands with various spacers bonds a number of macrocycles of three or four zinc-cites (figure 2.8) were reported, capable of forming columnar self-assembling stacks, as well as dinuclear zinc-salphen compounds (figure 2.9) [96, 99]. The later are expected to promote polymerisation via dimerization at each zinc-cite [96]. This property will be of a special interest for this work.

In dimer the two zinc-salphen molecules are strongly bonded via two Zn-O bonds forming almost ideal Zn_2O_2 square. In [100] a polymerization of standalone zinc-salphen dimers was demonstrated via breaking one of the two Zn-O bonds to connect with additional salphen complexes at each side. Another experimental-theoretical study [101] demonstrated self-assembly of bis-Schiff zinc-complexes into long fibers via two bonding mechanisms: primarily single complexes joined via Zn-O interaction into chain-like aggregates that in turn stacked into thicker rods via side chains interaction.

However, ionic attraction is not the only binding mechanism, available for salphen based complexes. Combined spectroscopic and quantum chemistry study of DNA intercalation with zinc-ligand complex was conducted in [102]. It was shown that binding of the two molecules occurs via two key mechanisms: electrostatic attraction between oppositely charged groups and intercalation of the phenyl rings of salphen complex between the stacked bases of DNA. Such stacking interaction between Cu and Ni complexes and DNA was also observed experimentally in [103], it is especially underlined that, unlike Zn, Cu and Ni ions in such compounds do not form a coordination bond with guanine oxygen, so intercalation occurs due to $\pi - \pi$ stacking and not due to electrostatic interaction.

Apart from self-assembly capabilities due to strong non-covalent bonding metal-substituted salen/salphen type compounds can participate in electronic charge transfer. A new thiophene-based salphen-type ligand was synthesized and studied in [104]. It was reported that replacement of salicylaldehyde with hydroxothiophene groups resulted in denser packaging in solid state (intermolecular distance of 3.253-3.265 Å) due to strong π-stacking and S-S interactions. In solid

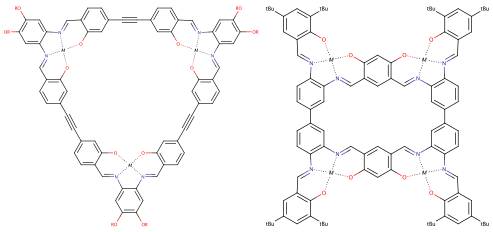

Figure 2.8: Salphen-based macrocycles synthesised by MacLachlan (reproduced from [96]) and Kleij [99]

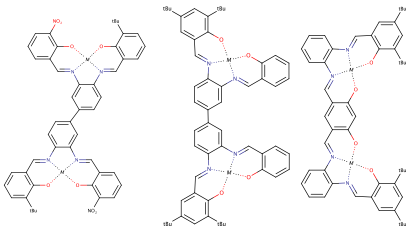

Figure 2.9: Dinuclear salphen-based compounds, synthesised by Kleij and coworkers [96, 99]

state Zn- and Cu-substituted compounds showed p-type conductivity with hole mobility of 1.5 and 0.7 cm^2/Vs respectively. It was also reported that methanol group was found coordinating Zn cation that wasn't removed when solvent was changed. No such behaviour was observed for Cu cation. Aforementioned ability of electronic transport via delocalised π-orbitals in combination with capability to control self-assembling process via ligand geometry and reaction conditions makes multi-center Schiff-base compounds a very perspective building block for advanced materials with controlled properties.

Furthermore, Schiff-based compounds can bind to metallic surface due to electron transfer between a metal-organic complex and vacant d-orbitals of substrate, such ability was extensively studied both experimentally and theoretically in [105] with the focus on corrosion inhibition.

2.4 Concluding remarks

In summary, the composites composed of polymer matrix and CNTs attract ever growing attention due to their highly valuable properties and flexibility. However, obtaining the stable electrical conductivity in such composites with optimal filler loading still represents a significant challenge. One of the perspective approaches to it is to use the additives, dispersion agents, to enable better distribution of CNTs inside polymer matrix.

Methods for production of structured arrays and lattices of rings deposited from evaporating solvents, based on hydrostatic effects, were developed and successfully employed. However, since the discovery of "porphyrin wheels" and their explanation by pinhole mechanism, most of the following works relied on that explanation for the formation of micrometer-sized ring-like structures. In many cases no careful numerical studies of rings formation during solvent evaporation

was actually done. While it is satisfactory for flat thiacyanine and circular-shaped hexamers and dodecamers, the ring-like structures, obtained by Balzer by deposition from gas, cannot be explained in the same way. Although the examples, described in this chapter look very similar two the "rings-and-rods" like networks, reported in [**?**], pinhole effect cannot explain the formation of the overlapping rings in 2D networks or loop-like string structures in polymer matrix.

In the same time self-assembled nano- and microstructures of Schiff-base metal-organic complexes were intensively studied and the possibility to promote different structures by controlling the ability of such complexes to aggregate via either ionic or $\pi - \pi$ interaction was demonstrated by many groups in various solvents. Basing on this results a mechanism, different from patterning by the curved surface of evaporating surface, may be suggested in case of tetrakis-Schiff zinc-complexes that can have more in common with the formation of cation-π bonded macrocycles and semi-flexible polymer folding.

Chapter 3

Methods of computer simulations of materials

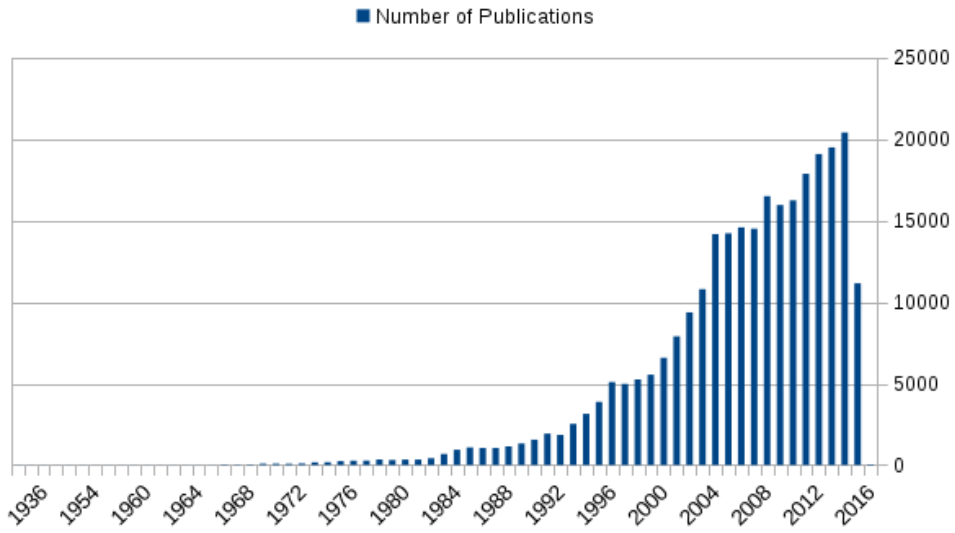

Figure 3.1: Statistics of publications mentioning simulation techniques in material research per year

Although according to a famous expression of Prof. Richard Feynman "the test of all knowledge is experiment" [106], computer simulation is gaining ever growing role in science, especially in the field of research of materials structure and behaviour. Figure 3.1 shows the number of publications per year, containing keywords "material" and either of "simulation", "molecular dynamics", "Monte Carlo" or "quantum mechanic" according to Scopus online database [107]. This trend is easy to explain as simulation techniques enable researchers to employ all previously accumulated knowledge of material properties and behaviour to predict the potential outcomes of experiments in a consistent and faster way, thus,

allowing the experimentalists to minimize the number of experiments needed to verify their expectations. This is especially important for extreme conditions where experiments are tremendously hard and expensive, but where remarkable changes of material properties are expected [108].

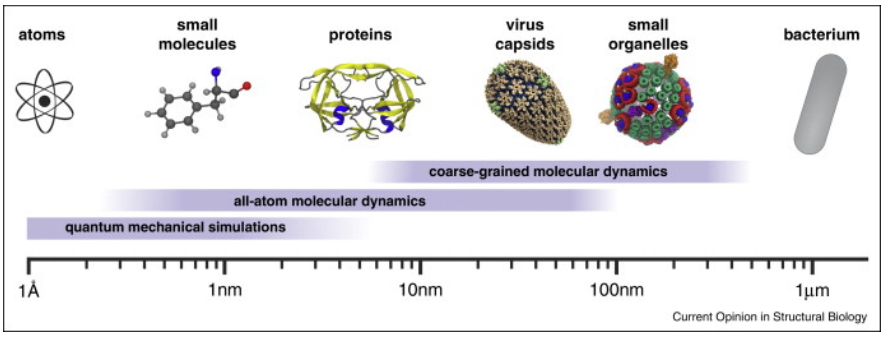

Figure 3.2: Size scales achievable for various simulation techniques (image from [109])

The objective of current work - charge transport in composite material - depends on factors, existing on different size and time scales. On atomistic scale these include nanotube's internal conductance and electron tunnelling across contacts between adjacent nanotubes. In the same time, as was shown in chapter 2 nanotube dispersion quality and agglomeration plays a crucial role in composite conductivity on macroscale. Despite of the progress in the field of computer design and computational algorithms, it is still impossible to treat systems of any size using the same approach. Thus, techniques operating on different levels of approximations emerged and occupied their niches as demonstrated on figure 3.2. This chapter briefly reviews the theoretic grounds of the three methods of computer study, employed in the current work: Monte Carlo modelling, molecular dynamics and quantum mechanical calculations. The details of the application of each method will be described in corresponding chapters.

3.1 Monte Carlo methods

Monte Carlo (MC) methods is a wide group of methods for statistical calculations [110]. Basic idea of these methods is to estimate the desired quantities by generating a large number of random realizations and accept or reject each realization according to a predefined criterion. Its most easily illustrated by MC integration: to estimate the area under a curve, defined by a positive function $y = f(x)$ on any interval $x \in [a, b]$, N random points (x_i, y_i) need to be generated with uniform distribution in the rectangle $(a \leq x_i \leq b,\ 0 \leq y_i \leq \max_{a \leq x_i \leq b} f(x))$, then

the desired surface is approximated by the ratio N_A/N, where N_A is the number of points, for which $y_i \leq f(x_i)$.

If the uniform distribution in spherical coordinates is required, a special approach to generation of the angle coordinates (ϕ, θ) is used. A two random numbers u_1 and u_2 are drawn from uniform distribution on the interval $[0; 1)$. Then the following relations produce (ϕ, θ) uniformly distributed over a sphere:

$$\phi = 2\pi u_1; \tag{3.1.1}$$

$$cos(\theta) = 2u_2 - 1. \tag{3.1.2}$$

Such choice allows to avoid unwanted concentration of generated points near the poles ($\theta = 0$ and $\theta = \pi$).

When a non-uniform distribution is desired, an approach called von Neumann acceptance-rejection sampling (or in short "rejection sampling") can be used to convert a value u_1 picked with a uniform random number generator to a random number with the probability described by an arbitrary function $g(u_1)$. To achieve this one compares another uniform random value u_2, drawn from $[0; 1)$, with $g(u_1)$ and accepts u_1 in case $u_2 \leq g(u_1)$ and rejects otherwise.

In the field of polymer composites modelling a specific type of MC simulation became popular [111]. Within this approach the composite is represented with a continuous dielectric media, into which filler particle models are randomly inserted. The particles are modelled with either unpenetrable or "soft" inclusions. In the former case a newly generated randomly placed inclusion must be rejected if it intersects any already existing in the simulation volume. In the "soft" case the intersection is allowed, but restricted to a certain depth.

Basic algorithm of this method is quite simple, however, it allows to control a wide range of parameters, manipulating the probability distribution functions. In case of CNT reinforced composites the inclusions are most commonly represented with either line segments or rigid spherocylinders [112]. Modifying the aspect ratio (length to diameter ratio) distribution, packing density or distribution of axis vectors percolation threshold of CNT composites was studied in many studies [113–117].

However, the application of this method to study a non-uniform, agglomerated distribution of CNTs on a large scale was not reported so far. In the current work such study is performed by augmenting this standard approach with rejection sampling technique.

3.2 Molecular dynamics method

Starting from the pioneer work of Alder and Wainwright [118] where a system of 32 hard spherical particles in a rectangular box with Maxwell-Boltzmann velocity distribution was simulated during hours to accumulate several thousands of collisions, molecular dynamics (MD) method has been employed in more then 284 000 research papers [107]. A special purpose computers are designed to solve extreme tasks such as study a peptide in explicit solvent folding process during a millisecond simulation time at the speed ~18 µs/day [119]. Simulating the systems starting from single molecules up to $4*10^{12}$ particles [120], it occupied an important domain bridging quantum mechanics level of theory up almost to the lowest boundaries of continuum mechanics [121] and, in some cases, experimental observation [122]. The general description of the molecular dynamics is given according to [123, 124].

3.2.1 Governing equations

The main idea behind the molecular dynamics method is to represent a molecular system as a collection of N interacting particles, that obey classical laws of Newtonian mechanics :

$$m_i \frac{d\vec{r}_i^2}{dt^2} = \sum_{j \neq i} \vec{F}_{ij} + \vec{F}_{ext}, i = \overrightarrow{1, N} \tag{3.2.1}$$

here: $\vec{r_i}$ - the coordinates of i-th particle, $\vec{F}_{ij}$ - the force, with which j-th particle acts on i-th, $\vec{F}_{ext}$ - the force, acting from external field, such as electric or gravitational. To follow a molecular system evolution on a computer, the differentiation by time t in the equation 3.2.1 is replaced with the finite difference over the timestep δt. There are several approaches to do this including "leap-frog", "RESPA" and higher order methods. The most common is "velocity-Verlet" representation:

$$\begin{cases} \vec{r}_i^{t+\delta t} = \vec{r}_i^t + \vec{v}_i^t \delta t + \frac{\vec{F}_i^t}{2m_i} \delta t^2 \\ \vec{v}_i^{t+\delta t} = \vec{v}_i^t + \frac{\vec{F}_i^{t+\delta t} + \vec{F}_i^t}{2m_i} \end{cases} \tag{3.2.2}$$

where m_i is the mass of the i-th particle, $\vec{r}_i^t$, $\vec{v}_i^t$ and $\vec{F}_i^t$ - are the coordinates and velocity vectors of the i-th particle and the total force acting on it (including interactions with other particles and the external field if present) at the time t. δt is the time step of the integration. The set of equations 3.2.2 are, of course, an approximation and the trajectories of the same particle with an initial perturba-

tion, however small, will diverge in time [124]. For this reason the outcome of an MD simulation is not the exact trajectories of particles, but the average system parameters, such as thermodynamic quantities or distribution and correlation functions.

Kinetic (K), potential (U) and total energy(E) of the system can be evaluated directly from the set of simulated particles coordinates and velocities:

$$K = \sum_i \frac{m_i \vec{v}_i}{2}; \tag{3.2.3}$$

$$U = \sum_b U_b^{bond} + \sum_i U^{ext}(\vec{r}_i) + \sum_{i,j}^{i \neq j} U^{nb}(|\vec{r}_j - \vec{r}_i|); \tag{3.2.4}$$

$$E = K + U; \tag{3.2.5}$$

where U_b^{bond} - is the energy of covalently bonded interaction of the bond or angle with index b, $U^{ext}(\vec{r}_i)$ is the potential energy of ith particle in the external field (gravity or electric), $U^{nb}(|\vec{r}_j - \vec{r}_i|)$ - is potential energy of non-bonding interaction between the particles i and j. In rear cases such as metals a many-body term is also required. Other quantities, such as temperature (T) and pressure (P) can be estimated through thermodynamic and molecular theory relations:

$$T = \frac{1}{k_B N} \sum_i m_i \vec{v}_i; \tag{3.2.6}$$

$$P = \frac{1}{V} \left(N k_B T + \frac{1}{3} \sum_i \vec{r}_i \cdot \vec{F}_i \right); \tag{3.2.7}$$

here k_B is the Boltzmann constant, $\vec{v}_i$ speed vector of ith atom. Other observables can be estimated as the average changes of the quantities, described before. For example, the diffusion coefficient (D_{diff}) can be estimated from the mean square displacement of the particle:

$$D_{diff} = \lim_{t \to \infty} \frac{1}{6t} \langle |\vec{r}_i(t) - \vec{r}_i(0)| \rangle; \tag{3.2.8}$$

here the brackets $\langle ... \rangle$ denote ensemble average over either all particles of the same time in a simulation or all trajectories of a single particle in a set of independent trajectories. An example of a solute molecule diffusion rate evaluation in explicit solvent via this approach is given in [125].

3.2.2 Ensembles

The set of equations 3.2.2 is accompanied by the initial coordinates and velocities of the particles and simulation box geometry and boundary conditions (which can be opened or periodic in any or all directions) to form so called microcanonical or *NVE* ensemble. The last abbreviation underlines that the number of particles N, the system volume V and the system total energy E are conserved in the simulation. This corresponds to adiabatic closed system. This is the simplest case to implement, however, the experimental conditions in practice rarely satisfy *NVE* conditions.

If instead of fixing the energy one desire to keep the temperature this situation corresponds to a canonical or *NVT* ensemble. Such conditions correspond to a system connected to a heat bath. To mimic this connection a thermostating procedure is needed. The are many ways to perform this, including velocity rescaling or the approaches of Berendsen or Andersen. The two methods, used in this work are:

- Nose-Hoover thermostat [126] introduces the additional variable s to rescale the velocities in 3.2.1 and associated with it mass (Q) and impulse (p_s), then the change of ith coordinate with time becomes:

$$\frac{d\vec{r_i}}{dt} = \frac{\vec{v_i}}{s^2}; \tag{3.2.9}$$

  and the evolution of the new degree of freedom is governed by:

$$\frac{ds}{dt} = \frac{p_s}{Q}; \tag{3.2.10}$$

$$\frac{dp_s}{dt} = \frac{\sum_i \frac{m_i v_i^2}{s^2} - g k_B T}{s}; \tag{3.2.11}$$

  where g is the number of independent degrees of freedom.
- Langevin thermostat [127] modifies the equation 3.2.1 introducing the two additional terms: the viscous dumping (F_{vis}) and random impulse exchange from the collision with "virtual" particles representing the heat bath (F_{rand}):

$$\vec{F}_i^{vis} = -\gamma m_i \vec{v}_i; \tag{3.2.12}$$

$$\vec{F}_i^{rand} = \vec{R}_i(t)\sqrt{2\gamma k_B T m_i}; \tag{3.2.13}$$

  where γ is the dumping parameter, usually ~ 100, and $\vec{R}_i(t)$ - is a random vector.

If the volume is set free, but the target pressure is fixed during the simulation this corresponds to an isothermal-isobaric or NPT ensemble. Keeping the pressure fixed is done via algorithm called barostat. As in case of temperature, there are several schemes for this. In this work the Nose-Hoover approach is used: the dynamics equations 3.2.1 are extended similar to 3.2.9,3.2.10 and 3.2.11 to introduce additional variable, this time linking volume and pressure.

3.2.3 Parameter sets

To solve the equations 3.2.1, one more component is needed: forces acting on particles. In aforementioned abinitial calculations, the forces can be derived as the gradients of potential energy functional. In classical MD, however, a set of rules and parameters, connecting the particles displacement and forces acting on them. Such sets are called "force fields". There is a significant variety of choices: AMBER [128], GROMOS [129], DREIDING [130], - to name just a few. In this work AMBER (more precisely, its generalized version GAFF) and DREIDING are used. Within both the bonded (or covalent) interactions are described with harmonic potential:

$$U_b^{bond} = K_b(\xi_b - \xi_0)^2; \tag{3.2.14}$$

where K_b is spring constant, ξ_b - is the variable (bond length, flat angle between two bonds, dihedral angle - the skew angle between bonds linked to two bonded atoms, improper angle - the angle between a bond and a plane of two other bonds originating from the same atom), ξ_0 is its equilibrium value.

Non-bonding interactions, however, are treated differently by the two force fields. In AMBER van der Waals interactions are described by commonly used Lennard-Jones potential:

$$U_{ij}^{t_i t_j} = 4\epsilon_{t_i t_j}\left[\left(\frac{\sigma_{t_i t_j}}{r_{ij}}\right)^{12} - \left(\frac{\sigma_{t_i t_j}}{r_{ij}}\right)^{6}\right]; \tag{3.2.15}$$

where the indexes i and j refer to the two interacting particles, while t_i and t_j refer to their types (elements for atoms), r_{ij} - is the current distance between the two particles, $\epsilon_{t_i t_j}$ - is a "potential well depth" (minimum value of the potential energy for the particles of the two types), $\sigma_{t_i t_j}$- is the distance at which the potential 3.2.15 equals to 0, related to the minimum distance ($r_{t_i t_j}^{min}$) as $r_{t_i t_j}^{min} = \sigma_{t_i t_j}\sqrt[6]{2}$. DREIDING recommends Morse type potential:

$$U_{ij}^{t_i t_j} = A_{t_i t_j}\exp(-C_{t_i t_j} r_{ij}) - B_{t_i t_j} r_{ij}^{-6}; \tag{3.2.16}$$

where $A_{t_i t_j}$, $B_{t_i t_j}$ and $C_{t_i t_j}$ are force field parameters.

Both force fields treat electrostatic attraction or repulsion as Coulomb interactions between point-charge particles:

$$U_{ij} = \frac{q_i q_j}{4\pi\varepsilon_0 \varepsilon r_{ij}}; \tag{3.2.17}$$

where ε_0 is the electric constant, ε is dielectric permittivity of environment, q_i and q_j are the charges of the particles. The difference between the two sets is in the way the charged are assigned. Since the point charge of atom is just a simplification of real distribution of electrons, arising from quantum laws, different approaches exist to obtaining a good point-charge approximations. DREIDING parameters were fitted to the charges derived according to Gasteiger approach [131], based on elements electronegativity. AMBER uses the charges, fitted to reproduce electrostatic potential of the molecule, obtained from abinitial calculations [132]. The van der Waals parameters were fitted by the force field developers along the charges to reproduce $\pi - \pi$ and cation-π interactions indirectly. Apart of this DREIDING has a separate term to explicitly account for hydrogen bonding.

A special issue is the interaction between coordinated ion and ligand. For a covalently bonded systems, electrostatic interactions between atoms bonded together are excluded from the potential energy 3.2.4, equilibrium bond length and spring constant are fitted to reproduce the experimentally observed bonds. Coordination bond, however, is purely electrostatic in nature. There are two main directions in the literature to simulate such interactions: in [133] the virtual bonds were introduced between ion and ligand atoms, while assigning the ion the charge, typically expected for the free ion in solution ("bonded model"), in the same time in [134] no explicit bonds were applied, instead the ion charge was tuned to maintain geometry of ion-ligand complex close to optimized with abinitial calculations.

Free energy calculation

As it was already stated before, replacement of the equation 3.2.1 by finite difference representation 3.2.2 is an approximation that only holds as long as the timestep δt is smaller than the characteristic time of the fastest motion in the model system. For the all-atom representation of organic molecules this is usually the period of vibration of hydrogen covalent bonds which is of the order 1 fs (10^{-15} seconds) [135]. Thus, it is infeasible to track such processes as evolution

of conformation of large molecules in solvents, which take millisecond to second time. Instead to compare the probability to encounter conformations in a solution a change in a free energy is estimated between them [136]. Free energy is defined as the amount of energy required to create a system, thus the free energy difference between various conformations of a molecule in solvent can be seen as the difference between solvation energies of the conformations. There are two definitions of a free energy depending on the process conditions (i.e. which quantities remain fixed): 3.2.18 is a Helmholtz free energy (A) for a system under constant temperature, volume and number of particles (NVT ensemble), while 3.2.19 is a Gibbs free energy (G) for an NPT ensemble (varying volume, but constant pressure):

$$A = E - TS; \tag{3.2.18}$$

$$G = E - TS + PV; \tag{3.2.19}$$

here E - is the internal energy if the system, consisting of the kinetic of all particles, the energy of molecular bonds and van der Waals and Coulomb interactions, S - is the entropy, characterizing conformational disorder of the current state, P, V and T are the pressure, volume and temperature correspondingly. It is clear from the definitions 3.2.18 and 3.2.19 that in vacuum ($P = 0$) $\Delta G = \Delta A$ and the difference only exist in explicit solvent if the volume change is significant. Although theory of the free energy methods was initially derived for Helmholtz free energy, but is routinely used in NPT simulations as an estimate for Gibbs free energy change as it is the later quantity that determines the probability of the process under normal conditions (i.e. room temperature and pressure) and, therefore, is the value of interest for chemists. For this reason in what follows Gibbs free energy notation (G) is used to avoid confusion.

Thorough evaluation according to the expressions 3.2.18 and 3.2.19 according to their definition is unfeasible, however changes in free energy of a system in the two not too different states (denoted with indexes "S" and "F") can be estimated numerically using the Zwanzig expansion [137]:

$$\Delta G_{S\to F} = -k_B T \ln \left\langle \exp\left(-\left(U_F - U_S\right)/k_B T\right)\right\rangle_S \tag{3.2.20}$$

where $\langle ... \rangle_S$ denotes averaging by the microstates of the starting state "S".

Direct evaluation of free energy difference corresponding to molecular conformation change and multi-molecular chains fracture in liquid environment would

require hundreds of independent nanoseconds-long simulations in explicit solvent that are computationally expensive and, thus, such approach is impractical. There are several approaches to this task seeking for a balance of the computational efficiency and precision trade-off. A number of implicit solvent approaches such as generalized Born [138] and Poisson-Boltzmann [139] models represent the solvent as a dielectric continuum. This way they allow a more robust evaluation, although they lack the correct contribution of solvent molecules, which is expected to have significant impact on the tetrakis-Schiff self-assembly process, as follows from the studies, reviewed in the section 2.3. Explicit solvent approaches, in contrary, produce the thermodynamic quantities naturally, but require long simulation runs. However it is possible to reduce the computational effort using a thermodynamic principle that the free energy change is not the function of the process, but only of initial and final state. Benefiting from the later, in the reported work the change of the free energy during the process, occurring in solvent environment, can be estimated using the "alchemical transformation" [140] approach:

$$\Delta G^{S\to F}_{solvent} = \Delta G^{F}_{v\to s} + \Delta G^{S\to F}_{vacuum} - \Delta G^{S}_{v\to s} \tag{3.2.21}$$

where $\Delta G^{S\to F}_{solvent}$ and $\Delta G^{S\to F}_{vacuum}$ are the free energy change for the process in solvent and in vacuum consequently, $\Delta G^{S}_{v\to s}$ and $\Delta G^{F}_{v\to s}$ are the solvation free energy of initial and final states. Following this route the extensive calculations of the conformational change is done in vacuum for a systems, containing a few hundreds of atoms, and only limited number of demanding calculations are required to determine the solvation free energies for initial and final states.

In practice, it is often required to estimate the free energy difference between two states, corresponding to a pair of local free energy minima separated with potential barrier. In this case $(U_F - U_S)$ estimated for a system in state 0 is large and the equation 3.2.20 is not applicable. However, it is possible to separate the transition from initial to final states into a set of small steps, so that for each Ith step $(U_{I+1} - U_I) \sim k_B T$ and ΔG_I can be estimated via 3.2.20. Then a free energy profile along such path, also called "potential of mean force" (PMF),can be calculated as:

$$\Delta G_{S\to I} = \sum_{K=0}^{I-1} \Delta G_{K\to K+1}. \tag{3.2.22}$$

Umbrella sampling

If the initial and final states of the system of interest represent two different conformations of a molecule, it is convenient to define a number of gradual geometry changes from one conformation to another as the set of intermediate states in 3.2.22. A generalized parameter, corresponding to the gradual change over such defined set of molecular geometries, is call "reaction coordinate" (ζ). This approach is called "Umbrella sampling" (US) [141]. To constrain the molecule to the intermediate state ζ_I a restraining potential $U_R^I(\zeta)$ is added to the systems potential energy. Then the behavior of the system is described with a restrained state probability distribution ($\mathcal{P}_R^I(\zeta)$), related to the initial unrestrained distribution ($\mathcal{P}(\zeta)$) as:

$$\mathcal{P}(\zeta) \sim \mathcal{P}_R^I(\zeta) \exp\left(\frac{U_R^I}{k_B T}\right). \tag{3.2.23}$$

In statistical mechanics the free energy of the system is related to its microscopic probability distribution as:

$$G = -k_B T \log\left(\mathcal{P}(\zeta)\right). \tag{3.2.24}$$

Substituting here the relation 3.2.23 one obtains:

$$G_I = -k_B T \log\left(\mathcal{P}_R(\zeta)\right) - U_R^I + const; \tag{3.2.25}$$

where the additional constant is the offset, different for different intermediate states. To combine G_i for different restraining potentials into one PMF the weighted histogram analysis method (WHAM) is used [142]. Within one of the free energy values (generally G^S) is set to 0 and the following relations are used self-consistently to evaluate the other G^I (which are essentially $\Delta G_{S\to I}$ now):

$$\mathcal{P}(\zeta) = \sum_I w_I(\zeta) \mathcal{P}_R^I(\zeta); \tag{3.2.26}$$

$$w_I(\zeta) = \frac{N_I \exp\left[\left(G^I - U_R^I(\zeta)\right)/k_B T\right]}{\sum\limits_K N_K \exp\left[\left(G^K - U_R^K(\zeta)\right)/k_B T\right]}; \tag{3.2.27}$$

$$\exp\left(-\frac{G^I}{k_B T}\right) = \int_S^F \mathcal{P}(\zeta) \exp\left(-\frac{U_R^I(\zeta)}{k_B T}\right) d\zeta; \tag{3.2.28}$$

where $w_I(\zeta)$ are the weighting coefficients, used to renormalize the restrained probability distributions in 3.2.26 so that $\sum\limits_K w_K(\zeta) = 1$ and $\partial\sigma^2\left[\mathcal{P}(\zeta)\right]/\partial w_K(\zeta) = 0$ ($\sigma^2\left[\mathcal{P}(\zeta)\right]$ is the statistical error).

Although, theoretically, the free energy difference between initial and final states does not depend on the choice of intermediate states, careful selection of the path, along which ζ changes can minimize the number of simulations required and emerging numerical errors. Ideally, the intermediate states should sample the maximum probability path, i.e. the path along which the potential barrier between initial and final states is the smallest. A good approximation to such path is not always obvious, which is especially true for a complex flexible molecules, such as studied in this work.

The so-called "nudged elastic band" method (NEB) helps to identify such path numerically [143]. This approach implies simultaneously running a set of copies of the same system, called "replicas", corresponding to the different intermediate conformations. However, these simulations are not independent. Their potential energy 3.2.4 is modified to include the spring-like forces between the neighbouring replicas:

$$U^I(\vec{r}) = U(\vec{r}) - k_{NEB}\left(\vec{r} - \vec{r}^{I-1}\right) - k_{NEB}\left(\vec{r}^{I+1} - \vec{r}\right); \tag{3.2.29}$$

where subscript I refers to the number of replica, the spring constant k_{NEB} is the parameter of the method and the vector $\vec{r}$ represents set of all coordinates in the subsystem of interest (in this case, of the molecule, the conformation of which is studied). The expression 3.2.29 is used for all replicas, excluding the initial and the final, the dynamics of which is modelled around the corresponding equilibrium states. Coordinate optimization, performed in parallel for all set of thus connected replicas after the certain period of dynamics simulation at elevated temperatures, results in a good approximation of the minimum barrier path.

Free energy perturbation

Another way to get the estimation of ΔG in a simulation is the free energy perturbation (FEP). It was carefully studied for a large collection of simple solute molecules and can give a very precise results with the relative errors of the order of 1-2 kcal/mole [144]. The core of the method is extending the model system internal energy by introduction of the coupling parameter λ, $0 \leq \lambda \leq 1$, so that at the two conformations under study correspond to the opposite ends of the interval. Then the generalized expression for U in case, when initial state corresponds to a macromolecule in a vacuum environment and the final state - to the molecule in solvent, can be written [144] :

$$U(\lambda) = U_{MM}^{bonded} + U_{MM}^{vdW+Coul} + U_{SLV}^{bonded} + U_{SLV}^{vdW+Coul} + \lambda U_{SLV-MM}^{vdW+Coul} \quad (3.2.30)$$

where the indices MM and SLV corresponds to macromolecule's and solvent molecules' contributions: energies of covalent bonds U^{bonded}, dispersion and electrostatic interactions $U^{vdW+Coul}$, - while the subscript $SLV - MM$ indicates the contributions due to the interaction between the solvated macromolecule and the solvent molecules. The dynamics of the system of interest is simulated for a certain time fixing the λ parameter in 3.2.30 at each value from a predefined set λ_I, $0 \leq I \leq N_\lambda$ ($U_0 = U(\lambda_0 = 0)$, $U_1 = U(\lambda_{N_\lambda} = 1)$) and "forward" ($\delta U_{FWD}(\lambda_I) = U(\lambda_{I+1}) - U(I)$) and "backward" ($\delta U_{BWD} = U(\lambda_{I-1}) - U(\lambda_I)$) potential energy change are estimated every few timesteps in the geometry, obtained at $\lambda = \lambda_I$. Then the free energy change at each interval $[\lambda_I; \lambda_{I+1}]$ can be estimated via equation 3.2.20 both in forward and backward directions. In practice the estimation error could be minimized if both forward and backward potential energy changes are used and the free energy change is estimated via numerical solution of the following equation:

$$\begin{aligned} &\sum_{K=1}^{n_I} \frac{1}{1+\exp\left(\log\left(n_I/n_{I+1}\right)+\delta U_{FWD}^K(\lambda_I)/k_BT-\Delta G\right)} - \\ &- \sum_{k=1}^{n_{i+1}} \frac{1}{1+\exp\left(\log(n_{I+1}/n_I)+\delta U_{BWD}^K(\lambda_{I+1})/k_BT-\Delta G\right)} = 0; \end{aligned} \quad (3.2.31)$$

where n_L is the number of δU values, sampled at $\lambda = \lambda_L$, L is either I or $I+1$. This approach is called Bennett acceptance ratio (BAR) was introduced in [145] and became the standard in FEP calculations [146].

Theoretically, free energy of a system does not depend on the root from state A to state B, but on practice a careful choice of the set of λ values can significantly improve the simulation stability and final precision of free energy [144]. Although comparison of several independent trajectories is still required for error estimation, a strategy to identify the potential pitfalls in λ-schedule by observing the overlap between the distributions of $U(\lambda_I) + \delta U_{FWD}(\lambda_I)$ and $U(\lambda_{I+1}) + \delta U_{BWD}(\lambda_{I+1})$ [147].

Steered molecular dynamics

Another approach to estimate the free energy difference between the two states is to estimate the work needed to force system from one state to another in an non-equilibrium process, which is related to a free energy change via Jarzynski's equality [148]:

$$e^{-\beta\Delta G} = \langle e^{-\beta W} \rangle; \tag{3.2.32}$$

where W is thermodynamic work and $\beta = 1/k_B T$.

Equation 3.2.32 provides an important tool to estimate the free energy change of a near equilibrium process from a distribution of work values of a set of non-equilibrium trajectories, achievable to MD simulation. This approach is called steered molecular dynamics (SMD) [149, 150]. An extensive study of SMD application to a small biomolecule was reported in [149]. Simulation of helix-coil transition of a 104-atom deca-alanine molecule was performed at various pulling speeds. Near reversible simulation was achieved at pulling speed of 0.1 Å/ns for a such small molecule in vacuum due to short relaxation time. The required time of simulation was 200 ns. Potential of mean force (PMF) - a free energy profile vs a reaction coordinate - estimated during such simulation was compared to the PMF obtained with two sets of 100 trajectories each with pulling speeds 10 and 100 Å/ns.

The difficulty of this approach is that, although Jarzynski's equality holds regardless of the speed of the process, it is the trajectories with the smallest work needed that approximate the equilibrium process and contribute the most to exponential averaging. Those, however, occur rarely in the simulation, which affects the accuracy of the averages over limited number of simulations. Cumulant expansion can improve the accuracy of free energy estimation:

$$\log\langle e^{-\beta W} \rangle = -\beta\langle W \rangle + \frac{\beta^2}{2}\left(\langle W^2 \rangle - \langle W \rangle^2\right) - \frac{\beta^3}{3!}\left(\langle W^3 \rangle - 3\langle W^2 \rangle\langle W \rangle + 2\langle W \rangle^3\right) + ... \tag{3.2.33}$$

It was shown, that for a limited number of trajectories 2-nd-cumulant expansion performs best, while the third cumulant experiences large fluctuations. The exponential averaging, exact in the limit of the infinite number of samples, for a limited set of trajectories produces a PMF with small relative fluctuations, however, with a noticeable bias from the near-equilibrium one. In fact, all measures suffer from such bias, however, in case of 2-nd cumulant expansion it can be corrected if an unbiased estimator of variance of a set of M work values is used:

$$-\beta\Delta G_M \cong -\beta\frac{\sum_{m=1}^{M} W_m}{M} + \frac{\beta^2}{2}\frac{M}{M-1}\left[\frac{\sum_{m=1}^{M} W_m^2}{M} - \left(\frac{\sum_{m=1}^{M} W_m}{M}\right)^2\right] \tag{3.2.34}$$

The first order correction to PMF for a spring constant of 500 pN/Å was

estimated as 0.5 kcal/mole, which is small, compared to a change of the free energy of 21.4 kcal/mole. It was also shown that choosing a force constant larger than necessary can give high fluctuations of PMF, which was attributed to raising fluctuations of force, needed to keep the pulling speed constant. So use of unnecessary large spring force is not recommended. The comparable performance was achieved with US for a set of 10 values of a reaction coordinate and biasing spring forces of 70 pN/Å, however it was advocated that the analysis is simpler and better treatment of narrow barrier regions is obtained with SMD (or non-equilibrium TD integration) due to uniform sampling of reaction coordinate.

The preliminary simulation using the SMD method for the ionically bonded association of tetrakis-Schiff molecules produced unstable results, so this method was not used in this work and is described here only for complete overview of free energy methods. However, this method might be used in future for evaluation of the association free energy for long self-assembled chains of $\pi - \pi$ interactions.

3.3 Electronic structure methods

The previously described MD and MC methods require the initial knowledge of interaction parameters (MD) and probability distribution functions (MC). However, in molecular studies these often may be absent (not fitted for a particular molecule) or the approximations accepted while deriving them may not be valid (non-negligible polarization during molecular interaction). In this case the molecule needs to be studied with so-called "abinitial" or "first principles" methods ("*ab initio*" from latin "from the beginning"). The general description of these methods is given according to [151].

In molecular physics and chemistry this term designates the group of approaches, also known as quantum chemistry (QC), which study molecule's behaviour by solving Schroedinger's equation:

$$\hat{H}\Psi = E\Psi; \tag{3.3.1}$$

where Ψ and E are respectively the eigenfunction and eigenvalue of the Hamiltonian $\hat{H}$, or energy operator, corresponding to multi-electron wavefunction and its energy. However, the exact solution for such many-body problem is impossible for a system with more than 2 electrons, so the set of approximations is used to make 3.3.1 solvable:

1. the first approximation is to separate the heavy atomic nuclei from much faster electrons and leave in 3.3.1 only their electrostatic potential V_{nuc}

(Born-Oppenheimer approximation);

2. the multi-electron wave function Ψ is expressed in terms of single-electron wave functions (or molecular orbitals) ϕ_i in the form of Slater determinant to ensure wavefunction antisymmetry (the Pauli Principle):

$$\Psi = \frac{1}{\sqrt{N}} \begin{vmatrix} \phi_1(\mathbf{r}_1) & \phi_1(\mathbf{r}_2) & \dots & \phi_1(\mathbf{r}_N) \\ \phi_2(\mathbf{r}_1) & \phi_2(\mathbf{r}_2) & \dots & \phi_2(\mathbf{r}_N) \\ \vdots & \vdots & \ddots & \vdots \\ \phi_N(\mathbf{r}_1) & \phi_N(\mathbf{r}_2) & \cdots & \phi_N(\mathbf{r}_N) \end{vmatrix}; \tag{3.3.2}$$

where N is the number of electronic orbitals in system, $\mathbf{r}_i$ is a vector describing the ith electron position ($\vec{r_i}$) and spin (s_i);

3. in turn, the molecular orbitals ϕ_i are expressed in terms of linear combination of atomic orbitals χ_l (LCAO):

$$\phi_k(\mathbf{r}) = \sum_l C_{kl}\chi_l(\mathbf{r}); \tag{3.3.3}$$

where the constants C_{kl} are the expansion coefficients than need to be determined and obey the orthogonality condition for single-electron wavefunctions: $\langle\phi_i|\phi_j\rangle = \delta_{ij}$, where δ_{ij} is the Kronecker delta-function.

The choice of χ_l is not unique. In this work the three popular sets are used: Gaussian-type orbitals [152], numerical atomic zeta-orbitals [153] and non-orthogonal generalized Wannier functions (NGWF), expanded in terms of periodic cardinal sine functions [154].

In addition to assumptions 1-3 for atoms of heavy elements electrostatic potential of nucleus and of internal electron shells may be replaced with a "pseudopotential" V^*_{nuc} - a function fitted to reproduce their combined effect on the valence electrons which are left to be treated treated explicitly [155].

If the many-body Coulomb interaction between all electrons in the systems Hamiltonian is approximated by the sum of pair interactions one reduces 3.3.1 to the set of Hartree-Fock (HF) equations [151]:

$$\begin{aligned} -\tfrac{\hbar^2}{2m_e}\Delta\phi_i(\mathbf{r}) - eV^{(*)}_{nuc}\phi_i(\mathbf{r}) + \tfrac{e^2}{4\pi\varepsilon_0}\Big[\textstyle\sum_j \int \frac{|\phi_j(\mathbf{r}')|^2}{|\vec{r}-\vec{r'}|}\phi_i(\mathbf{r})d\vec{r'} - \\ \textstyle\sum_j \delta_{s_i s_j}\int \frac{\phi_j^+(\mathbf{r}')\phi_i(\mathbf{r}')}{|\vec{r}-\vec{r'}|}\phi_j(\mathbf{r})d\vec{r'}\Big] = \epsilon_i\phi_i(\mathbf{r}); \end{aligned} \tag{3.3.4}$$

where ϵ_i is the single electron energy and the superscript "+" designates the complex conjugation. Here the first term corresponds to electron's kinetic energy, second one refers to its energy in the (pseudo)potential of nuclei, the third is the

Coulomb potential energy of electron-electron repulsion, the last one, so-called "exchange" energy, accounts for the antisymmetry of electron wavefunctions. In operator form 3.3.4 can be written as

$$\hat{F}\phi_i = \epsilon_i \phi_i; \tag{3.3.5}$$

where $\hat{F}$ is so-called Fock operator. Substituting 3.3.3 in 3.3.5 one receives a system of linear equations from which the unknown coefficients C_{kl} can be determined iteratively.

To improve the speed of such calculation and to approximately account for electron many-body interaction (named "correlation" energy), disregarded in 3.3.4, the explicit product of orbital wavefunctions may be replaced with the interaction with a combined density of electron cloud $n(\mathbf{r})$. Then all two- and many-body interaction terms are replaced with functionals of $n(\mathbf{r})$. This transforms 3.3.1 into Kohn-Sham equations, the key element of electron density functional theory (DFT) [156]:

$$\left[-\frac{\hbar^2}{2m_e}\Delta - eV_{nuc}^{(*)} + \frac{e^2}{4\pi\varepsilon_0}\int \frac{n(\mathbf{r}')}{|\vec{r}-\vec{r'}|}d\vec{r'} + \int V_{XC}[n(\mathbf{r}')]d\vec{r'}\right]\phi_i(\mathbf{r}) = \epsilon_i\phi_i(\mathbf{r}); \tag{3.3.6}$$

where $V_{XC}[n(\mathbf{r}')]$ is the approximated exchange-correlation functional. The later term has a variety of implementations, developed in attempts to capture certain effects such as molecular geometry, excitation energies or non-local interactions.

In this work the initial geometry optimization of the molecules of interest was done using generalized gradient approximation (GGA) to V_{XC} in the popular robust parametrization Perdew-Burke-Ernzerhof (PBE) [157] and then refined using more complex functional composed of Perdew-Wang local density approximation (LDA) for correlation [158], Becke exchange [159] and non-local correction to account for van der Waals interactions by Dion and co-workers [160].

Another parametrization, known as Becke 3-parameter Lee-Yang-Parr hybrid finctional (B3LYP), is commonly used to prepare a single molecule's geometry before electrostatic potential is calculated with HF calculation. This functional is composed of Lee-Yang-Parr correlation part [161] and a combination of exchange functionals in LDA and GGA forms and exact term from HF theory [162].

In this work, apart from the geometry optimization, *ab initio* calculations were used to derive approximate electrostatic charges. Since the atomic charges are merely approximation for electron cloud around nuclei, there is no unique way to assign point-like charges to atom models. One approach used in the current

work is the natural bond orbital analysis (NBO) [163]. Within its framework single electron wavefunctions, derived with DFT calculations, are projected on the so-called natural atomic orbitals to estimate the population of each atom with electrons. Another scheme, more widely used to prepare input parameters for MD simulations, consists in fitting the atomic charges to reproduce the HF electrostatic potential (ESP) [132] on a set of points, located on a concentric spherical surfaces around the atoms at the distance $\sim 1.2 - 2.0$ van der Waals radii from the atomic cores [164].

Chapter 4

Modelling DC resistivity of the polymer composite with non-uniformly distributed CNT

As it was described in the section 2.1 of the review chapter 2, one of the main problems standing in front of vast industrial application of CNTs is the significant variation of the properties of CNT reinforced composite materials, especially when the electrical conductivity is concerned. There are several factors behind such deviation and some of them, like variation of CNT electrical properties and Schottky barriers between metallic and semiconducting CNTs, can be controlled by selection of CNTs with narrow properties deviation, but the most important - the quality of CNT distribution inside polymer matrix - is inherently connected with the manufacturing process of the composite. As can be seen on the microscopic images of such composites, the CNTs distribution can be quite inhomogeneous and contain micron-scale agglomerates (figure 4.1) that act at a single, low aspect ratio particle, decreasing the effective volume fraction of the nanotubes. Although longer processing can decrease the side of such agglomerates, it also increases production cost of the material. Furthermore, the sparser the CNTs are distributed, the smaller part of them is connected and, thus, participates in the charge transfer. To optimize production costs, mechanical and electric properties of such composite, one have to study the change of its electric conductivity as a function not only of the CNT content, but also of agglomerates size and fraction.

This part of study was devoted to provide an insight on the role of agglomerates in the composite's electric conductivity via numerical modelling. For this purpose a software tool was developed that is capable of modelling the electric

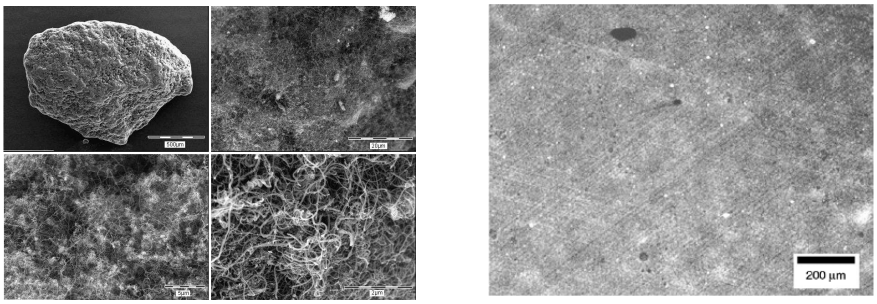

Figure 4.1: Electron microscopy image of a CNT nanotubes [165] (left) and optical microphotograph of agglomerated CNT distribution in a CNT-polymer composite [166] (right)

conductivity of an agglomerated CNT distribution on 100-micron scale, where the influence of the agglomerates become important. Description of the algorithm and details of its implementation are given in the methods' section of this chapter, followed by verification of the modelling results with the theoretically known percolation behavior for low CNT content and experimental data for CNT-reinforced composite's samples, provided by our colleagues. Finally, the effect the CNTs shape change on the composite's elasticity is studied using molecular dynamics simulation to highlight important drawback, arising when the high CNT content is used to achieve electric conductivity.

4.1 Methods

4.1.1 The algorithm in brief

Within the chosen approach a CNT-reinforced polymeric composite is represented by a network of perfectly conducting particles embedded in insulating environment. The focus of this work is DC conduction, so the current is assumed to flow only through CNTs and the junctions between them, where the CNT-to-CNT distance is smaller than tunnelling distance. The CNTs were modelled as rigid spherocylinder inclusions[1], randomly distributed without intersections in a cubic simulation box. A random distribution of such particles was generated using a common Monte Carlo technique: the set of spherocylinder model coordinates $\vec{\mathcal{X}}$ was generated by picking random numbers within the simulation boundaries and subsequently checked for intersections of the newly generated inclusion with

[1]Although the focus of this work is on modelling CNT containing composites, the same tool could be used to model distributions of a range of similar objects (nanofibers/wires etc.), so, for generality, the technical terms "filler particle", "filler" and "inclusion", common in the composite material science, will be used across this chapter along with "CNT model".

all the other already present in the system. If the distance between the current and any other filler particle was found smaller than the allowed limit, the current set of coordinates $\vec{\mathcal{X}}$ was rejected and the process was repeated until the required volume fraction was achieved. Here $\vec{\mathcal{X}}$ is the generalized set of coordinates, including, in addition to a set of Cartesian 3D coordinates of the model particle's center $\vec{X}$, a set of directional coordinates in 3D $\vec{V}$ and the length l of the cylindrical part of spherocylinder and its diameter d.

As was mentioned in the section 3.1 of Methods chapter 3, such approach was successfully used in a number of research papers to estimate electrical propertied of composites. In this study this approach was augmented with non-uniform distribution of filler particles to simulate a percolation network spanning across compact dense agglomerates and vast regions with sparse distribution of fillers. This was achieved by exploiting the von Neumann acceptance-rejection algorithm [110] in a following manner: after the three coordinates of the center $\vec{X}$ were picked, another random value p_i was drawn in the interval $[0; 1]$ and compared to the probability to find the particle center at this point, evaluated from the predefined density map $p(\vec{X})$. The particle center coordinates $\vec{X}$ were accepted if $p_i \leq p(\vec{X})$ and rejected otherwise. $\vec{V}$, l and d were also assigned randomly according to their distributions $p(\vec{V})$, $p(l)$ and $p(d)$ in a similar manner independently of each other.

Thus, the modelling procedure consists of three main stages (figure 4.2):

- preparation: generation of probability density map, $p(\vec{X})$;
- main step: population of CNT spherocylindrical models according to $p(\vec{X})$, $p(\vec{V})$, $p(l)$ and $p(d)$;
- final processing: connectivity check and volume resistivity evaluation.

The required input data for the procedure is:

ϕ_{vol}	desired volume fraction of filler particles;
f_A	fraction of fillers entangled into agglomerates;
$\{\langle D\rangle, \sigma_D\}$	average diameter of agglomerate and its standard deviation;
$\{\langle l\rangle, \sigma_l\}$	average spherocylinder's length and its standard deviation;
$\{\langle d\rangle, \sigma_d\}$	average spherocylinder's diameter and its standard deviation;
$\left\{\vec{N}, \sigma_\theta\right\}$	vector of preferred orientation of spherocylinders and the half-width of directional angles' distribution, where θ is defined as the angle between $\vec{N}$ and randomly generated $\vec{V}$.

The distribution of the agglomerate's diameters can be obtained from the experimental analysis of optical microphotographs as described in [167]: using computer-aided processing of thin film cuts of the composite's sample agglomerate's cross-sectional area can be calculated, form which the average diameter of

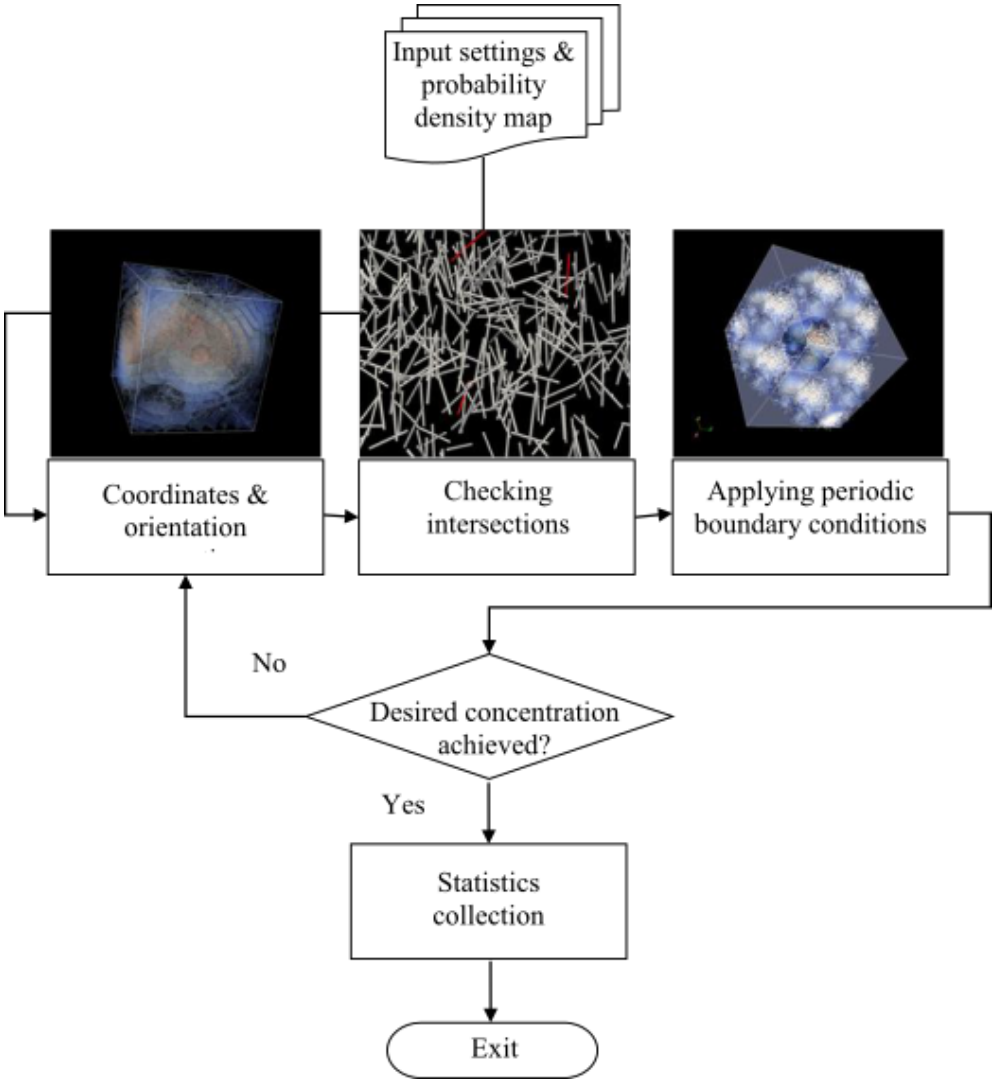

Figure 4.2: Block diagram of the CNT distribution generation process

agglomerate and its standard deviation can be evaluated assuming the spherical shape of agglomerates.

On the preparation stage the probability density map $p(\vec{X})$ is generated using ϕ_{vol}, f_A and $\{\langle D\rangle, \sigma_D\}$ and the desired side length B of the cubic simulation box. The probability density map is directly connected with the filler density which equals to the summation of agglomerate's densities p_A^i, $i \in [1, N_A]$ (N_A - the total number of agglomerates in the simulated sample), and the uniform background density p_B:

$$p(\vec{X}) = \sum_{i=1}^{N_A} p_A^i(\vec{X}) + p_B; \tag{4.1.1}$$

$$N_A = \frac{\phi f_A B^3}{\frac{4}{3}\pi\left(\frac{\langle D\rangle}{2}\right)^3}; \tag{4.1.2}$$

$$p_B = \frac{\phi(1-f_A)B^3}{\pi d^2 l + \frac{4}{3}\pi d^3}. \tag{4.1.3}$$

The agglomerates are represented as spherical objects, inside which the probability density changes with the distance from the agglomerate's center $\vec{X_A^i}$ by bell-like 4.1.4 or Gaussian-like4.1.5 formula:

$$p_A^i(\vec{X}) = p_A^i(\vec{X} - \vec{X_A^i}) = \frac{A}{1 + \left|\frac{\vec{X} - \vec{X_A^i}}{w}\right|^\delta}; \tag{4.1.4}$$

$$p_A^i(\vec{X}) = p_A^i(\vec{X} - \vec{X_A^i}) = A\exp\left(-\frac{(\vec{X} - \vec{X_A^i})^2}{2w^2}\right); \tag{4.1.5}$$

where the parameter δ controls the shape of a bell-like function, A is the normalization factor and the width parameter $w = D/2$ in both cases.

The agglomerates' models were generated in a fashion similar to spherocylindrical inclusion models: however the center coordinates $\vec{X_A^i}$ were assigned as uniform random numbers, spread within the interval $[0; B)$, and the criteria of acceptance was that any two agglomerates should be resolvable, i.e. for any pair of adjacent agglomerates there should be a minimum between their centers. The diameter of the agglomerate was assigned by acceptance-rejection algorithm according to log-normal distribution, for which median and variance were equal to $\langle D\rangle$ and σ_D.

Such defined probability density was renormalized so that its values in any point of the grid were in the interval $[0; 1]$ and evaluated on a 3D grid. After the density map $p(\vec{X})$ was defined the acceptance-rejection procedure, described in

the beginning of this section, was applied to generate $N_{incl} = \phi_{vol} B^3 / \left(\pi d^2 l + \frac{4}{3}\pi d^3\right)$ inclusions. The values of $p(\vec{X})$ between the grid points were evaluated by trilinear interpolation.

On the post processing stage the sample's resistance is evaluated. The spherocylinders were considered to be the perfect conductors and electric resistance arises only from the contacts between them. As was discussed in the literature review section, the contact resistance of two nanotubes can vary significantly depending on many factors. As the focus of this research is on the composite's morphology effect on conductivity, which is mainly described by the number of contacts between filler particles, within this chapter all the contacts were assigned a uniform resistance of 1 a.u. (arbitrary unit).

To evaluate sample's resistance numerically, the periodic boundary conditions were replaced with impenetrable surfaces in one chosen direction. The inclusions, intersecting any one of them are treated as belonging to the set of left or right electrode and are assigned a corresponding potential ($V_L = 0$ for the left or $V_R = 1$ for the right electrode). Than a system of Kirchhoff's laws can be written for the sample's inclusions [168]:

$$\begin{gathered} \begin{cases} \sum_{i,j} I_{ij} = 0, \quad j \neq i,\ i,j \notin \{\mathbb{L},\mathbb{R}\}\,; \\ I_{i,j} = \frac{V_i - V_j}{R_{ij}}, \quad j \neq i,\ i,j \in \{\mathbb{L},\mathbb{R},\mathbb{N}\}; \end{cases} \Rightarrow \\ \Rightarrow V_i \sum_{j\in\mathbb{N}} a_{ij} = \sum_{j\in\mathbb{N}} a_{ij} V_j + V_R \sum_{j\in\mathbb{R}} a_{ij} + V_L \sum_{j\in\mathbb{L}} a_{ij} = 0 \Rightarrow \\ \Rightarrow (\boldsymbol{I} - \boldsymbol{A})\,\boldsymbol{V} = \boldsymbol{B}; \end{gathered} \tag{4.1.6}$$

where a_{ij} - are the conductances of particle-particle contacts (set to 0 if there is no contact between the two particles), $\mathbb{L}$ is the , set $\mathbb{R}$ - correspondingly the right electrode set indexes and $\mathbb{N}$ - the set of indexes of those inclusions that belong to an interconnected network of spherocylinder models, but do not belong to any of $\mathbb{L}$ or $\mathbb{R}$. $\boldsymbol{I}$ is the identity matrix and the elements of the matrices $\boldsymbol{A}$ and $\boldsymbol{B}$ are:

$$A_{i,j} = \left[\frac{a_{ij}}{\sum_{j\in\mathbb{N}} a_{ij}}\right];\ B_{i,j} = \left[\frac{\sum_{j\in\mathbb{R}} a_{ij}}{\sum_{j\in\mathbb{N}} a_{ij}}\right]. \tag{4.1.7}$$

The inter-particle conductances a_{ij} and the matrices $\boldsymbol{A}$ and $\boldsymbol{B}$ are evaluated from the inclusions coordinates. The sparse linear system of equations 4.1.6 can then be solved with a standard linear solving library [169].

4.1.2 GPU Implementation

The described algorithm was implemented for execution on NVIDIA CUDA enabled GPU. The main functionality (i.e. generation of non-overlapping inclusions) is architecture independent, however floating point atomic functions are used in statistics collection, so compute capability 2.0 ("Fermi" architecture GPU) is required for currently implemented data processing kernels.

The inclusion model is described by its' own class containing inclusion parameter fields (for currently implemented cylinder-shaped particles those are: 3 spatial coordinates of the center point, 3 directional cosines, length and radius) and methods to evaluate particle volume (for volume fraction estimation) and interparticle shortest distance (for intersection correction). Additional methods could be defined for custom post processing.

For faster global and shared memory access data fields of all models are grouped into a single array where the element $I + N_{incl}J$ stores the value of the field number J of I-th model. Probability density map, provided in external file, is stored on GPU as texture to benefit from hardware implemented interpolation and separate texture cash. Local orientation distribution and local distributions of sizes and other parameters can also be provided in the same form to induce non-uniform alignment or size/property dependent segregation.

Within CUDA GPGPU approach [170] two levels of parallelism could be defined: fine-grained – tasks executed by single threads, - and coarse-grained – tasks carried out by blocks of threads, executed on the same multiprocessor and thus having access to the same shared memory. To better exploit this two-level scheme the whole system volume is divided into domains processed by blocks of threads, while each thread only handles single inclusion model.

As a good load balancing is required to achieve best performance, dealing with non-uniform distribution of objects requires a special data arrangement for faster processing. In 3D scene rendering it is common use tree-like structures to divide space according to the number of objects [171]. In addition to that specifics of GPU organization requires coalesced memory access and keeping common execution path within warps (groups of threads that are executed simultaneously on the same thread blocks) to prevent branching and serialization for optimal device utilization. While a tree-like space partition can indeed improve the work sharing for highly non-uniform distributions, neighbour cell search in such structure implies recursive check of tree leaves from top down to the corresponding level. For randomly oriented particles it would induce additional computational load and multiple branching while checking intersections for particles belonging

to neighbouring domains.

To avoid such complication a "tree of cells" scheme is adopted in our code. First the whole system volume is represented as a regular 3D grid of rectangular cells and the total number of inclusion models to be created in each cell is evaluated from probability density integration (plus some adjustable margin). The cell edge is defined in a way so that the maximum amount of inclusion models in any cell is not higher than the maximum number of threads per block (1024 for "Fermi" architecture GPU). As the particle data is stored in global memory in one continuous block, three additional arrays are needed for correct data access. The first one (ADDR) stores in element number I the total value of inclusions to be created in cells with numbers from 0 to I. Thus for cell J the displacement from the beginning of the array to the space allocated for this particular cell is given by the $J-1$-th element of the array (or 0 for the first cell). Two more arrays store the number of inclusions stored from the previous iterations (OCC) and the number of the inclusions created on current iteration (NEW).

For better load balancing cells are grouped by tree-like structure (figure 4.3): initially all system volume belongs to the root of the tree, then the root is split in two so that the nodes carry approximately equal load and the area of separating plane is smallest. This procedure is repeated recursively until the maximum load of each leave is again not higher than can be processed by single block. Each node is characterized by 6 integer values representing the coordinates of its origin cell and the sizes of its sides (in cells). "Leaves" of the tree structure form a non-uniform (in case of non-uniform inclusion distribution) approximately equal load domain structure.

During Monte Carlo generation of new inclusion models and checking intersections within the cells each thread block is assigned to process single domain of cells. While intersections are checked with neighbouring cells each thread block processes single cell. Since different symmetrical multiprocessors work asynchronously, errors or excessive inclusion elimination can occur when one thread block reads from the memory which the other block is rewriting. There are different mechanisms to prevent this, for example "locking" is widely used in parallel programming [172]: processes have to check the lock-variable value before accessing the data, the first process to capture the data "locks" the data for other processes until it is safe to access it. However in this code we avoid using of locks by splitting the cell grid in three parts and run kernel to check for intersections between particles of different cells on each part of the grid consequently so that no active block is checking intersections with the inclusions belonging to another

active block. This way we completely avoid the stated above error without atomic operations and storing additional values needed for locking. We also avoid excessive inclusion elimination in cases where one thread block eliminates an inclusion due to intersection with another one that would also be eliminated by its thread block. Preventing this with locks causes a noticeable performance drop as one part of multiprocessors always have to wait before the other one completes.

4.1.3 MD simulation

To investigate the effect of nanotube's shape on the composite's elastic properties series of molecular dynamics simulations were conducted using the LAMMPS molecular dynamics package [173]. A DREIDING force field [130] was used to describe interatomic forces. Composite models were prepared by random allocation of initial polymer molecules in a sparse box, which was reduced during the MD simulation of the evolution of the polymer chains at T=500 K in the course of 1–3 $\cdot$ 10^6 timesteps (1 timestep equaled to 0.2 fs) under periodic boundary conditions until the experimentally observed polymer density was reached, followed by box relaxation at 300 K. After initial preparation each sample was subjected to simulated expansion and contraction in each direction at an effective rate of 2% per 10^5 timesteps during which the stress, experienced by simulation sample, was calculated every 500 time steps as pressure, acting on the box boundary in the direction of strain. After collecting the strain-stress data, averaged over 10^5 timesteps were fitted with linear relations was used for extracting the Young's modulus (or elasticity modulus E).

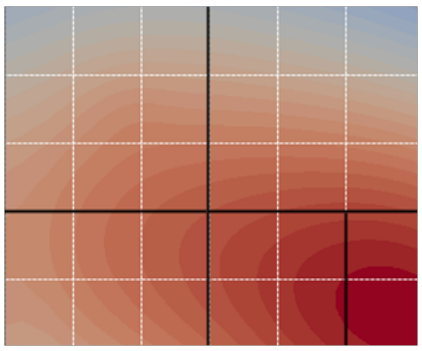

Figure 4.3: 2D representation of system volume divided into equal cells, grouped into tree-like structure according to probability density (colour map)

4.2 Results and discussion

4.2.1 Performance evaluation

The reported code was tested on NVIDIA GeForce GTX 480 (peak float performance – 1345 Gflops, total memory – 1503 MB) and Tesla C2050 (peak performance 1027.7 Gflops, total memory – 2687 MB). The typical times of simulation is sum-

marized in Table 4.1. In all cases cubic sample with the side length 168 μm was filled with cylindrical, spherically capped inclusions. Length of cylindrical part was 4 μm and diameter was 20 nm – comparable to those of commercial nanotubes [174]. The non-uniform probability density map was generated using Gaussian distribution of the agglomerate's diameters with $\langle D \rangle = 5\mu$m and $\sigma_D = 5\mu$m, ratio of agglomerated to background CNTs f_A was set to 0.25.

Although dividing the work according to the number of inclusions to be created makes the work distribution better, still much longer times are required for non-uniform distribution as in the cells with higher than average concentration of inclusions larger fraction is eliminated at each step as well. To speed up the generation process orientation distribution map with local alignment in those cells or complex inclusions representing a number of coalesced inclusions can be used.

ϕ_{vol},%	N_{incl}	$p(\vec{X})$	GPU	t, min
0.5	$18 \cdot 10^6$	uniform	GTX 480	5.0
0.5	$18 \cdot 10^6$	nonuniform	GTX 480	9.2
1.0	$35 \cdot 10^6$	uniform	Tesla C2050	33.5
1.0	$35 \cdot 10^6$	nonuniform	Tesla C2050	155.0

Table 4.1: Typical running times

4.2.2 Validation: percolation threshold in uniform distribution

At first the uniform spatial distribution of CNTs was used to assess the CNT content dependence of composite conductivity. The results are presented on figure 4.4.

In agreement with percolation theory the numerical model exhibits a drop below 0.2 vol. % and power dependence above. Formula 2.1.8 predicts percolation threshold value in the range $0.3 - 0.7$ vol.% which is quite close.

The effect of nanotube alignment on conductivity was also studied by assigning orientation according to Gaussian distribution, the dispersion parameter of which was used to control the degree of alignment. The results for a model sample with 1.5 vol. % content are summarized on the figure 4.5.

Orientation dispersion of 30 radian corresponds to almost uniform distribution. Nonlinear character of conductivity-alignment dependence is attributed to interplay of the two processes: alignment of CNTs perpendicular to electrode decreases the number of CNTs requires to form a conductive path, however it also

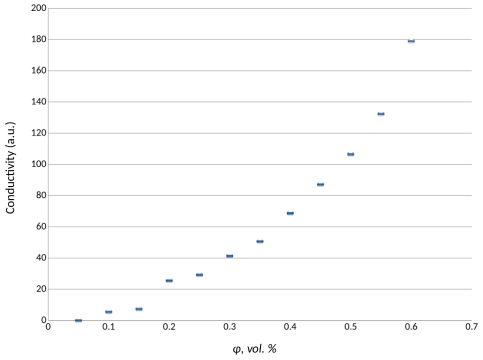

Figure 4.4: Uniform sample conductivity dependence on volume fraction of CNT

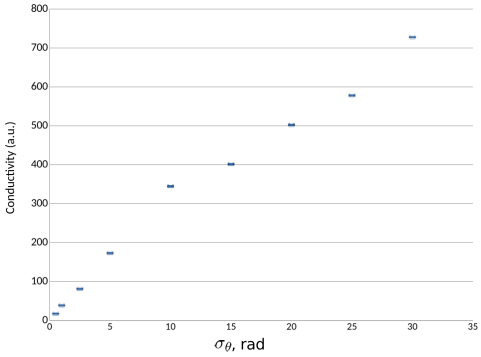

Figure 4.5: The effect of alignment on the conductivity of 1.5 vol. % sample

decreases the probability of intertube contacts. The later results in an order of magnitude decrease of conductivity for highly aligned samples.

4.2.3 Comparison with experiment: the agglomerated distribution

The suggested method was used in the combined experimental-theoretical study in collaboration with Anna Y. Matveeva (Institute of Polymers and Composites) and Juri Tiusanen (Promolding). The aim of this study was to analyse the agglomerates' size distribution in series of PC-CNT composite samples produced with varying parameters of processing and to compare the variations of the conductivity with the results of simulation.

4.2.3.1 Experimental and characterization results

The composite material was produced by Juri Tiusanen by tween screw extrusion process using the Nanocyl's polycarbonate master batch with 15 wt. % of CNTs. The nanotubes (commercial name NC7000) had the average diameter of 9.5 nm and length 1.5. The final CNT weight fraction ϕ_w in the resulting composite equaled to 3.0 wt.% (corresponding to $\phi_{vol} = \phi_w \cdot \rho_{MB}/\rho_{CNT}$ using $\rho_{MB} = 1.175$ g/cm^3 [175] for master batch density and $\rho_{CNT} = 1.3 - 2.0$ g/cm^3 for CNT density [176]). The final samples for resistivity measurements were prepared by injection molding. The temperature of the composite melt (T_{melt}) and the injection speed (V_{inject}) of the composite material into mold were varied during the injection to obtain different final morphology (table 4.2).

After volume resistivity measurements, 5 μm thick slices were cut form the same samples and analyzed with optical microphotography by Anna Y. Matveeva.

During this characterization the agglomerates' area distribution and the total fraction of agglomerates' surface area (relative to the whole image area) ϕ^A_{surf} were calculated. Assuming the spherical shape of agglomerates the average diameter $\langle D \rangle$ and its standard deviation were evaluated. As the slices for optical characterization are very thin, the agglomerates' volume fraction ϕ^A_{vol} can be estimated as:

$$\phi^A_{vol} \approx \frac{2\langle D \rangle}{3b} \phi^A_{surf}, \tag{4.2.1}$$

where $b = 5\,\mu$m is the slice thickness.

Sample	Processing		Agglomerates			ρ_{exp}
	T_{melt}	V_{inject}	ϕ^A_{vol}	$\langle D \rangle$	σ_D	
	$^\circ C$	mm/s	%	μm	μm	$\Omega \cdot$ cm
1	280	18	0.41	0.28	1.55	78.9 ± 4.0
2	280	42	0.32	0.40	1.47	6171.0 ± 2205.5
3	300	6	0.68	0.41	0.85	27.9 ± 2.0
4	300	30	1.11	0.10	0.66	46.5 ± 7.0
5	300	42	1.40	0.14	0.53	156.9 ± 28.6
6	320	42	1.69	0.10	0.76	23.3 ± 4.2

Table 4.2: PC-CNT samples' production parameters and characterization results

The DC volume resistivity ρ_{exp}, measured by Juri Tiusanen, and the agglomerates' diameter distribution parameters from optical microscopy studies by Anna Y. Matveeva are summarized in the table 4.2 along with injection parameters. The results of the optical characterization suggest that two groups could be spotted according to CNT distribution: the first group is formed by the samples 1 and 2 with average agglomerate size $\sim 0.3 - 0.4\,\mu$m with large deviation $\sim 1.5\,\mu$m, but smaller total area fraction of agglomerates, while the second, formed by the samples 4-6, has smaller agglomerate size $\sim 0.1\,\mu$m with deviation $\sim 0.6 - 0.7\,\mu$m, but larger total area of agglomerates, i.e. "less, but larger agglomerates" and "smaller agglomerates, but more". The sample 3 resides in between the two groups with intermediate values. It is interesting that measured resistivity have huge variation even within the group.

4.2.3.2 Modeling results

Based on the results of the above analysis the two types of probability density functions were generated:

1. $\langle D \rangle = 0.4\,\mu$m, $\sigma_D = 1.47\,\mu$m, total agglomerate $\phi^A_{vol} = 0.32\,\%$ (corresponding to F2 sample);

2. $\langle D \rangle = 0.1\,\mu$m, $\sigma_D = 0.66\,\mu$m, $\phi_{vol}^A = 1.1\,\%$ (corresponding to F4 sample).

In the first set of simulations uniform orientation distribution and CNT content of 2 vol. % was used (2 vol. % this was found to be the upper limit for CNTs of given size to be distributed with uniform orientation distribution). The results are summarized on figure 4.6 (left) and compared to uniform spatial distribution of CNTs. The simulated samples' conductivities ($\mathcal{S}$) for the two selected distributions were found to be a bit higher than that of the ideal uniform distribution of CNTs ($\mathcal{S}_0$), however, this effect is quite small (the difference of mean conductivities is comparable with the confidence interval, estimated to be $\sim 10\%$) when compared to the orders of magnitude difference between the experimental measurements for samples 1 and 2 or 4 and 5.

In the second set of simulations Gaussian distribution of directional vectors was used. This time the samples were filled up to 3 vol. % and the orientation distribution width σ_θ was varied from 9 to 0.5 radian. The results for aligned nanotubes are presented on figure 4.6 (right). It becomes clear that, for the agglomerates' size and volume fraction, used in the experimental measurements, the alignment of nanotubes plays much more important role than the agglomeration itself.

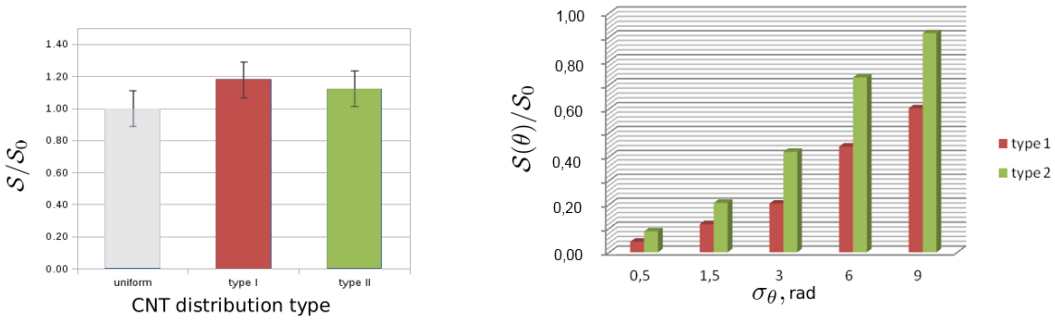

Figure 4.6: Variation of the electric conductivity of the simulated samples with uniform (left) and aligned (right) orientational distribution

As expected, the agglomerated distributions can provide better DC conductivity ($\mathcal{S}$) than the uniform one ($\mathcal{S}_0$). However in this test case the agglomerate's volume fraction was too small for the size of agglomerate to be the determining factor of the samples resistivity. As was seen in the experiments, the lowest resistivities, obtained in each group are comparable to each other. The large difference of the measured resistivities within each group must be attributed to different degree of CNT's alignment.

4.3 The effect of the nanotube's flexibility on the composite's mechanical properties

It follows from the reported results of calculations and experimental observations, mentioned previously, that, although theoretically the electric conductivity can be achieved at very low CNT content, in practice the stable electric properties for such composites are hard to obtain at small loadings due to the high impact of CNT's alignment, emerging during the processing stage. It was also observed during the numerical MC calculations in this chapter that the hard limit of the CNT content, up to which the simulation box can be filled with straight sphero-cylinderical models of the nanotubes, lies within several volume percent ($\sim$ 2 vol.% for the CNTs used in the referenced experiment). Separately, to explain the saturation character of CNT-polymer composite's mechanical properties with CNT concentration it was proposed by our collaborators, Dr. Anna Y. Matveeva and Dr. Ferrie W.J. van Hattum, that nanotubes' shape deviates from the straight more significantly as the CNT loadings increases [1]. An independent experimental observation, reported recently [166], supports this speculation. To validate the effect of nanotubes' shape on the composite's mechanical properties molecular dynamic study was conducted and compared with analytical predictions and finite element modelling (FEM) calculations by the aforementioned colleagues.

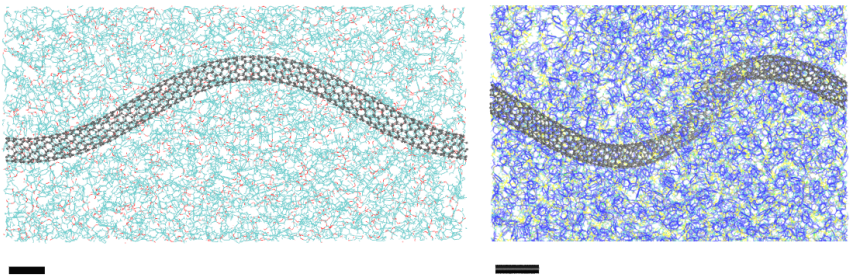

Figure 4.7: Examples of curved CNT geometries, used in simulation, embedded in PC matrix: sine-shaped (left) and spiral-like (right), - scale bar's length equal to 10 Å

To investigate the effects of curved CNT on the composites' mechanical properties via molecular dynamics, CNTs in the shape of sine-like waves or spirals (figure 4.7) of different curvature were embedded in a polymer matrix. In all cases a 13.2 nm long section of a (9, 0) CNT (diameter 0.7 nm) was used. The bisphenol-A (BPA) polycarbonate (PC) matrix was modeled by some 50-300 BPA-PC molecules 5-60 BPA blocks in length, resulting in a CNT volume frac-

tion of approximately 0.4 vol.%. The overall number of atoms in the model was kept at some 50,000 due to computational limitations. The initial sparse random distribution of PC molecules was compressed until the target density of density of 1.2 g/cm^3 [177] was reached and equilibrated with Nose-Hoover NPT barostat for $4 \cdot 10^5$ timesteps.

As expected, a linear strain-stress relation was observed for all simulated cases (figure 4.8, ϵ is stress and L_X is the sample length in X direction). For pure PC a Young's modulus of 2.33 ± 0.13 GPa was obtained, which is in good agreement with typical experimental values of 2.1–2.4 GPa [177]. For single straight carbon nanotubes the Young's modulus along the tube axis was evaluated as 2 TPa, which is within range of experimentally observed values [178].

To characterize the shape of the CNT a "curviness parameter" was introduced:

$$\omega = A/h, \tag{4.3.1}$$

where A - is the amplitude of sine-wave or the spiral's radius, while h - is the period for the former and step for the later. The normalized variation of the composite's Young's modulus with such defined ω is shown on the figure 4.9 along with results of FEM calculations and analytical modelling by our colleagues. All the methods are in qualitative agreement and predict a rapid almost hyperbolic decrease of the composites mechanical strength as shape of the nanotubes becomes non-straight. This is expected, as the CNT are highly flexible and, being curved, can easily react on stress by change of conformation, while the stress, applied to a straight nanotube, immediately leads to stretching of large number of covalent bonds.

4.4 Conclusions and future directions

An iterative Monte Carlo approach with intersection correction was implemented in the reported code to enable generation of large systems of non-overlapping complex shaped particles using NVIDIA CUDA GPGPU approach. Systems containing the number of particles as high as 10^7 can be generated within minutes using modern consumer class GPUs. The results can be outputted directly in text or binary format for post processing, visualization or molecular dynamic simulations. A number of procedures for statistics collection and tiff-image generation are also implemented.

The simple numerical procedure adopted to estimate the effect of morphology on CNT-based composites' electrical properties was validated against known ana-

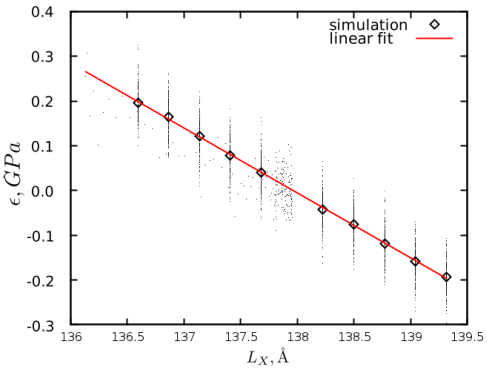

Figure 4.8: Example of the linear fit of the straining simulation results: dots designate the instantaneous measurements, diamonds - average result for the fixed elongation, line - linear fit

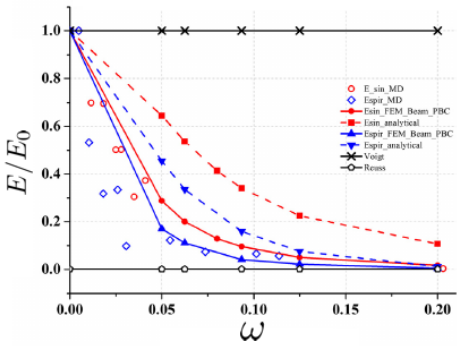

Figure 4.9: Variation of the composite's Young's modulus (E) with CNT's curvyness parameter (ω): open symbols designate the results of this work, lines with filled symbols - the results of continuous models [179]

lytic relations of percolation theory and a number of experimental results. With the given data it was shown that the difference in CNT agglomerates' size in the compared samples has only minor effect on the samples' resistivity and the variations in measured conductivity more likely must be described with the effect of alignment.

Further development of the model would be focused on incorporation the results of abinitial calculations for better quantitative agreement with experiment. The code will be also expanded to include various filler particle shapes, capability to combine particles of different shapes, interparticle forces evaluation, equivalent resistance network construction, evaluation of equivalent continuum distribution of mechanical properties.

Although the model developed in this work seems to offer the potential to predict optimized morphology leading to the desired composite properties, further analysis and understanding of the nanocomposites' behavior are still essential, especially focused on processing-morphology relationships, which is outside of the scope of the present work.

Another important outcome of the calculations, reported in this chapter, is that, in agreement with other theoretical estimates, deviation of the nanotubes' shape form straight decreases their effect on the composite's mechanical properties. As such bending of CNTs is stronger at higher filler concentrations an attempt to achieve stable electric properties by increasing the CNT content results in lower value of the added fillers and, thus, suboptimal cost-property ratio.

Chapter 5

Study of percolation behavior of self-assembled "rings-and-rods" networks

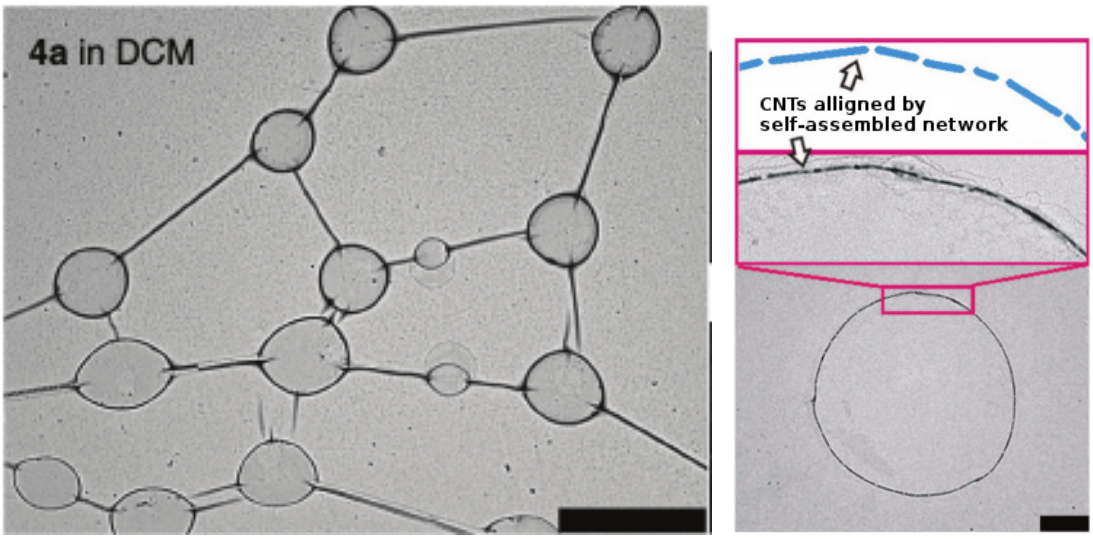

Figure 5.1: Electron microscopy images of "rings-and-rods" networks self-assembled from tetrakis-Schiff-zinc complex (referred as 4a) reprinted from [2]: pristine (left, scale-bar 5 μm) and intercalated with CNT (right, scale-bar 1 μm)

This chapter summarizes the results of numerical studies of the conductive properties of "rings-and-rods" molecular networks, resembling those produced by solvent evaporation of twinned salphen-zinc complexes as was reported in [2]. The remarkable capability of such molecular assemblies to incorporate carbon nanotubes from solution makes them potential dispersing agents for preparation of CNT-containing films and composites. As was discussed in the previous chapter, due to the percolation nature of the electric properties of the CNT-reinforced

composites, their electric conductivity can emerge even at low filler concentration in otherwise insulating polymer matrix. However, growing tendency of the nanotubes to agglomerate and bend with increasing concentration prevents the achievement of metal-like conductivity in composites. The deteriorating impact of those factors can be avoided if the nanotubes are incorporated into a self-assembled molecular network. In this case, however, the electrical properties of the composite are not anymore described by the percolation law of randomly distributed CNTs. Instead, the percolation characteristics of the networks themselves must be determined. Namely, how the network sparsity, characterized in 2D case by the average surface per ring $\mathcal{S}_\mathcal{R}$ or average volume per ring $\mathcal{V}_\mathcal{R}$ in 3D, and the number of rods ($\mathcal{N}_{r/\mathcal{R}}$), connecting the rings[1], combined with the rings' dimensions and mutual orientation (in 3D case) determine the resistivity of a flat film or a bulk composite.

Since little is yet known about how the rings and rods network emerges from solution and the experimental data is limited, it is hard to suggest a physically sound model describing the morphology of such networks. An attempt to explain this phenomenon with the help of molecular dynamics will be done in the next chapter. The task of this part of work was to provide a modelling tool, capable to simulate random "rings-and-rods"-like networks in 2D and 3D using ring's diameter and rim thickness from experimental estimates for thin films drop-casted from solution and to estimate relative change of sample resistance due to varying $\mathcal{S}_\mathcal{R}$ (or $\mathcal{V}_\mathcal{R}$), $\mathcal{N}_{r/\mathcal{R}}$ and rings' orientational distribution. Its algorithm is briefly described in section 5.1.

With Its help, a set of network models were generated, filling flat square (2D), cubic and thin film (3D) samples, and their resistances were compared across the range of values of $\mathcal{S}_\mathcal{R}(\mathcal{V}_\mathcal{R})$, $\mathcal{N}_{r/\mathcal{R}}$, film thickness ($h_{film}$) and rings alignment (in bulk composite). The results of these calculations are summarized in section 5.2. The aim of these studies was to figure out, what characteristics of "rings-and-rods" networks mainly determine the total resistivity of the sample and what results potentially can be achieved. It will be shown that there is a clear percolation like dependence of network connectivity on the number of rods per ring and, through it, on the network's sparsity. However only weak impact of alignment was found, indicating that experimentally observed difference between surface conductivity

[1]One can imagine a point contact between the intersecting rings as a rod of zero length. Such point connections occur mostly in case of high density networks far from percolation threshold. For this reason hear and after the term "rods per ring" and more general expressions "connections per ring" or "links per ring" are used as synonyms, unless the opposite is clearly stated.

enhancement and Its bulk counterpart can only be explained by different density and size distribution for the rings on surface and in the bulk of the composite.

5.1 Methods

As the details of such network's assembly process is yet to be understood, in this study the molecular network was represented with a set of randomly placed toroidal rings connected with conical rods. The diameters of the endpoint cross sections of each rod were equal to the diameters of the cross sections of the rings, the rod was connecting. Both rings and rods consisted of the same material with uniform volume resistivity $\rho_{\mathcal{R}} = 1$ a.u. The experimental parameters used in the simulations are summarized in the paragraph 5.1.1. The paragraph 5.1.2 briefly describes general procedure of "rings-and-rods" network sample simulation and evaluation of Its resistance. The paragraph 5.1.3 covers several strategies used in this study to keep the average number of rods per ring $\mathcal{N}_{r/\mathcal{R}}$at the desired level. Finally, the paragraph 5.1.4 describes the estimation of the percolation threshold for "rings-and-rods" networks and the network's parameters at percolation. The suggested algorithm was implemented as a tool written in C++ [180, 181]. Visualization Toolkit (VTK version 6.0) was used for plotting [182].

5.1.1 Parameters taken from experimental source

The parameters of the experimentally observed networks are summarized in table 5.1. These parameters were provided by the co-authors of [2]. "Pristine" column refer to pure tetrakis-Schiff zinc complex networks, self-assembled by drop-casting from solution, while "CNT-filled" contains the parameters of the networks with intercalated nanotubes, produced with the same method. Application of these parameters, especially of rings' diameters and thicknesses distributions, to the case of polymer composite samples requires caution. However, experimental characterization of such composite samples is a nontrivial task and, so far, drop-casted films remain the only viable source of statistically solid information.

For a system of intersecting sticks randomly distributed on a surface Pike and Seager have obtained the estimation for percolation threshold [34] given by the equation 2.1.7 of the literature review section 2.1. Defining the surface fraction as $\phi_{surf} = \frac{N_{CNT}S_{CNT}}{S_{box}} = N_S l_{CNT} d_{CNT}$, where N_{CNT} and $S_{CNT} = l_{CNT}d_{CNT}$ is correspondingly the number of nanotubes in the sample and the area of their projection on the sample's surface, S_{box} - is the surface area of the sample itself

	pristine	CNT-filled
Ring diameter ($\mathcal{D}_\mathcal{R}$),μm	2.100 ± 0.180	5.514 ± 1.974
Rim thickness ($t_\mathcal{R}$),μm	0.138 ± 0.011	0.110 ± 0.008
Surface per ring ($\mathcal{S}_\mathcal{R}$), μm^2	$27.69 - 79.37$	75.56
Number of rods per ring ($\mathcal{N}_{r/\mathcal{R}}$)	2.840 ± 0.729	
Film thickness (h_{film}), μm	50.0	
CNT length (l_{CNT}), μm	1.04	
CNT diameter (d_{CNT}), nm	16.0	
CNT aspect ratio (α_{CNT})	65.0	

Table 5.1: "Rings-and-rods" network parameters from experimental source

and N_S - is the sticks density (in sticks per unit square), one can estimate the percolation threshold of nanotubes in 2D as:

$$\phi_{2D} \approx \ 5.7/\alpha_{CNT} \ ; \tag{5.1.1}$$

where $\alpha_{CNT} = l_{CNT}/d_{CNT}$ is called "aspect ratio".

For 3D case the percolation threshold could be estimated from excluded volume theory as 2.1.8. Here it is accompanied by the expression for CNT's average excluded volume [183, 184]:

$$\begin{aligned} &1 - exp\left(-\frac{1.4V_{CNT}}{\langle V_{ex}\rangle}\right) \leq \phi_{3D} \leq 1 - exp\left(-\frac{2.8V_{CNT}}{\langle V_{ex}\rangle}\right); \\ &\langle V_{ex}\rangle = \frac{4\pi}{3}d_{CNT}^3 + 2\pi d_{CNT}^2 l_{CNT} + d_{CNT} l_{CNT}^2 \langle sin(\gamma)\rangle ; \end{aligned} \tag{5.1.2}$$

where $\phi_{2D(3D)}$ - surface (or bulk) percolation threshold, V_{CNT} - nanotube's average volume and $\langle V_{ex}\rangle$ is the average excluded volume, or the part of the system's volume around any nanotube, inaccessible to the other nanotubes to prevent their overlap, $\langle sin(\gamma)\rangle$ - average value of sin of angle between nanotubes' axes (in the idealized uniform case $\langle sin(\gamma)\rangle = \frac{\pi}{4}$).

Based on the data of table 5.1 the theoretical estimates for percolation thresholds for the CNTs, used in the experiment, are: $\phi_{2D} = 8.8$ surf.% and $\phi_{3D} \in [1.02; 2.02]$ vol.%. Here surf.% and vol.% are consequently the percent of the film surface area (in 2D) or of sample volume (in 3D).

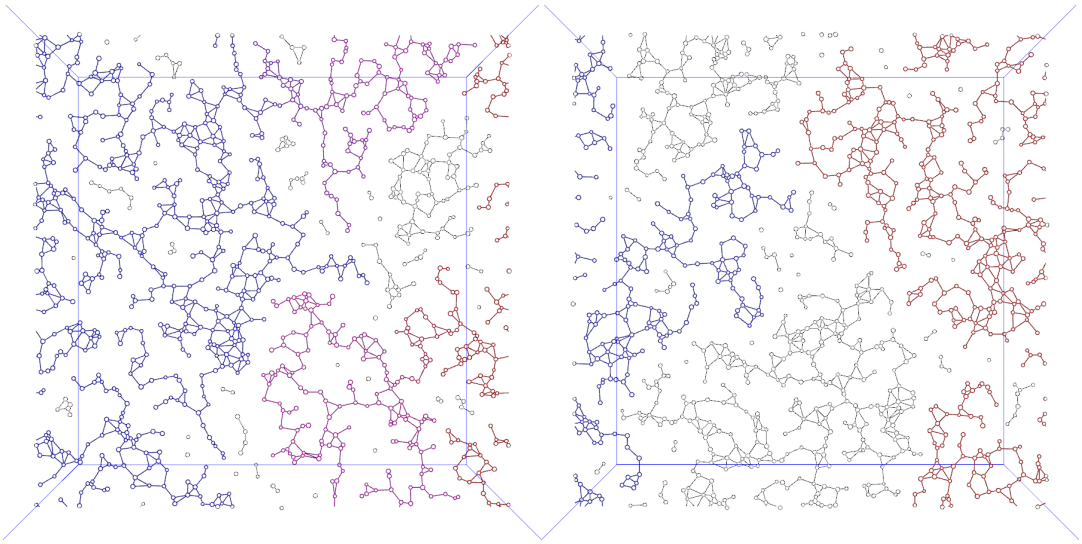

Figure 5.2: Electrostatic potential change (color) in the simulated "rings-and-rods" networks: connected (left) and disconnected (right)

5.1.2 Network generation and processing

Each simulation sample was prepared as follows:

First, a predefined number of rings was distributed randomly over the volume (across the surface in 2D case) using a von Neumann acceptance-rejection algorithm, as described in the section 3.1 of the Methods chapter. The diameter of the rings was assigned according to Gaussian distribution with the parameters taken from experimental data. In this case, however, a ring was allowed to intersect with any of the rings created before, if their center-to-center distance was greater, than the radius of the largest of them. In other words: no ring could enclose the center of the other ring. This reflects the expected physical picture that the molecules, present in the volume of such pair, would rather merge into a single ring.

In 3D case the alignment of the rings was characterized by the angle between a ring axis and z-axis of the simulation cell. The angle is taken as random value with either uniform (no alignment) or Gaussian distribution. In the later case, the width of distribution $\sigma_{\mathcal{R}\theta}$ is the parameter controlling the alignment.

On the second stage, the rings were connected with rods to their direct neighbors: the space was separated into polyhedral cells, representing the part of space that was closer to current ring center, and only those rings, whose cells had common face (or edge in 2D) were connected if the length of the rod was smaller than limit (taken to be equal to the circumference of the largest ring). To bring the average number of rods per ring to a desired value certain percent of the remain-

ing rods were randomly chosen and deleted according to one of the algorithms described in 5.1.3.

After a sample is generated, Its connectivity is verified by Dijkstra-like algorithm [185]: vertexes (points where rod or ring segments connect) a visited first starting from any selected plane of the box (left electrode), then starting from the opposite plane (right electrode). Vertexes, not connected to either of planes, are disregarded in future. If no vertexes could be achieved both from left and right electrode, network is disconnected (figure 5.2).

For a connected network, a linear system of Kirchhoff current laws [168] is solved to identify vertexes' voltages and currents, flowing along the segments. The resistances of rod and ring segments are taken to be $\int_{t1}^{t2} \rho_{\mathcal{R}} s(t) dt$, where *s(t)* is the cross sectional area of the segment at coordinate *t*. The total sample resistance is calculated as the ratio of the applied voltage to the total current flowing into negative electrode;

For each parameter combination a set of 50 independent calculations were carried out. The samples' resistances were averaged over the subset of realizations, for which the network was connected, and confidence intervals with the probability of 95% were calculated. Similar to the previous chapter the percolation threshold of the network (at given $\mathcal{N}_{r/\mathcal{R}}$, $\sigma_{\mathcal{R}\theta}$ and h_{film}, if applicable) was defined as the network's sparsity at which the probability to obtain a connected network was 50%. This can be translated into CNTs' surface or volume fraction, required to fill the generated network (if connected) with one nanotube thick string of nanotubes (lower estimate) or the total volume (or surface) fraction of the network (upper estimate). During fitting of percolation equation the data points were weighted by their connectivity rate to decrease the importance of the points beyond percolation, were resistivity of accidentialy connected networks has large fluctuations.

5.1.3 Ring connection strategies

As the detailed mechanism of the formation of the rods is yet to be determined, several algorithms of rings connection were compared. These strategies were introduced to provoke slightly different network morphology during elimination of excessive connections (figure 5.3):

- "FULL": all the rods connecting direct neighbors were kept if the rod length is less than maximum allowed distance. Tends to "overconnect" networks, but was used as the base for comparison and as an absolute lower estimate of percolation threshold: if the network with certain volume/surface fraction

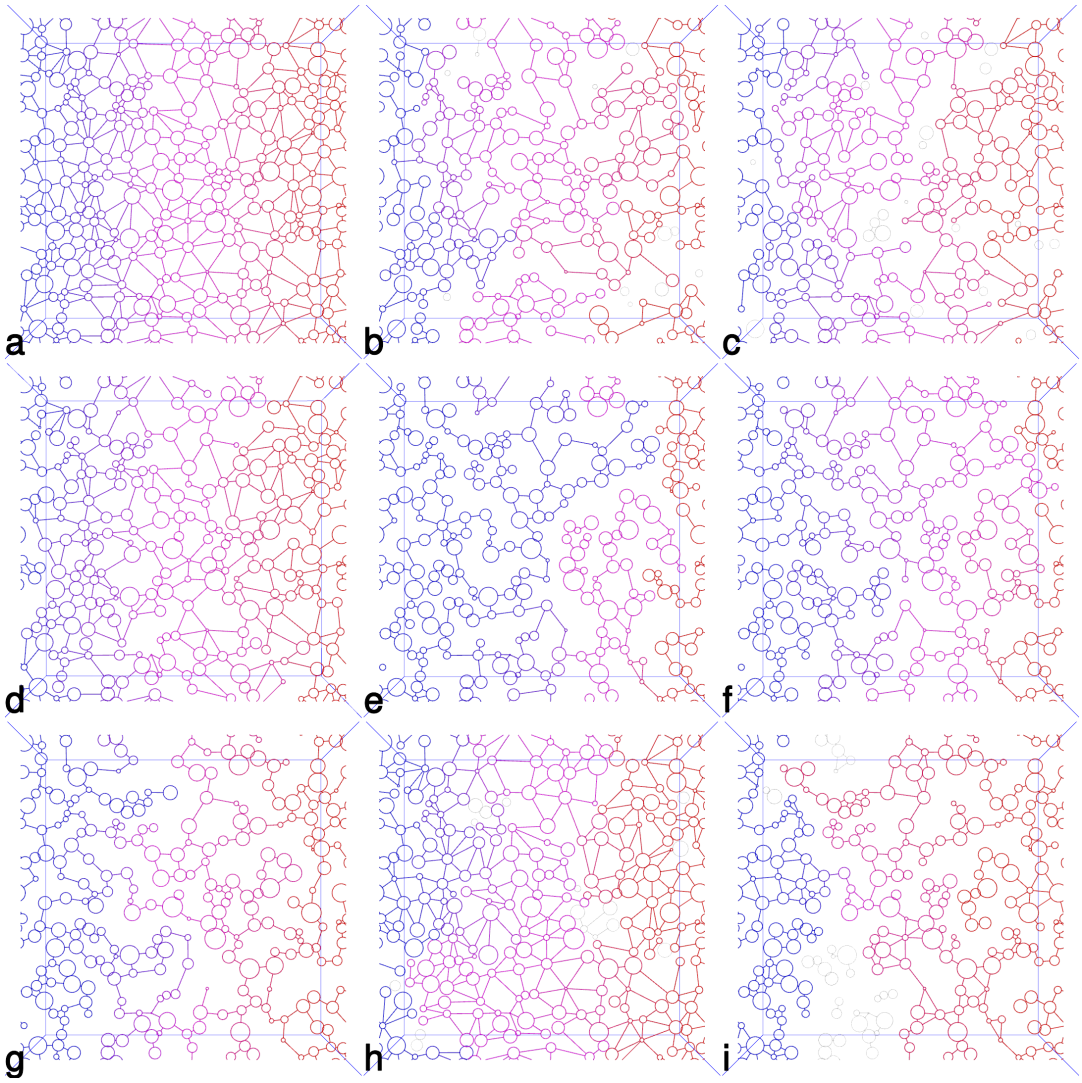

Figure 5.3: Examples of the structures of "rings-and-rods" networks, simulated from the same distribution of rings but with different connection strategies: "FULL" (a), "STAT_RND" (b), "STAT_N" (c), "STAT_N_NZ" (d), "STAT_N_L" (e), "STAT_ALN" (f), "COMP_ALN" (g), "STRETCH" (h), "CRIT_RAD" (i)

is disconnected when all the possible rods are included, than the network is too sparse.

- "STAT_RND": rods were eliminated randomly with uniform probability until the target average number of connections per ring was reached. The easiest for implementation method, but lacks any physical meaning. Used mainly for comparison with other methods.
- "STAT_N": Rods were removed until the target rods-per-ring ratio was reached in a following fashion: on each iteration one ring was selected randomly with the probability of selection being proportional to the number of connections to this ring (including finite length rods and direct ring-ring connections) and the rod, connecting the selected ring to the ring with highest number of connections among the ring's first order neighbors (i.e. rings directly connected to it) was erased.
- "STAT_N_NZ": Similar to the previous one (STAT_N) but the probability of selecting a ring was proportional only to the number of finite length rods regardless the number of direct point contacts.
- "STAT_N_L": on each iteration the ring was selected as in "STAT_N" method, but this time the longest rod was deleted.
- "STAT_ALN": sophistication of the previous line of methods: for each rod of the selected ring "weight" was estimated based on combination of factors: number of connections for both rings that were connected by the rod (N_i and N_j), the rod's length (L_{ij}) and sector angles (α_i and α_j) that the rod's endpoint made with the closest endpoint of another rod of the same ring (or point contact). The "weight" of the rod connecting rings i and j (W_{ij}) was calculated as follows:

$$
\begin{gathered}
W_{ij} = W_L(L_{ij})W_N(N_i)W_N(N_j)W_\alpha(\alpha_i)W_\alpha(\alpha_j); \\
W_L(l) = exp\left(-\tfrac{l}{\langle L\rangle}\right); \qquad \langle L\rangle = \begin{cases} 2\left(3\sqrt[3]{V}/4\pi - \langle R_{\mathcal{R}}\rangle\right) & \text{in 3D} \\ 2\left(\sqrt{S}/\pi - \langle R_{\mathcal{R}}\rangle\right) & \text{in 2D} \end{cases}; \\
W_N(n) = exp\left(-\frac{\left(n-\mathcal{N}_{r/\mathcal{R}}^{R\&R}\right)}{2\sigma_{r/\mathcal{R}}^2}\right); \qquad W_\alpha(\alpha) = exp\left(-\tfrac{(\alpha-\langle\alpha\rangle)}{2\sigma_\alpha^2}\right);
\end{gathered}
\tag{5.1.3}
$$

where $\langle L\rangle$ is the average distance between rings with average radius $\langle R_{\mathcal{R}}\rangle$, uniformly distributed in simulation cubic box of volume V or a flat square of surface S; $\mathcal{N}_{r/\mathcal{R}}$ and $\sigma_{r/\mathcal{R}}$ - are the target average number of rods per ring and its standard deviation; $\langle\alpha\rangle = 2\pi/\mathcal{N}_{r/\mathcal{R}}$ is the average sector angle and $\sigma_\alpha = 2\pi\sigma_{r/\mathcal{R}}/\mathcal{N}_{r/\mathcal{R}}$ - Its standard deviation. On each iteration the rod

with the smallest weight out of all rods connected to the selected ring was deleted. Such approach was intended to empirically reproduce the expected uniform distribution of the rods around the current ring.

- "COMP_ALN": generalization of the previous method, however unlike "STAT_ALN" where weights were calculated on each iteration only for rods connected to randomly selected ring, here weights were calculated for all the rods present in simulation and the rod with the smallest weight among all was deleted, after which weights of the affected rods were recalculated.
- "STRETCH": this method exploits the hypothesis that rods - were formed from the rings that have collapsed and stretched by their shrinking neighbors. Within this model the length of the rods should follow the distribution of the rings' circumferences. For this reason, the rods weights were estimated using the given average ring diameters and their standard deviations as the probability to find a ring with given circumference. A particular feature of this method is that extremely short rods are just as uncommon as extremely long.
- "CRIT_RAD": the method exploits another hypothesis: that the rings were formed from bubble-like globules that collapsed into rings when solvent evaporated. The rods remained between the rings, whose globules were in direct contact in the initial foam of globules. The algorithm estimates maximum radius that the globule, representing the current ring, could have without absorbing the closest neighbors (center of globule remains constant). If any two connected rings could be represented by touching globules, the rod between them remained, otherwise it was deleted. Apart from "FULL", this is the only method that doesn't exploit average number of contacts per ring as an external parameter and should reproduce the expected behavior that the number of contacts increases with the networks density.

If the rings had a point of intersection - this connection is maintained no matter what algorithm was used.

5.1.4 Percolation threshold calculations

To estimate the percolation threshold of the "Rings-and-rods" networks in 2D and 3D as the function of both network sparsity and average number of rods per ring series of calculations were conducted with increasing sparsity for a set of predefined values of $\mathcal{N}_{r/\mathcal{R}}$. It is convenient to characterize the sparsity of a

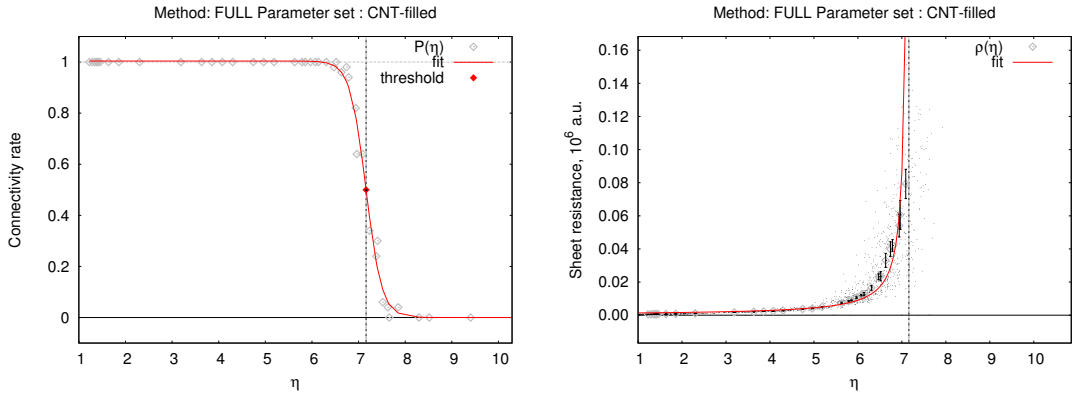

Figure 5.4: Profiles of connectivity rate (left) and sheet resistance (right): numerical results (dots), averages (diamonds) and fit (red line)

"rings-and-rods"-like network with a scaling parameter η, defined as:

$$\eta = \begin{cases} 2\sqrt{\mathcal{S}_\mathcal{R}/\pi}/\mathcal{D}_\mathcal{R}, & in\,2D; \\ 2\sqrt[3]{3\mathcal{V}_\mathcal{R}/4\pi}/\mathcal{D}_\mathcal{R}, & in\,3D; \end{cases} \tag{5.1.4}$$

where $\mathcal{S}_\mathcal{R}$, $\mathcal{V}_\mathcal{R}$ and $\mathcal{D}_\mathcal{R}$ are correspondingly the average surface and volume per ring and the average diameter of ring as defined before.

A set of 50 independent calculations was conducted for each scaling parameter value and the probability P to obtain the connected network at given values of η and $\mathcal{N}_{r/\mathcal{R}}$ was estimated. For each value of $\mathcal{N}_{r/\mathcal{R}}$ the profile of $P(\eta)$ was fitted with sigmoid function as shown on figure 5.4 (left):

$$P(\eta) = A\left(1 - \tanh\left(\alpha(\eta - \eta_0)\right)\right), \tag{5.1.5}$$

where A, α and η_0 are the fitting parameters. The critical value of the scaling parameter η_C was estimated as the solution of $P(\eta_C) = 0.5$.
At each point $\left(\eta, \mathcal{N}_{r/\mathcal{R}}\right)$ the sample's resistance was estimated as the average among the connected realizations and the profile of $R(\eta)$ for each target value of $\mathcal{N}_{r/\mathcal{R}}$ was fitted with the percolation-like equation [184] as shown on the figure 5.4 (right):

$$\rho(\eta) = \rho_0\left(\eta - \eta_C\right)^\delta \tag{5.1.6}$$

where $\rho(\eta)$ - is the sample's resistance characteristic (sheet resistance in 2D or resistivity in 3D), η_C - the critical value of scaling parameter at which the percolation threshold occurs, ρ_0 and δ - the fitting parameters.

The fitting and parameter variance estimation was done using the non-linear least squares algorithm [186] as implemented in SciPy numerical methods library

[187]. Other network's parameters, namely the average number of connections per ring and the average surface (or volume) per ring , was estimated by linear interpolation between the closest numerical values. Another important value - the surface (or volume) fraction of CNTs, required to fill the network - was estimated from the combined length L_{net} of all the rods and rings' circumferences according to:

$$\phi_{surf} = {}^{S_{CNT}\frac{L_{net}}{l_{CNT}}}/_{S_{box}};\ \phi_{vol} = {}^{V_{CNT}\frac{L_{net}}{l_{CNT}}}/_{V_{box}}; \tag{5.1.7}$$

where S_{box} and V_{box} - are the surface and volume of the simulation sample correspondingly in 2D and 3D case, $S_{CNT} = d_{CNT}l_{CNT}$ - the average surface of a nanotube projection on the network's plane and and $V_{CNT} = l_{CNT}\pi^{d^2_{CNT}}/_4$ is the average volume of a nanotube.

5.2 Results and discussion

Analysis of "rings-and-rods"-like network is a non-trivial task as, although Its basic constituting components - ring-like assemblies - do behave as randomly scattered particles, the probability of connection between them is not defined by the presence of a direct contact, but by presence of a rod-like link that very well can exist between the two rings that are far apart while absent between another pair that is much closer. In these studies this task was decomposed into several parts according to parameter range and acting factor. Paragraph 5.2.1 covers the preliminary comparison of the strategies introduced in the methods subsection of this chapter on the set of parameters, corresponding to the known experimental data (table 5.1) to get their first interpretation from geometrical point of view and to identify the potential drawback of the chosen methods. In the next paragraph 5.2.2 the selected methods are applied to a wider range of network densities and varied number of rods per ring to estimate theoretical percolation threshold. Finally, the effect of the orientation of the rings and finite thickness of the composite film is introduced in the paragraph 5.2.3.

5.2.1 Connectivity strategy comparison

To compare the morphology effect on the network's connectivity (and, through it, on sample's resistance) several sets of "ring-and-rod" networks were simulated in 2D using the parameters for both the pristine and CNT-filled molecular networks. Within each set the simulation box side was varied from 50 to 300 microns while the concentration of rings (surface per ring) was kept fixed. As the simulated

sample represents a flat square, Its resistance beyond percolation threshold should not depend on the side of the square. In all cases (where applies) target number of tubes per ring was equal to 2.84 ± 0.729. As experimentally the connected networks were observed in the range $27.7 - 79.4$ μm^2 per ring for empty networks and about 75.6 μm^2 for networks containing CNTs, in this part of work $\mathcal{S}_\mathcal{R}$ was varied in the range $[25.0; 85.1]$ μm^2 per ring.

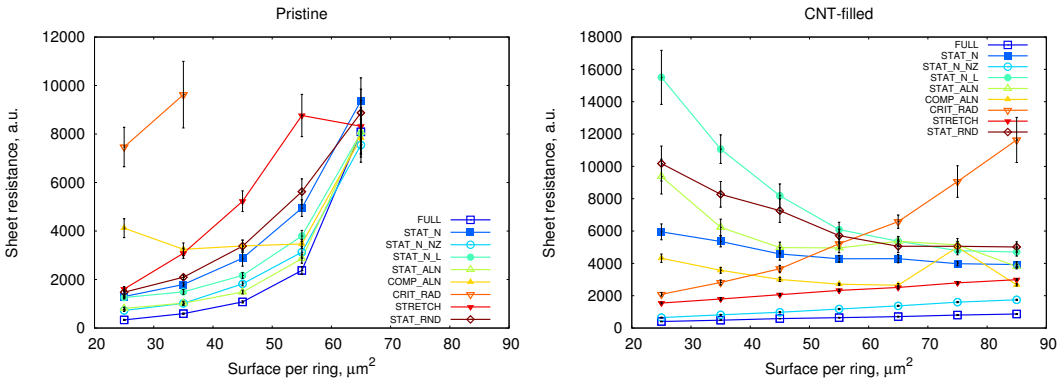

Figure 5.5: Sheet resistance of simulated 2D "rings-and-rods" networks: left - pristine, right - intercalated with CNT

The calculated sheet resistances for both sets of parameters (pristine networks and CNT-intercalated) are presented on the figure 5.5. Here each point represents the average over those samples, where a connected network was obtained. It is clear that the two data sets have strikingly different behavior: while the results for pristine networks show growing resistance, approaching the percolation threshold, the results for CNT-filed networks looks counter-intuitive with most strategies giving raising resistance at denser end of range. This seemingly contradiction can be explained if instead of average surface per ring $\mathcal{S}_\mathcal{R}$, directly obtained from experiment, sparsity is characterized by the scaling parameter η, as defined by equation 5.1.4. Plotting the probability to obtain the connected network against the scaling parameter η one can see (figure 5.6) that, due to more than twice larger diameter, CNT-intercalated networks with the studied densities fall into the range of small scaling ratios approaching the critical value $\eta_R = 1.22$ corresponding to circle surface fraction 0.676 - the percolation threshold for fully penetrable disks in 2D [188]. Given the fact, that unlike in the system studied by Quintanilla and coworkers, rings' overlap is restricted by the rings centers, it is clear that for such "soft" disks the percolation is achieved at smaller surface fraction (larger scaling parameter η). The effect of this on the network morphology is seen on the figure 5.7: as the scaling parameter η approaches η_R the contacts between the rings are dominated by direct intersections rather than by finite rods and

the strategies that try to keep the number of finite rods around the predefined value cut the longer links between the clusters, thus leaving fewer paths across the whole sample. “STRETCH” and “STAT_N_NZ” are the two exceptions from this trend as they do not give the shorter rods priority over the longer ones. The same trend could be seen in the case of "CRIT_RAD" method but for other reason: due to high packing density of rings the growth of initial "globules" is blocked by closest neighbors, preventing "touching" with those somewhat more distant.

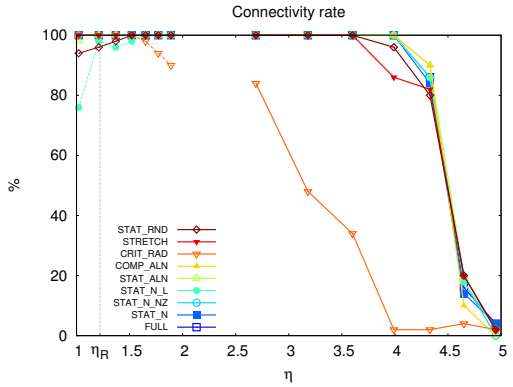

Figure 5.6: Probability to find a connected network as the function of η for pristine (thick solid lines) and CNT-intercalated (thin dashed lines)

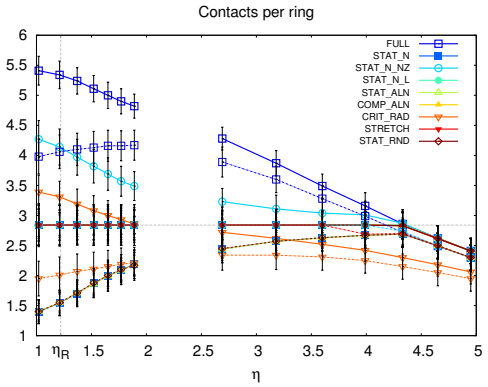

Figure 5.7: Number of contacts per ring as the function of η: finite rods only (thin dashed lines) and sum of finite and point contacts (thick solid lines)

On the contrary, it is clear that for pristine networks the percolation threshold lies within the selected range: resistance trend for networks sparser than 55 per ring diverges with box size (as can be seen in more details in appendix A.1), while for denser networks sheet resistance saturates with box side. Overall deviation between the strategies, based on random rod elimination until, is not quite significant. "STAT_ALN" method produces the most optimal networks: lowest resistance very close to "FULL" with lower number of rods and, hence, surface fraction. "CRIT_RAD" method looks completely off there with the lowest number of connections and fast deterioration of conductivity with increasing sparsity of network. From the figure 5.7 it is clear, that the loss of percolation with increasing sparsity correlates with the decrease of the average number of contacts per ring below $\sim$ 2.5, which for “CRIT_RAD” strategy happens much faster than for random methods.

5.2.2 Percolation threshold calculation

As was shown previously, strategies based on random elimination of rods give close results in the region of interest, so in this part only the "STAT_ALN" strategy was used to study the effect of the number of connections per ring. The average of the results calculated with the "FULL" strategy applied to the same networks is used as asymptotic. Besides the critical value of scaling parameter η_C and resistance fitting parameters ρ_0 and δ, for each target number of rods per ring ($\mathcal{N}^T_{r/\mathcal{R}}$) the values of $\mathcal{N}_{r/\mathcal{R}}$, $\mathcal{S}_\mathcal{R}$ and ϕ_{surf} (or $\mathcal{V}_\mathcal{R}$ and ϕ_{vol} in 3D) actually achieved at $\eta = \eta_C$ were estimated by linear interpolation (designated by superscript C).

5.2.2.1 2D networks

A square sample with uniform random distribution of 1000 rings was used for the percolation threshold study of the flat networks. The fitting parameter ρ_0 in 2D case corresponds to the sample's sheet resistance. From the results of the previous section it is clear, that the percolation threshold for a 2D network occurs in the region $\eta \geq 3$. So the sample side length was varied from 70 to 500 μm for pristine networks and from 200 to 1600 μm for CNT-intercalated. This corresponds to η varying from 3 to 11. The target average number of rods per ring $\mathcal{N}^T_{r/\mathcal{R}}$was varied in the interval $[2.0; 3.0]$.

The resulting profiles of the connectivity rate and sheet resistance as the function of η are shown at the figure 5.8. Here dots designate the results of single simulations, while diamonds correspond to the average value for the fixed η, thin dashed lines designate the fit with the percolation equation, vertical dashed lines indicate the critical value of the scaling parameter η_C, at which the percolation threshold occurs. The values of the fitting parameters for different $\mathcal{N}^T_{r/\mathcal{R}}$ are summarized in the tables A.19 (pristine) and A.20 (CNT-intercalated) in the appendix section A.2 The change of η_C, ρ_0 and δ together with $\mathcal{N}^C_{r/\mathcal{R}}$ (the number of rods per ring, actually achieved at percolation) for CNT-intercalated networks are shown on the figure 5.9 (the results for pristine networks follow the same trends with the exception of scale).

For both pristine and CNT-intercalated networks no percolation was found for $\mathcal{N}^T_{r/\mathcal{R}} = 2$, the probability to obtain a connected network was below 45%. Starting from $\mathcal{N}^T_{r/\mathcal{R}} = 2.2$ the calculated profiles of $P(\eta)$ and $R(\eta)$ have a clear percolation-like behavior with the percolation threshold value dependent on average number of connections allowed. The mechanism of percolation is, however different. For $\mathcal{N}^T_{r/\mathcal{R}} \leq 2.6$ the percolation threshold is achieved before the limit of total number of connections is reached, so for those series networks get disconnected because

of low probability to have connected cluster stretching over the whole sample. For the average number of contacts higher than 2.6 in the observed region the conductivity disappears with decreasing ring density not because the probability to have connected network with the target number of connections per ring is low, but because the target number of contacts can't be achieved at such density as the rings are spread beyond the maximum allowed distance from their closest neighbors. This trend is clearly shown at figure 5.9: all parameters approach their asymptotic values as $\mathcal{N}_{r/\mathcal{R}}^{T}$ gets over 2.6.

The table 5.2 summarizes network's characteristics, corresponding to percolation threshold. From the table it is clear, that the critical surface density of rings (for contacts per ring > 2.6) lies in the range of $\sim 60 - 70$ μm^2 per ring for pristine networks, which complies with the experimental observation of connected networks of tetrakis-Schiff zinc complexes with the surface ring density 27.69-79.37 μm^2 per ring and on average 2.8 rods per ring. In the view of the results of this section, it can be suggested that at higher densities ($\eta < 2$) the rings of the same size would have to overlap with each other too much. As the molecules, constituting the network, interact with only weak Coulomb and van der Waals forces, they could relatively easy rearrange at high density form interconnected rings into a more uniform agglomeration. Sparser networks ($\eta > 5$) are beyond the percolation threshold, thus the probability to obtain a large interconnected network is negligible.

Extrapolating the same tendency on CNT-intercalated networks one can expect the interconnected networks as sparse as $\sim$1000 μm^2 per ring ($\eta_C \sim 7$). Such network can be filled with CNT content as low as $\sim$0.06 surf. % which is 2 orders of magnitude smaller than the theoretical prediction of 8.8 surf. % for the CNTs used in the experiment according to expression 5.1.1.

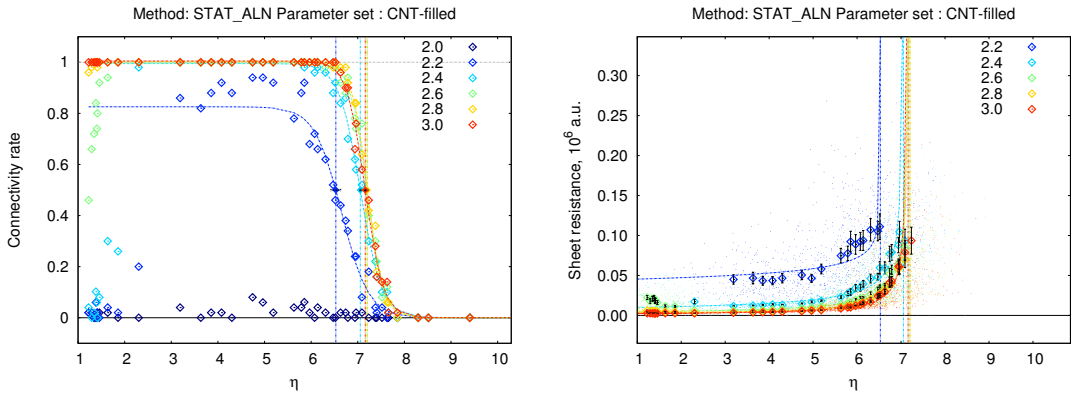

Figure 5.8: Variation of the 2D network's connectivity (left) and sheet resistance (right) with target number of rods per ring $\mathcal{N}_{r/\mathcal{R}}$ (shown with color)

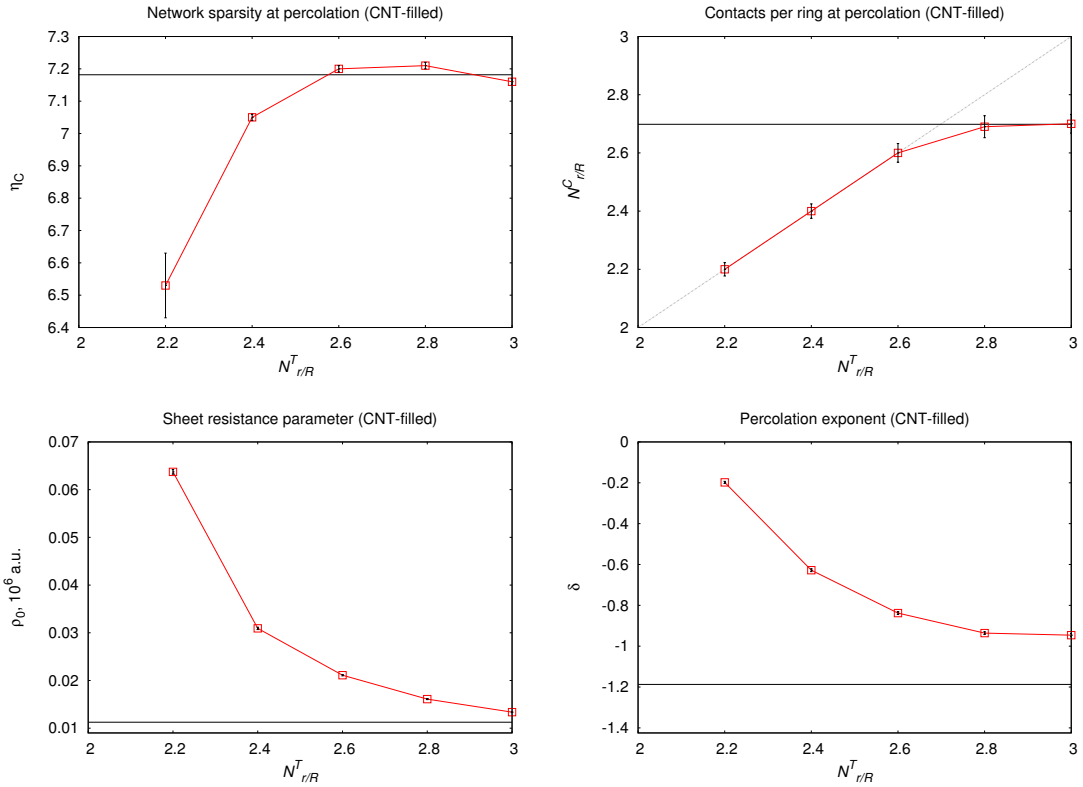

Figure 5.9: Variation of the "rings-and-rods" 2D network's parameters at percolation with target number of rods per ring $\mathcal{N}_{r/\mathcal{R}}$ (red line) and the asymptotic value (black horizontal line)

$\mathcal{N}^T_{r/\mathcal{R}}$	Pristine				CNT-intercalated			
	η_C	$\mathcal{N}^C_{r/\mathcal{R}}$	$\mathcal{S}^C_{\mathcal{R}}$	ϕ^C_{surf}	η_C	$\mathcal{N}^C_{r/\mathcal{R}}$	$\mathcal{S}^C_{\mathcal{R}}$	ϕ^C_{surf}
	-	-	μm^2	surf. %	-	-	$10^3 \mu m^2$	surf. %
2.0	-	-	-	-	-	-	-	-
2.2	4.04±0.34	2.2±0.1	56.7±4.7	0.3±0.2	6.53±0.20	2.2±0.1	1.018±0.033	0.06±0.06
2.4	4.38±0.02	2.4±0.1	66.4±0.4	0.3±0.2	7.05±0.02	2.4±0.1	1.188±0.004	0.06±0.04
2.6	4.47±0.02	2.6±0.2	69.4±0.3	0.3±0.3	7.20±0.02	2.6±0.1	1.237±0.004	0.06±0.05
2.8	4.51±0.02	2.7±0.2	70.5±0.2	0.3±0.3	7.21±0.02	2.7±0.2	1.240±0.003	0.06±0.05
3.0	4.50±0.00	2.7±0.2	70.1±0.1	0.3±0.3	7.16±0.02	2.7±0.1	1.224±0.004	0.06±0.04

Table 5.2: "Rings-and-rods" network's sparsity characteristics at percolation threshold in 2D

5.2.2.2 3D networks

A cubic sample with uniform random distribution of 1000 rings was used for the percolation threshold study of the "rings-and-rods" networks in 3D. The sample side length was varied from 16 to 135 μm for pristine networks and from 80 to 663

μm for CNT-intercalated. This corresponds to η varying from 1 to 8 for pristine networks and from 1.8 to 15 for CNT-intercalated. The target average number of rods per ring $\mathcal{N}^T_{r/\mathcal{R}}$ was varied in the interval $[1.2; 4.0]$.

The resulting profiles of the connectivity rate and volume resistivity as the function of η are shown at the figure 5.10. As previously, dots designate the results of a single simulations, while diamonds correspond to the average value for the fixed η, thin dashed lines designate the fit with the percolation equation, vertical dashed lines indicate the critical value of the scaling parameter η_C, at which the percolation threshold occurs. The values of the fitting parameters for different $\mathcal{N}^T_{r/\mathcal{R}}$ are summarized in the tables A.21 (pristine) and A.22 (CNT-intercalated) in the appendix section A.2 The change of η_C, ρ_0 and δ together with $\mathcal{N}^C_{r/\mathcal{R}}$ (the number of rods per ring, actually achieved at percolation) for CNT-intercalated networks are shown on the figure 5.11 (the results for pristine networks follow the same trends with the exception of scale).

Overall, the observations made in the previous section for flat networks stay valid in bulk case. The only exception that in 3D space the percolation cluster is possible for networks with fewer connections per ring as can be seen from the data presented on the figure 5.11 and in the table 5.3: successful fits for both pristine and CNT-intercalated networks were obtained already for $\mathcal{N}^T_{r/\mathcal{R}} = 2$ and the estimated network's parameters reached the saturation for $\mathcal{N}^T_{r/\mathcal{R}} \geq 2.4$. In the same time the critical scaling parameter η_C increases from 4.5 to 6.5 for pristine networks and from ~ 7 to 10.5 for CNT-intercalated. In other words: in bulk case the rings can be connected at much larger distance then on a flat surface. These observations can be explained purely from geometrical point of view: in 3D space each ring is surrounded with more neighbors than in 2D, thus it is more likely that the two rings, having a common neighbour, will be further apart; it is also less likely that a direct connection between the two rings will be obstructed by another ring, so the longer rods can exist without intersection with other network's components.

The increased η_C and decreased $\mathcal{N}^T_{r/\mathcal{R}}$ for 3D networks results in very small CNT content required to fill such network: the values as law as $10^{-4} - 10^{-5}$ vol. % can be achieved which is much lower then the estimate 1-2 vol. % according to expression 5.1.2. Comparable theoretical estimate is only achievable for millimeter-long nanotubes. Such extraordinary effect emerges from the fact that being intercalated into "rings-and-rods" network the nanotubes act as parts of an object of higher aspect ratio, which also preserves the contacts due to stronger interaction.

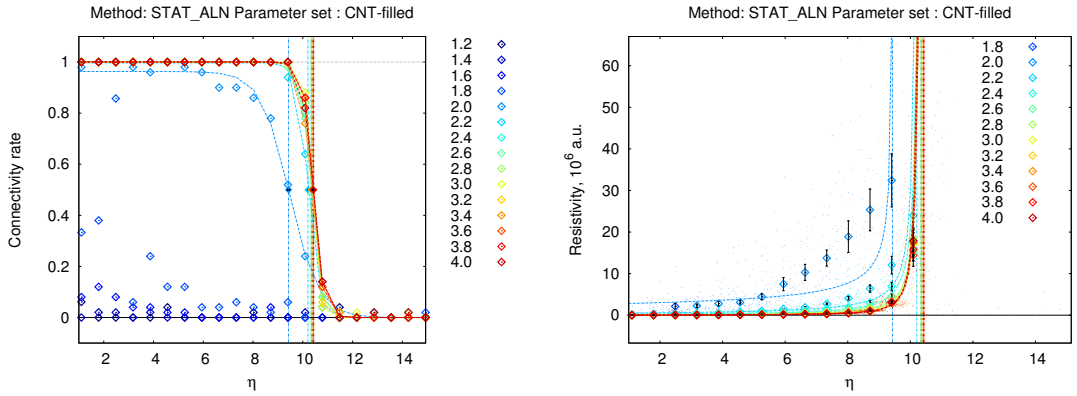

Figure 5.10: Variation of the 3D network's connectivity (left) and volume resistivity (right) with target number of rods per ring $\mathcal{N}_{r/\mathcal{R}}$ (shown with color)

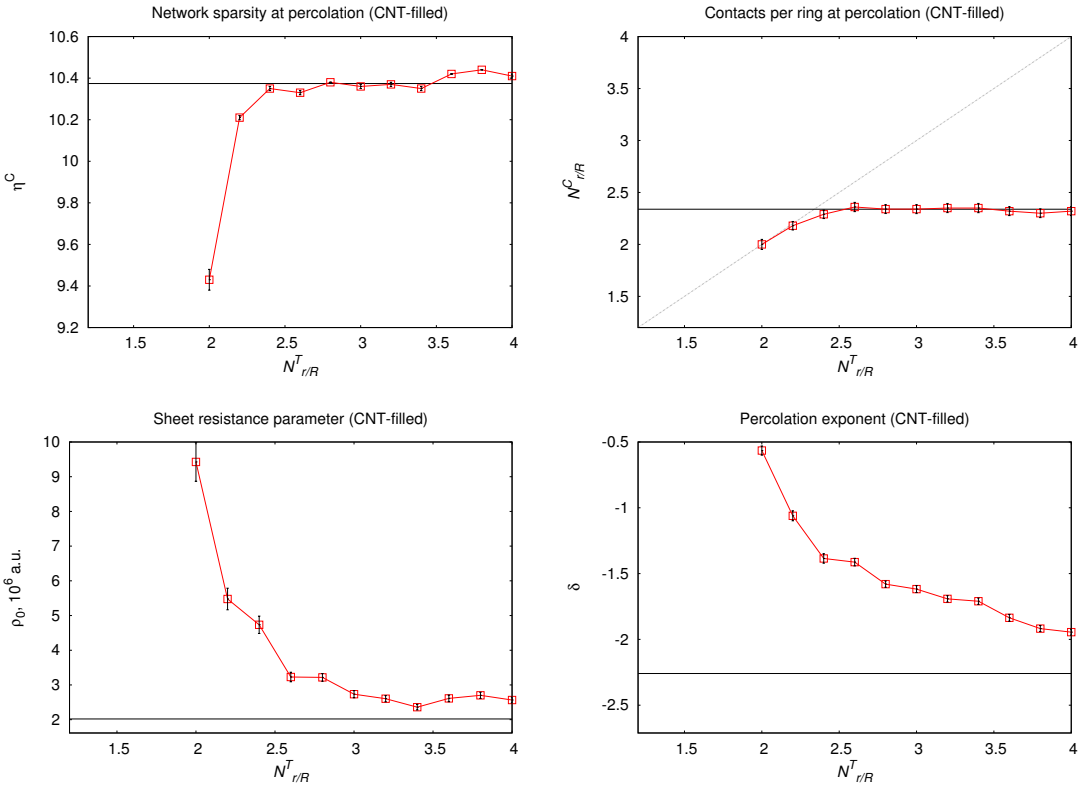

Figure 5.11: Variation of the "rings-and-rods" 3D network's parameters at percolation with target number of rods per ring $\mathcal{N}_{r/\mathcal{R}}$ (red line) and the asymptotic value (black horizontal line)

5.2.3 The effect of finite thickness and orientation

As it was reported in [2], the addition of 0.07 weight % of tetrakis-Schiff zinc compounds to a polycarbonate matrix with 2-3 vol. % of CNTs increased the

$\mathcal{N}^T_{r/\mathcal{R}}$	Pristine				CNT-intercalated			
	η_C	$\mathcal{N}^C_{r/\mathcal{R}}$	$\mathcal{V}^C_{\mathcal{R}}$	ϕ^C_{vol}	η_C	$\mathcal{N}^C_{r/\mathcal{R}}$	$\mathcal{V}^C_{\mathcal{R}}$	ϕ^C_{vol}
	-	-	$10^3\mu m^3$	10^{-3}vol. %	-	-	$10^3\mu m^3$	10^{-3}vol. %
1.2	-	-	-	-	-	-	-	-
1.4	-	-	-	-	-	-	-	-
1.6	-	-	-	-	-	-	-	-
1.8	-	-	-	-	-	-	-	-
2.0	6.0±0.1	2.0±0.2	1.03±0.02	1.06±1.04	9.4±0.1	2.0±0.2	73.5±0.8	0.05±0.05
2.2	6.5±0.1	2.2±0.2	1.34±0.02	0.87±0.73	10.2±0.0	2.2±0.2	93.3±0.2	0.04±0.04
2.4	-	-	-	-	10.4±0.0	2.3±0.2	97.2±0.1	0.04±0.03
2.6	-	-	-	-	10.3±0.0	2.4±0.2	96.8±0.1	0.05±0.03
2.8	6.6±0.1	2.3±0.2	1.37±0.02	0.87±0.77	10.4±0.0	2.3±0.2	98.0±0.1	0.04±0.03
3.0	-	-	-	-	10.4±0.0	2.3±0.2	97.7±0.3	0.04±0.03
3.2	6.5±0.7	2.3±0.3	1.34±0.15	0.90±0.75	10.4±0.0	2.4±0.2	97.9±0.1	0.04±0.03
3.4	6.5±0.5	2.4±0.2	1.33±0.10	0.91±0.74	10.4±0.0	2.4±0.2	97.3±0.1	0.04±0.03
3.6	6.5±0.1	2.3±0.2	1.35±0.02	0.88±0.75	10.4±0.0	2.3±0.2	99.4±0.0	0.04±0.03
3.8	6.6±0.1	2.3±0.2	1.36±0.01	0.88±0.76	10.4±0.0	2.3±0.2	99.9±0.0	0.04±0.03
4.0	6.5±0.1	2.3±0.2	1.34±0.03	0.89±0.74	10.4±0.0	2.3±0.2	99.0±0.2	0.04±0.03

Table 5.3: "Rings-and-rods" network's sparsity characteristics at percolation threshold in 3D

composite's surface conductivity by 7 orders of magnitude and bulk conductivity by 2 in comparison with polycarbonate composite with the same CNT content. This may indicate, that the effect of the "rings-and-rods" networks on the final resistivity is more pronounced for the surface, then for the bulk of the material. This might be attributed to several reasons, such as segregation of compound to the surface or difference in the ring's diameter and rod's length distribution on the surface and in the bulk or difference in alignment of the rings in the near-surface layer and in the bulk. The first two factors rely on the physical nature of the self-assembly of "rings-and-rods" like networks and their investigation is out of the scope of this study. In this section the impact of only the last factor will be estimated.

In the previous section the orientation of ring's axis was chosen uniformly in space. In this section, to study the effect of the rings alignment, the axis vector of the ring (the vector, normal to the plane of the ring) was chosen in such a way, that the angle θ between the vector and the selected axis has Gaussian distribution with the width $\sigma_{\mathcal{R}\theta}$. A cubic sample with uniform random distribution of 1000 rings was used. The sample side length was varied from 370 to 510 μm for pristine networks and from 80 to 663 μm for CNT-intercalated. This corresponds to η

varying from 5 to 8 for pristine networks and from 9 to 12.6 for CNT-intercalated. The target average number of rods per ring $\mathcal{N}_{r/\mathcal{R}}^{T}$ was fixed at 2.6. The width of the angle distribution was varied in the interval $[0°; 90°]$ with the step 15°. The two separate series of calculations were conducted: with the alignment axis parallel to the gradient of voltage and perpendicular to it. the results are presented on the figure 5.12.

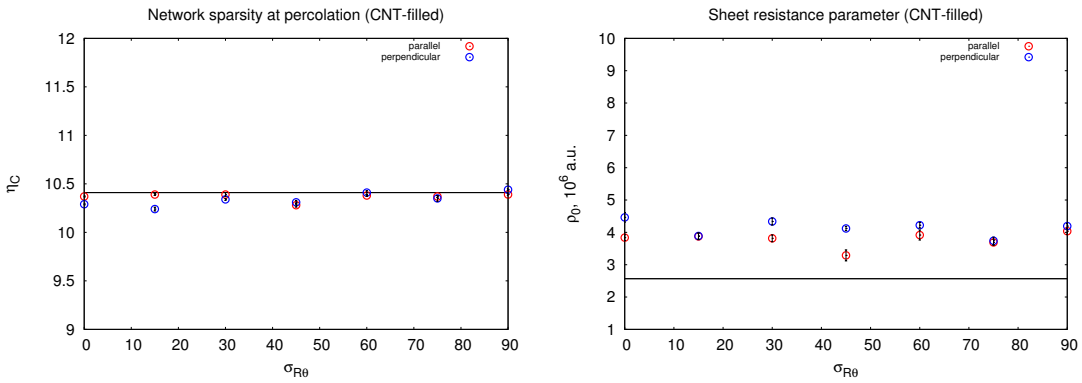

Figure 5.12: Variation of 3D network parameters with the ring's axis alignment

In contrast with the expectation, no visible change for either of the estimated parameter was found. This means that even when the rings are aligned perpendicular to the voltage gradient, the rods still provide connections along the field and the overall effect is negligible. Partially, this can be attributed to the limitation of the used methodology: in a real system the ring orientation may not be independent of Its neighbors, rather it could be rotated to minimize the stress in the rods, connecting the rings. Whether this takes place in the tetrakis-Schiff compound networks in a polymer matrix is yet unclear.

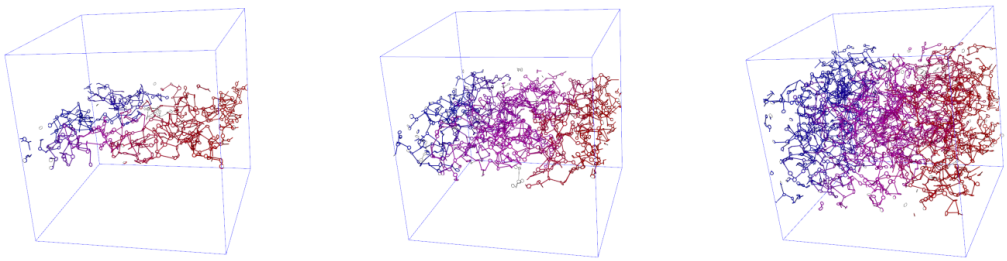

Figure 5.13: "Rings-and-rods" 3D networks in thin film geometry

Until here the box geometry was assumed periodic in all dimensions during network generation. In the second part of the investigation of surface vs. bulk effect of "rings-and-rods" networks on the composite's conductivity the effect of finite volume was introduced by replacing the periodic boundaries in one of

the directions, perpendicular to the electric field, with impenetrable surfaces. Rings, created near one of the surfaces were still oriented uniformly, but this time not in entire 4π spherical angle, but in a sector, such that no part of the ring would stretch outside of the surface. The thickness h_{film} of such thin film was varied separately from the box side length in the two other dimensions. Sample's resistivity in such geometry was, as in 2D case, characterized by sheet resistance $\rho = R_{sample}h_{film}$, where R_{sample} - is the sample's resistance. The box side length was varied from 115 to 240 μm for pristine networks and from 300 to 1080 μm for CNT-intercalated. The number of rings per sample was varied proportionally to h_{film} so that η varied from 5 to 9 for pristine networks and from 5 to 12.6 for CNT-intercalated. The thickness of the film varied from 2 to 5 maximum lengths of the rod (or maximum ring's circumference), which gives $h_{film} \in [17.4; 87.0]$ μm for pristine and $h_{film} \in [45.6; 288.0]$ μm for CNT-intercalated networks. The target number of rods per ring was fixed at 2.5.

The estimated critical scaling factor η_C and sheet resistance fitting parameter ρ_0 for pristine networks are shown on figure 5.14. It is clear that for very small film thickness η_C decreases from its bulk value 6.5 closer to 4.5 - Its value in 2D. The parameter ρ_0, which can be interpreted as the sheet resistance far from percolation threshold, decreases by half as h_{film} changes from 87 to 34 μm (the thinnest film appeared to be disconnected within the studied region of η). This observation supports the expected trend that the surface layer has better conductivity then the bulk of the composite. In the view of the previous results for the orientation effect in 3D periodic box, the last observation must be explained not only by the orientation effect of the surface, but also by the limited number of neighbors for the rings close to it. While the rings in the bulk can form links in all directions, the rings in the surface layer are restricted by the impenetrable surface and thus they more likely to form rods within the surface layer. It, however, requires quite small film thickness to make a difference. No noticeable effect was found for CNT-intercalated networks, where minimum thickness was 45.6 μm. Still even the observed difference is very far from 4 orders of magnitude relative difference between surface and bulk conductivity improvement reported in the experiment [2].

5.3 Conclusion and future directions

In this chapter it was shown using MC modeling based on simple geometrical considerations and data available from experiments that the percolation behavior of

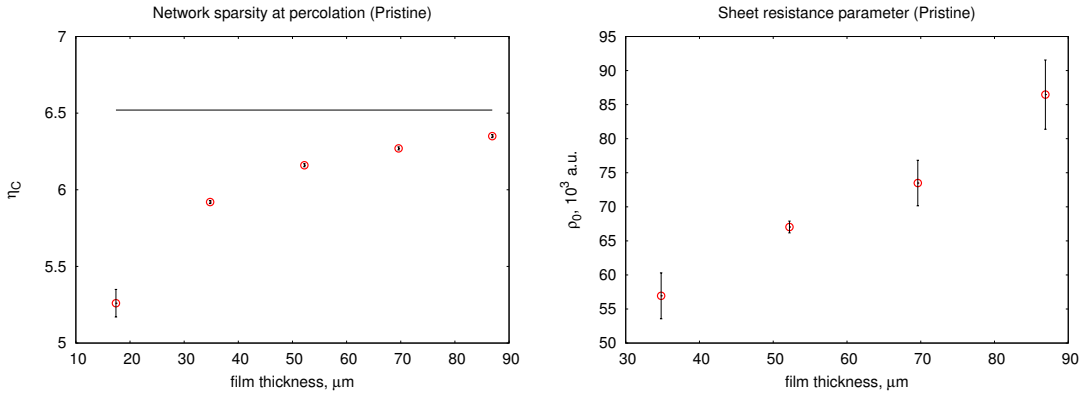

Figure 5.14: Variation of 3D network parameters with the film thickness

"rings-and-rods" networks strongly depends on the average number of rods per ring $\mathcal{N}_{r/\mathcal{R}}$ and the density of the rings, more conveniently characterized by the scaling parameter η defined by equation 5.1.4. Furthermore, the network's behavior around the percolation threshold (sparse network region) weakly depends on method to choose which of the possible connections between rings to maintain.

In case of flat networks it was shown, that the percolation threshold occurs in the region $\eta_C \sim 4 - 4.5$, which corresponds to the average surface per ring $\mathcal{S}^C_{\mathcal{R}} \sim 56 - 70$ μm² for pristine tetrakis-Schiff compound rings. The condition of extended network formation is $\mathcal{N}_{r/\mathcal{R}} \geq 2.4$. For the most sparse networks $\mathcal{N}_{r/\mathcal{R}}$ saturates around the value 2.7. On the other side the region of clearly distinguishable networks is limited by the critical value $\eta_R = 1.22$ - the percolation threshold of penetrable circles in 2D - close to which the rings overlap too much and weakly bonded tetrakis-Schiff compounds may rearrange into a more uniform structure. This matches the experimental observation of the large interconnected networks in the region $27.69 - 79.37$ μm² per ring and ratio of rods per ring $\sim 2.8 \pm 0.7$.

Experimentally observed CNT-intercalated networks with the average surface per ring ~ 75.56 μm² belong to the dense side of the of connected networks' region. Due to more than twice larger diameter of the rings with CNTs the scaling factor of such network is $\eta \sim 1.8$ far from the percolation threshold value $\eta_C \sim 6.5 - 7$, corresponding to the surface density $\mathcal{S}^C_{\mathcal{R}} \sim 1.0 - 1.2\,10^3$ μm². The critical surface fraction in this case was found ~ 0.06 surf.%, which is 2 orders of magnitude smaller, than the theoretical estimation of 8.8 surf.% for intersecting sticks.

Applying the same methodology in 3D even sparser connected networks were obtained: $\eta_C \sim 6.5$ for pristine networks and $\eta_C \sim 10 - 10.5$ for CNT-intercalated.

The number of rods per ring also saturated at smaller value 2.3-2.4. The CNT content required to fill such network can be as low as $10^{-4} - 10^{-5}$ vol. % - orders of magnitude smaller then for randomly distributed nanotubes of the same aspect ratio.

As the detailed mechanism of tetrakis-Schiff compounds self-assembly into "rings-and-rods" networks is yet to be investigated as well as to what extent such model, based on the experimental data for flat networks, can be applied to the networks, self-assembled in polymer matrix, the last theoretical prediction needs to be taken with caution. Still, it shows the high potential of the self-assembled molecular networks for creation of thin films and composite materials with advanced microstructure.

The clear limitation of the method used in this chapter is the assumption of the same ring's and rod's sizes distribution both for the surface and bulk of the composite and lack of physical relations between ring's and rod's orientation. As was shown in the last section, within this approach it is impossible to explain $\sim 10^4$ difference between the improvement of the surface and bulk resistivity of the CNT-polycarbonate by addition of tetrakis-Schiff compounds. Adaptation of the model to capture this effect requires deeper understanding of the mechanism of rings and rods formation and interaction of the compound with nanotubes and polymer matrix.

Chapter 6

Self-assembly of tetrakis-Schiff molecular networks

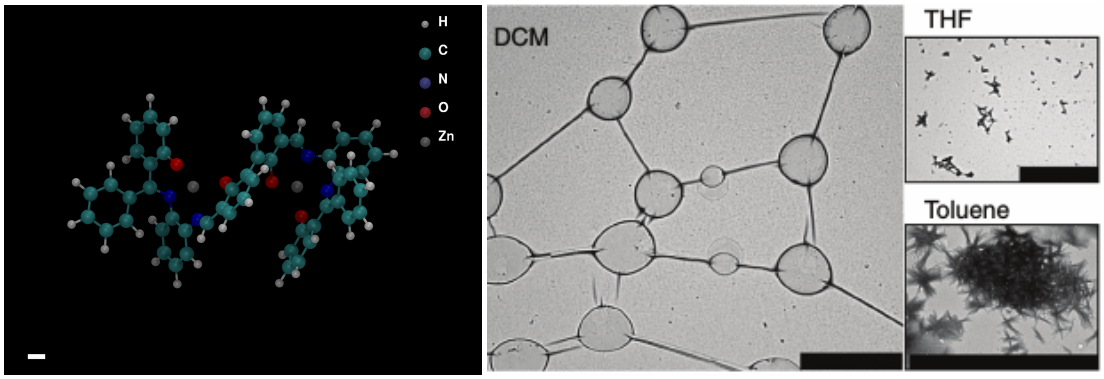

Figure 6.1: Tetrakis-Schiff metal complex molecular structure (left) and its self-assembled structures, obtained by drop-casting from various solvents (right) [2], the scale bars equal to 1 Å on the left image and 5 μm on the right

As was mentioned in the Introduction (1), the remarkable possibility of tetrakis-Schiff based metal complexes[1] to self-assemble into extended networks was recently discovered by the group of Dr. Kleij and investigated both experimentally and theoretically by an international group of collaborators including the author of present study [**?**]. Analysing the electron micro-photographic images of the micro-structures left on the support after solvent evaporation our colleagues have shown that metal ion substituted symmetrical double tetrakis-Schiff base ligands functionalized with phenyl groups, shown on the figure 6.1, can form molecular networks, composed of micrometer-sized rings, connected with molecular strings, when drop-casted from dichloromethane (DCM). This self-arranging structure

[1]There is a certain ambiguity in the literature concerning the naming of such molecules. As the molecule shown on figure 6.1 (left) is the main object of study in this chapter, the terms tetrakis-Schiff complex or bis-salphen compound are used throughout this chapter as synonyms.

has a high potential as a guiding dispersing agent for carbon nanotubes [189]. No network of rings and rods was observed for other solvents: drop-casting from tetrathydrofuran (THF) produced only short strings, while star-like aggregates of needle-like nanocrystalls condensed from toluene (TOL). Replacement of phenyl side chain by methyl group resulted in well separated spherical globules in dichloromethane with no detectable agglomerates for the other solvents. Similar, however weaker defined, interconnected networks were formed from Ni-centered and metal-free ligands. The diffusion ordered spectroscopy estimated the diameter of the compound molecule in DCM as 19.68 nm. The dynamic light scattering (DLS) study indicated that molecular assemblies with the average radius 10-40 nm, 80-400 nm and 4.2-5.6 μm are present in DCM solution and their ratios are not affected by filtration through 50 nm sized pores. These experimental evidences led authors to conclusion, that $\pi - \pi$ interactions, mediated by phenyl side rings have the key role for formation of extended structures rather than cation-oxygen interaction, typically found in similar systems. To explain the process of the network self-assembly, the authors have suggested a model according to which the ligands or metal ion complexes fist agglomerate into vesicles that shrink and collapse into donut-like shape as the solvent evaporates. The molecular rods, connecting the rings, are presumably formed at the points, where vesicles contacted each other. The solvent was regarded only as environment mediating solute molecules non-bonding interactions. This was supported by cryo-environmental scanning electron microscopy images where interconnected globular structures were clearly visible.

This explanation, however, left a lot of questions without answer, namely: what is the internal structure of the vesicles, how they assume a donut-like shape in DCM and why this does not happens in THF and TOL. Using of cryogenic freezing to get time-resolved evolution of self-assembling structures is also tricky: as was mentioned in the literature review chapter, folding of extended molecular systems is a multi-well problem and rapid cooling may alter the trajectory and kinetically confine the system to one of local minima.

In this chapter a detailed computational study is reported, aiming to close the aforementioned white spots. For this purpose a combined density functional theory (DFT) level and all-atom molecular dynamics (MD) study was performed to investigate in details of the Schiff-base complexes self-assembly and behaviour various environments, such as vacuum and DCM, THF and TOL, used in the experimental studies. The structure of this chapter is as follows. Section 6.1 provides a concise summary of the computational methods used in this chapter.

Section 6.2 summarizes preliminary calculations with simplified four-rigid-parts model of the compound, demonstrating the ability of such molecular complexes to form a stable donut-like structure. The aim of calculations, described in section 6.3, is to verify the all-atom parametrization of the tetrakis-Schiff zinc-complex chosen for more in-depth MD simulations against the quantum chemistry level calculations of single compound, its dimer and between compound and solvent molecule, as well as the experimentally available crystallographic data for similar compound. The conformational stability of a single molecule and its diffusion in explicit solvents are studied in section 6.4. The relative stability of multi-molecular assemblies in different possible conformations in explicit solvents is investigated in section 6.5. Finally, section 6.6 describes the proposed mechanism of the "rings-and-rods" like network self-assembly, linking it to a coil-to-toroidal globule transition phenomenon, already known for semi-flexible polymer systems, as described in the literature review chapter. To support the proposed mechanism, free energy perturbation calculations were preformed to compare the stability of the proposed structure in the three aforementioned solvents, explaining the role of metal cation and phenyl groups in the self-assembly process. The results of these calculations are presented in the section 6.7.

6.1 Methods

Throughout this chapter a number of molecular modelling approaches were applied to study the behaviour of the tetrakis-Schiff zinc-complexes from molecular perspective. The theory behind these methods and state of the art examples of their application to similar molecular systems were outlined previously in the section 3.2 of the Methods chapter. This section enumerates the software tools used for each type of calculations and describes the general technical details of the calculations and procedures used.

6.1.1 Density functional calculations

The three quantum chemical software packages were used for DFT calculations: SIESTA [190], ONETEP [191] and GAUSSIAN [192]. While the last one is the most mature and widely used due to its large range of functionalities, it has limited optimization for massively parallel calculations, where the first two excel. This becomes especially important when large molecular associations are under study. For this reason the most intensive task of the optimal molecular geometry search was done at the first step using the more robust SIESTA and then fine-

tuned with the more precise ONETEP. GAUSSIAN calculations were applied to derive the atomic charges in the discovered geometries.

Within SIESTA method valence electrons were expanded in double zeta plus polarization (DZP) basis set of numerical atomic orbitals, generated using the split-valence method [153] with energy shift of 50 meV. Popular for its efficiency and sufficient accuracy in most cases, this basis allows quite robust geometry optimization. In dimer binding energy calculations basis set superposition error (BSSE) was corrected using the counterpoise method [193]. Core electrons were replaced by Troullier-Martins pseudo-potentials [155] for faster computation. A cutoff of 300 Ry was used for grid integration.

ONETEP package represents electronic orbitals using non-orthogonal generalized Wannier functions (NGWFs), which are in turn expanded in periodic *sinc* functions [154, 194]. Due to such choice of basis, no BSSE correction is needed and very accurate atomic forces and geometry optimization can be achieved [195], however much more intensive computation is required than in SIESTA case. NGWFs' radii was set to 8 r_B (Bohr radius). Pseudo-potentials, generated by OPUIM package [196], were used to replace core electrons. For fully converged energies plain wave cutoff was set to 1000 eV.

Single point k-space sampling and local density approximation (LDA) in Perdew & Zanger parametrization [197] were used for electron exchange and correlation functional for the binding energy calculations in these two packages. While the geometry optimization was done using the generalized gradient approximation (GGA) in Perdew-Burke-Ernzerhof form (PBE). Iterative self-consistent calculations were conducted until energy convergence below 50 meV and maximum forces below 50 meV/atom for single molecule and 100 meV/atom for molecular dimer were achieved.

In GAUSSIAN the final geometry optimization was done using the standard 6-31g* (5d) orbital basis along with hybrid Becke 3 parameter Lee-Yang-Parr (B3LYP) functional for exchange and correlation energy. Molecule's electrostatic potential map in the optimized geometry was calculated using the same basis and Hartree-Fock exchange. The potential values were sampled according Merz-Singh-Kollman scheme [164].

6.1.2 Parametrization of the tetrakis-Schiff zinc-complex model

For the preliminary calculations the atomic charges were calculated using natural bond orbital (NBO) approach as implemented in ONETEP [198]. The

DREIDING force field was used for bonded and van der Waals interactions' parameters [130].

For more accurate molecular dynamics calculation the atomic charges were fitted to electrostatic potential from GAUSSIAN calculations according to the "RESP" method using Red Tools software package [132]. The covalent and van der Waals parameters for the compound and solvent molecules were assigned according to all-atom general AMBER force field (GAFF) [199] using ANTECHAMBER program form AmberTools package [200]. Zinc ions were treated as free charged centers. This approach was chosen to allow cations to occupy the optimal position under the effect of electrostatic interactions with other ionic centers avoiding any influence of the explicit virtual bonds.

6.1.3 Input structure preparation

Initial idealized atomic structures of the compound molecules were prepared and visualized using TopoTools and Molefacture packages of the VMD molecular visualization program [201]. For the simulations, basing on the experimental X-ray resolved structures, the initial ligand and complex coordinate files were processed and rendered with Mercury molecular visualization software [202]. Initial coordinates of the solvent molecules in the liquid state were obtained from VirtualChemistry online database [203]. Input structures for explicit solvent simulations were prepared by merging coordinates of solvent and compound molecules taken from random snapshots of separate simulations and deleting solvent molecules within van der Waals distance from the atoms of the solute compounds. MOLTEMPLATE package [204] was used to create the input files for MD simulation storing the parameters and initial coordinates.

To remove the initial stress while keeping the solute structure close to initial, each simulation started with a relaxation procedure similar to described in [205]. The atoms of the compound were restrained to their initial positions with virtual strings, the strength of which decreased exponentially from 600 to 1 kcal/mole/Å during a set of 4-10 50 ps long runs (depending on the number of solute molecules in association) with the timestep of 0.5 fs. Additional virtual springs with the spring constant 5.0 kcal/mole/Å were attached to prevent non-covalently interacting parts of adjacent compounds (for example, oxygen atoms and metal cations) from moving initially too far apart during another 100 ps.

6.1.4 Molecular Dynamics simulation

Molecular dynamics (MD) simulations were performed using LAMMPS software package [173] under normal conditions, i.e. 293.15 K temperature and 1 atm. pressure (in the explicit solvent). The temperature of the tetrakis-Schiff molecules was controlled by Langevin thermostat [127]. In case of explicit solvent, the temperature and pressure of the solvent molecules were controlled by a separate Nose-Hoover barostat and thermostat. All bonds with hydrogen atoms were constrained after the initial relaxation stage by SHAKE algorithm [135] to increase time step to 2.0 fs. The "particle-particle particle-mesh" algorithm (PPPM) [206] was used to treat long range Coulombic interactions. Cutoff radius of 12 Å was used for van der Waals and short-range electrostatic potentials. Van der Waals interactions were modelled using Lennard-Jones 6-12 potential with a switching function to smooth down the potential profile between 10 and 12 Å as proposed in [207].

The stability of thus formed structures was studied by performing 1-5 nanosecond long equilibration run during which the conformation of the multi-molecular assembly as well as the change of complex-to-complex and complex-to-solvent interaction energy were monitored. The final data was accumulated during the last nanosecond run after monitored parameters stabilized around equilibrium values. Instantaneous thermodynamics quantities: temperature, pressure, solvent density, total and interaction energy components, - were sampled every 100 timesteps. Every 1000 time steps (or 2 ps) the average over the last 20 samples was collected. At the same timestep the atomic coordinates were dumped to inspect the structure evolution.

6.1.5 Free energy calculations

Free energy of conformational change

To study the free energy changes associated with the conformational change of the tetrakis-Schiff based zinc-complexes in vacuum the umbrella sampling technique (US) was used as described in 3.2.3. The restraining potential had quadratic form $U_k = K\left(\zeta - \zeta_k\right)^2$, where ζ is the reaction coordinate to be constrained (one of the two dihedral angles, as will be defined further in section 6.4.1) and ζ_k - is the value of that coordinate around which the molecular behaviour is studied. For each value of ζ_k 8-16 simulations in vacuum were performed, each starting from a different initial structure, selected from a preceding "nudged elastic band" simulation (NEB) of the transition from one configuration to another.

Each US simulation consisted of the two parts: during the first 500 ps the system was driven to the target value of the reaction coordinate by gradually changing either the spring constant K of the biasing potential from 0 to 128 kcal/mole/$\mathring{A}^2$, or by gradual changing the value of the reaction coordinate at which the biasing potential has it's minimum from initial to the target value. During the consequent 500 ps the value of the reaction coordinate was sampled every 500 timesteps (or 0.25 ps) while the spring constant was kept at its final value. The weighted histogram analysis (WHAM) of the collected data was performed using the utility with the same name by Alan Grossfield [208].

Free energy of association

Association free energies for selected multi-molecular assemblies in solvent were estimated as the difference between the solvation free energy change (ΔG_{sol}) of the associated and separated molecules. Following [144] the free energy perturbation method (FEP) was used to evaluate the individual fee energies of solvation as described earlier in 3.2.3. Within this approach the interaction between tetrakis-Schiff complexes and solvent molecules was gradually scaled form fully interacting system to the two completely isolated subsystems. Similar approach, but with scaling down the interactions between the compound molecules, was used for the free energy of dissociation in vacuum. For better stability of results van der Waals and Coulomb interactions were scaled separately as proposed in [209]. Within the FEP method, the full system's potential energy is decomposed into:

$$U_{AB} = U_A + U_B + \lambda_{vdW} U_{AB}^{vdW} + \lambda_{Coul} U_{AB}^{Coul}, \tag{6.1.1}$$

where the subscripts A and B refer to the two subsystems (solute-solvent or parts of multi-molecular association), U_{AB} is the potential energy of the full system, $U_{A(B)}$ - potential energy of the interaction between the atoms of one of the subsystems (covalent and non-bonding), U_{AB}^{vdW} - the potential energy of the van der Waals interactions between the subsystems and U_{AB}^{Coul}- the potential energy of the Coulomb interactions between them. λ_{vdW} and λ_{Coul} are the corresponding scaling parameter (also called "the coupling parameter") for van der Waals and Coulomb interactions between the subsystems correspondingly.

Van der Waals and electrostatic interactions between solvent and tetrakis-Schiff complex were modelled with "soft-core" versions of the Lennard-Jones and Coulomb potential, as implemented in LAMMPS [210]:

$$U_{LJ}^{soft} = 4\epsilon \left\{ \frac{1}{\left[\alpha_{LJ}\left(1-\lambda\right)^2 + \left(\frac{r}{\sigma}\right)^6\right]^2} - \frac{1}{\alpha_{LJ}\left(1-\lambda\right)^2 + \left(\frac{r}{\sigma}\right)^6} \right\}, \tag{6.1.2}$$

$$U_{Coul}^{soft} = -\frac{Q_i Q_j}{4\pi\varepsilon_0\varepsilon\sqrt{\alpha_C\left(1-\lambda\right)^2 + r^2}}, \tag{6.1.3}$$

where U_{LJ}^{soft} is the potential energy of a soft-core van der Waals interaction, ϵ and σ correspond to their mining for standard Lennard-Jones potential, defined by equation 3.2.15, λ - the scaling parameter ($\lambda \in [0;1]$), α_{LJ} and α_C - parameters, controlling the change of shape of the potentials as λ approaches 0. In current studies $\alpha_{LJ} = 0.5$ and $\alpha_C = 10$ Å^2.

After the initial equilibration as described earlier in section 6.1.3, the interaction potentials between subsystems were gradually scaled, changing the corresponding parameter λ in the expression 6.1.1 according to a set of predefined values, called λ-schedule. The profiles of the λ-schedules used in each calculation were chosen after a set of preliminary simulations and will be described in the corresponding section of the results discussion. At each point λ_i after the relaxation period the perturbation of the potential energy was calculated for both forward ($\delta U_{FWD}(\lambda_i) = U(\lambda_{i+i}) - U(\lambda_i)$) and backward ($\delta U_{BWD}(\lambda_i) = U(\lambda_{i-i}) - U(\lambda_i)$) directions every 10 timesteps. The ParseFEP plugin to VMD [211] was used to estimate the change of the free energy, corresponding to each transition using Bennett acceptance ratio method (BAR) [145], as well as to compare the distributions of backward and forward potential perturbations as suggested in [147].

6.2 Preliminary calculations

As was discussed in the literature review section, ring-like structures can emerge due to different processes, starting from the "coffee-ring" and "pin-whole opening" effects, spontaneously arising in evaporating solvent, to the Marangoni flows and template approaches, created deliberately. The aim of this section was to verify that emergence of the "rings-and-rods" networks can indeed be attributed to molecular self-assembly, i.e. that the tetrakis-Schiff zinc-complexes are able to form ring-like assemblies, stabilized by inter-molecular forces.

On the first step systems, containing a single tetrakis-Schiff molecule or its dimer, were studied using electron density functional (DFT) calculations to ac-

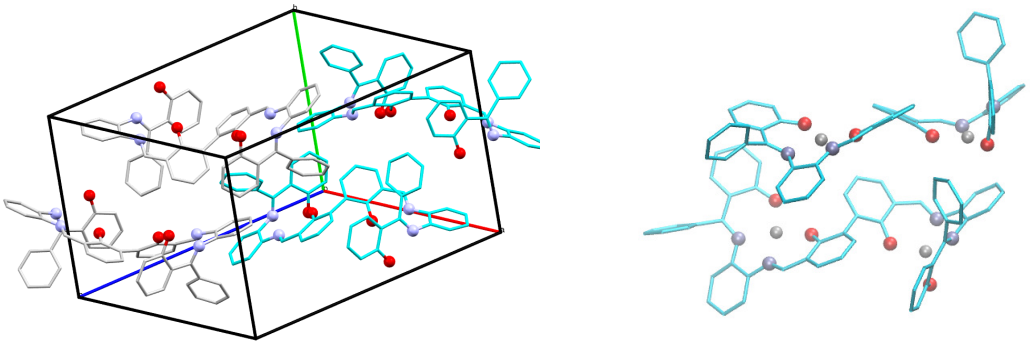

Figure 6.2: The crystal structure of unsubstituted tetrakis-Schiff ligand, reconstructed from X-ray scattering [**?**] (left) and the DFT optimized molecular structures of a zinc-complex dimer (right), hydrogen atoms are omitted for clarity, while the carbon backbones are drawn as tubes. Grey and cyan on the X-ray based structure outline the two stacked chains, facing in the opposite directions. Red, blue and grey balls designate oxygen, nitrogen and zinc respectively.

curately evaluate their lowest energy state, the most favourable geometry, charge distribution and the dimers' binding energies. Single and double molecular complexes were placed in a 50x50x50 Å simulation box and their geometries were optimized first using more robust SIESTA code, than using more precise ONETEP. The initial wedge-like atomic configuration was based on the result of X-ray scattering study of unsubstituted (metal free) tetrakis-Schiff ligand crystals (figure 6.2 left), reported in [**?**]. The calculated binding energy of molecular dimer is estimated to be ~-0.5 eV: -0,48 eV (SIESTA) and -0.50 eV (ONETEP), - equivalent to about -11,5 kcal/mole (negative sign designates attraction).

On the second stage series of MD simulations of molecular complex dimers were performed using a simplified model of the molecule consisting of four rigid parts (as shown on the figure 6.3 right, flexible bonds are shown in yellow). Covalent and van der Waals interactions were parametrized using DREIDING force field. The atomic charges for these calculations were estimated from the previous calculations using NBO method as implemented in ONETEP (the charge distribution is shown on figure 6.3 left). In these simulations one molecule was fixed in the center of the periodic box and initial position and orientation of the other were chosen randomly. Molecular system evolution was simulated during 10^5 time steps (~100 ps). From the pool of final structures those, where stabilized dimeric complexes had formed, were selected and analysed. The distribution of their binding energies is shown on the figure 6.5.

Due to their wedge-like geometry tetrakis-Schiff zinc-complexes have anisotropic binding ability. Simplistically, one can imagine the complex's geometry

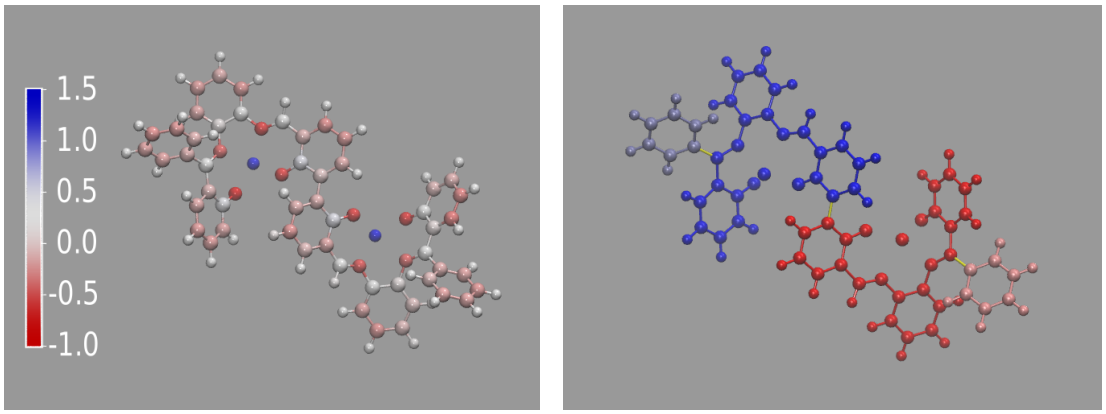

Figure 6.3: The NBO charge distribution in a single tetrakis-Schiff molecule (left) and a simplified “four-rigid-parts” model (right)

as a wedge, the ends of which originate on zinc ions and the tip at the center of C-C bond connecting the two symmetric halves (figure 6.4a). For clarity, the side into which tip points will be designated as "face" and the opposite side as "back". Then the following most stable mutual orientations could be outlined (figure 6.4b):

- *"back-to-back"* is the most stable of all configurations as almost flat "backs" of the tetrakis-Schiff complexes allow a good contact to be established by van der Waals forces even at the cost of some electrostatic repulsion. However, strongly attached to each other, such molecular pairs weakly interact with other molecules so they are mostly encountered on opened ends of multi-molecular assemblies;
- *"face-to-face"* configuration, on the contrary, favours Coulomb interaction as the oppositely charged ions are placed closer and aromatic rings attached to the "face" sides help to stabilize molecules. As their "backs", capable of the strongest van der Waals attraction, stay opened, such pairs often link molecular changes with different orientation;
- *"stacked"* molecules form the most ordered structures. As in "stacked" configuration molecules are biased relatively to each other (because of electrostatic interaction and presence of side groups) chains composed of "stacked" molecules easily bend as it is energetically more favourable for molecules to flip to the same side which improves interaction with second-order neighbours and lowers total system energy;
- *"side contact"* configurations are weaker than all other due to small surface of contact and only weak $\pi - \pi$ interactions. Single molecule thick chains composed of zinc-complexes in such initial configuration quickly fold to form more stable contacts. In thicker molecular strings "side contacts" however

Dimer type	E_b^{vdW}	E_b^{Coul}	E_b
	kcal/mole	kcal/mole	kcal/mole
“Back-to-back”	~-40	+6 - +7	>30
“Face-to-face”	~-20	-6 - -7	~30
“Stacked”	~-30	-4 - 0	~30
“Side contact”	~-20	-7 - 0	~15-30

Table 6.1: Contributions to tetrakis-Schiff dimer's binding energy

play supportive role as they link molecular chains together.

The decomposition of the dimer binding energy (E_b) into electrostatic (E_b^{Coul}) and van der Waals (E_b^{vdW}) contributions for the outlined structures is shown in the table 6.1. As the result of such anisotropic dependence of binding energy on mutual orientation of molecules it is kinetically favourable for the tetrakis-Schiff zinc-complexes to form chain-like structures. However small value of binding energy and tiny difference between binding energies of various molecular configurations allow multi-molecular structures to keep significant flexibility as molecular chains can easily relax stress by local "flip" of orientation and, therefore, develop non-uniform structures. It is important to note here that as electrostatic interaction plays an important role in binding energy configurations, it might be possible to control the structure of tetrakis-Schiff molecular systems in solution by changing dielectric properties of solvent or application of external electric field.

On the final step the evolution of systems containing up to 450 tetrakis-Schiff molecular models were studied with MD simulations using same simplified “semi-rigid” parametrization as in previous simulations of dimer formation. Several periodic structures were taken as the starting point for further simulation. In each simulation molecular system was initiated as a string with free ends 9-64 molecules long, 1 to 9 molecules in cross-section and left at constant volume box under the temperature of 300 K. The main driving force of observed structural changes is the tendency of molecules to form maximally closed configuration, especially at opened ends of the chain and in surface layer. As the result of binding energy anisotropy of the tetrakis-Schiff molecules, spontaneous fluctuations of molecular orientation cause local ordering, leading to bending of entire sections to one side. Starting from end points chains tend to fold to close the ends with the body of the chain and form a circle-like structure. Monomolecular chains quickly break into segments of small curvature, where initial "stacked" orientation is preserved, connected with "kinks" formed by more stable but non-periodic configurations

like "face-to-face" or "back-to-back" (figure 6.4).

Thicker molecular chains are more rigid as their molecules have better contact with their neighbours and more resistant to structure changes, which results in larger curvature of bending, dependent on the thickness of molecular string. A frequent event observed in multi-molecular strings is orientation of surface molecules with their "tip" a bit inclined outside. Such molecules preserve a good contact with interior of the string with their most strongly binding "backs" and with other surface molecules through "stacked" and "side" contacts. This behaviour also improves the string bending resistance and helps to preserve arc-like structure without collapsing into a droplet. The half-circular segment, the evolution of which is shown on the figure 6.7, was mirrored to form a full ring, which was further simulated as a single object during additional 10^7 time steps (~10 ns). No structural changes were observed with system's kinetic and potential energies fluctuating around equilibrium. This observation indicates that zinc-substituted tetrakis-Schiff complexes are indeed capable of assembling into elongated rod- and donut-like structures that can maintain their shape, stabilized by the interplay of van der Waals and electrostatic inter-molecular forces.

6.3 Validation of molecular model parameters

As was discussed in chapter **??**, the appropriate choice of the molecular modelling parameters (i.e. force field and charges) is crucial for the predictive power of the simulation. The choice of electric charge for cation in metal-ligand complex is not trivial. As the interaction of tetrakis-Schiff compounds is the result of a balance between electrostatic and van der Waals interactions, accurate description of Zn-O is of great importance to the current work. What is even more important is that variations of charge with the geometry variation during molecular dynamic run must be small so that a fixed charge approach is valid.

In chemistry such complexes are usually defined as Zn(II) compounds, corresponding to +2 charge (in the units of elementary charge $|e^-|$) [**?**]. Previously various groups have successfully employed zinc-cation charges varying from +2 down to +1 [212]. However, the standard RESP procedure (as was described in the Methods section), suggests for the complex of interest the charge of zinc cations equal to Q_{Zn}~+0.98.

To verify the validity of the RESP derived set of charges molecular structures, optimized using GAFF force field parameters in LAMMPS, were compared for four selected charge sets and the result of DFT optimization in GAUSSIAN. The

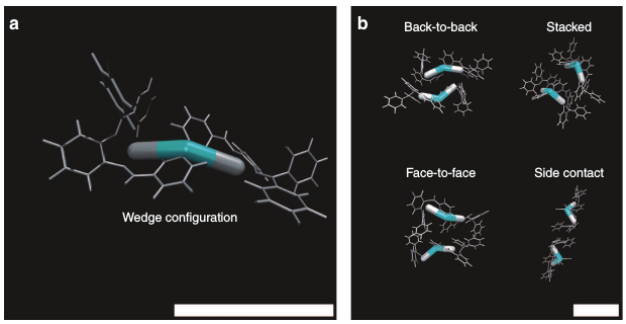

Figure 6.4: "Wedge" representation of tetrakis-Schiff zinc-complex (a) and the main dimeric motives, observed in semi-rigid MD calculation (b) (The scale bars' length is 10 Å)

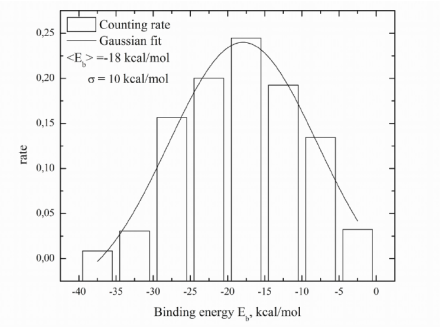

Figure 6.5: Binding energy distribution of semi-rigid dimer models from DREIDING MD calculations

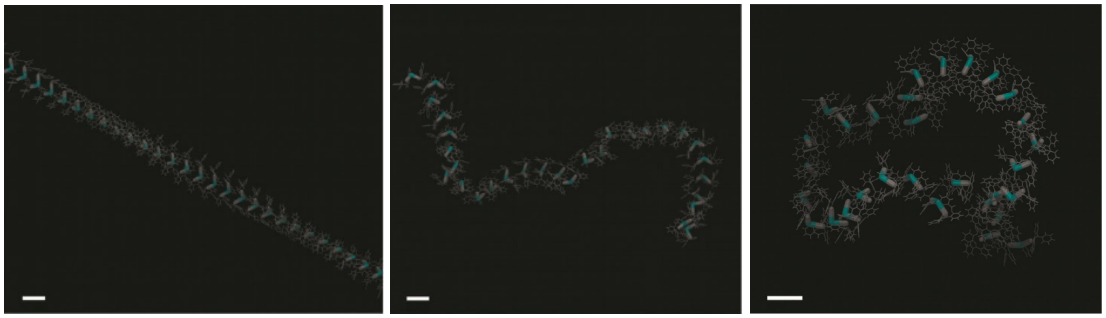

Figure 6.6: The evolution of a single molecule thick chain (The scale bars' length is 10 Å)

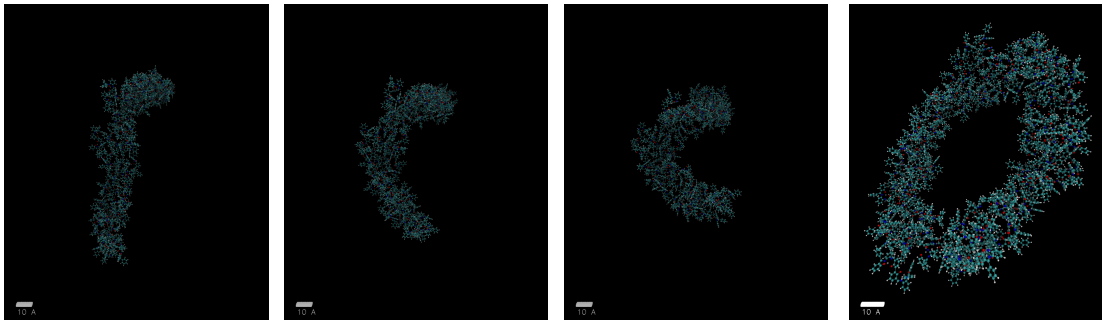

Figure 6.7: The evolution of a two molecules thick chain and the donut-like structure, obtained from it (The scale bars' length is 10 Å)

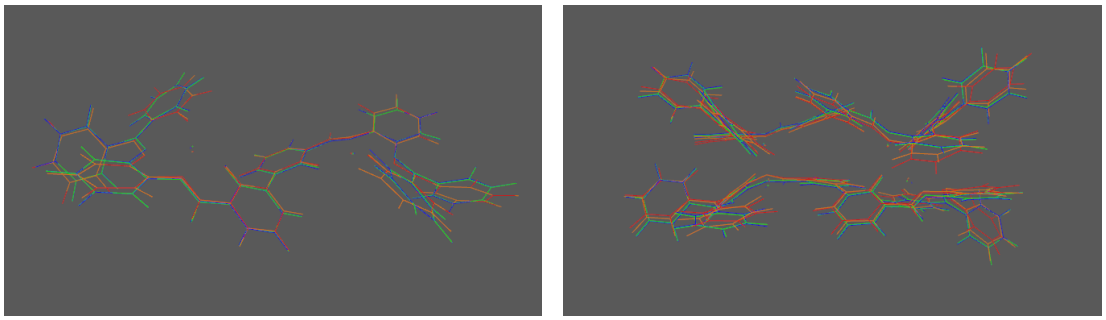

Figure 6.8: Comparison of the molecular structure of a single (left) and dimer (right) tetrakis-Schiff compound obtained with DFT (blue) and GAFF for zinc charges +1.0 (iceblue), +1.2 (green), +1.5 (orange) and +2.0 (red)

charge sets were obtained with RESP method restricting the value of zinc charge correspondingly to +1.0, +1.2, +1.5, +2.0. The optimized atomic structures of a single tetrakis-Schiff compound and its dimer are shown on figure 6.8. It can be seen with the naked eyes that while the geometry, obtained with the charges of zinc cations +1.0 and +1.2 follow the DFT-optimized geometry closely, the molecular structure for the charges +1.5 and +2.0 deviates from the reference structure. This deviation is especially striking for dimer structure, were the increased electrostatic interactions force Zn and O atoms closer, distorting the initial geometry.

As the second test, the same procedure was repeated for a single salphen-based zinc-complex, for which the crystallographic structure is known [**?**]. A 4x4x4 supercell was created by translation of the experimentally derived coordinates and optimized in LAMMPS using the same parameter sets as previously and equilibrated during 50 ps under Nose-Hoover NPT barostat (T=293.15 K, P=1 atm.). The estimated lattice vectors of the resulting crystal structures are summarized in the table 6.2 together with the root mean square deviations RMSD $= \sqrt{\sum_i (\vec{r_i}(t) - \vec{r_i}^{exp})}$ of the atomic positions ($\vec{r_i}(t)$) from experimental result ($\vec{r_i}^{exp}$). Although the lattice vectors, obtained with the last two charge sets ($Q_{Zn} = +1.5$ and $Q_{Zn} = +2.0$), maintain the right angles of the initial cell, the lattice parameters of $Q_{Zn} = +1.0$ charge are closer to the experimental which is also supported by RMSD value. Here a, b and c are the lengths of the lattice vectors $\vec{a}$, $\vec{b}$ and $\vec{c}$, the angles between which are: $\alpha = \angle(\vec{b}, \vec{c})$, $\beta = \angle(\vec{c}, \vec{a})$ and $\gamma = \angle(\vec{a}, \vec{b})$.

To assess the stability of atomic charges ESP charge fitting were conducted in Gaussian for a set of 90 snapshots, extracted from molecular dynamics trajectories for a single tetrakis-Schiff zinc-complex in all three solvents under study. Opened, closed and inverse configurations of the complex were equally repres-

	RMSD	a	b	c	α	β	γ
	Å	Å	Å	Å	deg	deg	deg
experiment		11.362	12.263	17.973	90.0	80.1	90.0
$Q_{Zn} = +1.0$	0.947	12.000	12.859	16.521	90.0	86.1	90.0
$Q_{Zn} = +1.2$	1.653	11.960	13.847	15.387	90.0	81.0	90.0
$Q_{Zn} = +1.5$	1.672	11.891	13.735	15.481	90.0	80.1	90.0
$Q_{Zn} = +2.0$	1.729	11.763	13.468	15.708	90.0	80.2	90.0

Table 6.2: Comparison of primitive cell parameters and RMSD of atomic coordinates form the reference positions for the experimental and simulated crystal structures

ented. The effect of the solvent atoms was included as a potential from frozen point charges with ONIOM method [213, 214] as implemented in Gaussian. The estimated charges of Zn ions are summarized on 6.9. Here ESP "Snapshot" lines/circles correspond to the charges fitted for the complex geometry restricted to the coordinates from MD trajectory. Additionally, the complex geometry was optimized using DFT and B3LYP exchange-correlation functional in the environment of "frozen" solvent molecules, which resulted only in a negligible correction. As expected ESP charges are a bit higher then computed with RESP [132], however both ESP methods produced zinc ion charges, varying around +1.1 with 0.1 standard deviation with their average remaining within 10% deviation from the result of the standard RESP fitting method for a complex geometry optimized in vacuum.

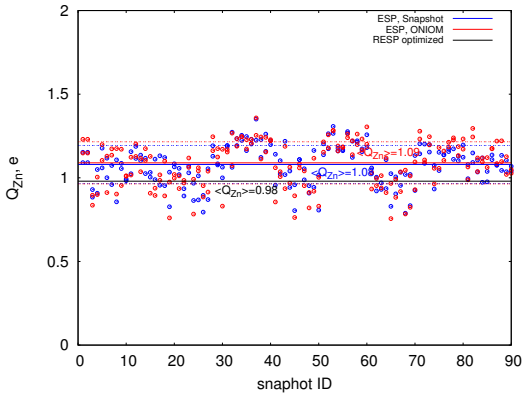

Figure 6.9: Variation of ESP Zn charges across MD simulations in solvent: open circles represent the results for single snapshots, solid lines - the average values over 90 snapshots, dashed lines mark single standard deviation from the average

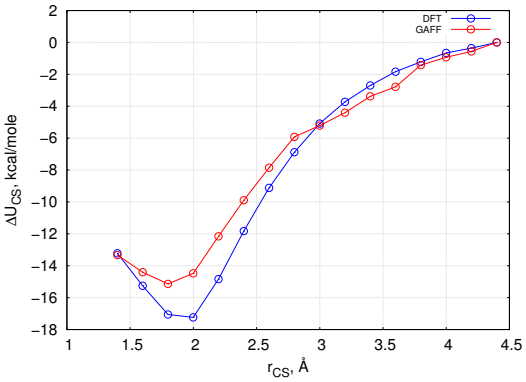

Figure 6.10: Comparison of the complex-solvent interaction energy distance profile from DFT (ONETEP) and GAFF force field with RESP charges (LAMMPS) calculations

As the last test, the interaction energy between a single salphen-based zinc-complex and a single THF molecule was calculated for a set of fixed distances (r_{CS}) between the solvent's oxygen and the initial position of zinc cation in ONETEP and in LAMMPS using GAFF and the RESP-derived charge set. In both cases the carbon backbone of zinc-complex and solvent's oxygen were constrained to their redefined positions, while the rest atoms were allowed to relax. The distance dependent interaction energy between complex and solvent molecules ($\Delta U_{CS}(r_{CS})$) in LAMMPS were estimated directly as the sum of pair energies of non-bonding interactions between atoms form the two molecules, while in case of ONETEP it was evaluated as:

$$\Delta U_{CS}(r_{CS}) = E_{CS}(r_{CS}) - \left(E_C^0 + E_S^0\right); \tag{6.3.1}$$

where $E_{CS}(r_{CS})$ - is the total system's energy, evaluated after coordinate relaxation at the distance r_{CS}, and E_C^0 and E_S^0 are the ground state energies of the standalone complex and solvent molecules respectively. The resulting plots are shown on the figure 6.10 (zero level of the potential energy was set to the value estimated at the largest separation in both cases). It is clear that, despite the fixed charge model is used in force field based calculation, the deviation from quantum chemical calculation is marginal.

6.4 MD study of a single tetrakis-Schiff molecule

6.4.1 Conformational free energy change

Before going on to investigate the self-assembly of the selected multi-molecular chains in various solvents it is important to investigate possible conformations of a single molecule. Due to the relative rigidity of cation-N_2O_2 sites, the conformational space of a tetrakis-Schiff compound can be reduced to the two dihedral angles shown on picture 6.11. The first one is the angle between the planes of the two central phenolic rings, linked with the single C-C bond, here and after designated by Θ. The second angle is the angle between one of the side phenolic rings and the closest to it side group (methyl or phenyl in the current work), here and after called Φ. There are two such angles: one per each symmetrical half, - however, only one of them needs to be studied, since any conformation, obtained by change of the other can be represented by corresponding changes of the first one and Θ with subsequent inversion of the molecule. For clarity, in what follows

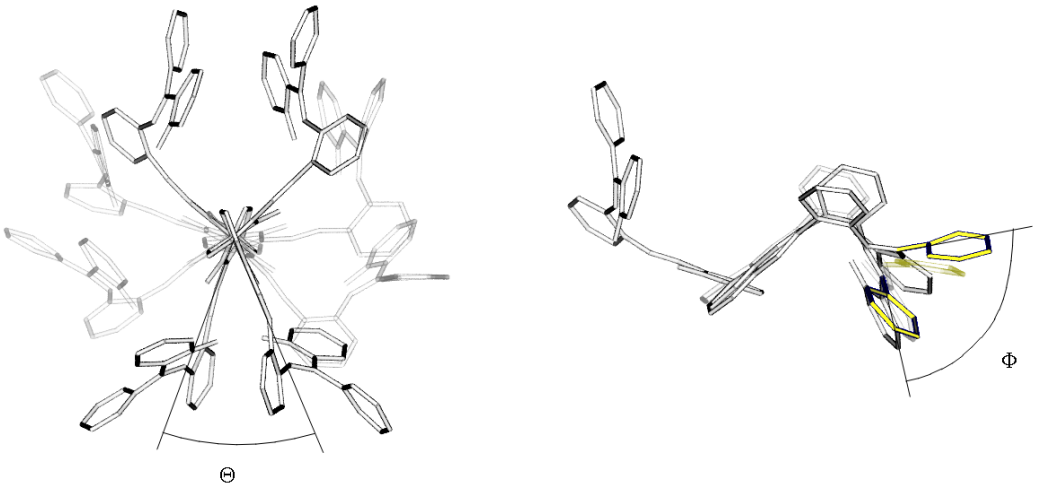

Figure 6.11: Conformational angles of a single tetrakis-Schiff compound

the conformation, in which both Φ angles have the same sign (side groups point in the same directions) will be designated with the letter "W", while the opposite case will be addressed as "S" conformation.

To sample the free energy profiles (or the potentials of mean field, PMF) profile during the conformational change the umbrella sampling approach was used, where the angles Φ and Θ were used as the reaction coordinates. Preliminary NEB calculations supported that such choice of transition coordinates indeed closely approximates minimum energy paths. In this study Θ was varied in range $[15°; 345°]$, Φ in $[-120°; 120°]$, angle values outside of this range are only possible with strong deformation of the molecule and are unlikely to occur. The step was chosen to be 2° and the spring constant of the biasing potential was 128 kcal/mole/degree^2 to ensure good sampling of the peak of the potential surface. To observe the effect of the phenyl side groups, the same calculations were conducted for the same compound with the side groups replaced by methyl groups. It is known from the experiments that the later compound does not form ring-like structures, collapsing into a droplet instead.

The free energy profiles and angle Θ probability distributions (P) are shown on the figures 6.12 and 6.13 for the phenyl- and methyl-terminated tetrakis-Schiff complexes respectively. As the calculations are only conducted in vacuum, the Helmholtz free energy ΔF is used here. The major motif, present on all the figures, is the ~7 kcal/mole peak of the free energy in the middle, while the conformational probability peaks around 50° and $250° - 310°$ where the PMF has basins before different parts of the molecule begin to overlap. A metastable conformation can be observed near $\Theta \sim 150°$ where PMF has a plateau before

the main peak. This plateau corresponds to the situation, when the two zinc-centers are far apart and the central aromatic rings form a close to equilibrium dihedral angle of 120°. For clarity, in what follows these three distinct cases will be referred as "closed" ($\Theta \sim 50°$), "opened" ($\Theta \sim 150°$) and "inverted" ($\Theta \sim 250°$) conformations. Since *S*-shaped conformation is completely symmetrical, unlike the *W*-shaped, it does not possess a special "inverted" conformation, as transition over the central peak is equivalent to mirror transformation.

It is interesting that, unlike phenyl-functionalized compound, the complex with methyl groups has one clearly preferred stable conformation - the "closed" one. The "inverted" conformation, although stable, is clearly less favourable and the transition barrier is much higher in this case. Such difference in PMF of almost similar compounds must be attributed to the role of side groups: besides increasing the conformational entropy, after a certain angle ($\Theta \sim 100° - 120°$ according to 6.12), when Zn-O attraction is already weak, the $\pi - \pi$ interaction between the two phenyl groups or between side groups and aromatic rings of the salphen bases lowers the potential energy growth due to electrostatic and covalent contributions. On the other hand, methyl groups do not possess such ability and only add repulsion for "inverted" conformer potential energy.

Thermal energy at 300 K is only about 0.5 kcal/mole, so the probability of transition from one basin to another in vacuum is only about 10^{-6}. This behaviour is expected for vacuum, as the two metal-NO sites attract each other strongly and in the absence of screening by solvent the molecule collapse to one or other side, while the "opened" configuration with $\Theta \sim 150°$ (or 210° for *S*-shaped conformer) is highly unstable.

Figure 6.14 shows the free energy profile for Φ angle for both side groups. Again there are two basins around the values of $\pm 55°$ with 6-8 kcal/mole high peak between them.

6.4.2 Diffusion in the selected solvents

To further investigate the behaviour of tetrakis-Schiff zinc-complex molecules and the effect of solvent series of MD simulations were conducted. The single compound molecule in one of the two *W*-shaped conformations: "closed" or "opened" - was inserted into the periodic cubic box of DCM, THF or toluene molecules. After the initial relaxation, as described in the methods section, the systems dynamics was modelled in LAMMPS under the normal conditions (T=293.15 K, P=1 atm) using AMBER force field and charges derived as described above. The systems dynamics was governed by the Nose-Hoover NPT barostat and thermo-

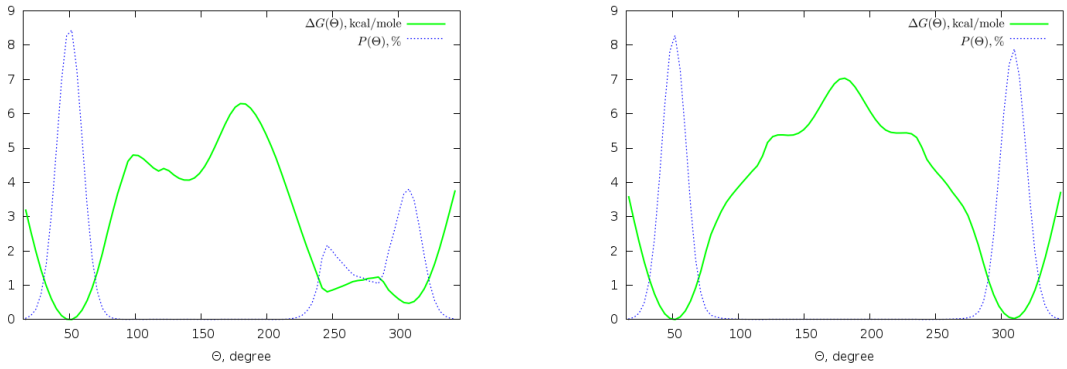

Figure 6.12: Free energy difference (ΔG) and probability (P) profiles for angle Θ for a phenyl functionalized compound. Left - alpha configuration, right - beta configuration

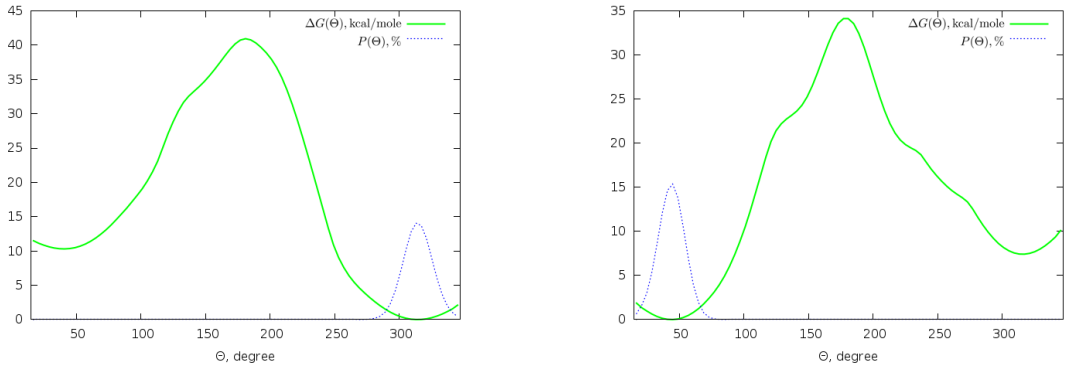

Figure 6.13: Free energy difference (ΔG) and probability (P) profiles for angle Θ for a methyl functionalized compound. Left - alpha configuration, right - beta configuration

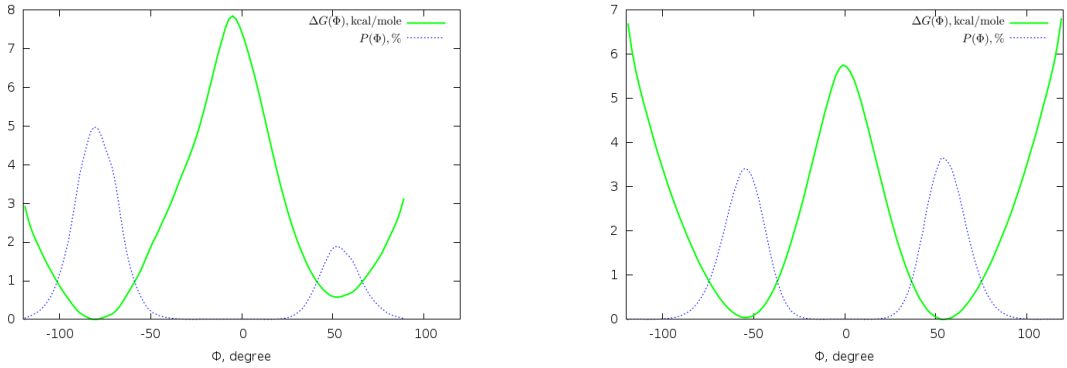

Figure 6.14: Free energy difference (ΔG) and probability *(P)* profiles for angle Φ for phenyl (left) and methyl (right) functionalized compounds

Solvent	D_{diff}, 10^{-5} Å$/fs$		
	"closed"	"opened"	total
DCM	8.29 ± 0.08	6.39 ± 0.06	7.34 ± 0.04
THF	4.14 ± 0.04	3.59 ± 0.04	3.86 ± 0.02
TOL	4.18 ± 0.04	4.25 ± 0.06	4.22 ± 0.02

Table 6.3: The estimated diffusion coefficients

stat with the 0.5 fs timestep. 20 independent 2 ns simulations were conducted for each starting conformation in each solvent, during which the solute molecule displacement (d), the absolute value of dipole moment (p) and complex-solvent pair interaction energy (U_{CS}) was evaluated.

The average diffusion coefficients were estimated according the method suggested in [125]. The collected displacements are shown on the figures presented in B.1. The average diffusion coefficients (D_{diff}), estimated for all trajectories as well as separately for those starting from "closed" and "opened" conformations, are summarised in table 6.3.

The interesting detail of the zinc-complex behaviour in various solvents is most strikingly seen on the plots of the dipole moment variation during simulation (a typical example is shown on figure 6.15). Here the blue and red lines correspond to the dipole moments of each of the two symmetrical halves of the molecule ($p_{L(R)}$), that remain almost constant along the simulation, while the total dipole moment (p_T, black line) has a two distinct levels that correspond to either "opened" configuration, where the vectors of dipole moments of the symmetrical halves face and almost neutralize each other, or "closed" and "inverted", where the $\vec{p}_L$and $\vec{p}_R$ are almost parallel, hence the total dipole moment is higher. Frequent transitions from the "opened" to "closed" state were observed in DCM, such as the one shown on the lower left plot of the figure 6.15. In THF and toluene such transitions are rare.

This difference in behaviour can be explained by the plots of radial pair distributions ($g(r)$) between the selected atom types (figure 6.16). Here the most striking feature is observed for "opened" zinc-complex in THF: a sharp peak at zinc - THF oxygen distance ~ 2.1 Å. This feature is the result of a strong attraction between Zn^+ cation and negatively charged oxygen of THF molecule, leading to a stable association of the solvent molecule and the cation center in the "opened" complex (figure 6.16 left). A similar, however quite weaker, peaks can be observed for cation-π and $\pi - \pi$ interactions between zinc ion and aromatic rings of the tetrakis-Schiff complex and the aromatic ring of toluene (figure 6.16 center and right). These interactions improve the solute-solvent interactions for

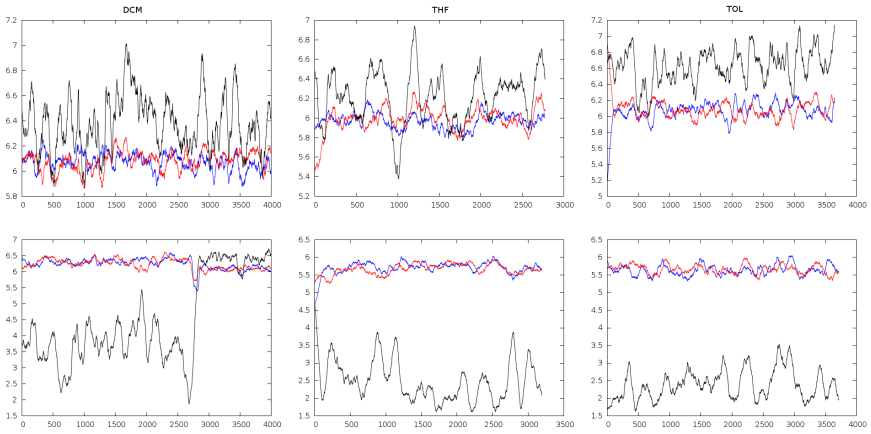

Figure 6.15: Variation of the dipole moment of a single tertakis-Schiff zinc-complex in DCM, THF and TOL correspondingly: upper row - starting from "closed" conformation, lower - from "opened", black line - total dipole moment, blue and red - left and right halves

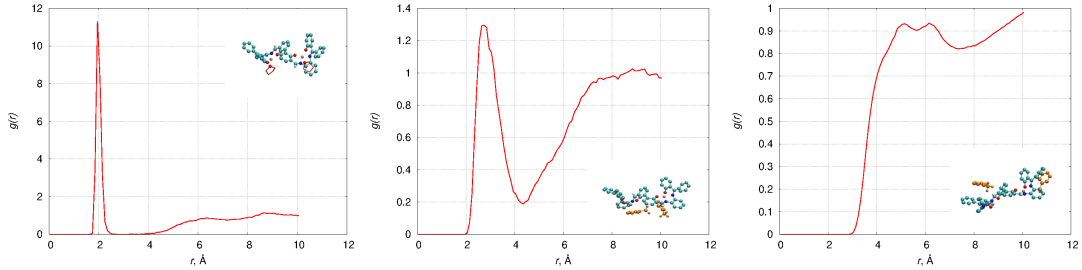

Figure 6.16: Radial pair distributions for zinc cation and oxygen of THF molecule (left) or aromatic carbons of toluene (center) and for aromatic carbons of salphen complex and toluene (right)

the "opened" complex, making such configuration relatively stable in THF and toluene. Somewhat similar interaction exists between hydrogen atoms of DCM and the oxygens of tertakis-Schiff complex, but obviously they are too weak to overcome Zn-O attraction in the solute. As the result, a polar "closed" conformation becomes dominant in DCM, increasing the rate of diffusion, while increased average radius and solute-solvent interactions additionally slow down diffusion in TOL and especially in THF (table 6.3).

6.5 Multi-molecular assembly in vacuum and explicit solvent

In section 6.2 it was shown using a simplistic 4-rigid part model in vacuum that, due to competing Coulomb, $\pi - \pi$ and van der Waals interactions, tetrakis-Schiff zinc-complex molecules can self-assemble into nanosized linear chain-like struc-

tures. Such chains could bend due to thermal fluctuations and rearrange to maintain a stable curved string or closed ring shape without collapsing into droplet. However, the spontaneously formed structures, observed there, contain many defects and disordered segments which made analysis of their structural motifs quite difficult. To investigate in details how the building blocks of "rings-and-rods" networks appear and how the choice of solvent affects their formation and behaviour, an approach from different perspective was used here. Basing on the results of the preliminary simulations of random dimer formation, reported in section 6.2, several dimer samples were selected that, taking into consideration the flexible structure of twinned salphen-based zinc-complex, can support periodic repetition in one dimension, i.e. from which potentially infinite chains can be constructed. The four selected arrangements are shown on the figure 6.17.

- The arrangement 6.17a is a periodic repetition of the "stack" arrangement of the W-shaped conformation reported in section 6.2. It is the most compact structure, stabilized by combined Coulomb and $\pi - \pi$ interactions and the only one where initially neighbouring molecules have the full surface contact;
- The arrangement 6.17b can be viewed as a result of outstretching of 6.17a, in which monomers are only bonded together at one side in an alternating "left-right" order. Deformation into S-like conformer allows the creation of the pockets where solvent molecules can enter;
- The arrangements 6.17c and 6.17d are based on the dimer structures proposed for single-base salphen-type zinc compounds as was discussed earlier in section **??**. The only difference between the two is that while 6.17d is obtained by consequent displacement and rotation of a monomer creating a ring- or spiral-like chain, the building block of 6.17c is a dimer with inversion symmetry which enables, in an idealised case, a linear structure with the highest aspect ratio.

Obviously the experimental realisations of molecular chains would be a random combination of those idealised structures. This simplification, however, allows to study relative stability of the selected segments in solvent and thus the rate of their appearance.

6.5.1 Association free energies for selected dimer structures in solvent

One reason why different self-assembled structures may emerge from different solvent is that the solvent molecules interact with different parts of the solute

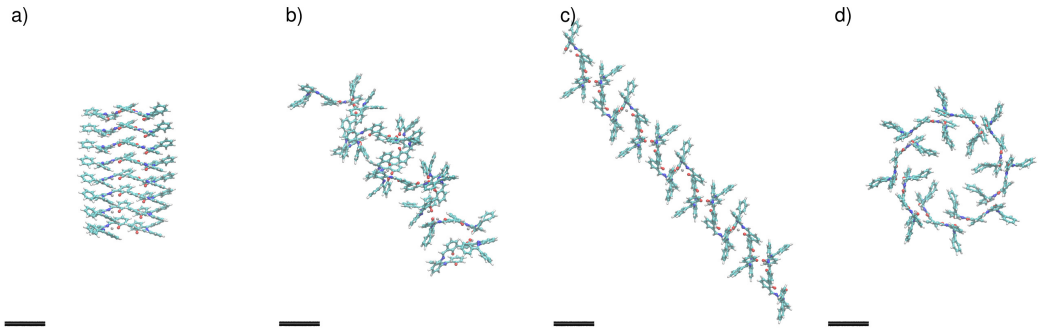

Figure 6.17: Possible 8-molecular chain-like arrangements, scale bar is 10 Å

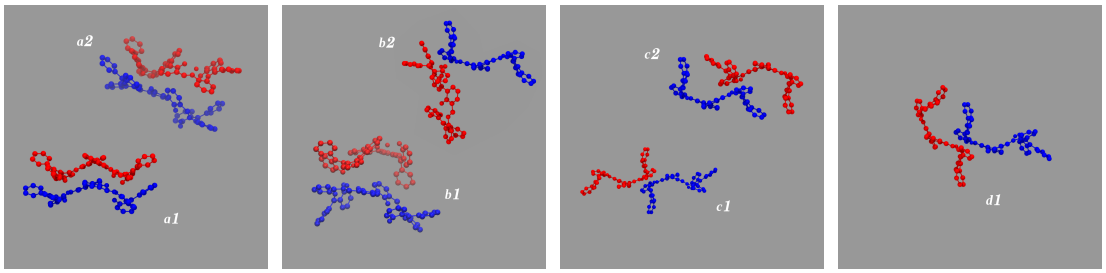

Figure 6.18: Selected dimeric structures (hydrogens are omitted for clarity)

molecules, affecting which conformation the solute molecules assume and strength of their interaction with each other. It was shown previously (section 6.4.2) that "opened" and "closed" conformations of the tetrakis-Schiff zinc complex apart of different gyration radius, affecting their speed of diffusion, but also different total dipole moment, thus different interaction with polar and non-polar solvents can be expected for the two conformations and, hence, different structure of multi-molecular arrangement, emerging from solvents with different dipole moment of solvent molecules.

To test this hypothesis series of calculations were carried out to estimate the free energy of formation of dimeric structures, serving the building blocks of the molecular arrangements, shown on figure 6.17. The selected dimer structures are shown on the figure 6.18. Here dimers *a1* and *a2* both refer to arrangement, designated on the figure 6.17 with the letter *a*, with one difference: while *a1* has both Zn-O sites of each symmetric complex interacting with its counterpart from the other complex, in *a2* the second molecule is rotated so that only one ionic bond is present leaving the other cation centers of both molecules free to form bonds with subsequent molecules, thus forming a some-what twisted version of the arrangement *a* with alternating Zn_2O_2 bridges. Dimers *b1*, *b2* and *c1*, *c2* refer two the two subsequent conformations, present in the arrangements *b* and *c* correspondingly. The last coil-like arrangement *d* is formed by a single dimer

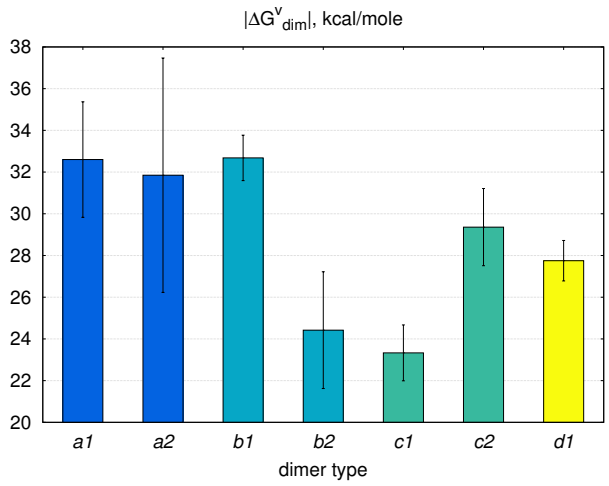

Figure 6.19: ΔG^v_{dim} for the selected dimers in vacuum

d1, translated and rotated by a constant amount.

6.5.1.1 Dimerization in vacuum

As the first stage, the free energy calculations in vacuum environment were estimated for all dimeric structures, shown on figure 6.18. The dimerization free energy ΔG^v_{dim} was estimated as the negative of the free energy change during dissociation of a dimer in vacuum ΔG^v_{diss}. After initial testing, the FEP method was selected from the free energy methods, described in Methods section as giving the most stable results. For each dimer type a set of 10 independent calculations were conducted during which both Coulomb and van der Waals interactions, modelled with soft-core versions of potentials 6.1.2 and 6.1.3, were scaled down simultaneously with the coupling parameter λ changing linearly with the step 0.05. For each λ-point the system dynamics was simulated in LAMMPS with Langevin thermostat during 10^6 timesteps (~0.5 ns) from which only the last quarter was used for FEP calculations, resulting in total 10 ns simulation per each sample. The interaction potential energy change in both forward δU_{FWD} and backward δU_{BWD} directions was sampled every 10 timesteps. δG between each pair of consequent λ-point were calculated using the Bennet acceptance ratio method.

From the results, presented on the figure 6.19, it is clear that in the model vacuum environment all dimeric structures are thermodynamically stable ($|\Delta G^v_{dim}| >$ 20 kcal/mole) with the arrangement *a* having the lowest formation energy with both conformations *a1* and *a2* having dimerization energies -32.6 ± 2.8 and -31.8 ± 5.6 kcal/mole correspondingly, while the arrangements *b* and *c* both have one of the dimers with formation energy in the same range (-32.7 ± 1.1 for

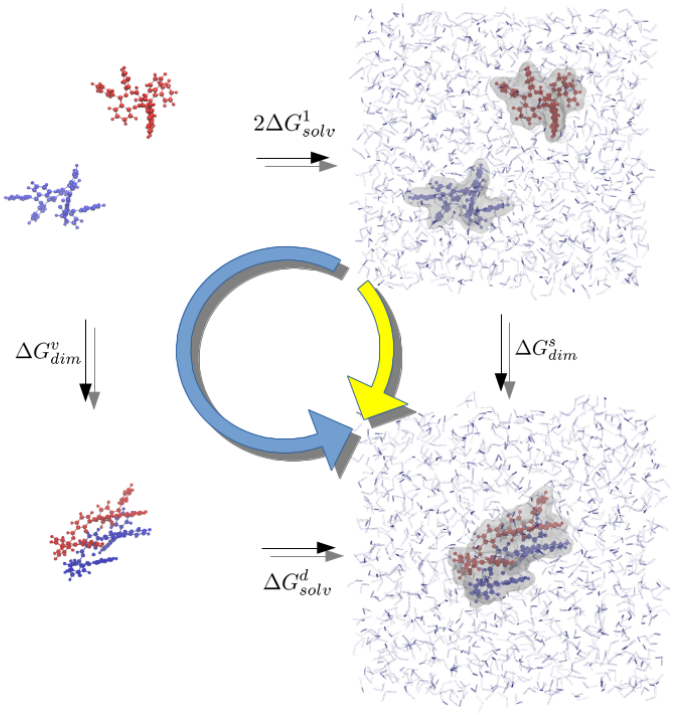

Figure 6.20: Thermodynamic cycle for the dimerization in solvent: direct transformation (yellow arrow) and the "alchemical transformation", corresponding to equation 6.5.1 (blue arrow)

b1 and -29.4 ± 1.8 for *c2*), their counterparts, needed for periodic structure, are a bit weaker (-24.4 ± 2.8 for *b2* and -23.3 ± 1.3 for *c1*). The dimer *d1* has the intermediate free energy value of -27.8 ± 1.0.

6.5.1.2 Dimerization in solvent

Calculation of the free energy of dissociation in solvent via the same route turned out to be quite unstable, since, as the interaction between the two solute molecules weakens, it becomes easier for the solvent molecules to enter the emerging gaps. This accelerates the dissociation process up and leads to unstable results. For this reason, the dimerization free energy in solvent ΔG^s_{dim} was estimated in the "roundabout" way of "alchemical transformations" (figure 6.20):

$$\Delta G^s_{dim} = \Delta G^d_{solv} + \Delta G^v_{dim} - 2 \cdot \Delta G^1_{solv}; \tag{6.5.1}$$

where ΔG^d_{solv} and ΔG^1_{solv} are, correspondingly, the free energy of solvation of a dimer and a single tetrakis-Schiff molecule, estimated using FEP method by gradually coupling the solute molecules from solvent by scaling up the strength of non-bonding interactions between them. Since the solute molecules are quite large and simultaneous decoupling of the whole molecule would induce a large stress

	ΔG^{d}_{solv}			ΔG^{v}_{dim}			ΔG^{s}_{dim}		
Dimer	DCM	THF	TOL	DCM	THF	TOL	DCM	THF	TOL
a1	-58.53	-51.45	-48.27	-39.01	-35.50	-49.66	**-24.46**	9.29	**-23.24**
a2	-60.68	-61.76	-52.37	-24.38	-32.18	-27.82	-11.98	2.30	-5.50
b1	-52.62	-57.74	-47.23	-32.97	-32.54	-39.59	-12.52	5.97	-12.14
b2	-53.18	-59.69	-49.28	-24.70	-32.32	-30.11	-4.81	4.23	-4.71
c1	-57.99	-61.01	-51.99	-24.61	-29.39	-25.94	-9.53	5.84	-3.25
c2	-63.88	-69.63	-56.63	-29.31	-38.50	-41.14	**-20.11**	**-11.89**	**-23.09**
d1	-59.54	-67.97	-51.97	-26.29	-37.96	-28.47	-12.75	-9.69	-5.76

Table 6.4: Free energy change during the dimer transformations for the selected dimers

on the system, in these simulations the following 3-parameter decomposition for the pair-interaction potential energy (equation 6.1.1) was used:

$$U_{SC} = U_S + U_C + \lambda^{A}_{vdW} U^{vdW}_{SC,A} + \lambda^{N}_{vdW} U^{vdW}_{SC,N} + \lambda_{Coul} U^{Coul}_{SC}; \tag{6.5.2}$$

here U_{SC}, U_C, U_S, U^{Coul}_{SC} are, correspondingly, the full pair interaction of the solvent-complex (solute) system, the energies of pair interaction between only the atoms belonging to either complex or solvent and Coulomb interaction energy between complex and solvent, as were defined earlier in Methods section. However the potential energy of van der Waals interaction U^{vdW}_{SC} is additionally decomposed into $U^{vdW}_{SC,A}$ and $U^{vdW}_{SC,N}$ - corresponding to the impact of aromatic and non-aromatic atoms of the solute molecules. Hence, the 3 coupling parameters: λ_{Coul}, λ^{A}_{vdW} and λ^{N}_{vdW}. In the attempt to minimize large fluctuations of δU_{FWD} and δU_{BWD} at the beginning and the end of scaling of each coupling parameter, the non-linear λ-schedule was used, as shown on figure 6.21. Each λ-point corresponds to a 600 fs long simulation, from which only the last 200 were used to sample data for FEP calculation.

The initial system was prepared by inserting the dimer structure into a cubic block of solvent molecules and relaxation as described in Methods section. As previously, the solvent dynamics was governed by Nose-Hoover NPT thermostat, while the solute dynamics was controlled by Langevin thermostat. Solvation simulation for each sample lasted 39.6 ns. During the preliminary runs, such solvation calculations proved to be more stable than dissociation, so a single simulation was conducted for each sample. After the solvation cycle was complete, the dissociation simulation, as described in the previous section, was conducted for the dimeric structure, as it remained at the end of solvation simulation.

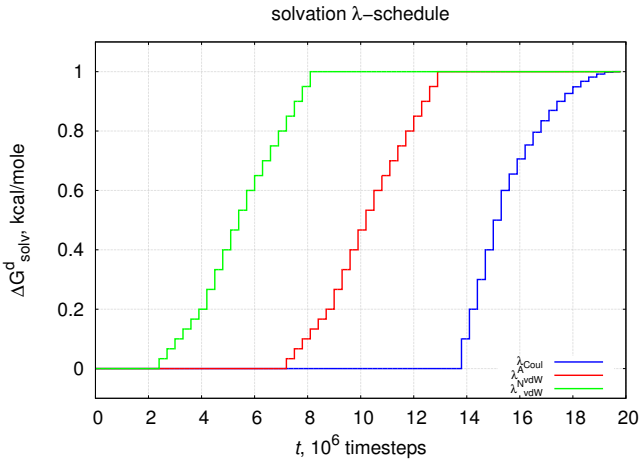

Figure 6.21: Variation of coupling parameters during solvation FEP simulation

The results of the calculations are summarized in the table 6.4. Here the most favorable dimer configurations are outlined with bold values of the corresponding free energy change during dimerization in solvent, while the red font marks the calculations, where dimerization in solvent was found unfavorable (positive ΔG^s_{dim}). From the results summarized in the table it becomes clear that, although all the selected dimeric structures can exist in DCM and toluene, *a1* and *c2* dimer are clearly the most stable out of all with $\left|\Delta G^S_{dim}\right| > 20$ kcal/mole. In THF all dimerization free energies turn out to be much lower, leaving only *c2* and *d1* dimers thermodynamically stable. These results bring to the conclusion that the self-assembly most likely starts from the association of single molecules into one of these dimers.

6.5.2 Evolution of selected molecular chain structures in solvent

To further investigate role of the solvent in the self-assembly of tetrakis-Schiff compound's networks series of all-atom molecular dynamic simulations of chains, containing several tetrakis-Schiff complexes were conducted in explicit solvent for the selected structures. The simulation in explicit solvent consisted of the initial relaxation as described earlier in Methods section followed by a 1 nanosecond long runs in each environment under room conditions (300 K temperature and 1 atm. pressure) with 1 fs timestep, during which the components of solute-solute and solute-solvent interaction energy and the chain conformation were monitored. 5 independent simulations were conducted for each arrangement in each solvent.

The collected data for all four selected strictures are summarised in the ap-

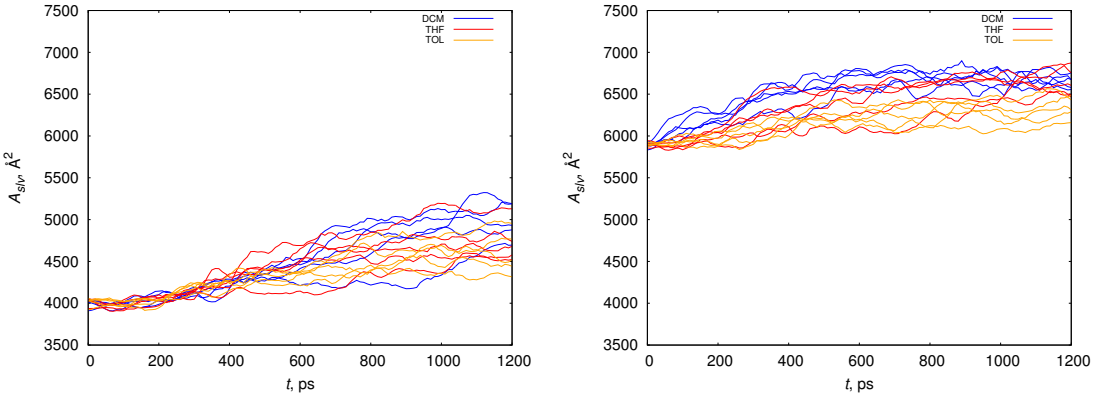

Figure 6.22: Variation of chain surface area for chains of type a (left) and c (right) averaged over 50 ps

pendix section B.2. The most important observation here is shown on the figure 6.22 - the surface area of the chain in solvent (A_{slv}), defined as the boundary of the volume around the solute, into which an atom with van der Waals radius of 1 Å cannot penetrate. From the results, presented here, it is clear, that although in model vacuum environment the arrangement a is the most thermodynamically stable, it becomes quite fragile in the explicit solvent: starting from the compact ~4000 Å^2, its values diverge abruptly after ~0.5 ns independently on the solvent. The reason for this can be seen on the figure 6.23: the initial chain structure breaks down into smaller parts containing 2-3 molecules. This most probably occurs because the metal centers, sandwiched between the other two alike, are in a metastable state, where the idealized configuration 6.24, in which zinc in of the intermediate molecule forms a Zn-O bond with one of the neighbour molecules, while the oxygen of the outer, mobile phenol-like ring, participates in ionic bond with the other neighbour molecule, turns out to be unstable against torsional deformations induced by surrounding molecules. The spontaneous displacement of either the phenol oxygen or zinc ion to form a more stable Zn_2O_2bridge with just one of the neighbour molecules results in breaking of the initial structure. As the arrangement a resembles a helix, another type of simulation was attempted: the two helix-like strings (shown in red and blue on the figure 6.25) wrapped around each other into a single rod were subjected to the same procedure. Although the torsional deformations are compensated in this way, another weakness of the arrangement a becomes clear: poor side-to-side interaction, originating only form van der Waals forces and not allowing a stable contact. Due to such weak interaction between the strings, the double helix arrangement rapidly decomposes in solvent into two separate strings that continue to break as in single helix simulations as indicated by continuous increase of solute-solvent attraction (figure

6.26).

On the other hand, the arrangement c proved to be quite stable both in vacuum and the explicit solvent: although immediately after relaxation, its solvent accessible surface area begin to grow, simulations do not diverge and arrive to a saturation within the first ~0.5 ns. Its remarkable stability arises from the combination of the strong Zn_2O_2links between the molecules and flexibility of rotation around the central bond of symmetric tetrakis-Schiff molecules, thanks to which it maintains integrity under stresses, induced by solvent molecules. The behaviour of the phenyl side rings in such arrangement is of particular interest: although they are not needed for the formation of the chain, they are playing an important role in the conformational change of the chain. Figure 6.27 shows the examples of the typical configurations the chain of this arrangement assumes in solvent. It can be seen that in DCM and THF the chain bends, so that on the one side the phenyl chains stick to each other due to $\pi - \pi$ interaction, while on the other they leave wide pockets opened for interaction with solvent. Thus the curved shape is assumed spontaneously in these two solvents improving solute-solvent interaction. On the other hand, this may also serve the increased rigidity of such structure, as covalently bonded core would resist further folding. In toluene, however the chain is straighter, with some of phenyl groups stretching aside at both sides, while the other stretch along the axis of the chain. The reason of such difference in behaviour becomes clear form the right-most plot on the figure 6.27: polar solvents interact more strongly with the ionic center of the salphen-based zinc complexes and the pockets, opening due to bending, result in a significant improvement of such interaction, resulting into lower solute-solvent interaction energy. Toluene on the other hand interacts with tetrakis-Schiff molecules through weaker $\pi - \pi$ and cation-π interactions, so the gain in solute-solvent interaction is countered by decrease of solute-solute interaction and stresses arising in covalently bonded backbone.

Another important role of the stretched aside phenyl groups in the arrangement c are bonding of the long strings together into a thicker rod. Although the $\pi - \pi$ interaction is weaker than ionic, as the chain grows longer, it becomes less and less probable that the ends of different chains would meet and the potential gain of free energy of bonding remains constant. At the same time, gain from binding the two strings side-by-side via $\pi - \pi$ grows proportionally to their length and the probability of such contact increases exponentially with the aspect ratio of the chain, as was shown in the second chapter.

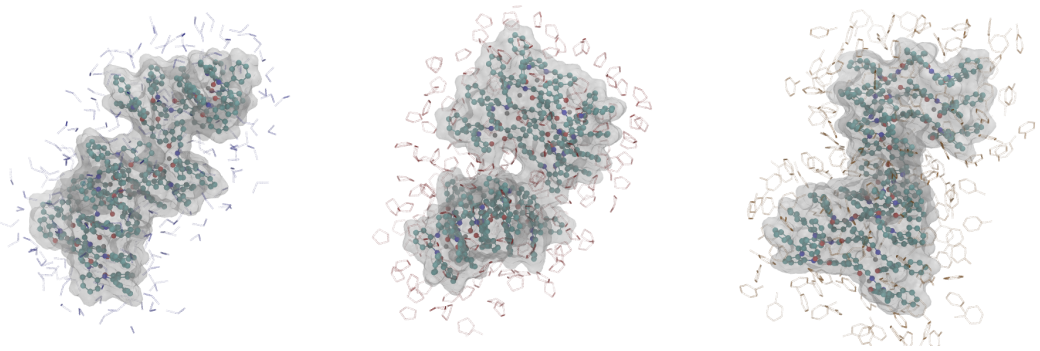

Figure 6.23: Single chain of type *a* in DCM (blue), THF (red) and TOL (yellow) after a 1 ns simulation (hydrogens are omitted for clarity, grey shows the surface as defined in text)

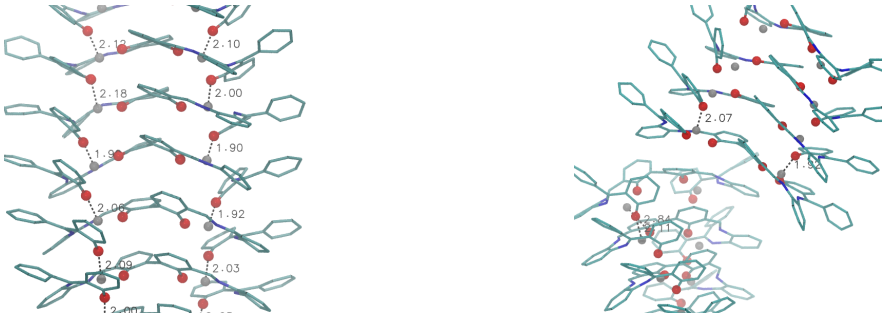

Figure 6.24: Zn-O ionic bonds in idealized (left) and broken (right) helix-like arrangement of type *a*

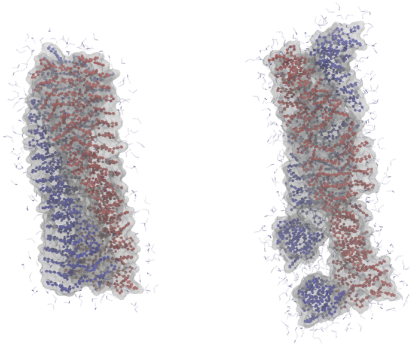

Figure 6.25: Double chain of type *a* in DCM: idealized (left) and relaxed after 1 ns simulation (right)

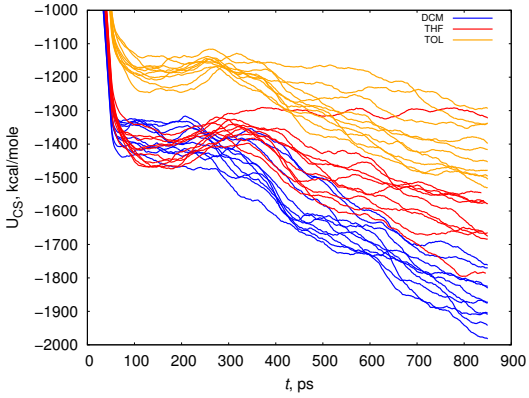

Figure 6.26: Energy of solute-solvent interaction in double chain of type alpha in explicit solvent, running average window 50 ps (negative value designates attraction)

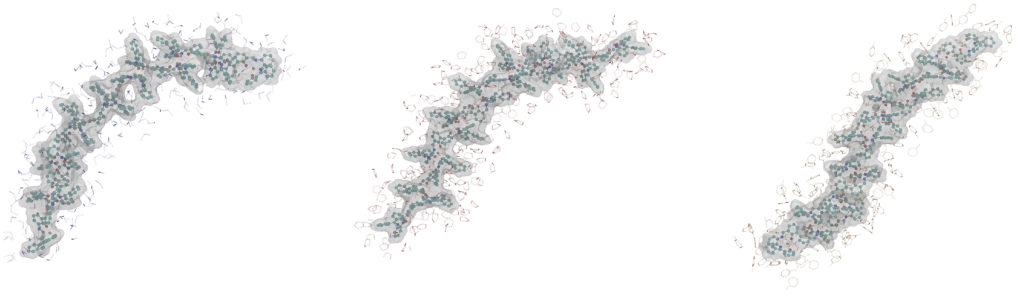

Figure 6.27: The shape variation of type c chain in DCM , THF and TOL (hydrogens are omitted for clarity, grey shows the surface as defined in text)

Figure 6.28: Possible types of $\pi - \pi$ interaction between strings of type c: "pincer" (left) and "sandwich" (right)

6.6 Proposed mechanism of "rings-and-rods" like networks self-assembly

Based on the observations of the zinc-substituted tetrakis-Schiff complex behaviour in the simulations above, the following explanation of the interconnected networks self-assembly is proposed:

- On the first step, single compound molecules join in dimer, resembling aforementioned "back-to-back" configuration through the strong Zn_2O_2 interaction between one of the two metal centers from each molecules. This interaction is quite strong ~ 35 kcal/mole, so must occur quite fast in all solvents. This interaction should also provoke the change of the molecule conformations as the zinc and oxygen atoms of both molecules, involved into inter-molecular bond, weaken the intra-molecular attraction between ionic centers of the same molecule. On this stage the symmetry between the minima of PMF, corresponding to the Θ and Φ angles, as defined in 6.4.1, is broken and the change of initial conformation to a dimer, bonded through Zn_2O_2 bridge is facilitated. Connection through both centers es-

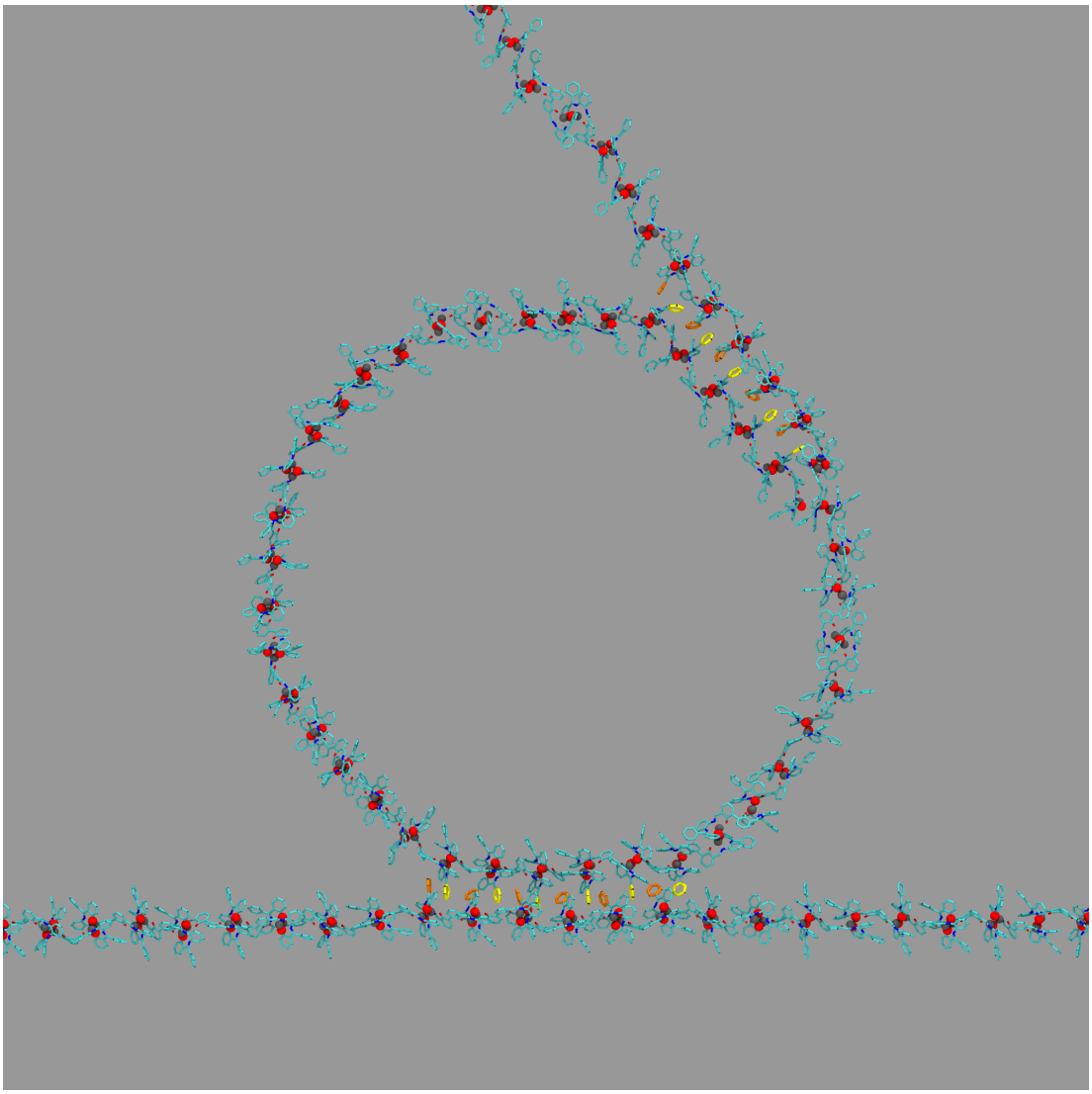

Figure 6.29: The idealised model of tetrakis-Schiff assembly of type c forming a ring-like structure with multiple connections via tangent $\pi - \pi$ connection and continuation of the same chain: hydrogens are omitted for clarity, grey and red spheres show the Zn_2O_2 bridges, connecting the linear structure of the chain, while yellow and orange rings indicate the interlocked phenyl side groups, holding different chains together

pecially in case of W-shaped conformer is possible as well, however, it puts significant stress on the C-backbone and must relax relatively easy to the single center interaction upon collision with another dimer or interaction with solvent molecules. Such dimer has the diameter of ~ 2 nm, so it must correspond to the smallest fraction with the diameter of 19.68 $\mathring{A}$ as was observed by DLS and DOSY measurements in [**?**]. As was already noted, a single tetrakis-Schiff molecule appears to maintain the closed form in DCM with the approximate diameter of $\sim 9\,\text{Å}$.

- Such dimers serve as the primary building blocks of the higher order supra-molecular structure. There are two ways, through which dimers interact with each other: formation of Zn_2O_2 bridge between the free halves of the adjacent dimers, leading to formation of long ionic bonded chain (figure 6.17c), or $\pi - \pi$ interaction via phenyl groups. Since each side of dimer has the two phenyl rings, interacting with each other in a standalone dimer, the two distinct types can be seen in the $\pi - \pi$ bonding: a "sandwich-like" arrangement with interleaved phenyl groups (figure 6.28 right) or a "pincer-like", where the phenyl rings of the same dimer primarily interact with each other, but are inserted into space between the like groups of another chain as pincer cogs (figure 6.28 left). The former type is stronger, but might be more rear to find as the interaction of the adjacent rings must be interrupted first (which can occur due to interaction with solvent). Unlike was initially suggested in [**?**], here it is suggested that both Zn-O and $\pi - \pi$ interaction are equally important for the self-assembling structure. In vacuum ionic interaction is stronger at first, promoting the formation of elongated supra-molecular chains, bonded with Zn_2O_2 bridges, leaving the phenyl groups stretching aside, supporting ionic bonds and providing rigidity to the chain. However, as the chains grow longer, the strength of each ionic bond remains constant, while the probability that the endpoints of long chains will meet each other decreases, as the elastic stress reduces the mobility of the dimers, residing on the ends of such chain. On the contrary, the importance of the $\pi - \pi$ bonding increases proportionally to the chain length as more phenyl groups participate in it and the probability of side to side contact of long linear chains growth by the power law with the aspect ratio, as was mentioned previously (equation 5.1.2).
- Due to the two types of interaction, the initial dimers assemble into long semi-flexible chains that are rigid enough on a nanometer scale, but bend freely on micron scale. Similar to the behaviour observed in covalently bon-

ded semi-flexible polymers (discussed in the literature review section 2.2), upon evaporation of solvent such supra-molecular chains undergo transition first from coil to spherical globule (the experimentally observed "vesicles") and then, depending on the rigidity and aspect ratio of the chains formed by that moment, from spherical to rod-like or toroidal globule. The important feature of self-assembled networks, setting them apart from the well investigated covalently bonded polymers, is their ability to form new connections with the chains from other coils. Thus for a certain range of concentrations an interconnected network is possible, arranged due to the integration of separate coils into higher order structure with the same non-bonding interactions that connect the chains of the same coil.

It is easy now to imagine a molecular arrangement such as shown on figure 6.29. Although such structure can in principle exist (and probably does on a tens of nm scale) it is, of course, idealised demonstration of concept, illustrating how such chain of ionically bonded dimers can form a network of interconnected coils, resembling the experimentally observed "rings-and-rods" networks. In the reality, the micrometer-sized rings and rods must be composed of shorter strings arranged in a beards-nest or threads-in-a-rope like fashion. The molecular "threads" are internally bonded by ionic Zn-O like interaction and hold together with $\pi - \pi$ bonds.

As well, the real coils may, and most likely do, contain the fragments corresponding to the other conformers of the studied tetrakis-Schiff complex. This increases the complexity of the chains' internal structure and introduces more randomness into the distribution of rings' diameters and rods' lengths. Furthermore, when solvent evaporates, the structure transition can take place from the arrangement shown on figure 6.17c as more open to solvent, to the arrangement on figure 6.17a as more dense. Such transition can induce stress in the rods, connecting the rings, causing a kink feature, seen on the micro-photographic images. However, it is proposed in this study, that it is the described mechanism of formation of the arrangement 6.17c dominates in the solution and is responsible for the formation of the "rings-and-rods" like networks as the other arrangements cannot on their own explain all the experimental observations, including the effects of metal center, the functional group and solvent in a way the selected arrangement can.

Within the proposed mechanism the role of both Zn-cations and phenyl functional groups becomes clear: while the same looking structures were observed even for unsubstituted ligands, the hydrogen bond, capable of formation similar

dimers and connecting them into strings, is weaker than interaction via Zn_2O_2 bridge, thus the structures of unsubstituted ligands are less distinct and disrupted. Replacing phenyl side group with methyl termination not only prevents $\pi - \pi$ linking of ionically bonded chains into larger assemblies, but also reduced the chains' rigidity. Thus the coils of methyl terminated complexes do not undergo coil - toroidal globule transition, but instead remain in the form of shrinking spherical globule.

Finally the strong effect of the solvent can be interpreted as the result of the solvent molecules intervention into one of the two types of dimer-dimer interaction, crucial for the extended network formation. If a non-coordinating and non-aromatic solvent is used, such as DCM, the self-assembly follows as described with the formation first of elongated dimer chains, followed by $\pi - \pi$ bonding of separate chains into longer semi-flexible strings, which folds as the solvent evaporates into coils, followed by transition into interconnected toroidal globules. However, if instead a coordinating solvent is used, such as THF, its molecules interact with the metal center, thus reducing the probability of dimer association into longer chains. For this reason only short, small aspect ratio strings can be obtained from THF. This effect is similar to the effect of pyridine on other zinc-substituted compounds [215]. Toluene, on the other hand, interacts much weaker with tetrakis-Schiff molecules, thus it is possible for them to stay aggregated on nanoscale, which, together with slow diffusion, prevents emergence of long flexible chains and leads to formation of collections of needle like crystals.

6.7 Molecular dynamics study of the free energies of association of tetrakis-Schiff zinc-complexes in solvent

To verify the proposed mechanism of formation of "rings-and-rods" like networks, free energies of association of zinc-substituted tetrakis-Schiff molecules into dimers and tetramers in each of the solvents. Preliminary calculations have shown that direct estimation of PMF during dissociation process via steered molecular dynamics method (SMD) face a certain difficulties: the free energy profile changes rapidly when the ionic Zn-O bond is broken and solvent molecules actively fill the emerging gap between the disjoint monomers. This creates an abrupt change in PMF that violates the condition of applicability of such method: near equilibrium transition. Hence, a large number of independent simulations are needed so

that the exponential average of non-equilibrium work functions would be close to the transition free energy change.

For this reason, a roundabout approach of alchemical transformations combined with free energy perturbation (FEP) method was chosen. Within this approach instead of simulating dissociation of the molecular cluster in solvent under external force, the transformation was spited in the two parts: estimation of free energy of dissociation in vacuum by scaling gradually the strength of non-bonding interactions between the associated molecules and estimation of the solvation free energies of both initial and final molecular structures. This allowed to circumvent the difficulties connected with a rapid PMF change by smoothing on the transition speed with careful selection of the scaling parameter schedule (λ-schedule) and separating the interaction between the compound molecules from the influence of solvent. The potential energy of pair interactions 6.1.1 in this case was decomposed as follows:

$$U_{SC} = U_S + U_C + \lambda^A_{vdW} U^{vdW}_{SC,A} + \lambda^B_{vdW} U^{vdW}_{SC,B} + \lambda_{Coul} U^{Coul}_{SC}; \tag{6.7.1}$$

here U_{SC}, U_C, U_S, U^{Coul}_{SC} are, again, the full pair interaction of the solvent-complex (solute) system, the energies of pair interaction between only the atoms belonging to either complex or solvent and Coulomb interaction energy between complex and solvent, as were defined earlier in Methods section. However the potential energy of van der Waals interaction U^{vdW}_{SC} is additionally decomposed into $U^{vdW}_{SC,A}$ and $U^{vdW}_{SC,B}$ - corresponding to the impact of phenyl side groups (subsystem A) and bis-salphen base of the complex (subsystem B). This separation allows the parts of calculations to be reused for the complexes with different functional groups.

Five independent samples were prepared for each of the selected association type and subjected to the same two stage procedure: the initial system, relaxed inside the periodic solvent box, as described in the Methods section of this chapter (section 6.1.3), was first decoupled from solvent, then dissociated in vacuum by switching off the interaction between its parts. The total free energy change during such process was averaged over those simulations, where the molecules remained associated during the first part.

The solvation free energy was estimated as the negative of the free energy change accumulated while scaling down the coupling parameter of solvent - compound interactions $\lambda = (\lambda^A_{vdW} + \lambda^B_{vdW} + \lambda_{Coul})/3$ from 1 to 0. For all simulations involving the explicit solvent molecules the list of values the coupling parameter consequently assumes (λ-schedule) consisted of 71 points in total (figure 6.30, left), where Coulomb interactions were gradually decoupled during the first 20

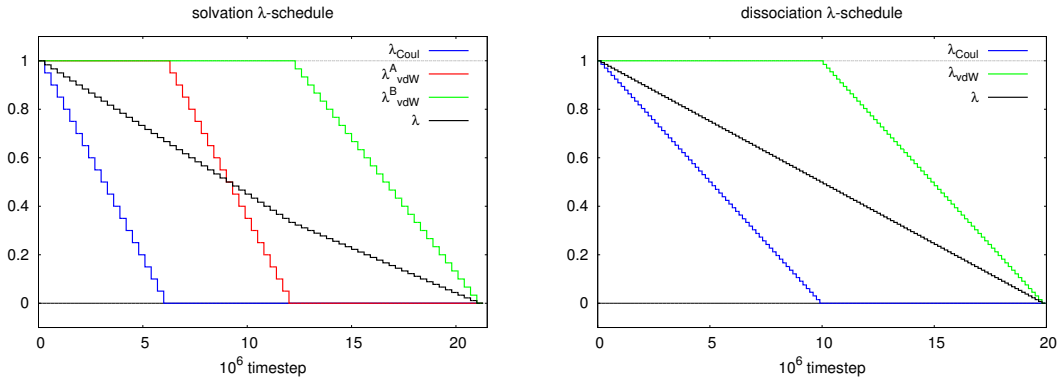

Figure 6.30: Variation of coupling parameters during solvation (left) and dissociation (right) simulations

points (λ_{Coul}), van der Waals interactions between solvent and phenyl side groups (λ^{A}_{vdW}) - during the next 20 points and between solvent and the rest of the complex (λ^{B}_{vdW}) - during the last 31 (figure 6.30, left). All interactions were scaled down linearly. At each λ-point the system behaviour was modelled during 600 ps, from which the first 400 were used for equilibration and the last 200 - for data collection, resulting in 42.6 ns long calculations. The potential energy, associated with solvent-compound interaction, was sampled every 10 iterations (20 fs). Such schedule was chosen after a number of preliminary calculations as giving the most stable results. The evolution of different components of interaction potential energy between the two halves of tetrakis-Schiff molecular association during simulation are summarised in appendix B.3.

A similar approach was used for dissociation energy in vacuum. This time, however, λ-schedule consisted of 66 points for Coulomb interaction (λ_{Coul}), followed by 67 for the van der Waals attraction (λ_{vdW}), separated from repulsion with WCA decomposition (figure 6.30, right). The combined coupling parameter, used as the reaction coordinate, in this case is $\lambda = (\lambda_{vdW} + \lambda_{Coul})/2$. Each λ-point was equal to 300 ps, from which only the last 100 were used for data collection, resulting in 39.9 ns long runs.

6.7.1 "Opening" free energy

Structures on figure 6.31 both represent a single S-shaped conformation of phenyl terminated tetrakis-Schiff complex in "closed" and "opened" states respectively. The difference of their solvation free energy (ΔG^{c}_{solv} and ΔG^{o}_{solv} correspondingly), combined with the free energy of "opening" in vacuum $\Delta G^{v}_{open} = 5.4 \pm 0.1$ kcal/mole (estimated earlier with WHAM method in 6.4.1), represent an estim-

ation of the free energy of closed-to-opened transition in solvent:

$$\Delta G^{s}_{open} = \Delta G^{o}_{solv} - \Delta G^{c}_{solv} + \Delta G^{v}_{open}; \tag{6.7.2}$$

where superscript "s" may refer to DCM, THF or TOL. ΔG^{s}_{open} serve as the indicator, which conformation is more stable in each solvent. Almost matching profiles of the PMF over the set of five simulations show good convergence of the calculations (figure 6.32). Even the "unsuccessful" runs, where the conformation changed yet in the first λ-point (shown with doted lines), follow the general trend closely. The estimated free energies of solvation are summarised in the table 6.5. Red color designates "unsuccessful" simulations. These results were excluded when calculating average.

Substituting the data from the last column of the table 6.5 into equation 6.7.2 one obtains:

- $\Delta G^{DCM}_{open} = +5.2 \pm 0.7$ kcal/mole;
- $\Delta G^{THF}_{open} = -5.6 \pm 0.7$ kcal/mole;
- $\Delta G^{TOL}_{open} = +3.7 \pm 1.7$ kcal/mole.

As expected, despite the twice increased surface, the "opened" configuration of a single tetrakis-Schiff zinc-complex is thermodynamically unstable in DCM due to strong attraction between zinc and oxygen ions of the two symmetric halves. On the contrary, the strong ability of THF's oxygen to interact with zinc cation of the complex makes the "opened" configuration more energetically favoured in this solvent. Toluene's $\pi - \pi$ interaction with aromatic rings of the compound decreases somewhat the transition barrier making the "opening" more easy in comparison with DCM, but for the molecule studied here it is still too weak to counter ionic attraction.

6.7.2 Dimerization free energy

Figure 6.33 demonstrates the thermodynamic cycle, corresponding to the calculation of the dimerization free energy in solvent: the red arrow indicates the direct transition, while the black one - the alchemical transformation route taken here. Depending on whether "opened" or "closed" conformation is more stable for a single solvated tetrakis-Schiff molecule, the dimerization free energy in solvent can be estimated as:

Figure 6.31: *S*-shaped tetrakis-Schiff complex in "closed" (left) and "opened" (right) conformations

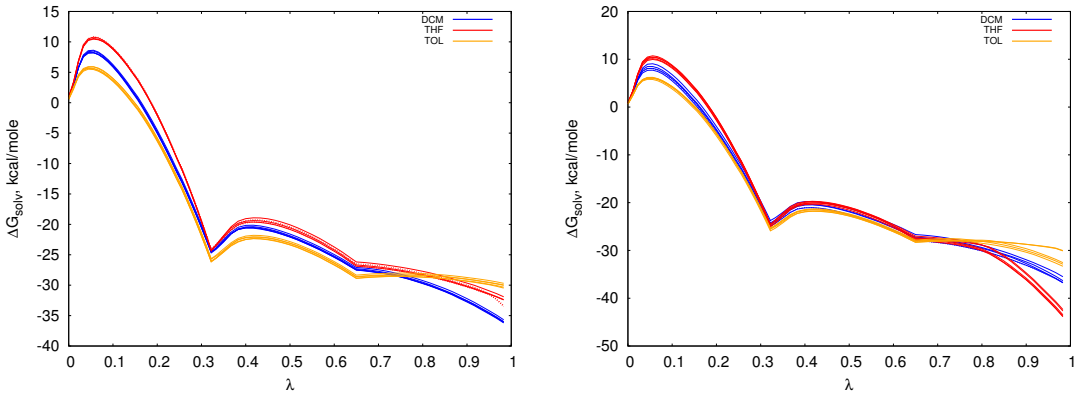

Figure 6.32: Dispersion of the calculated PMFs for "closed" (left) and "opened" (right) conformations

ΔG_{solv}, kcal/mole								
	Solvent	1	2	3	4	5	$\langle \Delta G_{solv} \rangle$	δ
Closed	DCM	-35.98	-36.11	-35.69	-36.21	-36.06	-36.01	0.20
	THF	-33.34	-32.37	-33.51	-32.42	-31.91	-32.23	0.28
	TOL	-29.96	-30.02	-30.32	-30.48	-29.70	-30.09	0.31
Opened	DCM	-36.73	-35.50	-36.78	-36.33	-36.73	-36.20	0.65
	THF	-43.47	-42.36	-43.88	-43.77	-42.67	-43.23	0.68
	TOL	-32.88	-30.10	-33.31	-32.56	-30.03	-31.78	1.59

Table 6.5: Solvation free energies of *S*-shaped tetrakis-Schiff complex in "closed" and "opened" conformations

$$\Delta G^s_{dim} = \begin{cases} \Delta G^d_{solv} + \Delta G^v_{dim} - 2 \cdot (\Delta G^v_{open} - \Delta G^c_{solv}), & if\ \Delta G^s_{open} > 0; \\ \Delta G^d_{solv} + \Delta G^v_{dim} - 2 \cdot \Delta G^o_{solv}, & if\ \Delta G^s_{open} < 0. \end{cases} \quad (6.7.3)$$

Again here superscript "s" may refer to DCM, THF or TOL. Quantity ΔG^v_{dim} - the free energy of dimerization in vacuum - is estimated as the negative of the free energy change of dimer dissociation in vacuum (ΔG^v_{diss}). Values of ΔG^s_{open}, ΔG^o_{solv} and ΔG^c_{solv} were taken from the previous calculation (section 6.7.1) and the same value of $\Delta G^v_{open} = 5.4 \pm 0.1$ kcal/mole from WHAM calculation (6.4.1) was used.

The calculated profiles of PMF during dimer solvation and dissociation in vacuum are shown on the figure 6.34. Again solvation simulations are well converged and a narrow overlapping deviation occurs for dissociation transition indicating no significant difference between dimers extracted from different solvents. Table 6.6 summarises the estimated free energy changes during the two transformations. Substituting the data from the table 6.6 into equations 6.7.3 one obtains:

- $\Delta G^{DCM}_{dim} = -8.61 \pm 1.8$ kcal/mole;
- $\Delta G^{THF}_{dim} = -9.9 \pm 1.7$ kcal/mole;
- $\Delta G^{TOL}_{dim} = -13.1 \pm 2.2$ kcal/mole.

As expected, association of single molecules in dimers, like the one presented on the figure 6.33, is thermodynamically preferred for all solvents. It is interesting that, in spite of additional "opening" transformation needed for tetrakis-Schiff molecules in DCM, the dimerization free energies in DCM and THF are quite close, as the solvent molecules associated with the "opened" complex slow down dimerization through Zn-O ionic interaction in THF. In toluene dimerization goes faster than in the other two solvents due to decreased barrier of "opening" and weak interaction with the surrounding molecules.

6.7.3 Free energy of dimer association via ionic interaction

The thermodynamic cycle, corresponding to the association of tetrakis-Schiff complexes' dimers into tetrameric chain is shown on figure 6.35. Again the red arrow shows the direct transition. while the black ones mark the route used for the calculation. The final free energy of association can be estimated as:

$$\Delta G^s_{tetr} = \Delta G^t_{solv} - 2 \cdot \Delta G^d_{solv} + \Delta G^v_{tetr}; \quad (6.7.4)$$

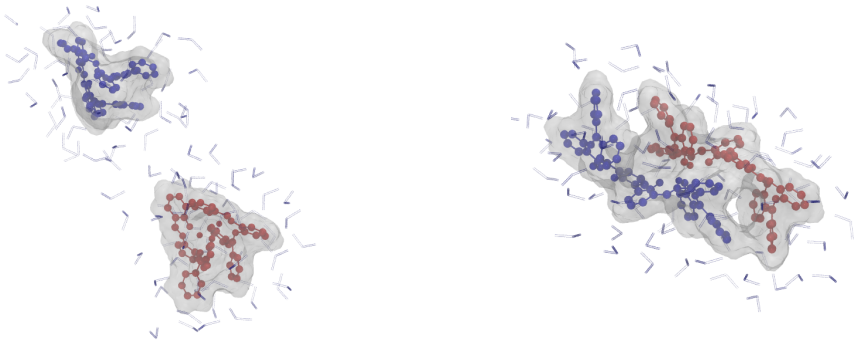

Figure 6.33: Association of tetrakis-Schiff complexes into dimer through ionic bond

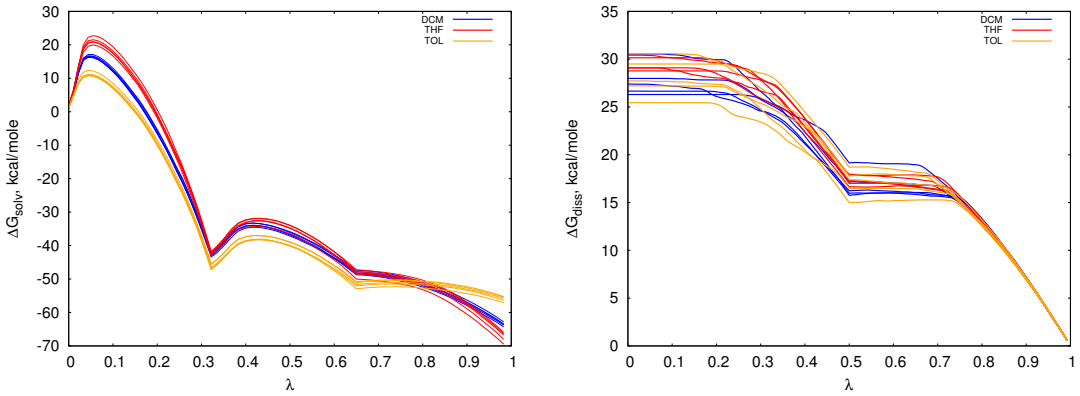

Figure 6.34: Dispersion of the calculated PMFs for solvation (left) and dissociation (right) transformations

ΔG, kcal/mole								
	Solvent	1	2	3	4	5	$\langle\Delta G\rangle$	δ
ΔG^{d}_{solv}	DCM	-64.31	-62.84	-63.52	-63.79	-63.52	-63.60	0.53
	THF	-66.36	-66.76	-69.48	-66.00	-67.99	-67.32	1.42
	TOL	-55.78	-55.22	-55.40	-57.10	-56.35	-55.97	0.77
ΔG^{v}_{dim}	DCM	-30.54	-26.31	-27.4	-26.66	-27.99	-27.78	1.68
	THF	-29.1	-30.15	-29.08	-28.77	-30.41	-29.50	0.73
	TOL	-27.2	-30.59	-27.73	-29.5	-25.45	-28.09	2.01

Table 6.6: Solvation free energies of tetrakis-Schiff complexes' dimers (ΔG^{d}_{solv}) and their dimerization free energies in vacuum (ΔG^{v}_{dim})

Here ΔG^{s}_{tetr} and ΔG^{v}_{tetr} represent the free energies of tetramer association in solvent and in vacuum correspondingly. As previously, the former is estimated as the negative of dissociation free energy of tetramer into two free dimers in vacuum. ΔG^{t}_{solv} - is the free energy of tetramer solvation, estimated here. Values of ΔG^{d}_{solv} for the three solvents were defined in the previous section.

The calculated profiles of PMF during tetramer solvation and dissociation in vacuum are shown on the figure 6.36. As previously, the solvation simulations are well converged, although a wide spread was found for tetramer dissociation in DCM. Table 6.7 summarises the estimated free energy changes during the two transformations. Substituting the data from the table 6.7 into equations 6.7.4 one obtains:

- $\Delta G^{DCM}_{dim} = -18.0 \pm 4.0$ kcal/mole;
- $\Delta G^{THF}_{dim} = -5.4 \pm 2.6$ kcal/mole;
- $\Delta G^{TOL}_{dim} = -14.7 \pm 1.8$ kcal/mole.

As expected, while dimer association via ionic bonding of the free metal centers of the two dimers is strongly thermodynamically favourable in DCM and toluene, in THF free energy gain from such association is quite small. This should be attributed to the solvent molecules associated with the free zinc centers (that do not participate in dimer bonding): the attraction of zinc cation to the oxygen of THF needs to be overcome before tetramer association can take place. This slows down the association process significantly and prevents the formation of long polymer-like chains with relatively strong ionic bonds that serve the basis for the proposed mechanism of "rings-and-rods" networks formation.

In DCM the free energy gain is the highest, so the association of dimers must go more rapidly yet before the solvent starts to evaporate. Relatively large error in this case is explained by higher flexibility of the compound molecules in this solvent, which can also be seen in the large deviation of association free energies in vacuum, much higher then for the other two solvents, while the solvation free energies in all calculations are quite close for the same solvent.

The average association free energy in toluene is somewhat smaller than that in DCM, although still within the confidence interval. The deviation of free energy changes during both transformations is the smallest in this case out of all solvents. This indicates that the association of the tetrakis-Schiff molecules in toluene behaves more rigidly, than in the DCM or THF, which can be the effect of higher viscosity of toluene or the $\pi - \pi$ interactions of aromatic rings in salphen bases and phenyl groups with surrounding solvent molecules, stabilizing a straight shape of tetramer.

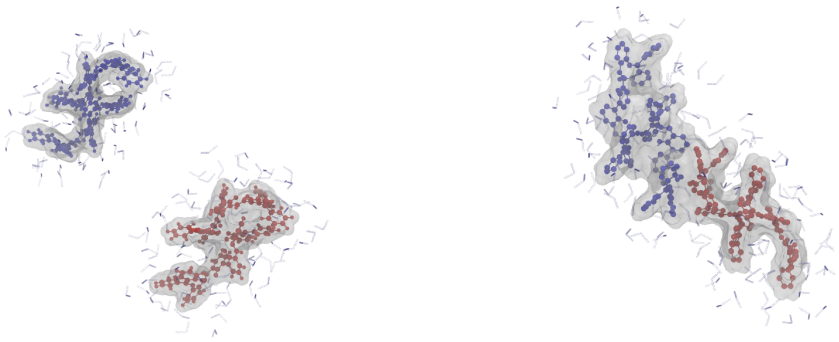

Figure 6.35: Association of tetrakis-Schiff complexes' dimers through ionic bond

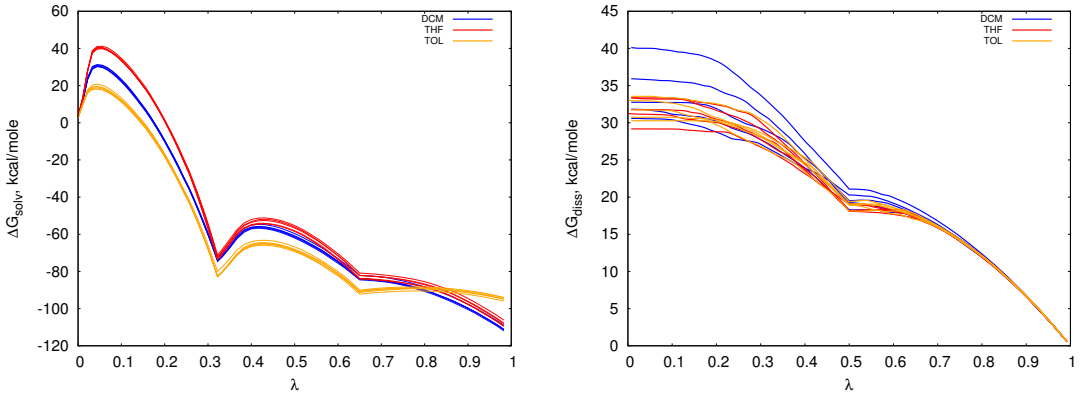

Figure 6.36: Dispersion of the calculated PMFs for solvation (left) and dissociation (right) transformations of tetrakis-Schiff complexes' tetramers, bonded through ionic interaction

ΔG, kcal/mole								
	Solvent	1	2	3	4	5	$\langle\Delta G\rangle$	δ
ΔG^t_{solv}	DCM	-111.92	-108.98	-111.32	-111.12	-111.26	-110.92	1.13
	THF	-106.20	-109.53	-109.38	-107.82	-108.09	-108.20	1.35
	TOL	-94.04	-94.78	-94.99	-95.92	-94.15	-94.78	0.76
ΔG^v_{tetr}	DCM	-35.92	-40.12	-32.76	-31.82	-30.59	-34.24	3.83
	THF	-33.34	-31.76	-33.37	-31.23	-29.18	-31.78	1.73
	TOL	-30.27	-30.74	-33.03	-33.55	-31.74	-31.87	1.42

Table 6.7: Solvation free energies of tetrakis-Schiff complexes' tetramers, bonded through ionic interaction (ΔG^t_{solv}) and their association free energies in vacuum (ΔG^v_{tetr})

6.7.4 Free energy of dimer association via $\pi-\pi$ interaction

The two types of structures, corresponding to the association of tetrakis-Schiff complexes' dimers into tetramer via $\pi - \pi$ interaction between are shown on figure 6.37. The same thermodynamic cycle as in the section 6.7.3 was used here, with the only difference in the tetramer arrangement. The final free energy of association can be estimated with the same equation 6.7.4 as for ionic bond.

From the results, presented in the table 6.8 it becomes clear that bonding via $\pi - \pi$ interactions is quite weak and association of two dimer turns out to be a too small system for stable bonding. In all simulations of "pincer" type, the initial structure lost initial configuration and either fell in two parts or rearranged into another structure up to tetramer chain with ionic bonding like those studied in the previous section. For this reason, no reliable data could be obtained on the free energy change during such transformation. "Sandwich" like arrangement proved to be a bit more stable, providing several samples where the initial relative positions of the two associated dimers was maintained throughout all the length of the simulation.

Unlike the three previous cases, the calculated PMF profiles, presented on the figure 6.38, are grouped into several stratified bands, indicating poor stability of this type of arrangement. The few "successful" runs, where the desired configuration of associated molecules was preserved, are shown with solid lines, while for simulations, where initial configuration rearranged, PMF is shown with dotted lines. As no stable configurations were observed for "pincer" arrangement, therefore only PMFs for "sandwich" arrangements were plotted.

Substituting the free energy changes for such successful samples from the table 6.7 into equations 6.7.4 one obtains:

- $\Delta G_{dim}^{DCM} = -9.8$ kcal/mole;
- $\Delta G_{dim}^{THF} = -7.2 \pm 1.8$ kcal/mole;
- $\Delta G_{dim}^{TOL} = -7.9 \pm 2.4$ kcal/mole.

It is interesting that, although only one sample finished successfully for DCM, it is also the one with the highest free energy of dissociation in vacuum thanks to the three phenyl rings remaining in contact (out of initial four). For the other two solvents only the "internal" pair of rings remained in contact. Toluene is the only solvent in which the success ratio (fraction of successful simulations) $> 50\%$ in this computer experiment. Even in the two simulations excluded from the averaging tetramer lost integrity only temporary, thus the values of ΔG for these trajectories are quite close to the average. Yet all the estimated association free energies are quite close. Maintaining the associated form in toluene despite

losing the contact between half of phenyl groups may simply be the result of week interaction between solvent and the compound molecule, and thus poor ability of toluene to dissolve such system, as was suggested by our co-authors in [**?**].

One can assume from the results of this section that the free energy of $\pi - \pi$ bonding due to phenyl side-groups is of the order of $\sim 8 - 10$ kcal/mole per dimer pair. This is approximately half of the ionic bonding free energy, for which all the simulations completed successfully. Thus the expected impact of the $\pi - \pi$ interaction with solvent might yet be found for a larger system, such as tetramer-tetramer association.

6.8 Conclusion and future directions

In this chapter an attempt was made to take a closer look at the behaviour of zinc-substituted tetrakis-Schiff complex molecules with the help of modern computer simulation of molecular systems. The results, summarized here, support the hypothesis that the experimentally observed emergence of the "rings-and-rods" networks can indeed be attributed to the self-assembling properties of the compound molecules without the need of "coffee-ring" or "pin-whole opening" effects, usually observed in evaporating solvents.

It was shown with the help of molecular dynamic calculations that the symmetric zinc-complexes, studied here, can assume a number of conformations and form a variety of supra-molecular structures due to the two equally important non-bonding interaction types: electrostatic attraction between zinc and oxygen ions and $\pi - \pi$ and cation-π attraction due to the aromatic rings of salphen-type ligand bases and phenyl side groups.

It was also shown both with quantum chemical calculations and molecular dynamic simulations that the role of the solvent is not restricted simply to mediating the strength of long-range Coulomb interaction and the diffusion speed of the solute molecules. Such assumption would lead to an incorrect result that the stable ring-like structures are more easily formed in toluene, than in DCM or THF. The solvent molecules interact actively with the compound molecules affecting the conformation the solute molecule assumes in this solvent. "Closed" form is the most thermodynamically stable for the tetrakis-Schiff zinc-complex in DCM. Such conformation has a higher diffusion rate and a total dipole moment, due to which standalone molecules, spread apart, can interact and join faster than in the other solvents. On the contrary, in THF "opened" conformation is more stable due to attraction between zinc cation and negatively charged oxy-

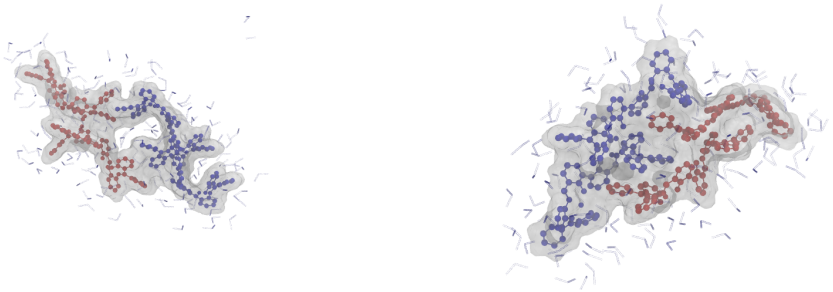

Figure 6.37: The types of tetramer association through $\pi - \pi$ bond: "pincer" (left) and "sandwich" (right)

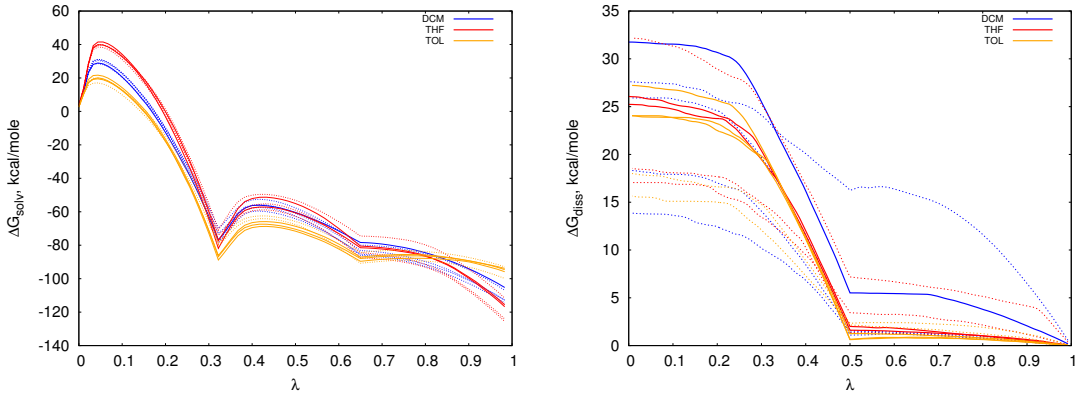

Figure 6.38: Dispersion of the calculated PMFs for solvation (left) and dissociation (right) transformations of tetrakis-Schiff complexes' tetramers, bonded through $\pi - \pi$ interaction in "sandwich" like arrangement

ΔG, kcal/mole								
	Solvent	1	2	3	4	5	$\langle \Delta G \rangle$	δ
ΔG^{pin}_{solv}	DCM	-109.74	-111.18	-107.78	-103.01	-105.09	-	-
	THF	-65.62	-111.99	-118.72	-123.58	-114.15	-	-
	TOL	-46.36	-92.01	-98.15	-106.23	-96.83	-	-
ΔG^{sand}_{tetr}	DCM	-105.25	-112.71	-114.57	-112.91	-106.94	-105.25	-
	THF	-116.76	-115.59	-124.08	-125.56	-111.59	-116.18	0.83
	TOL	-92.91	-94.59	-93.84	-95.83	-99.85	-94.76	1.00
ΔG^{v}_{sand}	DCM	-31.75	-27.61	-18.32	-25.91	-13.86	-31.75	-
	THF	-25.23	-26.06	-32.17	-17.06	-18.54	-25.65	0.59
	TOL	-18.00	-27.22	-24.05	-24.06	-15.65	-25.11	1.83

Table 6.8: Solvation free energies of tetrakis-Schiff complexes' tetramers, bonded through $\pi - \pi$ interaction in "pincer" (ΔG^{pin}_{solv}) and "sandwich" (ΔG^{sand}_{solv}) and the association free energies in vacuum for the later (ΔG^{v}_{sand})

gen of the solvent molecules, resulting in the formation of stable associates. In toluene, again. the "closed" conformation of the tetrakis-Schiff zinc-complex is more stable, than the "opened", however due to weak interaction with the solvent the difference between the two conformations is smaller than in DCM and the compound molecule may reside in the "opened" form for a quite a long time.

Based on these findings a mechanism of "rings-and-rods" networks formation was suggested in this chapter that allows to explain all the experimental observations available so far. Within the suggested model, zinc-complex dimers, connected via strong Zn-O ionic bond between one metal center from each side, are the primary building blocks of the higher level supra-molecular arrangements. To form extended structures the dimers continue to aggregate via ionic interaction between the free cation centers into long polymer-like chains. As the length of the chain increases the free energy gain from association of several chains via $\pi - \pi$ interaction between the stretched aside phenyl groups and aromatic rings of the salphen base of the ligand becomes large enough so the chains keep growing through attaching other chains via side-to-side contacts. Thus a system of long flexible strings is formed that can behave similarly to the semi-flexible polymers, such as DNA, for which the formation of donut-like structures and even multiple connected rings is known as "coil to toroidal globule transition". The key difference of the molecules studied here is that all connections are achieved through non-bonding interactions, so multiple coils keep connecting to each other forming a network of interconnected rings, spanning over hundreds of microns.

The suggested picture was supported by the calculations of free energy changes, corresponding to the described transitions: dimerization of single molecules and subsequent dimer association via ionic and $\pi - \pi$ interaction - in all the three solvents, used in experiments. These findings support that in DCM association of tetrakis-Schiff zinc-complexes into multi-molecular chains bonded through ionic interaction is thermodynamically stable. In THF this mechanism appears to be blocked due to aforementioned association of solvent molecules with zinc-complex through the same Zn-O ionic interaction. This decreases the free energy gain of dimer-dimer association to ~ 5 kcal/mole, compared to ~ 18 for DCM, resulting in a slower association of chains and large probability of coil to rod-like globule transition, as breaking of ionically bonded chain in THF is easier and may be compensated by the gain in $\pi - \pi$ interaction. The calculations for $\pi - \pi$ bonded associates resulted in approximately similar binding free energies in the three solvents. However the four-molecular systems modelled so far appeared to be too small for $\pi - \pi$ interaction to become significant, and its impact may

yet be seen in further simulations. Slow diffusion and poor ability of toluene to dissolve the initial aggregates of tetrakis-Schiff zinc-complexes so far remain the most probable explanation for the emergence of nanocrystals observed in toluene.

Chapter 7

Conclusion

7.1 Results summary

During the studies, reported in this thesis, three different approaches were applied to investigate the potential to improve the stability of electric properties of the CNT-polymer composites. The special focus of this work was to investigate the potential of the novel metal-organic compounds to assemble into "rings-and-rods" like networks and to serve the guiding agents for CNTs in highly transparent and conductive films and advanced composite materials. The key findings of this work are summarized here.

7.1.1 Statistical modelling of CNT reinforced composites

On the first place, the effect of CNT agglomerates on the polymer composites' electrical conductivity (DC) was studied in close collaboration with experimental researchers. The aim of this work was to model the agglomerated CNT distribution on the length scale of the order of hundreds of microns, on which collections of agglomerates are routinely observed by optical microscopic techniques. This goal was achieved by combining the popular Monte Carlo simulation technique, extensively applied in the literature to study such composites on a smaller scale and with uniform distribution, with von Neumann rejection-acceptance sampling method to model the predefined agglomerated distribution of CNTs. The algorithm was implemented with the help of NVIDIA CUDA GPGPU technology to benefit from the recent advances in the field of high performance computing. This software tool allowed to generate $\sim 10^6$ sphero-cylindrical models of CNTs with non-uniform distribution within ~ 1 hour time, sufficient to model resistivity of CNT network inside cubic volume with the side in $\sim 100\,\mu$m scale range

with filler content up to several vol. %.

Using such implementation of the method, statistical simulations were conducted to model electric conductivity of the three groups of samples with different probability distribution of CNTs. The first group had the perfect uniform distribution, while for the other two the distribution densities were derived from the agglomerates' distribution observed experimentally by our collaborators in the CNT-PC composite parts, prepared by injection moulding. The calculated relative differences in the samples' conductivities were compared to the experimental measurements. Although, as was expected from the previous works, the samples with agglomerated distribution of CNTs indeed had a slightly better average conductivity than the uniform distribution, however order of magnitude deviations, observed in experiments even for the parts with similar agglomerates' distribution, was not found in simulations. Subsequent simulations of the same agglomerated samples, but with non-uniform directional angles distribution, have shown that, depending on the degree of alignment, the conductivity difference can grow significantly.

It follows from these observations that on the current level of industrial processing, the agglomerates sizes can be reduced to the limit, where their impact on composite's conductivity is small compared to the influence of CNT alignment. The latter factor, in combination with CNT flexibility dominates large variations in experimental resistivity, so the future studies must focus on better control over CNTs alignment and shape in polymer matrix. The influence of agglomeration must be studied as a factor complementary to them and not as sole effect as it only becomes significant for large agglomerates.

Additionally, a molecular dynamics study of a sine-like and helical curved CNT inserted into PC matrix was conducted. The aim of this study was to investigate the effect of the filler waviness on the composite's elastic properties. The simulations have shown that as the amplitude of CNT profile deviation from straining axis increases, the sample's Young's modulus decreases hyperbolically. This trend was also confirmed in a parallel finite element study of the same systems by our co-workers. Combined with the rise of CNT curvature, expected for composites with high CNT loadings, this result indicates that the higher the CNT content in composite is, the smaller the added value of superfluous CNTs becomes both for electrical and mechanical properties, which results in suboptimal cost-property ratio for such composites.

7.1.2 Percolation studied of "rings-and-rods" networks

Percolation characteristics of "rings-and-rods" like networks was studied with a simple Monte Carlo model, based on the experimentally available statistics of rings' diameter distribution and rings density for pristine networks as well as for networks intercalated with CNTs [#NatComm]. On a flat surface in all cases connected model networks were obtained in simulations in the same density range as in experiments. A clear percolation transition was observed in all cases with rapid growth of simulated samples' resistance as networks density approached percolation threshold, defined as the point, where the probability to observe connected network decreased to 50%.

It was shown that the differences between the networks simulated with the diameter distribution of pristine and CNT-intercalated networks at the same density can be easily explained if network's morphology is characterized in terms of scaling factor η that can be interpreted as the ratio of average distance between rings' centers to average ring's diameter. In terms of such parameter pristine networks, observed in the experiment in the range 20-80μm^2 per ring, reside in the region close to percolation transition that in simulations occurs at $\sim 56-70$ μm^2 per ring ($\eta \sim 4-4.5$). It was also shown that average number of connections ≥ 2.4 is required to form extended connected network on a flat surface. This also is in a good agreement with experimental observation that interconnected networks had $\sim 2.8 \pm 0.7$ rods per ring.

In contrast, CNT-intercalated networks within the same density range in terms of scaling factor fall in the range of small η values, very close to the percolation of circles in 2D ($\eta_R \sim 1.22$). This explains why in experiment resolvable network was only observed at density ~ 75.56 μm² per ring ($\eta \sim 1.8$). Applying the same procedure as for pristine case to CNT-intercalated networks, their percolation transition should occur at $\sim 1.0-1.2\,10^3\mu$m^2 per ring, corresponding to CNT density ~ 0.06 surf.%. In comparison, theoretical estimation for percolation of random sticks with the same length is 8.8 surf.%.

Even more striking effect is achieved in a model bulk composite. Unfortunately, no statistical data are available on the parameters of networks of tetrakis-Schiff complexes formed in polymer matrix. However, if the same trend is applied here, even sparser networks could be obtained in experiment: the CNT content required to fill such network can be as low as $10^{-4}-10^{-5}$ vol. % - orders of magnitude smaller then for randomly distributed nanotubes of the same aspect ratio.

This is, of course, a very vague assumption and better understanding of the

mechanism behind tetrakis-Schiff self-assembly is needed before reliable calculations can be performed. However this estimation shows how significant the impact of self-assembling guiding agents, such as the one studied here, can be.

7.1.3 MD study of tetrakis-Schiff zinc-complex self-assembly

To improve the understanding of tetrakis-Schiff behaviour in different environments and uncover the mechanism of their self-assembly in "rings-and-rods" networks extensive studies with molecular dynamics were conducted both in model vacuum environment as well as in the three solvents, compared in experiment [2]: DCM, THF and toluene.

On the first step it was shown using a crude "four rigid parts" model that such molecules can indeed form donut-like associations, which stay stable over simulation time due to anisotropy of interaction between such molecules.

Using a more detailed all-atom GAFF simulations it was shown that, standalone or solvated, tetrakis-Schiff zinc-complex has a number of conformations apart from the one, obtained in [2] from X-ray experiments for unsubstituted ligand. Furthermore, it was shown that the three solvents, used in experiment, interact differently with the zinc-complex, provoking different configurations for a single solvated molecule. In DCM single molecule adopts "closed" configuration with ionic centers of the two symmetric halves bonded to each other with electrostatic attraction. In THF, on the contrary, "opened" configuration is more preferred due to electrostatic attraction between zinc cation and oxygen atom of THF molecule. Toluene showed no preference and was interacting with the complex via weaker $\pi - \pi$ and cation-π interactions. Furthermore basing on the dimer binding energies for tetrakis-Schiff molecules in a different mutual position a number of chain-like structures were proposed. Their behaviour in explicit solvents was observed during 1-2 ns.

Basing on these observations and on the review of previous publications for similar compounds and other ring-like structures, the following mechanism was proposed for the formation of "rings-and-rods" like networks of tetrakis-Schiff zinc-complexes was suggested. Single solvated molecules form chain-like associations, bonded via strong electrostatic interaction between Zn and O atoms of different monomers. This association most likely starts with the formation of dimers, bonded via Zn-O interaction of one half of each monomer, leaving the other capable to associate with other dimers. As the chains grow in length, they begin to associate with other chains via $\pi - \pi$ interaction between the side groups, the strength of which is proportional to the chain length. Thus semi-

flexible strings are formed in solvent that are capable to fold ring-like structures via the "coil - toroidal globule" transition, known for semi-flexible polymers. One important difference of tetrakis-Schiff complexes form the polymeric systems is that all interactions involved are not covalent. Therefore, the coils can bind to each other and, thus, an interconnected "rings-and-rods" network can be formed. This would explain the formation of extended networks, not observed previously, as well as the necessity of the phenyl side groups, observed in experiment: methyl functionalized complexes would not be unable to associate monomolecular chains into thicker strings by $\pi - \pi$ interaction.

This process occurs seamlessly in DCM. Almost two times difference in the diffusion speed for tetrakis-Schiff compounds in DCM in comparison with THF and toluene may also help to explain, why the structures self-assembled in DCM exceed in size those, formed in THF and toluene, so strongly. Apart from diffusion rate, in THF the growth of the chains is slowed down significantly by the aforementioned interaction between zinc cations and oxygens of THF molecules. Therefore only short strings could be obtained in THF, in agreement with experiment. In toluene this effect also takes place via cation-π interaction between zinc ion and aromatic ring of toluene molecule, however, its influence is much smaller then in THF. What is, probably, more important, is that toluene in general interacts with tetrakis-Schiff compounds weaker than DCM and THF, so zinc-organic complexes should tend to aggregate in it rather than to spread. Together with slower diffusion this leads to formation of bunches of needle-like crystals.

The suggested mechanism was supported with the calculation of free energies of association in the three solvents. In all solvents the formation of dimer of the selected type was found thermodynamically favourable. However, the association of dimers into tetramers via ionic bond, preferred in DCM and toluene (although a somewhat weaker), was found least preferable in THF: average association free energy in the later 5.4 kcal/mole in comparison with 14.7 in toluene and 18.0 in DCM. Thus chain growth should go much slower in THF. Similar calculations for free energies of association via $\pi - \pi$ interaction, unfortunately, were less stable: half of the $\pi - \pi$ bonded tetramers dissociated prematurely so the binding free energy could be estimated only by a few successful runs. This happened, obviously, because $\pi - \pi$ bonding of such chain is proportional to the length of the chain and a pair of dimers turned out to be a too small system to bind stably. Free energy of association of such tetramers was estimated to be around 7-10 kcal/mole, i.e. twice weaker than that of ionically bonded chains in DCM, so simulations of a larger systems may help to get more reliable estimate. It

must be noted, however, that, unlike DCM and THF, most tetramers remained associated via $\pi - \pi$ bonding in toluene and in 3 out of 5 runs even the initial structure was partially preserved. This might indicate that, indeed, toluene is poor solvent for tetrakis-Schiff compounds and the complex molecules tend to aggregate in it. Although further studies are needed to confirm this.

7.2 Future directions

Basing on the findings of the reported work the following directions can be outlined for the future work:

- To reach the current level of composite processing, Monte Carlo stimulation algorithm should be adopted to combine the effects of alignment and waviness of CNTs along the agglomeration;
- Association of single ionically bonded chains of tetrakis-Schiff metal-organic complexes into thicker rods via van der Waals and $\pi - \pi$ interactions should be studied on a larger length scale to check for potential effect of solvent on the stability of such associate;
- A coarse-grained, ideally multilevel, model must be fitted to all-atom molecular dynamics simulation data to extend the studies of such associates on the micrometer length scale to observe the coil-to-globule transition and the formation of interconnected networks;
- The backbone, functional groups and cation type of tetrakis-Schiff metal-organic complexes should be varied to investigate the effect on the micrometer scale chain dynamics and therefore to be able to control the morphology of "rings-and-rods" networks via molecular engineering;
- The interaction of tetrakis-Schiff metal-organic complexes with CNTs should be studied to understand the effect of CNTs on the "rings-and-rods" networks' morphology as well as the effect of metal-organic complexes on CNT's electrical properties, such as internal conductivity and work function.

7.3 Publications

The results obtained in this work were published in the following peer-reviewed publications:

1. Matveeva, A. Y., **Pyrlin, S. V.**, Ramos, M. M. D., Böhm, H. J., & van Hattum, F. W. J. (2014). Influence of waviness and curliness of fibres on

mechanical properties of composites. *Computational Materials Science*, 87, 1–11. http://doi.org/ 10.1016/j.commatsci.2014.01.061;

2. Escárcega-Bobadilla, M.V, Zelada-Guillén, G.A, **Pyrlin, S.V**, Wegrzyn, M., Ramos, M.M.D., Giménez, E., Kleij, A.W. (2013). Nanorings and rods interconnected by self-assembly mimicking an artificial network of neurons. *Nature Communications*, 4(May), 2648. http://doi.org/10.1038/ncomms3648.

They were also presented on the following international conferences:

1. Matveeva A.Y., van Hattum F.W.J., **Pyrlin S.V**. (2012). Orientation and dispersion influences on elastic properties of CNT/CNF polymer nanocomposites. Proceedings of SAMPE Tech 2012 Conference and Exhibition, North Charleston, USA (co-author);
2. **Pyrlin S.V.**, Ramos M.M.D., Anna Matveeva A.Y., van Hattum F.W.J. (2012) GPGPU-assisted polymer nanocomposite modelling and characterisation. E-MRS Spring Meeting, Strasbourg, France (poster);
3. **Pyrlin S.V.**, Ramos M.M.D., Haynes P.D., Hine N. (2012) The effect of carbon nanotube tip functionalization on electronic tunneling. E-MRS Spring Meeting, Strasbourg, France (oral);
4. Matveeva A.Y., Tiusanen J.M., **Pyrlin S.V.**, van Hattum F.W.J. (2013). Investigation of the mechanical properties of injection moulded CNT reinforced thermoplastic polymer parts. Proceedings of SAMPE 2013 Conference and Exhibition, Long Beach, USA (co-author);
5. **Pyrlin S.V.**, & Ramos M.M.D. (2013). Multiscale modelling of electron transport in carbon nanotube reinforced composites. In International Conference on Computational Modelling of Nanostructured Materials, Frankfurt-am-Main, Germany (poster);
6. **Pyrlin S.V.,** Ramos, M.M.D. (2013) The influence of polymer matrix-nanotube interaction on the composites' electrical properties: from atomistic calculations to Monte Carlo Simulation. NANOSMAT, Granada, Spain (poster);
7. **Pyrlin S.V.,** Ramos, M.M.D. (2013) Multiscale modeling of composite structure-property relations: application to electron transport in carbon nanotube reinforced polymer nanocomposites. EUROMAT, Sevilla, Spain (oral);
8. **Pyrlin S.V.,** Ramos, M.M.D. (2014) Multiscale modeling of composite structure-property relations: application to electron transport in carbon nanotube reinforced polymer nanocomposites. Nano Portugal, Porto, Portugal (oral);

9. **Pyrlin S.V.**, Hine N., Ramos, M.M.D., Escárcega-Bobadilla M., Zelada-Guillén G. (2014) Interaction of tetrakis-Schiff base compounds with carbon nanostructures from DFT: implications for charge transfer. Condensed matter in Paris, Paris, France (oral).

Bibliography

[1] A. Y. Matveeva, J. M. Tiusanen, S. V. Pyrlin, and F. W. J. Van Hattum, "Investigation of the mechanical properties of injection moulded CNT reinforced thermoplastic polymer parts," in *International SAMPE Technical Conference*, 2013, pp. 1714–1725. [Online]. Available: http://www.scopus.com/inward/record.url?eid=2-s2.0-84881164663{\&}partnerID=tZOtx3y1

[2] M. V. Escárcega-Bobadilla, G. a. Zelada-Guillén, S. V. Pyrlin, M. Wegrzyn *et al.*, "Nanorings and rods interconnected by self-assembly mimicking an artificial network of neurons." *Nature communications*, vol. 4, no. May, p. 2648, jan 2013. [Online]. Available: http://www.ncbi.nlm.nih.gov/pubmed/24177669

[3] M. Monthioux and V. L. Kuznetsov, "Who should be given the credit for the discovery of carbon nanotubes?" *Carbon*, vol. 44, no. 9, pp. 1621–1623, 2006.

[4] S. Iijima, "Helical microtubules of graphitic carbon," *Nature*, vol. 354, no. 6348, pp. 56–58, nov 1991. [Online]. Available: http://dx.doi.org/10.1038/354056a0

[5] S. Iijima, P. Ajayan, and T. Ichihashi, "Growth model for carbon nanotubes." *Physical review letters*, vol. 69, no. 21, pp. 3100–3103, nov 1992. [Online]. Available: http://journals.aps.org/prl/abstract/10.1103/PhysRevLett.69.3100

[6] S. Iijima and T. Ichihashi, "Single-shell carbon nanotubes of 1-nm diameter," *Nature*, vol. 363, no. 6430, pp. 603–605, jun 1993. [Online]. Available: http://dx.doi.org/10.1038/363603a0

[7] D. S. Bethune, C. H. Klang, M. S. de Vries, G. Gorman *et al.*, "Cobalt-catalysed growth of carbon nanotubes with single-atomic-layer walls," *Nature*, vol. 363, no. 6430, pp. 605–607, jun 1993. [Online]. Available: http://dx.doi.org/10.1038/363605a0

[8] S. Iijima, C. Brabec, A. Maiti, and J. Bernholc, "Structural flexibility of carbon nanotubes," *The Journal of Chemical Physics*, vol. 104, no. 5, p. 2089, feb 1996. [Online]. Available: http://scitation.aip.org/content/aip/journal/jcp/104/5/10.1063/1.470966

[9] P. M. Ajayan, T. W. Ebbesen, T. Ichihashi, S. Iijima *et al.*, "Opening carbon nanotubes with oxygen and implications for filling," *Nature*, vol. 362, no. 6420, pp. 522–525, apr 1993. [Online]. Available: http://dx.doi.org/10.1038/362522a0

[10] J. W. G. Wilder, L. C. Venema, A. G. Rinzler, R. E. Smalley *et al.*, "Electronic structure of atomically resolved carbon nanotubes," vol. 391, no. 6662, pp. 59–62, jan 1998. [Online]. Available: http://dx.doi.org/10.1038/34139

[11] M. S. Dresselhaus, G. Dresselhaus, and P. Avouris, *Carbon Nanotubes: Synthesis, Structure, Properties and Applications*, ser. Topics in Applied Physics. Springer, 2001, vol. 81. [Online]. Available: http://books.google.co.uk/books?id=dkvDhZJnafgC

[12] J. Nygard, D. Cobden, M. Bockrath, P. McEuen *et al.*, "Electrical transport measurements on single-walled carbon nanotubes," *Applied Physics A: Materials Science & Processing*, vol. 69, no. 3, pp. 297–304, sep 1999. [Online]. Available: http://link.springer.com/10.1007/s003390051004

[13] C. Zhou, J. Kong, and H. Dai, "Electrical measurements of individual semiconducting single-walled carbon nanotubes of various diameters," *Applied Physics Letters*, vol. 76, no. 12, p. 1597, mar 2000. [Online]. Available: http://scitation.aip.org/content/aip/journal/apl/76/12/10.1063/1.126107

[14] S. J. Tans, A. R. M. Verschueren, and C. Dekker, "Room-temperature transistor based on a single carbon nanotube," vol. 393, no. 6680, pp. 49–52, may 1998. [Online]. Available: http://dx.doi.org/10.1038/29954

[15] R. Martel, T. Schmidt, H. R. Shea, T. Hertel *et al.*, "Single- and multi-wall carbon nanotube field-effect transistors," *Applied Physics Letters*, vol. 73, no. 17, p. 2447, oct 1998. [Online]. Available: http://scitation.aip.org/content/aip/journal/apl/73/17/10.1063/1.122477

[16] K. Liu, M. Burghard, S. Roth, and P. Bernier, "Conductance spikes in single-walled carbon nanotube field-effect transistor," *Applied Physics*

Letters, vol. 75, no. 16, p. 2494, oct 1999. [Online]. Available: http://scitation.aip.org/content/aip/journal/apl/75/16/10.1063/1.125059

[17] H. Shea, R. Martel, T. Hertel, T. Schmidt *et al.*, "Manipulation of carbon nanotubes and properties of nanotube field-effect transistors and rings," *Microelectronic Engineering*, vol. 46, no. 1-4, pp. 101–104, may 1999. [Online]. Available: http://www.sciencedirect.com/science/article/pii/S0167931799000258

[18] J. Hu, M. Ouyang, P. Yang, and C. M. Lieber, "Controlled growth and electrical properties of heterojunctions of carbon nanotubes and silicon nanowires," vol. 399, no. 6731, pp. 48–51, may 1999. [Online]. Available: http://dx.doi.org/10.1038/19941

[19] C. Dekker, Z. Yao, H. W. C. Postma, and L. Balents, "Carbon nanotube intramolecular junctions," *Nature*, vol. 402, no. 6759, pp. 273–276, nov 1999. [Online]. Available: http://stacks.iop.org/0957-4484/18/i=39/a=395205?key=crossref.3821c254d4c837cf99ca03f1478f0545http://www.nature.com/doifinder/10.1038/46241

[20] A. A. Farajian, K. Esfarjani, and Y. Kawazoe, "Nonlinear Coherent Transport Through Doped Nanotube Junctions," *Physical Review Letters*, vol. 82, no. 25, pp. 5084–5087, jun 1999. [Online]. Available: http://journals.aps.org/prl/abstract/10.1103/PhysRevLett.82.5084

[21] S. Heinze, J. Tersoff, R. Martel, V. Derycke *et al.*, "Carbon nanotubes as schottky barrier transistors." *Physical review letters*, vol. 89, no. 10, p. 106801, sep 2002. [Online]. Available: http://journals.aps.org/prl/abstract/10.1103/PhysRevLett.89.106801

[22] M. Fuhrer, A. K. Lim, L. Shih, U. Varadarajan *et al.*, "Transport through crossed nanotubes," *Physica E: Low-dimensional Systems and Nanostructures*, vol. 6, no. 1-4, pp. 868–871, feb 2000. [Online]. Available: http://www.sciencedirect.com/science/article/pii/S1386947799002283

[23] P. N. Nirmalraj, P. E. Lyons, S. De, J. N. Coleman *et al.*, "Electrical Connectivity in Single-Walled Carbon Nanotube Networks," *Nano Letters*, vol. 9, pp. 3890–3895, 2009. [Online]. Available: <GotoISI>://000271566400039$\backslash$nhttp://pubs.acs.org/doi/pdfplus/10.1021/nl9020914

[24] S. Paulson, "Tunable Resistance of a Carbon Nanotube-Graphite Interface," *Science*, vol. 290, no. 5497, pp. 1742–1744, dec 2000. [Online]. Available: http://science.sciencemag.org/content/290/5497/1742.abstract

[25] A. Buldum and J. P. Lu, "Contact resistance between carbon nanotubes," *Physical Review B*, vol. 63, no. 16, p. 161403, apr 2001. [Online]. Available: http://journals.aps.org/prb/abstract/10.1103/PhysRevB.63.161403

[26] J. W. Do, D. Estrada, X. Xie, N. N. Chang *et al.*, "Nanosoldering carbon nanotube junctions by local chemical vapor deposition for improved device performance," *Nano Letters*, vol. 13, no. 12, pp. 5844–5850, 2013.

[27] V. Skákalová, A. B. Kaiser, Y.-S. Woo, and S. Roth, "Electronic transport in carbon nanotubes: From individual nanotubes to thin and thick networks," *Physical Review B*, vol. 74, no. 8, p. 085403, aug 2006. [Online]. Available: http://journals.aps.org/prb/abstract/10.1103/PhysRevB.74.085403

[28] C. Koechlin, S. Maine, S. Rennesson, R. Haidar *et al.*, "Opto-electrical characterization of infrared sensors based on carbon nanotube films," *Comptes Rendus Physique*, vol. 11, no. 5-6, pp. 405–410, 2010.

[29] P. Sheng, "Fluctuation-induced tunneling conduction in disordered materials," *Physical Review B*, vol. 21, no. 6, pp. 2180–2195, mar 1980. [Online]. Available: http://journals.aps.org/prb/abstract/10.1103/PhysRevB.21.2180

[30] H.-L. Zhang, J.-F. Li, B.-P. Zhang, K.-F. Yao *et al.*, "Electrical and thermal properties of carbon nanotube bulk materials: Experimental studies for the 328–958K temperature range," *Physical Review B*, vol. 75, no. 20, pp. 1–9, 2007.

[31] N. Lett., "Percolation in Transparent and Conducting Carbon Nanotube Networks," *Hu, L. Heclht, D.S. Gruner, G*, vol. 4, no. 12, pp. 2513–2517, 2004. [Online]. Available: http://dx.doi.org/10.1021/nl048435y

[32] H. E. Unalan, G. Fanchini, a. Kanwal, a. Du Pasquier *et al.*, "Design criteria for transparent single-wall carbon nanotube thin-film transistors." *Nano Lett.*, vol. 6, pp. 677–682, 2006. [Online]. Available: http://www.ncbi.nlm.nih.gov/pubmed/16608263

[33] M. Nakamura, "Two-dimensional continuum percolation and conduction. II," *Journal of Applied Physics*, vol. 58, no. 9, pp. 3499–3503, 1985.

[34] G. E. Pike and C. H. Seager, "Percolation and conductivity: A computer study. I," *Physical Review B*, vol. 10, no. 4, pp. 1421–1434, aug 1974. [Online]. Available: http://link.aps.org/doi/10.1103/PhysRevB.10.1421

[35] M. Y. Timmermans, D. Estrada, A. G. Nasibulin, J. D. Wood *et al.*, "Effect of carbon nanotube network morphology on thin film transistor performance," *Nano Research*, vol. 5, no. 5, pp. 307–319, 2012.

[36] Z. Spitalsky, D. Tasis, K. Papagelis, and C. Galiotis, "Carbon nanotube-polymer composites: Chemistry, processing, mechanical and electrical properties," *Progress in Polymer Science (Oxford)*, vol. 35, no. 3, pp. 357–401, 2010. [Online]. Available: http://dx.doi.org/10.1016/j.progpolymsci.2009.09.003

[37] A. V. Eletskii, A. a. Knizhnik, B. Potapkin, and J. Kenny, "Electrical characteristics of carbon nanotube doped composites," *Uspekhi Fizicheskih Nauk*, vol. 185, no. 3, pp. 225–270, 2015. [Online]. Available: http://ufn.ru/ru/articles/2015/3/a/

[38] M. Park, H. Kim, and J. P. Youngblood, "Strain-dependent electrical resistance of multi-walled carbon nanotube/polymer composite films," *Nanotechnology*, vol. 19, no. 5, p. 055705, 2008. [Online]. Available: http://stacks.iop.org/0957-4484/19/i=5/a=055705?key=crossref.7552299efe97f1782622bc92fef35409

[39] I. Balberg, C. H. Anderson, S. Alexander, and N. Wagner, "Excluded volume and its realtion to the onset of percolation," *Phsical Review B*, vol. 30, no. 7, pp. 3933–3943, 1984.

[40] Y. Simsek, L. Ozyuzer, A. T. Seyhan, M. Tanoglu *et al.*, "Temperature dependence of electrical conductivity in double-wall and multi-wall carbon nanotube/polyester nanocomposites," *Journal of Materials Science*, vol. 42, no. 23, pp. 9689–9695, 2007.

[41] P. Cardoso, J. Silva, A. J. Paleo, F. W. J. Van Hattum *et al.*, "The dominant role of tunneling in the conductivity of carbon nanofiber-epoxy composites," *Physica Status Solidi (A) Applications and Materials Science*, vol. 207, no. 2, pp. 407–410, 2010.

[42] K. Schulte, F. H. Gojny, B. Fiedler, and W. Bauhofer, "Carbon Nanotube-Reinforced Polymers: a State of the Art Review," *Polymer Composites From Nano- to Macro-Scale*, pp. 3–23, 2005. [Online]. Available: http://www.springerlink.com/index/10.1007/b137162

[43] D. M. Delozier, K. A. Watson, J. G. Smith, T. C. Clancy *et al.*, "Investigation of Aromatic / Aliphatic Polyimides as Dispersants for Single Wall Carbon Nanotubes," *Macromolecules*, pp. 1731–1739, 2006.

[44] J. Sandler, M. Shaffer, T. Prasse, W. Bauhofer *et al.*, "Development of a dispersion process for carbon nanotubes in an epoxy matrix and the resulting electrical properties," *Polymer*, vol. 40, no. 21, pp. 5967–5971, 1999.

[45] P. Costa, J. Silva, V. Sencadas, R. Simoes *et al.*, "Mechanical, electrical and electro-mechanical properties of thermoplastic elastomer styrene-butadiene-styrene/multiwall carbon nanotubes composites," *Journal of Materials Science*, vol. 48, no. 3, pp. 1172–1179, 2013.

[46] N. G. Sahoo, S. Rana, J. W. Cho, L. Li *et al.*, "Polymer nanocomposites based on functionalized carbon nanotubes," *Progress in Polymer Science*, vol. 35, no. 7, pp. 837–867, 2010. [Online]. Available: http://dx.doi.org/10.1016/j.progpolymsci.2010.03.002

[47] N. Chehata, "Charge Transfer Properties in MEH-PPV/PS:MWCNTs Nanocomposites," *Journal of Surface Engineered Materials and Advanced Technology*, vol. 02, no. 03, pp. 174–181, 2012.

[48] M. Palma, W. Wang, E. Penzo, J. Brathwaite *et al.*, "Controlled formation of carbon nanotube junctions via linker induced assembly in aqueous solution." *Journal of the American Chemical Society*, pp. 1–6, 2013. [Online]. Available: http://www.ncbi.nlm.nih.gov/pubmed/23656193

[49] S. K. Samanta, M. Fritsch, U. Scherf, W. Gomulya *et al.*, "Conjugated polymer-assisted dispersion of single-wall carbon nanotubes: the power of polymer wrapping." *Accounts of chemical research*, vol. 47, no. 8, pp. 2446–56, aug 2014. [Online]. Available: http://dx.doi.org/10.1021/ar500141j

[50] J. O. Aguilar, J. R. Bautista-Quijano, and F. Avilés, "Influence of carbon nanotube clustering on the electrical conductivity of polymer composite films," *Express Polymer Letters*, vol. 4, no. 5, pp. 292–299, 2010.

[51] X. Wang, P. D. Bradford, W. Liu, H. Zhao *et al.*, "Mechanical and electrical property improvement in CNT/Nylon composites through drawing and stretching," *Composites Science and Technology*, vol. 71, no. 14, pp. 1677–1683, 2011. [Online]. Available: http://dx.doi.org/10.1016/j.compscitech.2011.07.023

[52] F. Du, J. E. Fischer, and K. I. Winey, "Effect of nanotube alignment on percolation conductivity in carbon nanotube/polymer composites," *Physical Review B - Condensed Matter and Materials Physics*, vol. 72, no. 12, pp. 1–4, 2005.

[53] M. C. Lensen, K. Takazawa, J. A. A. W. Elemans, C. R. L. P. N. Jeukens *et al.*, "Aided self-assembly of porphyrin nanoaggregates into ring-shaped architectures." *Chemistry (Weinheim an der Bergstrasse, Germany)*, vol. 10, no. 4, pp. 831–9, feb 2004. [Online]. Available: http://www.ncbi.nlm.nih.gov/pubmed/14978810

[54] R. D. Deegan, O. Bakajin, T. F. Dupont, G. Huber *et al.*, "Capillary flow as the cause of ring stains from dried liquid drops," vol. 389, no. 6653, pp. 827–829, oct 1997. [Online]. Available: http://dx.doi.org/10.1038/39827

[55] M. Majumder, C. S. Rendall, J. A. Eukel, J. Y. L. Wang *et al.*, "Overcoming the "coffee-stain" effect by compositional Marangoni-flow-assisted drop-drying." *The journal of physical chemistry. B*, vol. 116, no. 22, pp. 6536–42, jun 2012. [Online]. Available: http://dx.doi.org/10.1021/jp3009628

[56] K. Sai Krishna and M. Eswaramoorthy, "Novel synthesis of carbon nanorings and their characterization," *Chemical Physics Letters*, vol. 433, no. 4-6, pp. 327–330, jan 2007. [Online]. Available: http://www.sciencedirect.com/science/article/pii/S0009261406017222

[57] S. B. Son, Q. Miao, J.-Y. Shin, D. Dolphin *et al.*, "Ring and Volcano Structures Formed by a Metal Dipyrromethene Complex," *Bulletin of the Korean Chemical Society*, vol. 35, no. 6, pp. 1727–1731, jun 2014. [Online]. Available: http://koreascience.or.kr/article/ArticleFullRecord.jsp?cn=JCGMCS{_}2014{_}v35n6{_}1727

[58] A. Shimoni, S. Azoubel, and S. Magdassi, "Inkjet printing of flexible high-performance carbon nanotube transparent conductive films by "coffee ring effect"." *Nanoscale*, vol. 6, no. 19, pp. 11 084–9, oct 2014. [Online]. Available: http://pubs.rsc.org/en/content/articlehtml/2014/nr/c4nr02133a

[59] P. C. Ohara and W. M. Gelbart, "Interplay between Hole Instability and Nanoparticle Array Formation in Ultrathin Liquid Films," *Langmuir*, vol. 14, no. 12, pp. 3418–3424, jun 1998. [Online]. Available: http://dx.doi.org/10.1021/la971147f

[60] A. P. H. J. Schenning, F. B. G. Benneker, H. P. M. Geurts, X. Y. Liu *et al.*, "Porphyrin Wheels," *Journal of the American Chemical Society*, vol. 118, no. 36, pp. 8549–8552, jan 1996. [Online]. Available: http://dx.doi.org/10.1021/ja961234e

[61] J. Hofkens, L. Latterini, P. Vanoppen, H. Faes *et al.*, "Mesostructure of Evaporated Porphyrin Thin Films: Porphyrin Wheel Formation," *The Journal of Physical Chemistry B*, vol. 101, no. 49, pp. 10 588–10 598, dec 1997. [Online]. Available: http://dx.doi.org/10.1021/jp972305e

[62] C. R. L. P. N. Jeukens, M. C. Lensen, F. J. P. Wijnen, J. A. A. W. Elemans *et al.*, "Polarized Absorption and Emission of Ordered Self-Assembled Porphyrin Rings," *Nano Letters*, vol. 4, no. 8, pp. 1401–1406, aug 2004. [Online]. Available: http://dx.doi.org/10.1021/nl049363d

[63] K. Takazawa, "Micrometer-Sized Rings Self-assembled from Thiacyanine Dye Molecules and Their Waveguiding Properties," *Chemistry of Materials*, vol. 19, no. 22, pp. 5293–5301, oct 2007. [Online]. Available: http://dx.doi.org/10.1021/cm071762x

[64] Y. Liu, H. Ma, Y. Tian, F. Xie *et al.*, "Fabrication of Durable Honeycomb-Patterned Films of Poly(ether sulfone)s via Breath Figures," *Macromolecular Chemistry and Physics*, vol. 215, no. 15, pp. 1446–1455, aug 2014. [Online]. Available: http://doi.wiley.com/10.1002/macp.201400137

[65] Q. Liu, H. Liu, Y. Bian, X. Wang *et al.*, "Two-dimensional "nano-ring and nano-crystal" morphologies in Langmuir monolayer of phthalocyaninato nickel complexes." *Journal of colloid and interface science*, vol. 300, no. 1, pp. 298–303, aug 2006. [Online]. Available: http://www.sciencedirect.com/science/article/pii/S002197970600244X

[66] S. V. S. V. Bhosale, S. V. Nalage, J. M. Booth, A. Gupta *et al.*, "Solvent induced ordered-supramolecular assembly of highly branched protoporphyrin IX derivative," *Supramolecular Chemistry*, vol. 24, no. 11, pp. 779–786, nov 2012. [Online]. Available: http://www.tandfonline.com/doi/abs/10.1080/10610278.2012.716841http://dx.doi.org/10.1080/10610278.2012.716841

[67] G. T. Carroll, M. G. M. Jongejan, D. Pijper, and B. L. Feringa, "Spontaneous generation and patterning of chiral polymeric surface toroids," *Chemical Science*, vol. 1, no. 4, p. 469, sep 2010. [Online]. Available: http://pubs.rsc.org/en/content/articlehtml/2010/sc/c0sc00159g

[68] Y.-F. Wei and P.-Y. Hsiao, "Role of chain stiffness on the conformation of single polyelectrolytes in salt solutions." *The Journal of chemical physics*, vol. 127, no. 6, p. 064901, aug 2007. [Online]. Available: http://www.scopus.com/inward/record.url?eid=2-s2.0-34547912942{\&}partnerID=tZOtx3y1

[69] T. Iwaki, N. Makita, and K. Yoshikawa, "Folding transition of a single semiflexible polyelectrolyte chain through toroidal bundling of loop structures." *The Journal of chemical physics*, vol. 129, no. 6, p. 065103, aug 2008. [Online]. Available: http://www.scopus.com/inward/record.url?eid=2-s2.0-49749086533{\&}partnerID=tZOtx3y1

[70] G. Maurstad, "Metastable and Stable States of Xanthan Polyelectrolyte Complexes Studied by Atomic Force Microscopy," 2004.

[71] V. V. Vasilevskaya, A. R. Khokhlov, S. Kidoaki, and K. Yoshikawa, "Structure of Collapsed Persistent Macromolecule : Toroid vs . Spherical Globule," vol. 41, 1997.

[72] T. H. Eickbush and E. N. Moudrianakis, "The compaction of DNA helices into either continuous supercoils or folded-fiber rods and toroids," *Cell*, vol. 13, no. 2, pp. 295–306, feb 1978. [Online]. Available: http://www.sciencedirect.com/science/article/pii/0092867478901988

[73] A. Leforestier, A. Siber, F. Livolant, and R. Podgornik, "Protein-DNA interactions determine the shapes of DNA toroids condensed in virus capsids." *Biophysical journal*, vol. 100, no. 9, pp. 2209–16, may 2011. [Online]. Available: http://www.pubmedcentral.nih.gov/articlerender.fcgi?artid=3149266{\&}tool=pmcentrez{\&}rendertype=abstract

[74] M. X. Tang, W. Li, and F. C. Szoka, "Toroid formation in charge neutralized flexible or semi-flexible biopolymers: potential pathway for assembly of DNA carriers." *The journal of gene medicine*, vol. 7, no. 3, pp. 334–42, mar 2005. [Online]. Available: http://www.ncbi.nlm.nih.gov/pubmed/15515145

[75] S. Y. Park, D. Harries, and W. M. Gelbart, "Topological defects and the optimum size of DNA condensates." *Biophysical journal*, vol. 75, no. 2, pp. 714–720, 1998.

[76] S. Danielsen and K. M. Va, "Structural Analysis of Chitosan Mediated DNA Condensation by AFM : Influence of Chitosan Molecular Parameters," pp. 928–936, 2004.

[77] G. G. Pereira, "Charged, semi-flexible polymers under incompatible solvent conditions," *Current Applied Physics*, vol. 8, pp. 347–350, 2008.

[78] J. Jeon and A. V. Dobrynin, "Necklace Globule and Counterion Condensation," pp. 7695–7706, 2007.

[79] N. Miyazawa, T. Sakaue, K. Yoshikawa, and R. Zana, "Rings-on-a-string chain structure in DNA Rings-on-a-string chain structure in DNA," vol. 044902, no. 2005, 2011.

[80] T. Iwaki, "Association-dissociation equilibrium of loop structures in single-chain folding into a toroidal condensate," *Journal of Chemical Physics*, vol. 125, no. 2006, 2006.

[81] T. Sakaue and K. Yoshikawa, "On the formation of rings-on-a-string conformations in a single polyelectrolyte chain : A On the formation of rings-on-a-string conformations in a single polyelectrolyte chain : A possible scenario," vol. 074904, no. 2006, 2010.

[82] O. Shoji, H. Tanaka, T. Kawai, and Y. Kobuke, "Single molecule visualization of coordination-assembled porphyrin macrocycles reinforced with covalent linkings." *Journal of the American Chemical Society*, vol. 127, no. 24, pp. 8598–9, jun 2005. [Online]. Available: http://dx.doi.org/10.1021/ja051344y

[83] F. Balzer, J. Beermann, S. I. Bozhevolnyi, A. C. Simonsen *et al.*, "Optically Active Organic Microrings," *Nano Letters*, vol. 3, no. 9, pp. 1311–1314, sep 2003. [Online]. Available: http://dx.doi.org/10.1021/nl034457t

[84] R. Takahashi and Y. Kobuke, "Hexameric macroring of gable-porphyrins as a light-harvesting antenna mimic." *Journal of the American Chemical Society*, vol. 125, no. 9, pp. 2372–3, mar 2003. [Online]. Available: http://dx.doi.org/10.1021/ja028325y

[85] Y. Kuramochi, A. Satake, and Y. Kobuke, "Light-harvesting macroring accommodating a tetrapodal ligand based on complementary and cooperative coordinations." *Journal of the American Chemical Society*, vol. 126, no. 28, pp. 8668–9, jul 2004. [Online]. Available: http://dx.doi.org/10.1021/ja048118t

[86] "Schiff bases (Schiff's bases)," in *IUPAC Compendium of Chemical Terminology*. Research Triagle Park, NC: IUPAC, jun 2009. [Online]. Available: http://dx.doi.org/10.1351/goldbook.S05498http://goldbook.iupac.org/S05498.html

[87] W.-K. Dong, X.-N. He, H.-B. Yan, Z.-W. Lv *et al.*, "Synthesis, structural characterization and solvent effect of copper(II) complexes with a variational multidentate Salen-type ligand with bisoxime groups," *Polyhedron*, vol. 28, no. 8, pp. 1419–1428, jun 2009. [Online]. Available: http://www.sciencedirect.com/science/article/pii/S0277538709001715

[88] M. V. Escárcega-Bobadilla, D. Anselmo, S. J. Wezenberg, E. C. Escudero-Adán *et al.*, "Metal-directed assembly of chiral bis-Zn(II) Schiff base structures." *Dalton transactions (Cambridge, England : 2003)*, vol. 41, no. 32, pp. 9766–72, aug 2012. [Online]. Available: http://pubs.rsc.org/en/content/articlehtml/2012/dt/c2dt30642e

[89] N. Kielland, E. C. Escudero-Adán, M. Martínez Belmonte, and A. W. Kleij, "Unsymmetrical octanuclear Schiff base clusters: synthesis, characterization and catalysis." *Dalton transactions (Cambridge, England : 2003)*, vol. 42, no. 5, pp. 1427–36, feb 2013. [Online]. Available: http://pubs.rsc.org/en/content/articlehtml/2013/dt/c2dt31723k

[90] S. J. Wezenberg, E. C. Escudero-Adán, J. Benet-Buchholz, and A. W. Kleij, "Anion-templated formation of supramolecular multinuclear assemblies." *Chemistry (Weinheim an der Bergstrasse, Germany)*, vol. 15, no. 23, pp. 5695–700, jun 2009. [Online]. Available: http://www.ncbi.nlm.nih.gov/pubmed/19388037

[91] M. Martínez Belmonte, E. C. Escudero-Adán, E. Martin, and A. W. Kleij, "Isolation and characterization of unusual multinuclear Schiff base complexes: rearrangements reactions and octanuclear cluster formation." *Dalton transactions (Cambridge, England : 2003)*, vol. 41, no. 17, pp. 5193–200, may 2012. [Online]. Available: http://pubs.rsc.org/en/content/articlehtml/2012/dt/c2dt30201b

[92] N. K. Al Rasbi, H. Adams, I. AlShabibi, and F. AlAmri, "Structure, aggregation and spectroscopic properties of self-assembled Zn(II) Schiff base complexes," *Journal of Photochemistry and Photobiology A: Chemistry*, vol. 285, pp. 37–43, jul 2014. [Online]. Available: http://www.sciencedirect.com/science/article/pii/S1010603014001105

[93] F. Dumur, L. Beouch, M.-A. Tehfe, E. Contal *et al.*, "Low-cost zinc complexes for white organic light-emitting devices," *Thin Solid Films*, vol. 564, pp. 351–360, aug 2014. [Online]. Available: http://www.sciencedirect.com/science/article/pii/S0040609014006506

[94] K. I. Ansari, S. Kasiri, J. D. Grant, and S. S. Mandal, "Fe(III)-salen and salphen complexes induce caspase activation and apoptosis in human cells." *Journal of biomolecular screening*, vol. 16, no. 1, pp. 26–35, jan 2011. [Online]. Available: http://jbx.sagepub.com/content/16/1/26.long

[95] R. M. Clarke and T. Storr, "The chemistry and applications of multimetallic salen complexes." *Dalton transactions (Cambridge, England : 2003)*, vol. 43, no. 25, pp. 9380–91, 2014. [Online]. Available: http://www.ncbi.nlm.nih.gov/pubmed/24722684

[96] A. W. Kleij, "Zinc-centred salen complexes: versatile and accessible supramolecular building motifs." *Dalton transactions (Cambridge, England : 2003)*, no. 24, pp. 4635–9, jun 2009. [Online]. Available: http://pubs.rsc.org/en/content/articlehtml/2009/dt/b902866h

[97] J. K.-H. Hui, Z. Yu, and M. J. MacLachlan, "Supramolecular assembly of zinc salphen complexes: access to metal-containing gels and nanofibers." *Angewandte Chemie (International ed. in English)*, vol. 46, no. 42, pp. 7980–3, jan 2007. [Online]. Available: http://www.ncbi.nlm.nih.gov/pubmed/17849495

[98] M. Martínez Belmonte, S. J. Wezenberg, R. M. Haak, D. Anselmo *et al.*, "Self-assembly of Zn(salphen) complexes: steric regulation, stability studies and crystallographic analysis revealing an unexpected dimeric 3,3'-t-Bu-substituted Zn(salphen) complex." *Dalton transactions (Cambridge, England : 2003)*, vol. 39, no. 19, pp. 4541–50, may 2010. [Online]. Available: http://pubs.rsc.org/en/content/articlehtml/2010/dt/b925560e

[99] G. Salassa, A. M. Castilla, and A. W. Kleij, "Cooperative self-assembly of a macrocyclic Schiff base complex." *Dalton transactions (Cambridge,*

England : 2003), vol. 40, no. 19, pp. 5236–43, may 2011. [Online]. Available: http://pubs.rsc.org/en/content/articlehtml/2011/dt/c1dt10069f

[100] I. P. Oliveri, G. Malandrino, S. D. Bella, S. Chimiche *et al.*, "Phase Transition and Vapochromism in Molecular Assemblies of a Polymorphic Zinc(II) Schi ff -Base Complex," *Inorg. Chem.*, vol. 53, no. Ii, pp. 9771–9777, 2014.

[101] I. P. Oliveri, S. Failla, G. Malandrino, S. Di Bella *et al.*, "Controlling the Molecular Self-Assembly into Nanofibers of Amphiphilic Zinc(II) Salophen Complexes," *The Journal of Physical Chemistry C*, vol. 117, no. 29, pp. 15 335–15 341, jul 2013. [Online]. Available: http://dx.doi.org/10.1021/jp4038182

[102] A. Biancardi, A. Burgalassi, A. Terenzi, A. Spinello *et al.*, "A Theoretical and Experimental Investigation of the Spectroscopic Properties of a DNA-Intercalator Salphen-Type Zn II Complex," *Chemistry - A European Journal*, vol. 20, no. 24, pp. 7439–7447, 2014. [Online]. Available: http://doi.wiley.com/10.1002/chem.201304876

[103] N. H. Campbell, N. H. A. Karim, G. N. Parkinson, M. Gunaratnam *et al.*, "Molecular basis of structure-activity relationships between salphen metal complexes and human telomeric DNA quadruplexes." *Journal of medicinal chemistry*, vol. 55, no. 1, pp. 209–22, jan 2012. [Online]. Available: http://dx.doi.org/10.1021/jm201140v

[104] A. K. Asatkar, S. P. Senanayak, A. Bedi, S. Panda *et al.*, "Zn(II) and Cu(II) complexes of a new thiophene-based salphen-type ligand: solution-processable high-performance field-effect transistor materials." *Chemical communications (Cambridge, England)*, vol. 50, no. 53, pp. 7036–9, jul 2014. [Online]. Available: http://pubs.rsc.org/en/Content/ArticleHTML/2014/CC/C4CC01360C

[105] S. K. Saha, A. Dutta, P. Ghosh, D. Sukul *et al.*, "Adsorption and corrosion inhibition effect of Schiff base molecules on the mild steel surface in 1 M HCl medium: a combined experimental and theoretical approach," *Phys. Chem. Chem. Phys.*, vol. 17, no. 8, pp. 5679–5690, 2015. [Online]. Available: http://xlink.rsc.org/?DOI=C4CP05614K

[106] R. P. Feynman, R. B. Leighton, and M. Sands, "The Feynman Lectures on Physics, Vol. I: The New Millennium Edition: Mainly Mechanics, Radiation, and Heat," *European Journal of Physics*, vol. 24, 2011.

[107] "Scopus." [Online]. Available: http://www.scopus.com

[108] W. Zhang, A. R. Oganov, A. F. Goncharov, Q. Zhu *et al.*, "Unexpected stable stoichiometries of sodium chlorides." *Science (New York, N.Y.)*, vol. 342, no. 6165, pp. 1502–5, dec 2013. [Online]. Available: http://www.scopus.com/inward/record.url?eid=2-s2.0-84890841921{\&}partnerID=tZOtx3y1

[109] J. R. Perilla, B. C. Goh, C. K. Cassidy, B. Liu *et al.*, "Molecular dynamics simulations of large macromolecular complexes," *Current Opinion in Structural Biology*, vol. 31, pp. 64–74, apr 2015. [Online]. Available: http://www.scopus.com/inward/record.url?eid=2-s2.0-84926161673{\&}partnerID=tZOtx3y1

[110] R. Y. Rubinstein and D. P. Kroese, *Simulation and the Monte Carlo Method*, ser. Wiley Series in Probability and Mathematical Statistics, Wiley Series In Probability And Statistics, Ed. Wiley-Interscience, 2008, vol. 707, no. November. [Online]. Available: http://books.google.de/books?id=1-ffZVmazvwC

[111] L.-P. Simoneau, J. Villeneuve, and A. Rochefort, "Electron percolation in realistic models of carbon nanotube networks," *Journal of Applied Physics*, vol. 118, no. 12, p. 124309, sep 2015. [Online]. Available: http://scitation.aip.org/content/aip/journal/jap/118/12/10.1063/1.4931676

[112] S. S. Rahatekar, M. S. Shaffer, and J. A. Elliott, "Modelling percolation in fibre and sphere mixtures: Routes to more efficient network formation," *Composites Science and Technology*, vol. 70, no. 2, pp. 356–362, feb 2010. [Online]. Available: http://www.sciencedirect.com/science/article/pii/S0266353809003935

[113] J. Silva, S. Ribeiro, S. Lanceros-Mendez, and R. Simões, "The influence of matrix mediated hopping conductivity, filler concentration, aspect ratio and orientation on the electrical response of carbon nanotube/polymer nanocomposites," *Composites Science and Technology*, vol. 71, no. 5, pp. 643–646, mar 2011. [Online]. Available: http://www.sciencedirect.com/science/article/pii/S0266353811000339

[114] J. Silva, S. Lanceros-Mendez, and R. Simoes, "Effect of cylindrical filler aggregation on the electrical conductivity of composites," *Physics*

Letters A, vol. 378, no. 40, pp. 2985–2988, aug 2014. [Online]. Available: http://www.sciencedirect.com/science/article/pii/S037596011400824X

[115] S. I. White, B. A. DiDonna, M. Mu, T. C. Lubensky *et al.*, "Simulations and electrical conductivity of percolated networks of finite rods with various degrees of axial alignment," *Physical Review B*, vol. 79, no. 2, p. 024301, jan 2009. [Online]. Available: http://journals.aps.org/prb/abstract/10.1103/PhysRevB.79.024301

[116] A. Dani and A. Ogale, "Percolation in short-fiber composites: Cluster statistics and critical exponents," *Composites Science and Technology*, vol. 57, no. 9-10, pp. 1355–1361, jan 1997. [Online]. Available: http://www.sciencedirect.com/science/article/pii/S0266353897000626

[117] D. C. Lee, G. Kwon, H. Kim, H.-J. Lee *et al.*, "Three-Dimensional Monte Carlo Simulation of the Electrical Conductivity of Carbon Nanotube/Polymer Composites," *Applied Physics Express*, vol. 5, no. 4, p. 045101, mar 2012. [Online]. Available: http://iopscience.iop.org/article/10.1143/APEX.5.045101

[118] B. J. Alder and T. E. Wainwright, "Phase transition for a hard sphere system," *The Journal of Chemical Physics*, vol. 27, no. 5, pp. 1208–1209, 1957. [Online]. Available: http://www.scopus.com/inward/record.url?eid=2-s2.0-34548717559{\&}partnerID=tZOtx3y1

[119] D. E. Shaw, K. J. Bowers, E. Chow, M. P. Eastwood *et al.*, "Millisecond-scale molecular dynamics simulations on Anton," in *Proceedings of the Conference on High Performance Computing Networking, Storage and Analysis - SC '09*. New York, New York, USA: ACM Press, 2009, p. 1. [Online]. Available: http://www.scopus.com/inward/record.url?eid=2-s2.0-74049112717{\&}partnerID=tZOtx3y1

[120] W. Eckhardt, A. Heinecke, R. Bader, M. Brehm *et al.*, *Supercomputing*, ser. Lecture Notes in Computer Science, J. M. Kunkel, T. Ludwig, and H. W. Meuer, Eds. Berlin, Heidelberg: Springer Berlin Heidelberg, 2013, vol. 7905. [Online]. Available: http://www.scopus.com/inward/record.url?eid=2-s2.0-84884487938{\&}partnerID=tZOtx3y1

[121] J. A. Zimmerman, E. B. WebbIII, J. J. Hoyt, R. E. Jones *et al.*, "Calculation of stress in atomistic simulation," *Modelling and Simulation in Materials Science and Engineering*, vol. 12, no. 4, pp. S319–S332, jul

2004. [Online]. Available: http://www.scopus.com/inward/record.url?eid=2-s2.0-3142605093{\&}partnerID=tZOtx3y1

[122] M. Zamponi, A. Wischnewski, M. Monkenbusch, L. Willner *et al.*, "Cooperative dynamics in homopolymer melts: a comparison of theoretical predictions with neutron spin echo experiments." *The journal of physical chemistry. B*, vol. 112, no. 50, pp. 16 220–9, dec 2008. [Online]. Available: http://www.scopus.com/inward/record.url?eid=2-s2.0-58049163209{\&}partnerID=tZOtx3y1

[123] D. Frenkel and B. Smit, "Understanding molecular simulation: from algorithms to applications," *Academic Press*, vol. New York„ 2002. [Online]. Available: http://books.google.com/books?hl=en{\&}lr={\&}ie=UTF-8{\&}id=XmyO2oRUg0cC{\&}oi=fnd{\&}pg=PR13{\&}dq="Understanding+Molecular+Simulation:+From+Algorithms+to+Applications"{\&}ots=Zw2B2{_}j5yT{\&}sig=M-ipI-NcSM93bV3DW0pfxY2{_}3iI$\backslash$npapers://8d0de5a1-e8b7-4a12-aaa3-152761650b49/Paper/p9

[124] D. Rapaport, *The art of molecular dynamics simulation*. Cambridge Univ Pr, 2004, vol. 1, no. 11. [Online]. Available: http://onlinelibrary.wiley.com/doi/10.1002/cbdv.200490137/abstract$\backslash$nhttp://books.google.com/books?hl=en{\&}amp;lr={\&}amp;id=iqDJ2hjqBMEC{\&}amp;oi=fnd{\&}amp;pg=PR9{\&}amp;dq=The+art+of+molecular+dynamics+simulation{\&}amp;ots=krKNuyen{_}N{\&}amp;sig=g1-T6{_}{_}a1yRWCS-iURxWrZ{_}IcY

[125] J. Wang and T. Hou, "Application of molecular dynamics simulations in molecular property prediction II: diffusion coefficient." *Journal of computational chemistry*, vol. 32, no. 16, pp. 3505–19, dec 2011. [Online]. Available: http://www.pubmedcentral.nih.gov/articlerender.fcgi?artid=3193570{\&}tool=pmcentrez{\&}rendertype=abstract

[126] S. Melchionna, G. Ciccotti, and B. Lee Holian, "Hoover NPT Dynamics for Systems Varying in Shape and Size," *Molecular Physics*, vol. 78, no. 3, pp. 533–544, 1993. [Online]. Available: http://www.tandfonline.com/doi/abs/10.1080/00268979300100371

[127] R. L. Davidchack, R. Handel, and M. V. Tretyakov, "Langevin thermostat for rigid body dynamics," *Journal of Chemical Physics*, vol. 130, no. 23, 2009.

[128] J. Wang, R. M. Wolf, J. W. Caldwell, P. A. Kollman *et al.*, "Junmei Wang, Romain M. Wolf, James W. Caldwell, Peter A. Kollman, and David A. Case, "Development and testing of a general amber force field"Journal of Computational Chemistry(2004) 25(9) 1157-1174," *Journal of Computational Chemistry*, vol. 25, no. 9, pp. 1157–74, jul 2004. [Online]. Available: http://www.scopus.com/inward/record.url?eid=2-s2.0-2942532422{\&}partnerID=tZOtx3y1http://www.scopus.com/inward/record.url?eid=2-s2.0-11144347566{\&}partnerID=tZOtx3y1

[129] C. Oostenbrink, A. Villa, A. E. Mark, and W. F. van Gunsteren, "A biomolecular force field based on the free enthalpy of hydration and solvation: the GROMOS force-field parameter sets 53A5 and 53A6." *Journal of computational chemistry*, vol. 25, no. 13, pp. 1656–76, oct 2004. [Online]. Available: http://www.ncbi.nlm.nih.gov/pubmed/15264259

[130] S. L. Mayo, B. D. Olafson, and W. A. Goddard, "DREIDING: a generic force field for molecular simulations," *The Journal of Physical Chemistry*, vol. 94, no. 26, pp. 8897–8909, dec 1990. [Online]. Available: http://dx.doi.org/10.1021/j100389a010

[131] J. Gasteiger and M. Marsili, "A new model for calculating atomic charges in molecules," *Tetrahedron Letters*, vol. 19, no. 34, pp. 3181–3184, jan 1978. [Online]. Available: http://www.sciencedirect.com/science/article/pii/S0040403901949779

[132] F.-Y. Dupradeau, A. Pigache, T. Zaffran, C. Savineau *et al.*, "The R.E.D. tools: advances in RESP and ESP charge derivation and force field library building." *Physical chemistry chemical physics : PCCP*, vol. 12, no. 28, pp. 7821–39, jul 2010. [Online]. Available: http://www.pubmedcentral.nih.gov/articlerender.fcgi?artid=2918240{\&}tool=pmcentrez{\&}rendertype=abstract

[133] U. Ryde, "Molecular dynamics simulations of alcohol dehydrogenase with a four- or five-coordinate catalytic zinc ion." *Proteins*, vol. 21, no. 1, pp. 40–56, jan 1995. [Online]. Available: http://www.ncbi.nlm.nih.gov/pubmed/7716168

[134] R. H. Stote and M. Karplus, "Zinc binding in proteins and solution: a simple but accurate nonbonded representation." *Proteins*, vol. 23, no. 1, pp. 12–31, sep 1995. [Online]. Available: http://www.ncbi.nlm.nih.gov/pubmed/8539245

[135] J.-P. Ryckaert, G. Ciccotti, and H. J. Berendsen, "Numerical integration of the cartesian equations of motion of a system with constraints: molecular dynamics of n-alkanes," *Journal of Computational Physics*, vol. 23, no. 3, pp. 327–341, mar 1977. [Online]. Available: http://www.sciencedirect.com/science/article/pii/0021999177900985

[136] C.-Y. Lin, N.-Y. Chen, and C. Y. Mou, "Folding a protein with equal probability of being helix or hairpin." *Biophysical journal*, vol. 103, no. 1, pp. 99–108, jul 2012. [Online]. Available: http://www.pubmedcentral.nih.gov/articlerender.fcgi?artid=3388226{\&}tool=pmcentrez{\&}rendertype=abstract

[137] R. W. Zwanzig, "High-Temperature Equation of State by a Perturbation Method. I. Nonpolar Gases," *The Journal of Chemical Physics*, vol. 22, no. 8, p. 1420, dec 1954. [Online]. Available: http://scitation.aip.org/content/aip/journal/jcp/22/8/10.1063/1.1740409

[138] M. Feig, W. Im, and C. L. Brooks, "Implicit solvation based on generalized Born theory in different dielectric environments," *The Journal of Chemical Physics*, vol. 120, no. 2, p. 903, dec 2004. [Online]. Available: http://scitation.aip.org/content/aip/journal/jcp/120/2/10.1063/1.1631258

[139] L. David, R. Luo, and M. K. Gilson, "Comparison of generalized born and poisson models: Energetics and dynamics of HIV protease," *Journal of Computational Chemistry*, vol. 21, no. 4, pp. 295–309, mar 2000. [Online]. Available: http://doi.wiley.com/10.1002/{\%}28SICI{\%}291096-987X{\%}28200003{\%}2921{\%}3A4{\%}3C295{\%}3A{\%}3AAID-JCC5{\%}3E3.0.CO{\%}3B2-8

[140] J. B. Abrams, L. Rosso, and M. E. Tuckerman, "Efficient and precise solvation free energies via alchemical adiabatic molecular dynamics." *The Journal of chemical physics*, vol. 125, no. 7, p. 074115, aug 2006. [Online]. Available: http://scitation.aip.org/content/aip/journal/jcp/125/7/10.1063/1.2232082

[141] P. Virnau and M. Mueller, "Calculation of free energy through successive umbrella sampling," *The Journal of Chemical Physics*, vol. 120, no. 23, p. 10925, may 2004. [Online]. Available: http://scitation.aip.org/content/aip/journal/jcp/120/23/10.1063/1.1739216

[142] S. Kumar, J. M. Rosenberg, D. Bouzida, R. H. Swendsen *et al.*, "THE weighted histogram analysis method for free-energy calculations on biomolecules. I. The method," *Journal of Computational Chemistry*, vol. 13, no. 8, pp. 1011–1021, oct 1992. [Online]. Available: http://doi.wiley.com/10.1002/jcc.540130812

[143] G. Henkelman, B. P. Uberuaga, and H. Jonsson, "A climbing image nudged elastic band method for finding saddle points and minimum energy paths," *The Journal of Chemical Physics*, vol. 113, no. 22, p. 9901, dec 2000. [Online]. Available: http://scitation.aip.org/content/aip/journal/jcp/113/22/10.1063/1.1329672

[144] D. Shivakumar, J. Williams, Y. Wu, W. Damm *et al.*, "Prediction of absolute solvation free energies using molecular dynamics free energy perturbation and the opls force field," *Journal of Chemical Theory and Computation*, vol. 6, no. 5, pp. 1509–1519, 2010.

[145] C. H. Bennett, "Efficient estimation of free energy differences from Monte Carlo data," *Journal of Computational Physics*, vol. 22, no. 2, pp. 245–268, oct 1976. [Online]. Available: http://www.scopus.com/inward/record.url?eid=2-s2.0-5244304444{\&}partnerID=tZOtx3y1

[146] M. R. Shirts and V. S. Pande, "Comparison of efficiency and bias of free energies computed by exponential averaging, the Bennett acceptance ratio, and thermodynamic integration." *The Journal of chemical physics*, vol. 122, no. 14, p. 144107, apr 2005. [Online]. Available: http://www.scopus.com/inward/record.url?eid=2-s2.0-23944432199{\&}partnerID=tZOtx3y1

[147] A. Pohorille, C. Jarzynski, and C. Chipot, "Good practices in free-energy calculations," *Journal of Physical Chemistry B*, vol. 114, no. 32, pp. 10 235–10 253, 2010.

[148] C. Jarzynski, "Nonequilibrium equality for free energy differences," *Physical Review Letters*, vol. 78, no. 14, pp. 2690–2693, 1997. [Online]. Available: http://www.scopus.com/inward/record.url?eid=2-s2.0-4243754128{\&}partnerID=tZOtx3y1

[149] S. Park, F. Khalili-Araghi, E. Tajkhorshid, and K. Schulten, "Free energy calculation from steered molecular dynamics simulations using Jarzynski's equality," *The Journal of Chemical Physics*, vol. 119, no. 6, p. 3559, 2003.

[Online]. Available: http://scitation.aip.org/content/aip/journal/jcp/119/6/10.1063/1.1590311

[150] S. Park and K. Schulten, "Calculating potentials of mean force from steered molecular dynamics simulations." *The Journal of chemical physics*, vol. 120, no. 13, pp. 5946–61, apr 2004. [Online]. Available: http://scitation.aip.org/content/aip/journal/jcp/120/13/10.1063/1.1651473

[151] R. M. Martin, "Electronic Structure: Basic Theory and Practical Methods," Cambridge, p. 624, 2004. [Online]. Available: http://books.google.com/books?id=dmRTFLpSGNsC

[152] P. M. Gill, "Molecular integrals Over Gaussian Basis Functions," *Advances in Quantum Chemistry*, vol. 25, pp. 141–205, 1994. [Online]. Available: http://www.sciencedirect.com/science/article/pii/S0065327608600192

[153] J. Junquera, O. Paz, D. Sanchez-Portal, and E. Artacho, "Numerical atomic orbitals for linear-scaling calculations," *Physical Review B - Condensed Matter and Materials Physics*, vol. 64, no. 23, pp. 2 351 111–2 351 119, 2001. [Online]. Available: http://www.scopus.com/inward/record.url?eid=2-s2.0-0035894201{\&}partnerID=tZOtx3y1

[154] P. D. Haynes, C.-K. Skylaris, A. A. Mostofi, and M. C. Payne, "ONETEP: linear-scaling density-functional theory with local orbitals and plane waves," *physica status solidi (b)*, vol. 243, no. 11, pp. 2489–2499, sep 2006. [Online]. Available: http://www.scopus.com/inward/record.url?eid=2-s2.0-33748565991{\&}partnerID=tZOtx3y1

[155] N. Troullier and J. L. Martins, "Efficient pseudopotentials for plane-wave calculations," *Physical Review B*, vol. 43, no. 3, pp. 1993–2006, jan 1991. [Online]. Available: http://www.scopus.com/inward/record.url?eid=2-s2.0-33645426115{\&}partnerID=tZOtx3y1

[156] W. Kohn and L. J. Sham, "Self-Consistent Equations Including Exchange and Correlation Effects," *Physical Review*, vol. 140, no. 4A, pp. A1133–A1138, nov 1965. [Online]. Available: http://www.scopus.com/inward/record.url?eid=2-s2.0-0042113153{\&}partnerID=tZOtx3y1

[157] J. P. Perdew, K. Burke, and M. Ernzerhof, "Generalized Gradient Approximation Made Simple," *Physical Review Letters*, vol. 77, no. 18, pp. 3865–3868, oct 1996. [Online]. Available: http://journals.aps.org/prl/abstract/10.1103/PhysRevLett.77.3865

[158] J. P. Perdew and Y. Wang, "Accurate and simple analytic representation of the electron-gas correlation energy," *Physical Review B*, vol. 45, no. 23, pp. 13 244–13 249, jun 1992. [Online]. Available: http://journals.aps.org/prb/abstract/10.1103/PhysRevB.45.13244

[159] A. D. Becke, "Density-functional exchange-energy approximation with correct asymptotic behavior," *Physical Review A*, vol. 38, no. 6, pp. 3098–3100, sep 1988. [Online]. Available: http://journals.aps.org/pra/abstract/10.1103/PhysRevA.38.3098

[160] M. Dion, H. Rydberg, E. Schröder, D. C. Langreth *et al.*, "van der Waals density functional for general geometries." *Physical review letters*, vol. 92, no. 24, p. 246401, jun 2004. [Online]. Available: http://journals.aps.org/prl/abstract/10.1103/PhysRevLett.92.246401

[161] C. Lee, W. Yang, and R. G. Parr, "Development of the Colle-Salvetti correlation-energy formula into a functional of the electron density," *Physical Review B*, vol. 37, no. 2, pp. 785–789, jan 1988. [Online]. Available: http://journals.aps.org/prb/abstract/10.1103/PhysRevB.37.785

[162] A. D. Becke, "Density-functional thermochemistry. III. The role of exact exchange," *The Journal of Chemical Physics*, vol. 98, no. 7, p. 5648, apr 1993. [Online]. Available: http://scitation.aip.org/content/aip/journal/jcp/98/7/10.1063/1.464913

[163] L. P. Lee, D. J. Cole, M. C. Payne, and C.-K. Skylaris, "Natural bond orbital analysis in the ONETEP code: applications to large protein systems." *Journal of computational chemistry*, vol. 34, no. 6, pp. 429–44, mar 2013. [Online]. Available: http://www.ncbi.nlm.nih.gov/pubmed/23065758

[164] U. C. Singh and P. A. Kollman, "An approach to computing electrostatic charges for molecules," *Journal of Computational Chemistry*, vol. 5, no. 2, pp. 129–145, apr 1984. [Online]. Available: http://doi.wiley.com/10.1002/jcc.540050204

[165] Heiko Hocke, "Baytubes: carbon nanotubes at Bayer," 2010. [Online]. Available: http://www.lidorr.com/{_}uploads/dbsattachedfiles/baytubesseminartechnicalpresentation2010.pdf

[166] S. Sathyanarayana, "Multiwalled carbon nanotubes incorporated into a miscible blend of poly(phenylenether)/polystyrene – Processing and

characterization," *Express Polymer Letters*, vol. 7, no. 7, pp. 621–635, may 2013. [Online]. Available: http://www.scopus.com/inward/record.url?eid=2-s2.0-84877312275{\&}partnerID=tZOtx3y1

[167] A. Y. Matveeva, F. W. J. Van Hattum, and S. V. Pyrlin, "Orientation and dispersion influences on elastic properties of CnT/CNF polymer nanocomposites," in *International SAMPE Technical Conference*, 2012. [Online]. Available: http://www.scopus.com/inward/record.url?eid=2-s2.0-84875882581{\&}partnerID=tZOtx3y1

[168] G. Strang, *Computational Science and Engineering*. Wellesley-Cambridge Press, 2007, vol. 1. [Online]. Available: https://books.google.com/books?id=GQ9pQgAACAAJ{\&}pgis=1

[169] E. Anderson, Z. Bai, J. Dongarra, A. Greenbaum *et al.*, "LAPACK: A Portable Linear Algebra Library for High-performance Computers," in *Proceedings of the 1990 ACM/IEEE Conference on Supercomputing*, ser. Supercomputing '90. IEEE Computer Society Press, 1990, pp. 2–11. [Online]. Available: http://portal.acm.org/citation.cfm?id=110385

[170] W. Nvidia, N. Generation, and C. Compute, "Whitepaper NVIDIA's Next Generation CUDA Compute Architecture," *Re-Vision*, vol. 23, no. 6, pp. 1–22, 2009. [Online]. Available: http://www.nvidia.com/content/PDF/fermi{_}white{_}papers/NVIDIA{_}Fermi{_}Compute{_}Architecture{_}Whitepaper.pdf

[171] T. Foley and J. Sugerman, "KD-tree acceleration structures for a GPU raytracer," *Proceedings of the ACM SIGGRAPH/EUROGRAPHICS conference on Graphics hardware - HWWS '05*, vol. 45, p. 15, 2005. [Online]. Available: http://portal.acm.org/citation.cfm?doid=1071866.1071869

[172] L. Lamport, "A fast mutual exclusion algorithm," *ACM Transactions on Computer Systems*, vol. 5, no. 1, pp. 1–11, 1987.

[173] S. Plimpton, "Fast Parallel Algorithms for Short-Range Molecular Dynamics," *Journal of Computational Physics*, vol. 117, no. 1, pp. 1–19, mar 1995. [Online]. Available: http://www.scopus.com/inward/record.url?eid=2-s2.0-0002467378{\&}partnerID=tZOtx3y1

[174] S. M. J. Schulz Mark J. , Kelkar Ajit D., *Nanoengineering of Structural, Functional and Smart Materials*. Boca Raton: CRC Press, 2005.

[175] Nanocyl, "Nanocyl PLASTICYL™ PC1501 Polycarbonate - Carbon Nanotube Masterbatch." [Online]. Available: http://www.matweb.com

[176] ——, "Nanocyl NANOCYL™ NC7000 Thin Multi-Wall Carbon Nanotubes." [Online]. Available: http://www.matweb.com

[177] J. E. Mark, *Physical properties of polymers handbook*, 2nd ed. New York: Springer-Verlag, 1997. [Online]. Available: http://books.google.com/books?id=fZl7q7UgEXkC{\&}pgis=1$\backslash$nhttp://linkinghub.elsevier.com/retrieve/pii/S0039914097800379

[178] A. Sears and R. C. Batra, "Macroscopic properties of carbon nanotubes from molecular-mechanics simulations," *Physical Review B*, vol. 69, no. 23, p. 235406, jun 2004. [Online]. Available: http://journals.aps.org/prb/abstract/10.1103/PhysRevB.69.235406

[179] A. Y. Matveeva, S. V. Pyrlin, M. M. Ramos, H. J. Böhm *et al.*, "Influence of waviness and curliness of fibres on mechanical properties of composites," *Computational Materials Science*, vol. 87, pp. 1–11, may 2014. [Online]. Available: http://linkinghub.elsevier.com/retrieve/pii/S0927025614000792

[180] B. Stroustrup, "The C++ Programming Language," *Imprint*, vol. 923, 1997. [Online]. Available: http://www.mendeley.com/catalog/c-programming-language-41/

[181] ISO, *ISO/IEC 14882:2011 Information technology — Programming languages — C++*. Geneva, Switzerland: International Organization for Standardization, feb 2012. [Online]. Available: http://www.iso.org/iso/iso{_}catalogue/catalogue{_}tc/catalogue{_}detail.htm?csnumber=50372

[182] W. J. Schroeder and K. M. Martin, *Visualization Handbook*. Elsevier, 2005. [Online]. Available: http://www.mendeley.com/catalog/visualization-toolkit-1/

[183] I. Balberg, C. H. Anderson, S. Alexander, and N. Wagner, "Excluded volume and its relation to the onset of percolation," pp. 3933–3943, 1984.

[184] H. Deng, R. Zhang, E. Bilotti, J. Loos *et al.*, "Conductive polymer tape containing highly oriented carbon nanofillers," *Journal of Applied Polymer Science*, vol. 113, no. 2, pp. 742–751, 2009. [Online]. Available: http://doi.wiley.com/10.1002/app.29624

[185] E. W. Dijkstra, "A note on two problems in connexion with graphs," *Numerische Mathematik*, vol. 1, no. 1, pp. 269–271, dec 1959. [Online]. Available: http://link.springer.com/10.1007/BF01386390

[186] D. W. Marquardt, "An Algorithm for Least-Squares Estimation of Nonlinear Parameters," *Journal of the Society for Industrial and Applied Mathematics*, vol. 11, no. 2, pp. 431–441, jun 1963. [Online]. Available: http://epubs.siam.org/doi/abs/10.1137/0111030

[187] T. E. Oliphant, "SciPy: Open source scientific tools for Python," *Computing in Science and Engineering*, vol. 9, pp. 10–20, 2007. [Online]. Available: http://www.mendeley.com/catalog/scipy-open-source-scientific-tools-python/

[188] J. Quintanilla, S. Torquato, and R. M. Ziff, "Efficient measurement of the percolation threshold for fully penetrable discs," *Journal of Physics A: Mathematical and General*, vol. 33, no. 42, pp. L399–L407, oct 2000. [Online]. Available: http://iopscience.iop.org/article/10.1088/0305-4470/33/42/104

[189] A. W. Kleij, M. V. Escárcega-Bobadilla, G. A. Zelada-Guillén, and G. Maier, "Bis-salphen compounds and carbonaceous material composites comprising them," 2015. [Online]. Available: https://www.lens.org/lens/patent/WO{_}2015{_}018940{_}A1

[190] J. M. Soler, E. Artacho, J. D. Gale, A. García *et al.*, "The SIESTA method for ab initio order- N materials simulation," *Journal of Physics: Condensed Matter*, vol. 14, no. 11, pp. 2745–2779, mar 2002. [Online]. Available: http://www.scopus.com/inward/record.url?eid=2-s2.0-0037171091{\&}partnerID=tZOtx3y1

[191] C.-K. Skylaris, P. D. Haynes, A. A. Mostofi, and M. C. Payne, "Introducing ONETEP: linear-scaling density functional simulations on parallel computers." *The Journal of chemical physics*, vol. 122, no. 8, p. 84119, feb 2005. [Online]. Available: http://www.scopus.com/inward/record.url?eid=2-s2.0-22944446425{\&}partnerID=tZOtx3y1

[192] M. J. Frisch, G. W. Trucks, H. B. Schlegel, G. E. Scuseria *et al.*, *Gaussian 03, Revision C.02*, 2004, vol. 24, no. 14. [Online]. Available: http://eutils.ncbi.nlm.nih.gov/entrez/eutils/elink.fcgi?cmd=prlinks{\&}dbfrom=pubmed{\&}retmode=ref{\&}id=12964193

[193] S. Boys and F. Bernardi, "The calculation of small molecular interactions by the differences of separate total energies. Some procedures with reduced errors," *Molecular Physics*, vol. 19, no. 4, pp. 553–566, oct 1970. [Online]. Available: http://www.tandfonline.com/doi/abs/10.1080/00268977000101561

[194] A. A. Mostofi, P. D. Haynes, C. K. Skylaris, and M. C. Payne, "ONETEP: Linear-scaling density-functional theory with plane-waves," in *2006 NSTI Nanotechnology Conference and Trade Show - NSTI Nanotech 2006 Technical Proceedings*, vol. 1, 2006, pp. 633–636. [Online]. Available: http://www.scopus.com/inward/record.url?eid=2-s2.0-33845189918{\&}partnerID=tZOtx3y1

[195] N. D. M. Hine, M. Robinson, P. D. Haynes, C.-K. Skylaris *et al.*, "Accurate ionic forces and geometry optimization in linear-scaling density-functional theory with local orbitals," *Physical Review B*, vol. 83, no. 19, p. 195102, may 2011. [Online]. Available: http://www.scopus.com/inward/record.url?eid=2-s2.0-79961102800{\&}partnerID=tZOtx3y1

[196] "OPIUM pseudopotential generation package." [Online]. Available: http://opium.sourceforge.net/

[197] J. P. Perdew, "Self-interaction correction to density-functional approximations for many-electron systems," *Physical Review B*, vol. 23, no. 10, pp. 5048–5079, may 1981. [Online]. Available: http://www.scopus.com/inward/record.url?eid=2-s2.0-26144450583{\&}partnerID=tZOtx3y1

[198] L. P. Lee, D. J. Cole, M. C. Payne, and C.-K. Skylaris, "Natural bond orbital analysis in the ONETEP code: applications to large protein systems." *Journal of computational chemistry*, vol. 34, no. 6, pp. 429–44, mar 2013. [Online]. Available: http://www.scopus.com/inward/record.url?eid=2-s2.0-84873450915{\&}partnerID=tZOtx3y1

[199] J. Wang, R. R. M. Wolf, J. W. Caldwell, P. a. Kollman *et al.*, "Development and testing of a general amber force field." *Journal of computational chemistry*, vol. 25, no. 9, pp. 1157–74, 2004. [Online]. Available: http://onlinelibrary.wiley.com/doi/10.1002/jcc.20035/full$\backslash$nhttp://www.ncbi.nlm.nih.gov/pubmed/15116359

[200] J. Wang, W. Wang, P. a. Kollman, and D. a. Case, "Antechamber, An Accessory Software Package For Molecular Mechanical Calculations," *Journal of computational chemistry*, vol. 25, no. 2, pp. 1157–1174, 2005.

[201] W. Humphrey, A. Dalke, and K. Schulten, "VMD: Visual molecular dynamics," *Journal of Molecular Graphics*, vol. 14, no. 1, pp. 33–38, 1996.

[202] C. F. Macrae, P. R. Edgington, P. McCabe, E. Pidcock *et al.*, "Mercury: Visualization and analysis of crystal structures," pp. 453–457, 2006.

[203] "VirtualChemistry.org." [Online]. Available: http://virtualchemistry.org/

[204] "Moltemplate." [Online]. Available: http://www.moltemplate.org/

[205] L. Ruiz and S. Keten, "Multi Scale Modeling of Elasticity and Fracture in Organic Nanotubes," *Journal of Engineering Mechanics*, no. March, p. 371, 2012.

[206] B. a. Luty, M. E. Davis, I. G. Tironi, and W. F. Van Gunsteren, "A Comparison of Particle-Particle, Particle-Mesh and Ewald Methods for Calculating Electrostatic Interactions in Periodic Molecular Systems," *Molecular Simulation*, vol. 14, no. 1, pp. 11–20, 1994.

[207] J. Norberg and L. Nilsson, "On the truncation of long-range electrostatic interactions in DNA." *Biophysical journal*, vol. 79, no. 3, pp. 1537–53, sep 2000. [Online]. Available: http://www.sciencedirect.com/science/article/pii/S0006349500764058

[208] A. Grossfield, "WHAM: the weighted histogram analysis method." [Online]. Available: http://membrane.urmc.rochester.edu/content/wham

[209] Y. Deng and B. Roux, "Hydration of Amino Acid Side Chains: Nonpolar and Electrostatic Contributions Calculated from Staged Molecular Dynamics Free Energy Simulations with Explicit Water Molecules," *The Journal of Physical Chemistry B*, vol. 108, no. 42, pp. 16 567–16 576, oct 2004. [Online]. Available: http://www.scopus.com/inward/record.url?eid=2-s2.0-7544232432{\&}partnerID=tZOtx3y1

[210] T. C. Beutler, A. E. Mark, R. C. van Schaik, P. R. Gerber *et al.*, "Avoiding singularities and numerical instabilities in free energy calculations based on molecular simulations," *Chemical Physics Letters*, vol. 222, no. 6, pp. 529–539, 1994.

[211] P. Liu, F. Dehez, W. Cai, and C. Chipot, "A Toolkit for the Analysis of Free-Energy Perturbation Calculations," *Journal of Chemical Theory and Computation*, vol. 8, no. 8, pp. 2606–2616, aug 2012. [Online]. Available: http://pubs.acs.org/doi/full/10.1021/ct300242f{\#}notes-1

[212] J. Koca, C.-G. Zhan, R. C. Rittenhouse, and R. L. Ornstein, "Coordination number of zinc ions in the phosphotriesterase active site by molecular dynamics and quantum mechanics." *Journal of computational chemistry*, vol. 24, no. 3, pp. 368–78, feb 2003. [Online]. Available: http://www.ncbi.nlm.nih.gov/pubmed/12548728

[213] L. W. Chung, H. Hirao, X. Li, and K. Morokuma, "The ONIOM method: Its foundation and applications to metalloenzymes and photobiology," pp. 327–350, 2012.

[214] A. Lauria, R. Bonsignore, A. Terenzi, A. Spinello *et al.*, "Nickel(II), copper(II) and zinc(II) metallo-intercalators: structural details of the DNA-binding by a combined experimental and computational investigation." *Dalton transactions (Cambridge, England : 2003)*, vol. 43, no. 16, pp. 6108–19, apr 2014. [Online]. Available: http://pubs.rsc.org/en/content/articlehtml/2014/dt/c3dt53066c

[215] A. W. Kleij, M. Kuil, M. Lutz, D. M. Tooke *et al.*, "Supramolecular zinc(II)salphen motifs: Reversible dimerization and templated dimeric structures," *Inorganica Chimica Acta*, vol. 359, no. 6, pp. 1807–1814, apr 2006. [Online]. Available: http://www.sciencedirect.com/science/article/pii/S0020169305003774

Appendix A

"Rings-and-rods" networks simulation data

A.1 Connectivity strategy comparison

This section covers the data collected during the comparison of rod elimination strategies. Each method is described by a table and two figures. The table contains the averaged data, used in the main text:

η - scaling parameter, $\eta = {}^2\sqrt{S/\pi}/\mathcal{D}_\mathcal{R}$;

$\mathcal{S}_\mathcal{R}$ - average surface per ring;

$P_{connect}$ - probability to get connected network;

$\mathcal{N}_{c/\mathcal{R}}$ - full number of connections per ring (including rods and point contacts);

$\mathcal{N}_{r/\mathcal{R}}^{NZ}$ - number of non-zero long rods per ring;

ϕ_{surf}^{L} - lower estimate for CNT surface fraction, calculated as $\phi_{surf}^{L} = {}^{S_{CNT}}\frac{L_{net}}{l_{CNT}}/S_{box}$, where $S_{CNT} = l_{CNT}d_{CNT}$ - average area of nanotube's projection on the sample's plane, L_{net} - total length of the simulated network, S_{box} - the surface area of a simulation box;

ϕ_{surf}^{V} - upper estimate for CNT surface fraction, calculated as $\phi_{surf}^{V} = {}^{S_{CNT}}\frac{V_{net}}{V_{CNT}}/S_{box}$, where V_{net} - total volume of the simulated network, $V_{CNT} = l_{CNT}\frac{\pi d_{CNT}^2}{4}$ - average volume of a nanotube.

The first of the two pictures represent the convergence of sample sheet resistance with simulation box size (colour refer to average surface per ring, $\mathcal{S}_\mathcal{R}$):

points - results of single calculations (with random horizontal displacement for better visibility);

circles - average sheet resistance at fixed box size and $\mathcal{S}_\mathcal{R}$;

bars - confidence interval with 95% probability;

lines - average sheet resistance at fixed $\mathcal{S}_\mathcal{R}$ (where it converged with box size).

The convergence was checked as follows: after all means $m_{\mathcal{S}_\mathcal{R},b}$ and standard deviations $s_{\mathcal{S}_\mathcal{R},b}$ were calculated for each pair of $\mathcal{S}_\mathcal{R}$ and simulation box length b where $P_{CNT} \geq 45\%$, a 2-tailed Welch's t-test was conducted for each pair of adjacent points $(\mathcal{S}_\mathcal{R}; b_i)$ and $(\mathcal{S}_\mathcal{R}; b_{i-1})$. If the means were found to belong to the same distribution with 90% probability at least for the last two box sizes, the calculation was considered converged. In this case the result for the largest box length (equal to 300 μm) was used as the sheet resistance for fixed $\mathcal{S}_\mathcal{R}$.

The last picture shows change of the sheet resistance with the ring's density (characterized by the average surface per ring $\mathcal{S}_\mathcal{R}$):

points - results of single calculations (with random horizontal displacement for better visibility);

circles - average sheet resistance at $\mathcal{S}_\mathcal{R}$ calculated at the largest box size;

line - connect the circles, where convergence was achieved.

Method: "FULL"

η	$\mathcal{S}_\mathcal{R}$, μm^2	$P_{connect}$,%	R, a.u.	$\mathcal{N}_{c/\mathcal{R}}$	$\mathcal{N}_{r/\mathcal{R}}^{NZ}$	ϕ_{surf}^{L},surf. %	ϕ_{surf}^{V},surf. %
2.69	25.00	100	336±25	4.28±0.19	3.89±0.25	0.80±0.20	13.80±4.10
3.18	35.01	100	593±28	3.87±0.21	3.60±0.22	0.60±0.20	10.20±2.90
3.60	45.00	100	1,078±45	3.49±0.20	3.28±0.22	0.50±0.10	7.90±2.20
3.99	55.01	100	2,375±157	3.16±0.22	2.99±0.24	0.40±0.10	6.30±1.80
4.33	64.98	86	8,090±881	2.86±0.23	2.72±0.22	0.30±0.10	5.20±1.50
4.65	75.00	16	-	2.62±0.21	2.49±0.21	0.30±0.10	4.40±1.20
4.95	84.99	4	-	2.41±0.21	2.30±0.21	0.20±0.10	3.70±1.10

Table A.1: Method: "FULL" Parameter set: Pristine

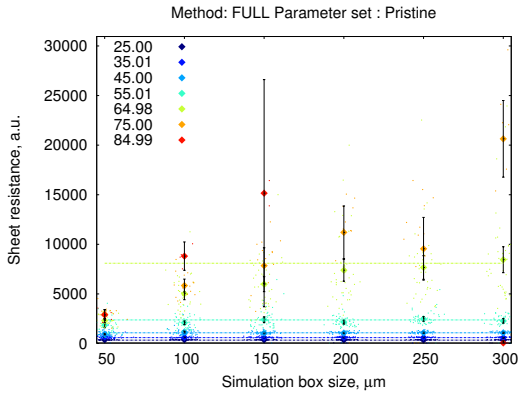

Figure A.1: Convergence of sample resistance with size for different $\mathcal{S}_{\mathcal{R}}$, method "FULL" pristine

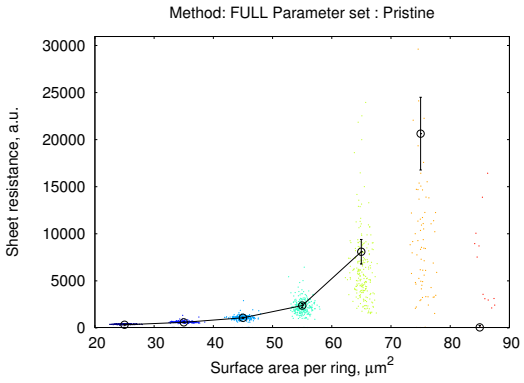

Figure A.2: Variation of the sheet resistance with ring's density, method "FULL" pristine

η	$\mathcal{S}_{\mathcal{R}}$, μm^2	$P_{connect}$,%	R, a.u.	$\mathcal{N}_{c/\mathcal{R}}$	$\mathcal{N}_{r/\mathcal{R}}^{NZ}$	ϕ_{surf}^{L},surf. %	ϕ_{surf}^{V},surf. %
1.02	25.00	100.00	405±21	5.41±0.24	3.98±0.29	1.00±0.30	10.70±3.10
1.21	35.01	100.00	486±22	5.34±0.23	4.06±0.28	0.90±0.30	9.00±2.60
1.37	45.00	100.00	585±10	5.24±0.22	4.10±0.27	0.80±0.20	7.90±2.20
1.52	55.01	100.00	642±22	5.11±0.22	4.13±0.27	0.70±0.20	7.00±2.00
1.65	64.98	100.00	706±29	5.00±0.22	4.16±0.26	0.60±0.20	6.40±1.80
1.77	75.00	100.00	803±14	4.90±0.21	4.16±0.25	0.60±0.20	5.90±1.70
1.89	84.99	100.00	869±16	4.82±0.20	4.17±0.25	0.50±0.10	5.40±1.50

Table A.2: Method: "FULL" Parameter set: CNT-filled

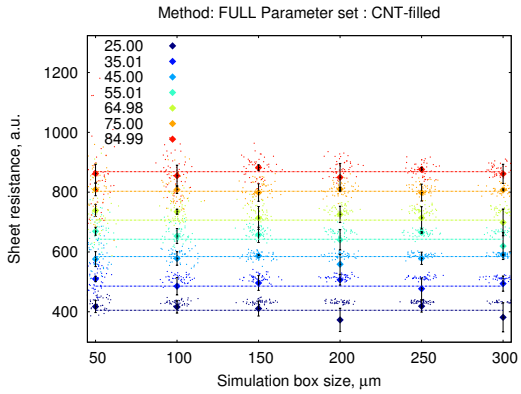

Figure A.3: Convergence of sample resistance with size for different $\mathcal{S}_{\mathcal{R}}$, method "FULL" CNT-filled

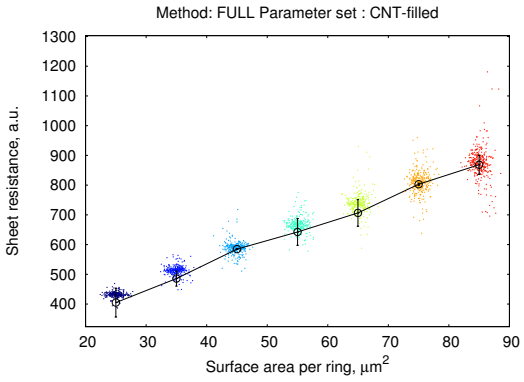

Figure A.4: Variation of the sheet resistance with ring's density, method "FULL" CNT-filled

Method: "STAT_RND"

η	$\mathcal{S}_{\mathcal{R}}$, μm^2	$P_{connect}$,%	R, a.u.	$\mathcal{N}_{c/\mathcal{R}}$	$\mathcal{N}_{r/\mathcal{R}}^{NZ}$	ϕ_{surf}^{L},surf. %	ϕ_{surf}^{V},surf. %
2.69	25.00	100	1,477±82	2.84±0.25	2.45±0.24	0.70±0.20	11.50±3.30
3.18	35.01	100	2,095±92	2.84±0.24	2.57±0.23	0.50±0.20	8.80±2.50
3.60	45.00	100	3,377±251	2.84±0.24	2.63±0.23	0.40±0.10	7.10±2.00
3.99	55.01	96	5,623±530	2.84±0.23	2.67±0.22	0.40±0.10	6.00±1.70
4.33	64.98	80	8,876±980	2.83±0.23	2.69±0.22	0.30±0.10	5.10±1.50
4.65	75.00	20	-	2.62±0.21	2.50±0.21	0.30±0.10	4.40±1.20
4.95	84.99	2	-	2.41±0.21	2.30±0.21	0.20±0.10	3.70±1.10

Table A.3: Method: "STAT_RND" Parameter set: Pristine

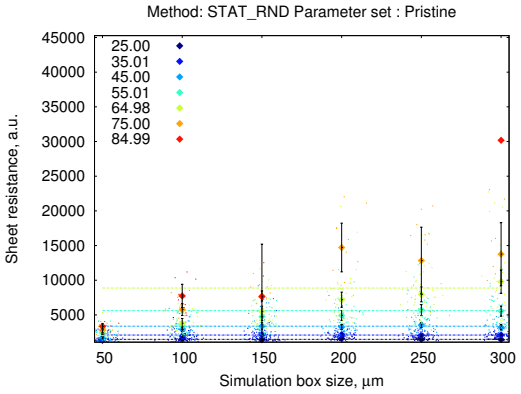

Figure A.5: Convergence of sample resistance with size for different $\mathcal{S}_{\mathcal{R}}$, method "STAT_RND" pristine

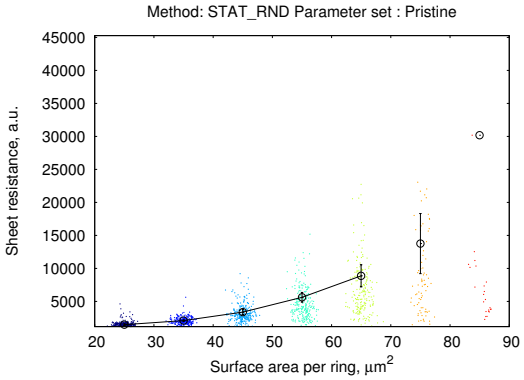

Figure A.6: Variation of the sheet resistance with ring's density, method "STAT_RND" pristine

η	$\mathcal{S}_{\mathcal{R}}$, μm^2	$P_{connect}$,%	R, a.u.	$\mathcal{N}_{c/\mathcal{R}}$	$\mathcal{N}_{r/\mathcal{R}}^{NZ}$	ϕ_{surf}^{L},surf. %	ϕ_{surf}^{V},surf. %
1.02	25.00	94	10,174±1,083	2.84±0.36	1.40±0.20	0.90±0.20	8.90±2.50
1.21	35.01	96	8,272±794	2.84±0.35	1.55±0.21	0.70±0.20	7.50±2.10
1.37	45.00	98	7,263±730	2.84±0.33	1.71±0.22	0.60±0.20	6.50±1.90
1.52	55.01	100	5,717±409	2.84±0.32	1.88±0.24	0.60±0.20	5.80±1.70
1.65	64.98	100	5,057±391	2.84±0.31	2.00±0.26	0.50±0.10	5.30±1.50
1.77	75.00	100	5,057±309	2.84±0.29	2.10±0.25	0.50±0.10	4.80±1.40
1.89	84.99	100	5,014±319	2.84±0.29	2.17±0.25	0.40±0.10	4.40±1.30

Table A.4: Method: "STAT_RND" Parameter set: CNT-filled

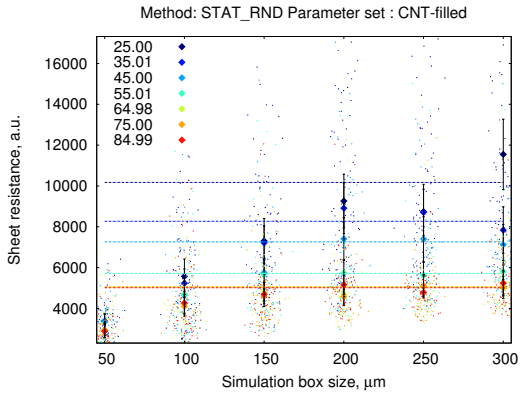

Figure A.7: Convergence of sample resistance with size for different $\mathcal{S}_{\mathcal{R}}$, method "STAT_RND" CNT-filled

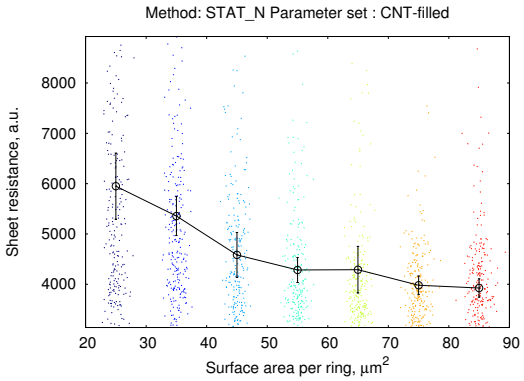

Figure A.8: Variation of the sheet resistance with ring's density, method "STAT_RND" CNT-filled

Method: "STAT_N"

η	$\mathcal{S}_{\mathcal{R}}$, μm^2	$P_{connect}$,%	R, a.u.	$\mathcal{N}_{c/\mathcal{R}}$	$\mathcal{N}_{r/\mathcal{R}}^{NZ}$	ϕ_{surf}^{L},surf. %	ϕ_{surf}^{V},surf. %
2.69	25.00	100	1,299±56	2.84±0.23	2.44±0.22	0.70±0.20	11.40±3.20
3.18	35.01	100	1,795±69	2.84±0.22	2.57±0.22	0.50±0.20	8.80±2.50
3.60	45.00	100	2,877±325	2.84±0.22	2.63±0.21	0.40±0.10	7.10±2.00
3.99	55.01	100	4,947±344	2.84±0.22	2.67±0.21	0.40±0.10	6.00±1.70
4.33	64.98	84	9,369±950	2.84±0.22	2.69±0.22	0.30±0.10	5.20±1.50
4.65	75.00	14	-	2.62±0.21	2.49±0.21	0.30±0.10	4.40±1.20
4.95	84.99	4	-	2.41±0.21	2.30±0.21	0.20±0.10	3.80±1.10

Table A.5: Method: "STAT_N" Parameter set: Pristine

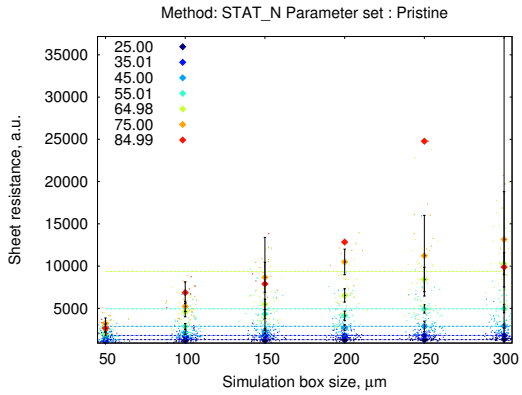

Figure A.9: Convergence of sample resistance with size for different $\mathcal{S}_{\mathcal{R}}$, method "STAT_N" pristine

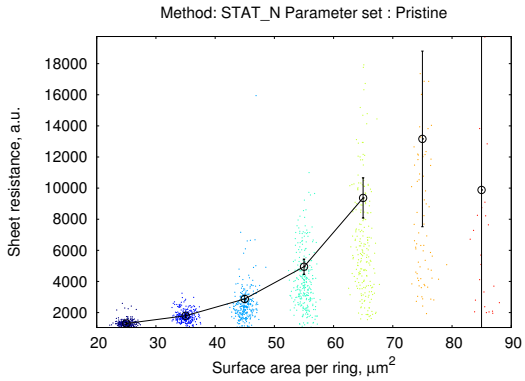

Figure A.10: Variation of the sheet resistance with ring's density, method "STAT_N" pristine

η	$\mathcal{S}_{\mathcal{R}}$, μm^2	$P_{connect}$,%	R, a.u.	$\mathcal{N}_{c/\mathcal{R}}$	$\mathcal{N}_{r/\mathcal{R}}^{NZ}$	ϕ_{surf}^{L},surf. %	ϕ_{surf}^{V},surf. %
1.02	25.00	100	5,950±490	2.84±0.34	1.40±0.20	0.90±0.20	8.90±2.50
1.21	35.01	100	5,356±337	2.84±0.33	1.54±0.21	0.70±0.20	7.50±2.10
1.37	45.00	100	4,584±385	2.84±0.31	1.70±0.22	0.60±0.20	6.50±1.90
1.52	55.01	100	4,285±213	2.84±0.30	1.87±0.24	0.60±0.20	5.80±1.70
1.65	64.98	100	4,290±256	2.84±0.28	1.99±0.25	0.50±0.10	5.30±1.50
1.77	75.00	100	3,981±123	2.84±0.27	2.10±0.25	0.50±0.10	4.80±1.40
1.89	84.99	100	3,926±174	2.84±0.26	2.19±0.24	0.40±0.10	4.40±1.30

Table A.6: Method: "STAT_N" Parameter set: CNT-filled

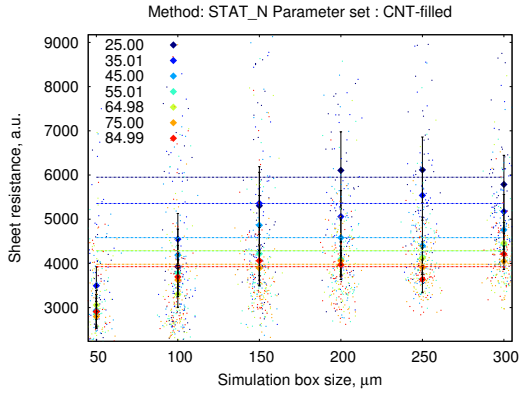

Figure A.11: Convergence of sample resistance with size for different $\mathcal{S}_{\mathcal{R}}$, method "STAT_N" CNT-filled

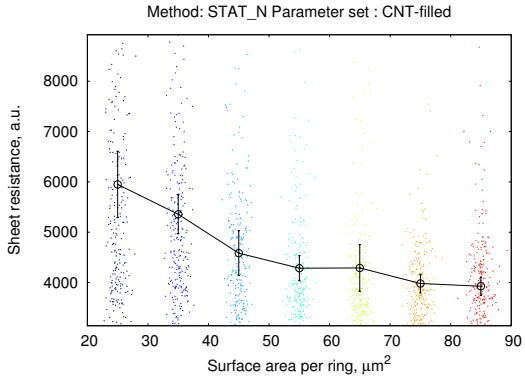

Figure A.12: Variation of the sheet resistance with ring's density, method "STAT_N" CNT-filled

Method: "STAT_N_NZ"

η	$\mathcal{S}_{\mathcal{R}}$, μm^2	$P_{connect}$,%	R, a.u.	$\mathcal{N}_{c/\mathcal{R}}$	$\mathcal{N}_{r/\mathcal{R}}^{NZ}$	ϕ_{surf}^{L},surf. %	ϕ_{surf}^{V},surf. %
2.69	25.00	100	724±40	3.23±0.22	2.84±0.24	0.70±0.20	12.00±3.40
3.18	35.01	100	1,018±88	3.11±0.23	2.84±0.23	0.60±0.20	9.10±2.60
3.60	45.00	100	1,823±79	3.04±0.23	2.84±0.22	0.50±0.10	7.40±2.10
3.99	55.01	100	3,127±238	3.01±0.23	2.84±0.23	0.40±0.10	6.20±1.70
4.33	64.98	86	7,551±714	2.87±0.23	2.74±0.22	0.30±0.10	5.20±1.50
4.65	75.00	18	-	2.62±0.21	2.49±0.21	0.30±0.10	4.40±1.20
4.95	84.99	0	-	2.41±0.21	2.30±0.21	0.20±0.10	3.70±1.10

Table A.7: Method: "STAT_N_NZ" Parameter set: Pristine

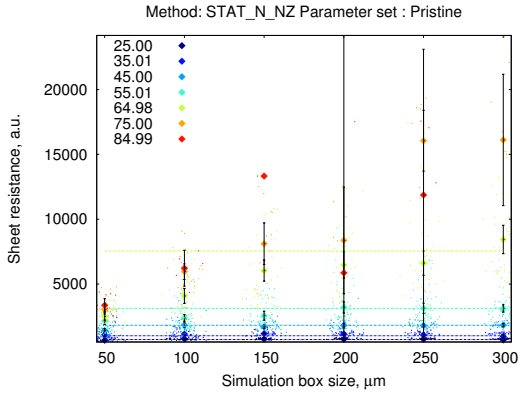

Figure A.13: Convergence of sample resistance with size for different $\mathcal{S}_{\mathcal{R}}$, method "STAT_N_NZ" pristine

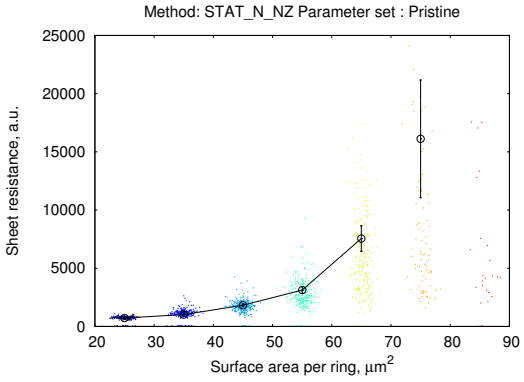

Figure A.14: Variation of the sheet resistance with ring's density, method "STAT_N_NZ" pristine

η	$\mathcal{S}_{\mathcal{R}}$, μm^2	$P_{connect}$,%	R, a.u.	$\mathcal{N}_{c/\mathcal{R}}$	$\mathcal{N}_{r/\mathcal{R}}^{NZ}$	ϕ_{surf}^{L},surf. %	ϕ_{surf}^{V},surf. %
1.02	25.00	100	646±27	4.27±0.31	2.84±0.26	1.00±0.30	9.90±2.80
1.21	35.01	100	818±27	4.14±0.30	2.84±0.25	0.80±0.20	8.30±2.40
1.37	45.00	100	976±41	3.97±0.30	2.84±0.25	0.70±0.20	7.20±2.00
1.52	55.01	100	1,176±39	3.82±0.28	2.84±0.25	0.60±0.20	6.30±1.80
1.65	64.98	100	1,371±39	3.69±0.27	2.84±0.24	0.50±0.20	5.70±1.60
1.77	75.00	100	1,601±36	3.57±0.25	2.84±0.24	0.50±0.10	5.20±1.50
1.89	84.99	100	1,746±37	3.49±0.24	2.84±0.24	0.50±0.10	4.70±1.30

Table A.8: Method: "STAT_N_NZ" Parameter set: CNT-filled

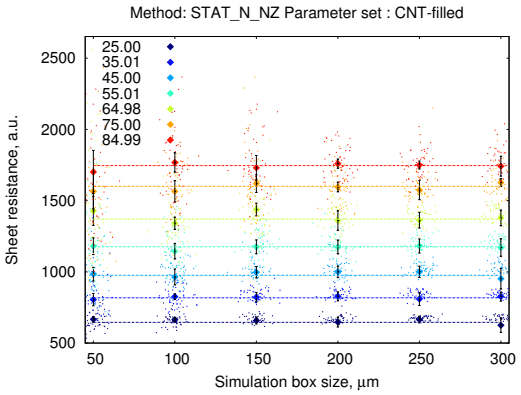

Figure A.15: Convergence of sample resistance with size for different $\mathcal{S}_{\mathcal{R}}$, method "STAT_N_NZ" CNT-filled

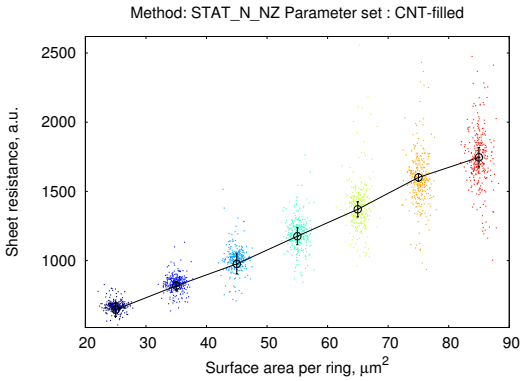

Figure A.16: Variation of the sheet resistance with ring's density, method "STAT_N_NZ" CNT-filled

Method: "STAT_N_L"

η	$\mathcal{S}_{\mathcal{R}}$, μm^2	$P_{connect}$,%	R, a.u.	$\mathcal{N}_{c/\mathcal{R}}$	$\mathcal{N}_{r/\mathcal{R}}^{NZ}$	ϕ_{surf}^{L},surf. %	ϕ_{surf}^{V},surf. %
2.69	25.00	100	1,258±59	2.84±0.12	2.44±0.16	0.60±0.20	10.40±3.00
3.18	35.01	100	1,493±96	2.84±0.13	2.57±0.15	0.50±0.10	8.20±2.30
3.60	45.00	100	2,170±116	2.84±0.15	2.63±0.16	0.40±0.10	6.80±1.90
3.99	55.01	100	3,795±232	2.84±0.18	2.67±0.18	0.40±0.10	5.80±1.70
4.33	64.98	86	8,039±885	2.83±0.22	2.69±0.22	0.30±0.10	5.10±1.50
4.65	75.00	18	-	2.62±0.21	2.50±0.21	0.30±0.10	4.40±1.20
4.95	84.99	2	-	2.40±0.21	2.29±0.22	0.20±0.10	3.70±1.10

Table A.9: Method: "STAT_N_L" Parameter set: Pristine

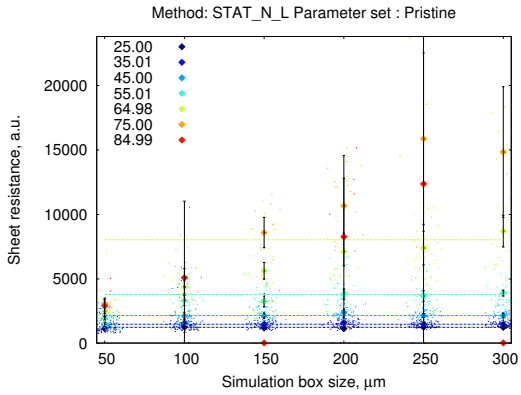

Figure A.17: Convergence of sample resistance with size for different $\mathcal{S}_{\mathcal{R}}$, method "STAT_N_L" pristine

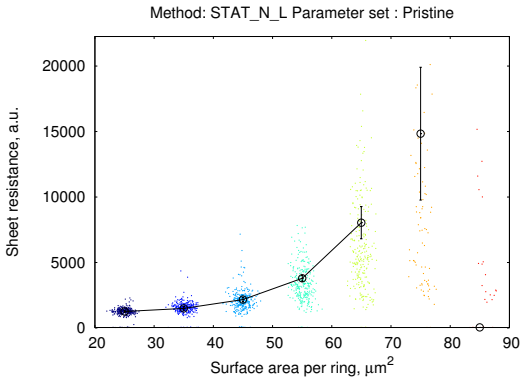

Figure A.18: Variation of the sheet resistance with ring's density, method "STAT_N_L" pristine

η	$\mathcal{S}_{\mathcal{R}}$, μm^2	$P_{connect}$,%	R, a.u.	$\mathcal{N}_{c/\mathcal{R}}$	$\mathcal{N}_{r/\mathcal{R}}^{NZ}$	ϕ_{surf}^{L},surf. %	ϕ_{surf}^{V},surf. %
1.02	25.00	76	15,505±1,673	2.84±0.22	1.40±0.19	0.80±0.20	8.50±2.40
1.21	35.01	98	11,066±884	2.84±0.20	1.54±0.20	0.70±0.20	7.10±2.00
1.37	45.00	96	8,185±733	2.84±0.19	1.71±0.20	0.60±0.20	6.20±1.80
1.52	55.01	98	6,087±457	2.84±0.17	1.87±0.21	0.50±0.10	5.40±1.50
1.65	64.98	100	5,372±295	2.84±0.16	2.00±0.22	0.50±0.10	4.90±1.40
1.77	75.00	100	4,787±260	2.84±0.15	2.09±0.21	0.40±0.10	4.40±1.30
1.89	84.99	100	4,705±256	2.84±0.15	2.19±0.20	0.40±0.10	4.10±1.20

Table A.10: Method: "STAT_N_L" Parameter set: CNT-filled

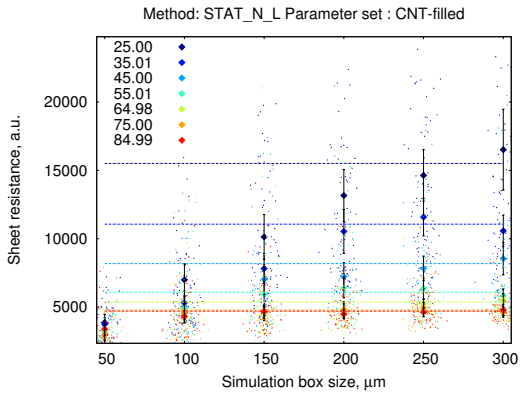

Figure A.19: Convergence of sample resistance with size for different $\mathcal{S}_{\mathcal{R}}$, method "STAT_N_L" CNT-filled

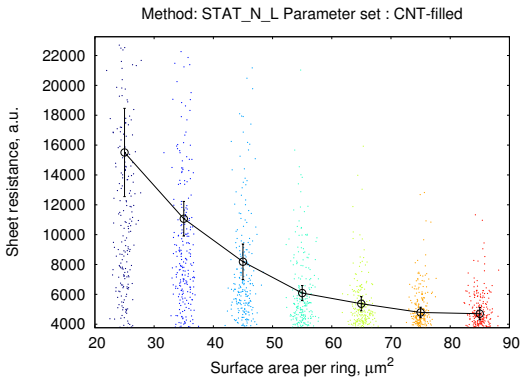

Figure A.20: Variation of the sheet resistance with ring's density, method "STAT_N_L" CNT-filled

Method: "STAT_ALN"

η	$\mathcal{S}_{\mathcal{R}}$, μm^2	$P_{connect}$,%	R, a.u.	$\mathcal{N}_{c/\mathcal{R}}$	$\mathcal{N}_{r/\mathcal{R}}^{NZ}$	ϕ_{surf}^{L},surf. %	ϕ_{surf}^{V},surf. %
2.69	25.00	100	809±48	2.84±0.10	2.44±0.13	0.60±0.20	10.60±3.00
3.18	35.01	100	1,027±55	2.84±0.09	2.57±0.11	0.50±0.10	8.40±2.40
3.60	45.00	100	1,485±77	2.84±0.12	2.63±0.12	0.40±0.10	6.90±2.00
3.99	55.01	100	2,860±187	2.84±0.16	2.67±0.16	0.40±0.10	5.90±1.70
4.33	64.98	90	8,079±693	2.84±0.22	2.69±0.21	0.30±0.10	5.10±1.50
4.65	75.00	20	-	2.62±0.21	2.50±0.21	0.30±0.10	4.40±1.20
4.95	84.99	2	-	2.41±0.21	2.30±0.21	0.20±0.10	3.70±1.10

Table A.11: Method: "STAT_ALN" Parameter set: Pristine

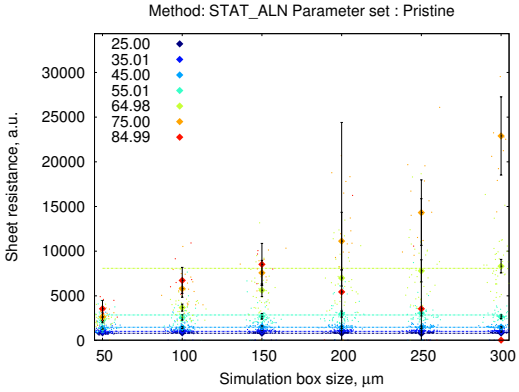

Figure A.21: Convergence of sample resistance with size for different $\mathcal{S}_{\mathcal{R}}$, method "STAT_ALN" pristine

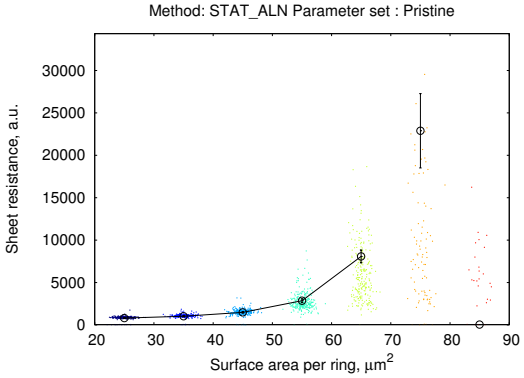

Figure A.22: Variation of the sheet resistance with ring's density, method "STAT_ALN" pristine

η	$\mathcal{S}_{\mathcal{R}}$, μm^2	$P_{connect}$,%	R, a.u.	$\mathcal{N}_{c/\mathcal{R}}$	$\mathcal{N}_{r/\mathcal{R}}^{NZ}$	ϕ_{surf}^{L},surf. %	ϕ_{surf}^{V},surf. %
1.02	25.00	98	9,367±1,079	2.84±0.27	1.40±0.14	0.90±0.20	9.00±2.50
1.21	35.01	100	6,230±507	2.84±0.25	1.55±0.14	0.70±0.20	7.60±2.20
1.37	45.00	100	4,976±340	2.84±0.24	1.71±0.14	0.60±0.20	6.70±1.90
1.52	55.01	100	4,957±302	2.84±0.24	1.86±0.15	0.60±0.20	6.10±1.70
1.65	64.98	100	5,366±295	2.84±0.26	1.99±0.17	0.50±0.20	5.60±1.60
1.77	75.00	100	5,144±388	2.84±0.32	2.09±0.16	0.50±0.10	4.80±1.40
1.89	84.99	100	3,808±152	2.84±0.14	2.19±0.19	0.40±0.10	4.10±1.20

Table A.12: Method: "STAT_ALN" Parameter set: CNT-filled

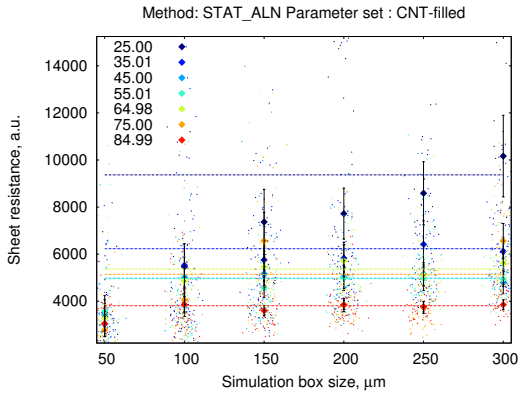

Figure A.23: Convergence of sample resistance with size for different $\mathcal{S}_{\mathcal{R}}$, method "STAT_ALN" CNT-filled

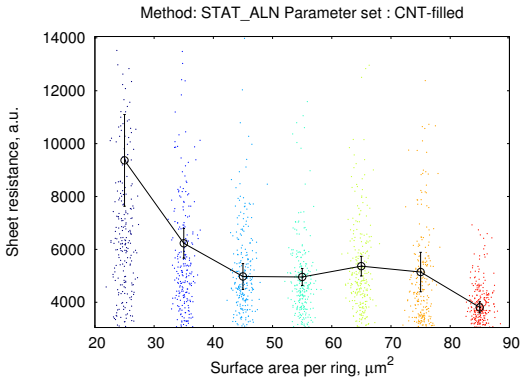

Figure A.24: Variation of the sheet resistance with ring's density, method "STAT_ALN" CNT-filled

Method: "COMP_ALN"

η	$\mathcal{S}_{\mathcal{R}}$, μm^2	$P_{connect}$,%	R, a.u.	$\mathcal{N}_{c/\mathcal{R}}$	$\mathcal{N}_{r/\mathcal{R}}^{NZ}$	ϕ_{surf}^{L},surf. %	ϕ_{surf}^{V},surf. %
2.69	25.00	100	4,118±390	2.84±0.20	2.44±0.19	0.60±0.20	9.90±2.80
3.18	35.01	100	3,246±263	2.84±0.19	2.57±0.18	0.50±0.10	7.80±2.20
3.60	45.00	100	3,384±241	2.84±0.18	2.62±0.17	0.40±0.10	6.60±1.90
3.99	55.01	100	3,470±182	2.84±0.18	2.67±0.17	0.40±0.10	5.80±1.60
4.33	64.98	90	7,832±784	2.83±0.21	2.69±0.21	0.30±0.10	5.10±1.50
4.65	75.00	10	-	2.62±0.21	2.50±0.21	0.30±0.10	4.40±1.20
4.95	84.99	0	-	2.41±0.21	2.30±0.21	0.20±0.10	3.80±1.10

Table A.13: Method: "COMP_ALN" Parameter set: Pristine

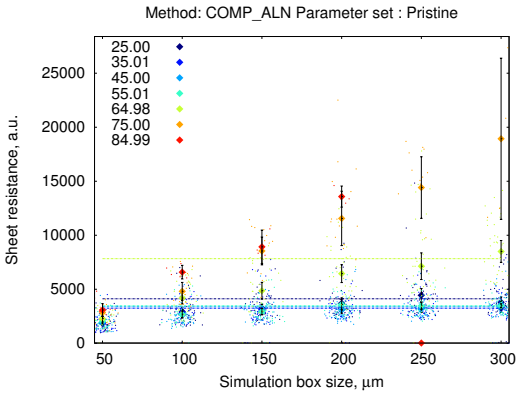

Figure A.25: Convergence of sample resistance with size for different $\mathcal{S}_{\mathcal{R}}$, method "COMP_ALN" pristine

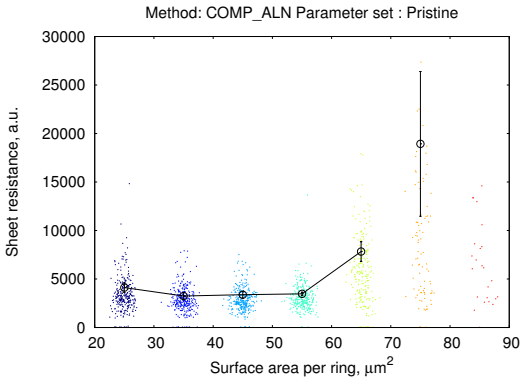

Figure A.26: Variation of the sheet resistance with ring's density, method "COMP_ALN" pristine

η	$\mathcal{S}_{\mathcal{R}}$, μm^2	$P_{connect}$,%	R, a.u.	$\mathcal{N}_{c/\mathcal{R}}$	$\mathcal{N}_{r/\mathcal{R}}^{NZ}$	ϕ_{surf}^{L},surf. %	ϕ_{surf}^{V},surf. %
1.02	25.00	100	4,320±258	2.84±0.19	1.41±0.17	0.80±0.20	8.60±2.40
1.21	35.01	100	3,570±182	2.84±0.17	1.55±0.17	0.70±0.20	7.20±2.00
1.37	45.00	100	3,006±127	2.84±0.16	1.71±0.17	0.60±0.20	6.20±1.70
1.52	55.01	100	2,710±64	2.84±0.15	1.86±0.18	0.50±0.10	5.40±1.50
1.65	64.98	100	2,651±102	2.84±0.15	2.00±0.18	0.50±0.10	4.80±1.40
1.77	75.00	100	5,001±328	2.84±0.20	2.09±0.19	0.40±0.10	4.30±1.20
1.89	84.99	100	2,674±74	2.84±0.14	2.18±0.16	0.40±0.10	4.00±1.10

Table A.14: Method: "COMP_ALN" Parameter set: CNT-filled

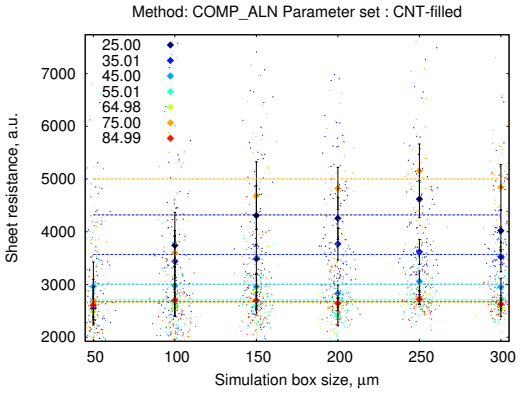

Figure A.27: Convergence of sample resistance with size for different $\mathcal{S}_{\mathcal{R}}$, method "COMP_ALN" CNT-filled

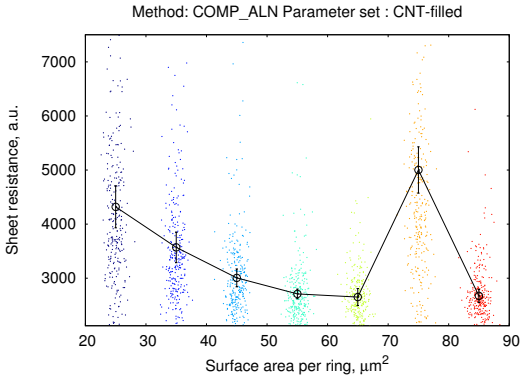

Figure A.28: Variation of the sheet resistance with ring's density, method "COMP_ALN" CNT-filled

Method: "STRETCH"

η	$\mathcal{S}_{\mathcal{R}}$, μm^2	$P_{connect}$,%	R, a.u.	$\mathcal{N}_{c/\mathcal{R}}$	$\mathcal{N}_{r/\mathcal{R}}^{NZ}$	ϕ_{surf}^{L},surf. %	ϕ_{surf}^{V},surf. %
2.69	25.00	100	1,608±97	2.84±0.30	2.84±0.30	0.70±0.20	12.20±3.50
3.18	35.01	100	3,083±210	2.84±0.26	2.84±0.26	0.50±0.20	8.90±2.50
3.60	45.00	100	5,229±427	2.84±0.24	2.84±0.24	0.40±0.10	7.00±2.00
3.99	55.01	86	8,765±872	2.84±0.23	2.69±0.22	0.40±0.10	5.80±1.60
4.33	64.98	82	8,321±776	2.83±0.22	2.70±0.22	0.30±0.10	5.10±1.50
4.65	75.00	20	-	2.61±0.21	2.49±0.21	0.30±0.10	4.40±1.20
4.95	84.99	2	-	2.41±0.21	2.30±0.21	0.20±0.10	3.70±1.10

Table A.15: Method: "STRETCH" Parameter set: Pristine

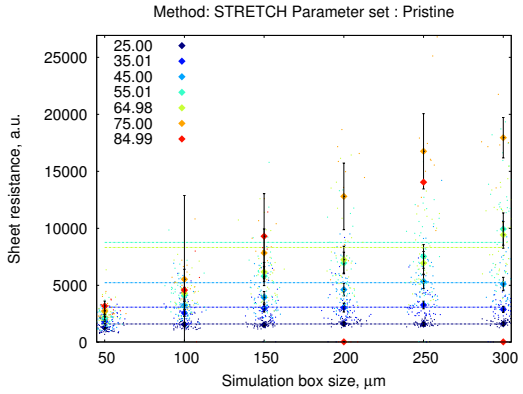

Figure A.29: Convergence of sample resistance with size for different $\mathcal{S}_{\mathcal{R}}$, method "STRETCH" pristine

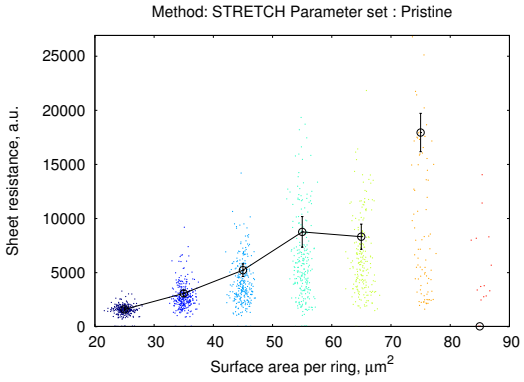

Figure A.30: Variation of the sheet resistance with ring's density, method "STRETCH" pristine

η	$\mathcal{S}_{\mathcal{R}}$, μm^2	$P_{connect}$,%	R, a.u.	$\mathcal{N}_{c/\mathcal{R}}$	$\mathcal{N}_{r/\mathcal{R}}^{NZ}$	ϕ_{surf}^{L},surf. %	ϕ_{surf}^{V},surf. %
1.02	25.00	100	1,546±54	2.84±0.33	2.84±0.33	1.00±0.30	10.50±3.00
1.21	35.01	100	1,797±83	2.84±0.33	2.84±0.33	0.90±0.20	8.80±2.50
1.37	45.00	100	2,064±76	2.84±0.33	2.84±0.33	0.70±0.20	7.70±2.20
1.52	55.01	100	2,328±79	2.84±0.34	2.84±0.34	0.70±0.20	6.80±1.90
1.65	64.98	100	2,511±97	2.84±0.34	2.84±0.34	0.60±0.20	6.20±1.80
1.77	75.00	100	2,795±79	2.84±0.34	2.84±0.34	0.50±0.20	5.60±1.60
1.89	84.99	100	2,991±63	2.84±0.34	2.84±0.34	0.50±0.10	5.20±1.50

Table A.16: Method: "STRETCH" Parameter set: CNT-filled

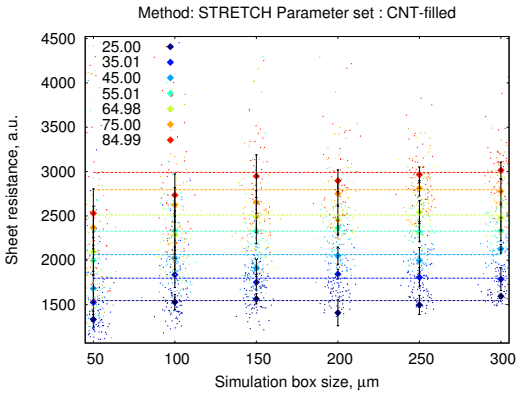

Figure A.31: Convergence of sample resistance with size for different $\mathcal{S}_{\mathcal{R}}$, method "STRETCH" CNT-filled

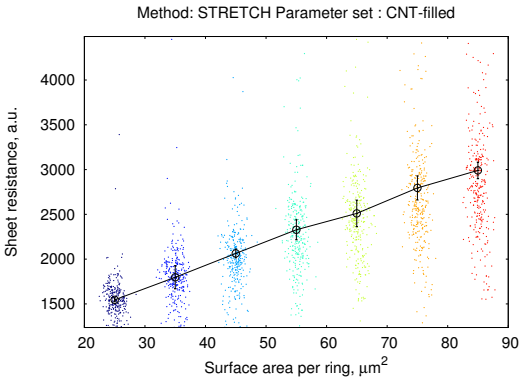

Figure A.32: Variation of the sheet resistance with ring's density, method "STRETCH" CNT-filled

Method: "CRIT_RAD"

η	$\mathcal{S}_{\mathcal{R}}$, μm^2	$P_{connect}$,%	R, a.u.	$\mathcal{N}_{c/\mathcal{R}}$	$\mathcal{N}_{r/\mathcal{R}}$	ϕ^L_{surf},surf. %	ϕ^V_{surf},surf. %
2.69	25.00	84	7,466±814	2.72±0.21	2.34±0.25	0.60±0.20	10.10±2.90
3.18	35.01	48	9,624±1,374	2.62±0.20	2.34±0.24	0.50±0.10	7.70±2.20
3.60	45.00	34	-	2.52±0.19	2.31±0.22	0.40±0.10	6.30±1.80
3.99	55.01	2	-	2.42±0.18	2.25±0.21	0.30±0.10	5.30±1.50
4.33	64.98	2	-	2.30±0.18	2.15±0.21	0.30±0.10	4.50±1.30
4.65	75.00	4	-	2.18±0.19	2.05±0.22	0.20±0.10	3.90±1.10
4.95	84.99	2	-	2.06±0.20	1.95±0.21	0.20±0.10	3.40±1.00

Table A.17: Method: "CRIT_RAD" Parameter set: Pristine

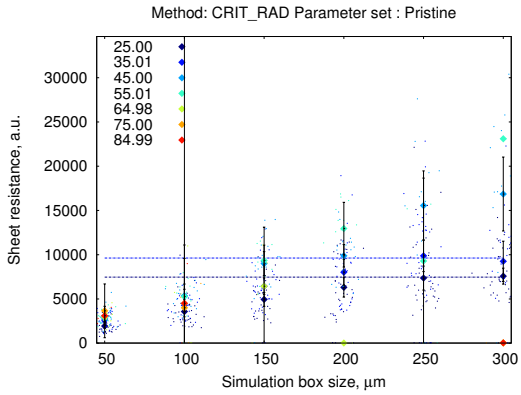

Figure A.33: Convergence of sample resistance with size for different $\mathcal{S}_{\mathcal{R}}$, method "CRIT_RAD" pristine

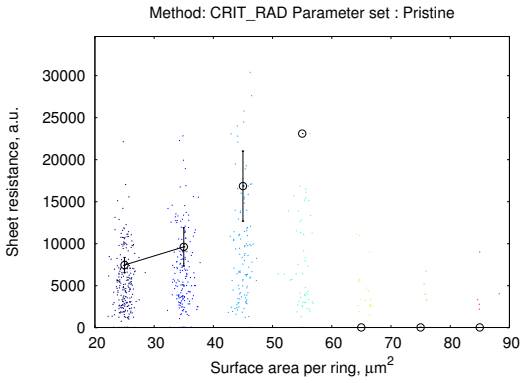

Figure A.34: Variation of the sheet resistance with ring's density, method "CRIT_RAD" pristine

η	$\mathcal{S}_{\mathcal{R}}$, μm^2	$P_{connect}$,%	R, a.u.	$\mathcal{N}_{c/\mathcal{R}}$	$\mathcal{N}_{r/\mathcal{R}}^{NZ}$	ϕ_{surf}^{L},surf. %	ϕ_{surf}^{V},surf. %
1.02	25.00	100	2,088±109	3.39±0.28	1.95±0.29	0.80±0.20	8.70±2.50
1.21	35.01	100	2,820±158	3.31±0.26	2.01±0.30	0.70±0.20	7.20±2.10
1.37	45.00	100	3,666±213	3.19±0.25	2.07±0.29	0.60±0.20	6.20±1.80
1.52	55.01	100	5,213±293	3.08±0.25	2.11±0.28	0.50±0.10	5.50±1.60
1.65	64.98	98	6,582±414	3.00±0.25	2.15±0.27	0.50±0.10	4.90±1.40
1.77	75.00	94	9,062±975	2.93±0.24	2.19±0.27	0.40±0.10	4.40±1.20
1.89	84.99	90	11,635±1,394	2.86±0.23	2.21±0.26	0.40±0.10	4.00±1.10

Table A.18: Method: "CRIT_RAD" Parameter set: CNT-filled

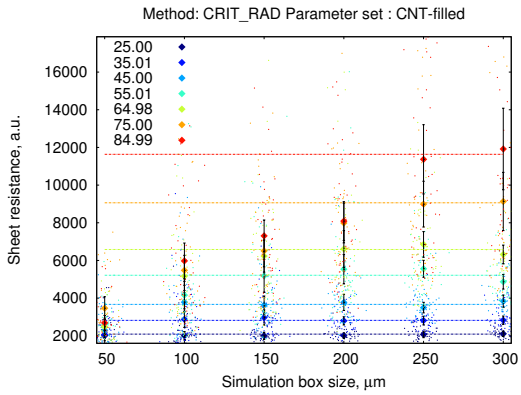

Figure A.35: Convergence of sample resistance with size for different $\mathcal{S}_{\mathcal{R}}$, method "CRIT_RAD" CNT-filled

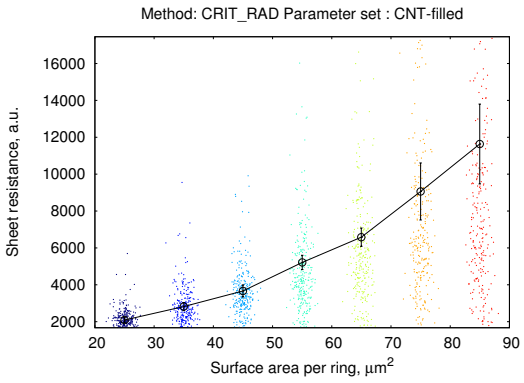

Figure A.36: Variation of the sheet resistance with ring's density, method "CRIT_RAD" CNT-filled

A.2 Percolation threshold calculations

As was explained in section 5.1.4 of main text, the network's connectivity rate and sheet resistance (or volume resistivity in 3D) were fitted to expressions 5.1.5 and 5.1.6:

$$P(\eta) = A\left(1 - \tanh\left(\alpha(\eta - \eta_0)\right)\right);$$

$$\rho(\eta) = \rho_0\left(\eta - \eta_C\right)^{\delta}.$$

For each target average number of rods per ring ($\mathcal{N}^T_{r/\mathcal{R}}$) the following parameters were estimated by non-linear least squares algorithm:

A normalization constant of sigmoid function (ideally equal to 0.5 for $P(0) = 1.0$);

α slope parameter of sigmoid function ($\alpha \to \infty$ for a abrupt transition);

η_0 inflection point of sigmoid function (in ideal case equal to η_C);

η_C is the critical scaling parameter, corresponding to percolation threshold;

ρ_0 and δ are the fitting parameters for equation 5.1.6;

r^2 is r-squared characteristic of the fitting $\rho(\eta)$ with equation 5.1.6.

$\mathcal{N}^T_{r/\mathcal{R}}$	$P(\eta)$			$\rho(\eta)$			
	A	α	η_0	η_C	ρ_0,10^3 a.u.	δ	r^2
2.0	-	-	-	-	-	-	-
2.2	0.28±0.04	5.0±5.0	4.27±0.11	4.04±0.34	10.9±0.2	-0.20±0.01	0.77
2.4	0.49±0.01	3.3±0.5	4.38±0.02	4.38±0.02	4.4±0.1	-0.40±0.01	0.88
2.6	0.50±0.01	4.3±0.5	4.47±0.02	4.47±0.02	2.2±0.0	-0.78±0.02	0.95
2.8	0.50±0.00	4.7±0.3	4.51±0.01	4.51±0.02	1.7±0.0	-0.63±0.02	0.83
3.0	0.50±0.00	5.9±0.4	4.50±0.01	4.50±0.00	1.5±0.0	-0.53±0.02	0.74

Table A.19: Variation of the fitting parameters with target number of connections per ring $\mathcal{N}_{r/\mathcal{R}}$ for pristine networks in 2D

$\mathcal{N}_{r/\mathcal{R}}^{T}$	$P(\eta)$			$\rho(\eta)$			
	A	α	η_0	η_C	ρ_0,10^6 a.u.	δ	r^2
2.0	-	-	-	-	-	-	-
2.2	0.41±0.04	1.7±0.8	6.65±0.15	6.53±0.20	0.064±0.000	-0.20±0.01	0.71
2.4	0.50±0.01	2.2±0.2	7.06±0.02	7.05±0.02	0.031±0.000	-0.63±0.01	0.93
2.6	0.50±0.01	2.8±0.3	7.20±0.02	7.20±0.02	0.021±0.000	-0.84±0.01	0.97
2.8	0.50±0.01	3.0±0.2	7.21±0.02	7.21±0.02	0.016±0.000	-0.94±0.01	0.97
3.0	0.50±0.01	2.6±0.2	7.16±0.02	7.16±0.02	0.013±0.000	-0.95±0.01	0.96

Table A.20: Variation of the fitting parameters with target number of connections per ring $\mathcal{N}_{r/\mathcal{R}}$ for CNT-intercalated networks in 2D

$\mathcal{N}_{r/\mathcal{R}}^{T}$	$P(\eta)$			$\rho(\eta)$			
	A	α	η_0	η_C	ρ_0,10^3 a.u.	δ	r^2
1.2	-	-	-	-	-	-	-
1.4	-	-	-	-	-	-	-
1.6	-	-	-	-	-	-	-
1.8	-	-	-	-	-	-	-
2.0	0.48±0.02	1.4±0.3	5.99±0.09	6.0±0.1	290.6±25.2	-0.35±0.05	0.41
2.2	0.50±0.01	3.1±1.5	6.51±0.07	6.5±0.1	242.6±21.5	-1.64±0.10	0.97
2.4	-	-	-	-	-	-	-
2.6	-	-	-	-	-	-	-
2.8	0.50±0.01	4.2±4.7	6.56±0.09	6.6±0.1	63.0±3.2	-1.61±0.05	0.99
3.0	-	-	-	-	-	-	-
3.2	0.50±0.01	5.9±33.6	6.51±0.72	6.5±0.7	47.3±1.4	-1.69±0.03	1.00
3.4	0.50±0.01	5.5±19.8	6.50±0.51	6.5±0.5	43.5±1.3	-1.80±0.03	1.00
3.6	0.50±0.01	4.0±2.7	6.53±0.07	6.5±0.1	43.4±0.8	-1.87±0.02	1.00
3.8	0.50±0.01	3.7±2.0	6.55±0.05	6.6±0.1	41.4±1.0	-1.91±0.03	1.00
4.0	0.50±0.01	4.6±5.0	6.52±0.13	6.5±0.1	39.1±1.3	-1.97±0.04	1.00

Table A.21: Variation of the fitting parameters with target number of connections per ring $\mathcal{N}_{r/\mathcal{R}}$ for pristine networks in 3D

$\mathcal{N}_{r/\mathcal{R}}^{T}$	$P(\eta)$			$\rho(\eta)$			
	A	α	η_0	η_C	ρ_0,10^3 a.u.	δ	r^2
1.2	-	-	-	-	-	-	-
1.4	-	-	-	-	-	-	-
1.6	-	-	-	-	-	-	-
1.8	-	-	-	-	-	-	-
2.0	0.48±0.01	0.9±0.1	9.47±0.09	9.4±0.1	9.4±0.6	-0.57±0.04	0.53
2.2	0.50±0.00	2.5±0.3	10.21±0.02	10.2±0.0	5.5±0.3	-1.06±0.04	0.83
2.4	0.50±0.00	2.8±0.1	10.35±0.01	10.4±0.0	4.7±0.3	-1.39±0.04	0.93
2.6	0.50±0.00	2.7±0.1	10.33±0.01	10.3±0.0	3.2±0.1	-1.41±0.03	0.95
2.8	0.50±0.00	3.0±0.1	10.38±0.01	10.4±0.0	3.2±0.1	-1.58±0.02	0.98
3.0	0.50±0.00	3.7±0.3	10.36±0.03	10.4±0.0	2.7±0.1	-1.62±0.03	0.97
3.2	0.50±0.00	3.3±0.1	10.37±0.01	10.4±0.0	2.6±0.1	-1.69±0.02	0.98
3.4	0.50±0.00	2.3±0.1	10.35±0.01	10.4±0.0	2.4±0.1	-1.71±0.02	0.98
3.6	0.50±0.00	2.8±0.0	10.43±0.00	10.4±0.0	2.6±0.1	-1.84±0.03	0.98
3.8	0.50±0.00	2.6±0.0	10.44±0.00	10.4±0.0	2.7±0.1	-1.92±0.02	0.99
4.0	0.50±0.00	2.4±0.1	10.41±0.02	10.4±0.0	2.6±0.1	-1.95±0.02	0.99

Table A.22: Variation of the fitting parameters with target number of connections per ring $\mathcal{N}_{r/\mathcal{R}}$ for CNT-intercalated networks in 3D

Appendix B

MD simulation of tetrakis-Schiff complex

B.1 Diffusion of a single molecule in solvent

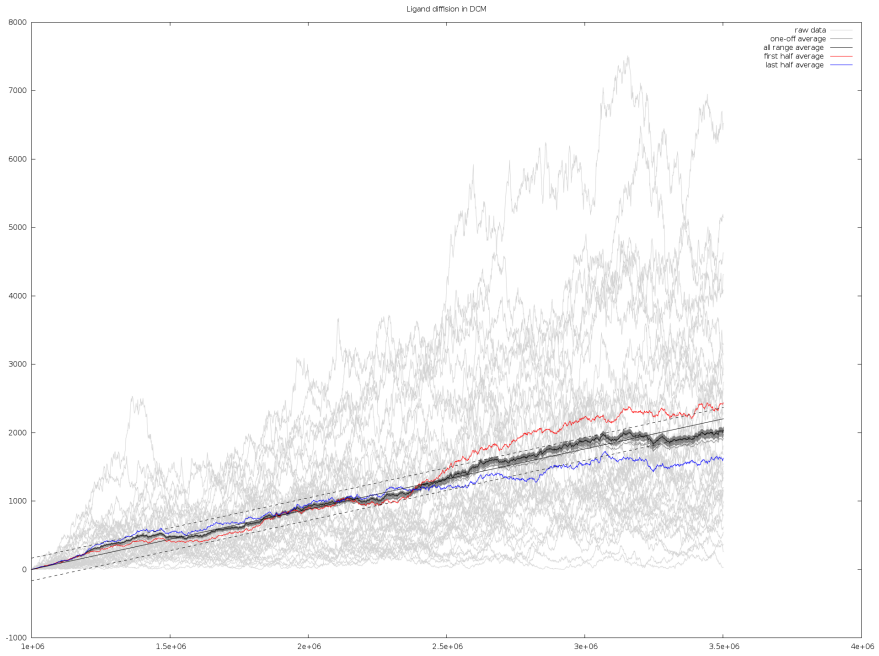

Figure B.1: Displacement of the single tetrakis-Schiff complex in DCM: light grey - the results of independent simulations, dark grey - "one-off" averages, blue an red lines are correspondingly the averages of the simulations, starting from "closed" and "opened" conformations, black - average over all trajectories.

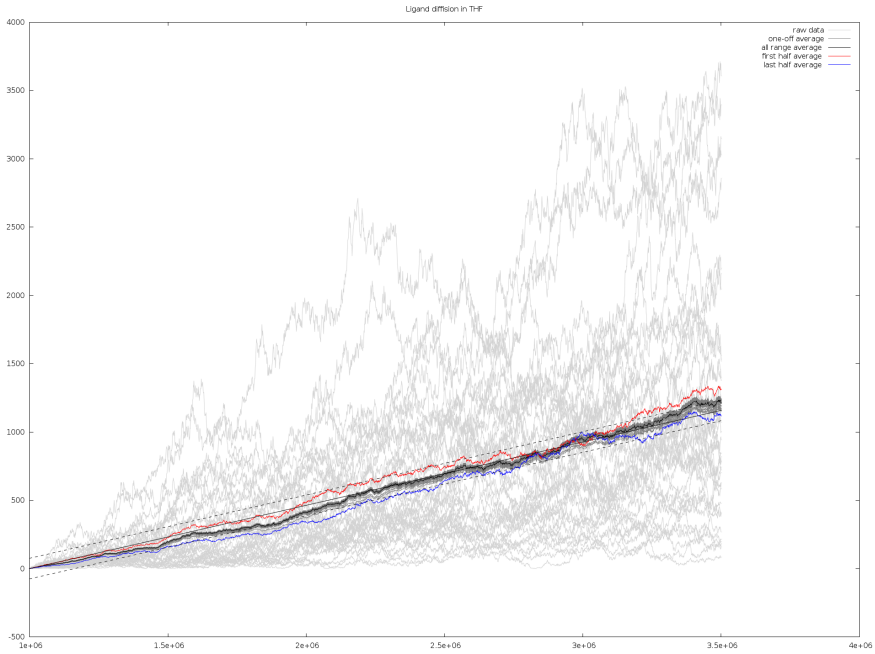

Figure B.2: Displacement of the single tetrakis-Schiff complex in THF: light grey - the results of independent simulations, dark grey - “one-off” averages, blue an red lines are correspondingly the averages of the simulations, starting from “closed” and “opened” conformations, black - average over all trajectories.

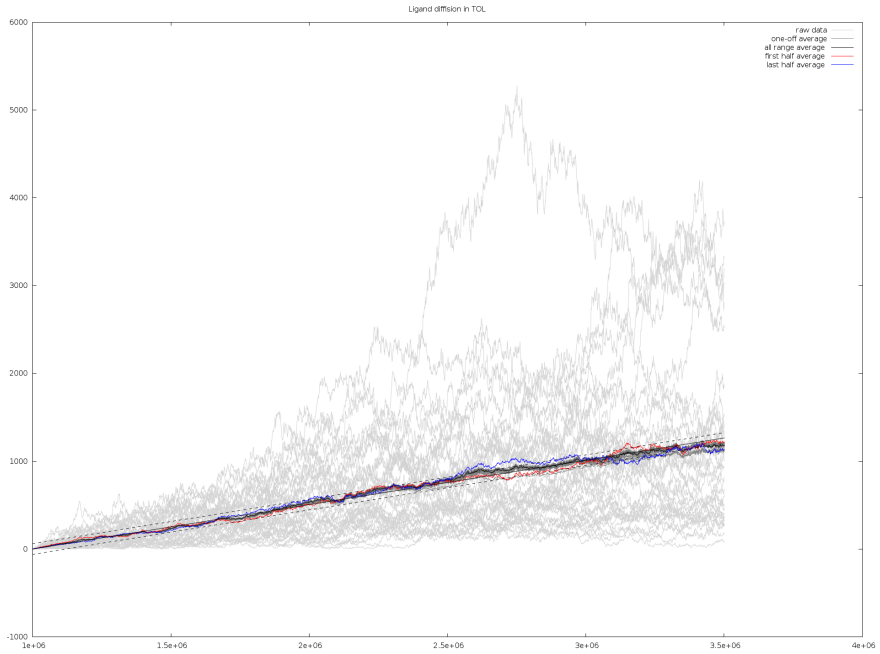

Figure B.3: Displacement of the single tetrakis-Schiff complex in toluene: light grey - the results of independent simulations, dark grey - “one-off” averages, blue an red lines are correspondingly the averages of the simulations, starting from “closed” and “opened” conformations, black - average over all trajectories.

B.2 Evolution of 8-molecular chains in solvent

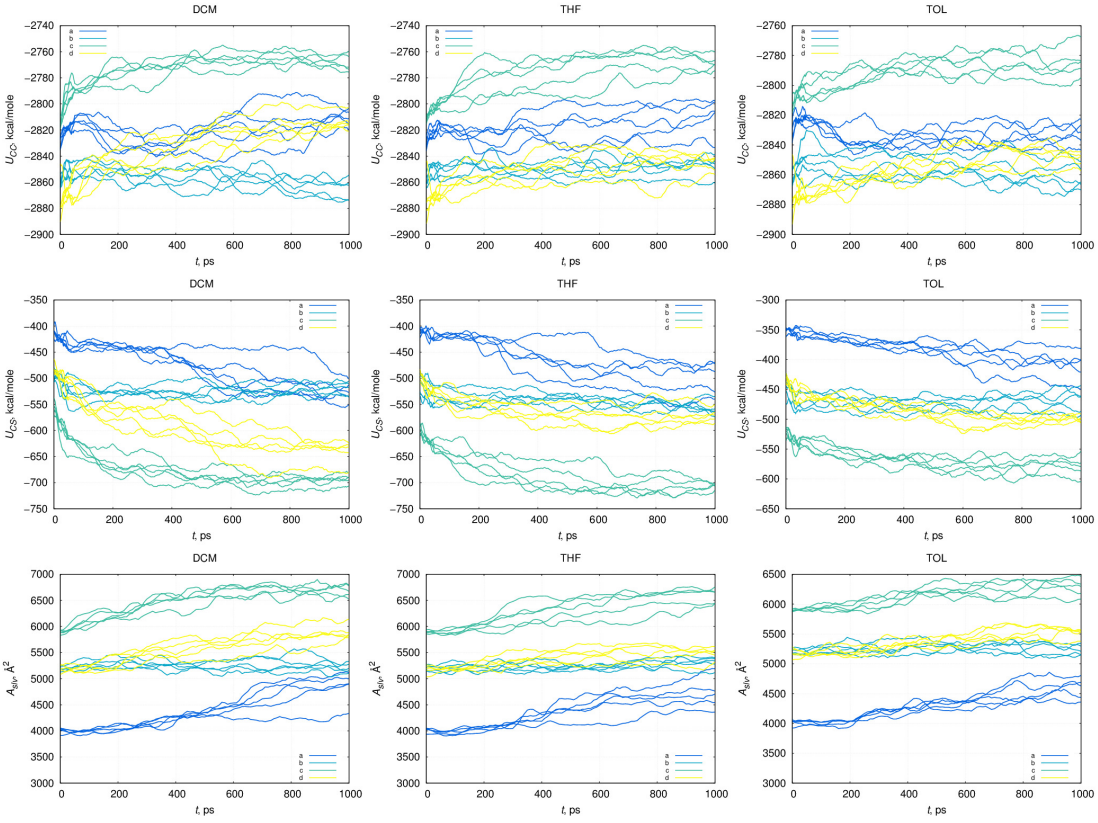

Figure B.4: Evolution of the 8-molecular tetrakis-Schiff chains in explicit solvent: complex-to-complex pair interaction (U_{CC}), complex-to-solvent pair interaction (U_{CS}) and the chain's surface area (A_{slv}) - averaged over 50 ps

B.3 Variation of tetrakis-Schiff self-interaction during solvation FEP calculation

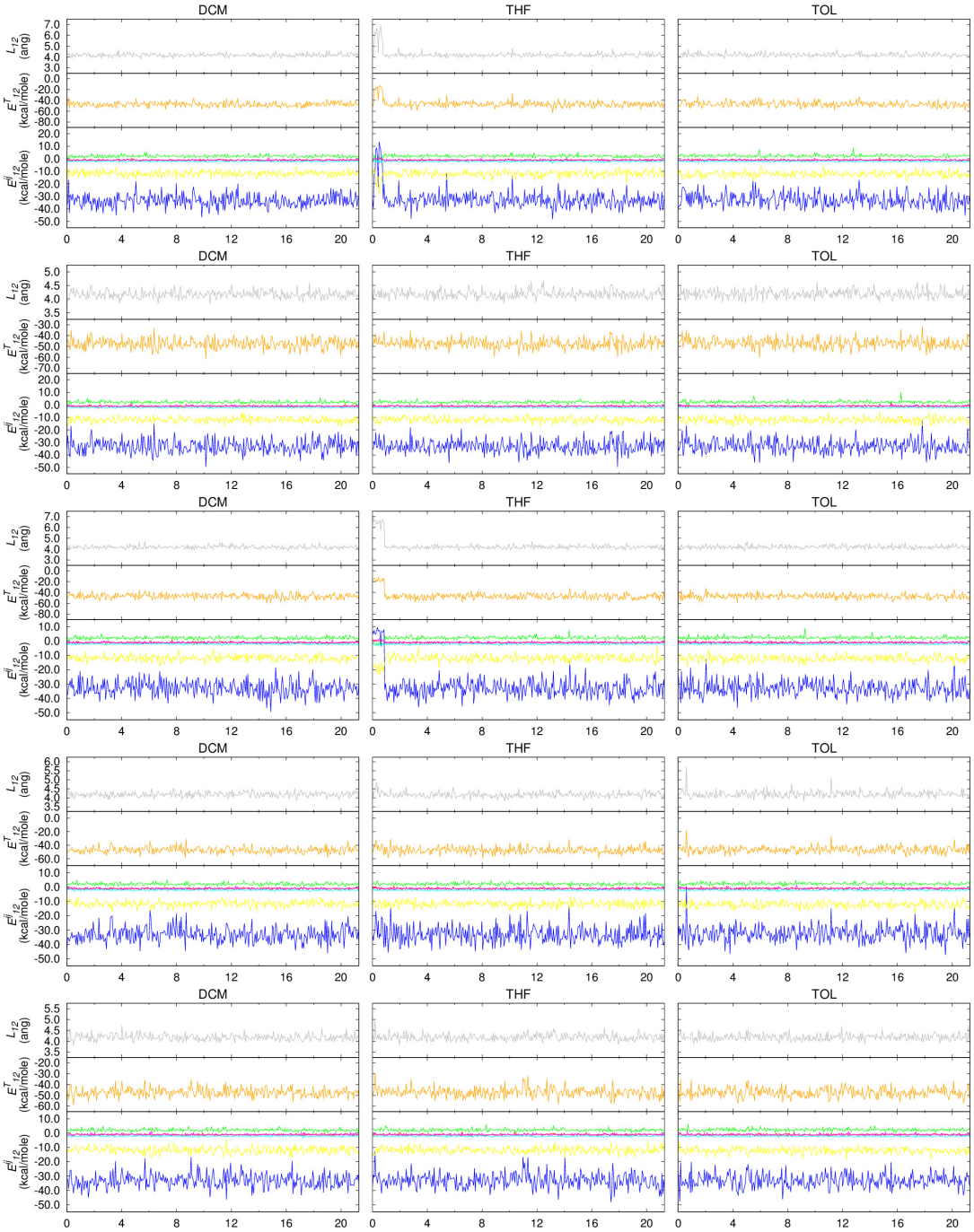

Figure B.5: Variation of complex-to-complex interaction in tetrakis-Schiff zinc-complex closed monomer during solution FEP simulations.

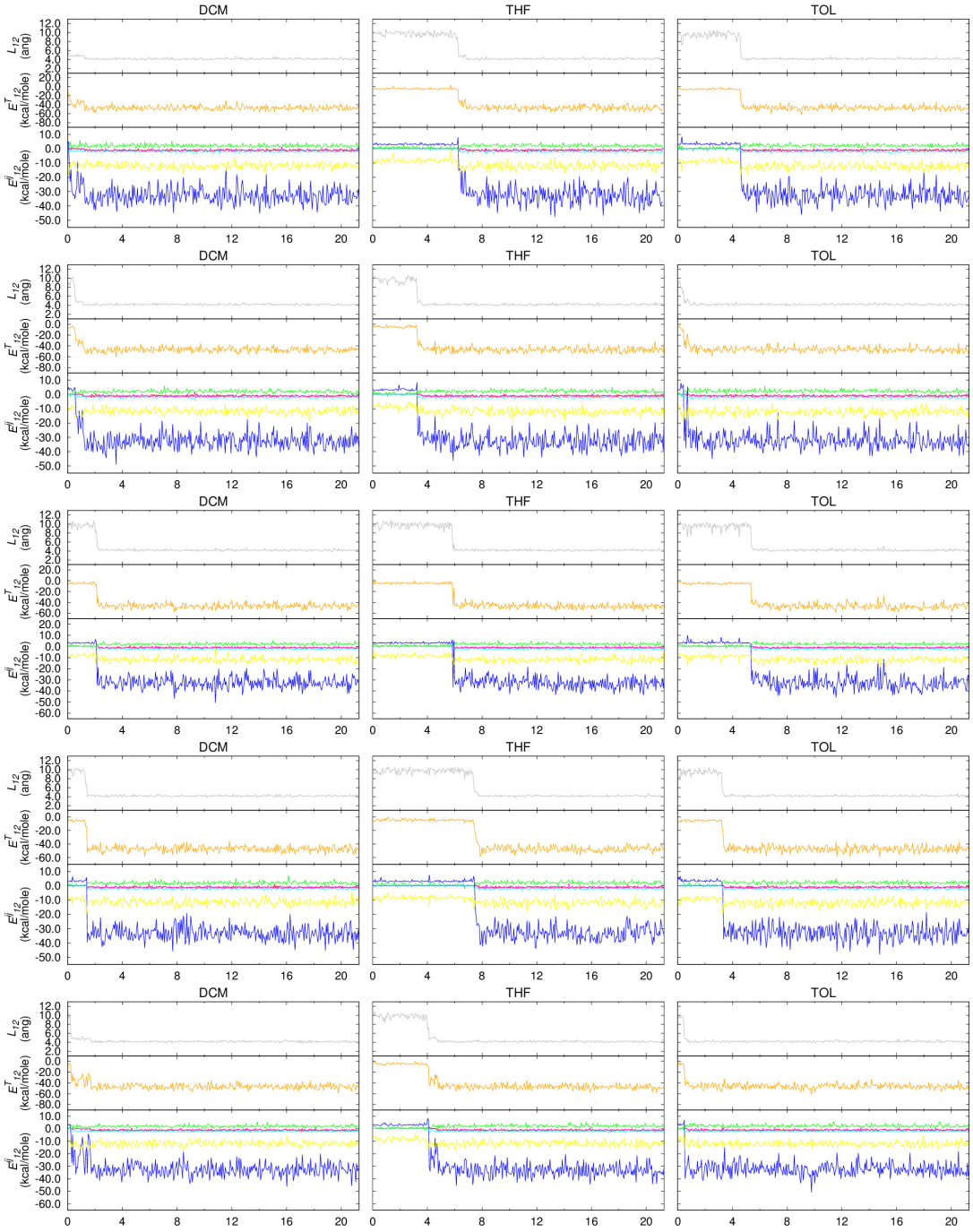

Figure B.6: Variation of complex-to-complex interaction in tetrakis-Schiff zinc-complex opened monomer during solution FEP simulations.

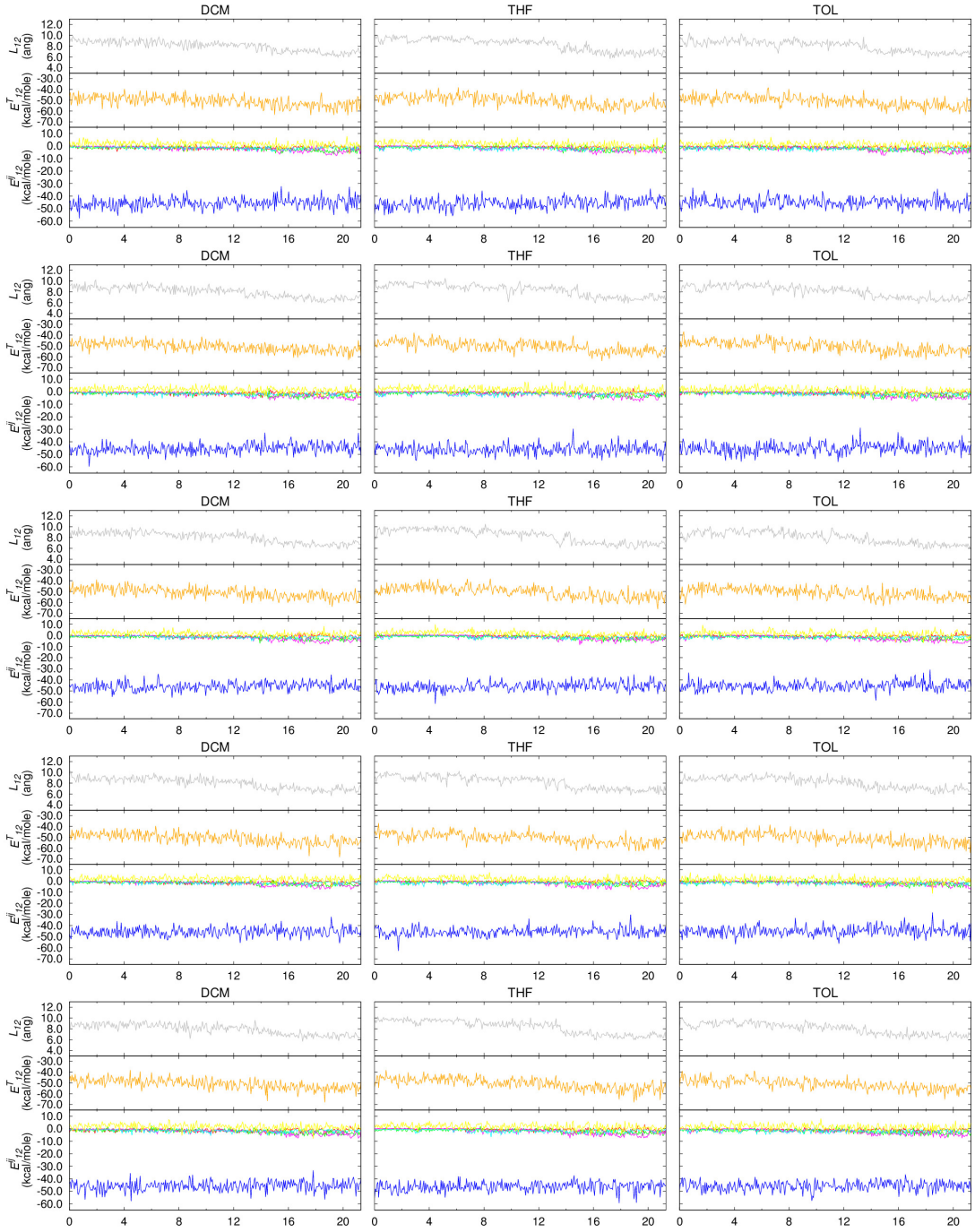

Figure B.7: Variation of complex-to-complex interaction in tetrakis-Schiff zinc-complex dimer during solution FEP simulations.

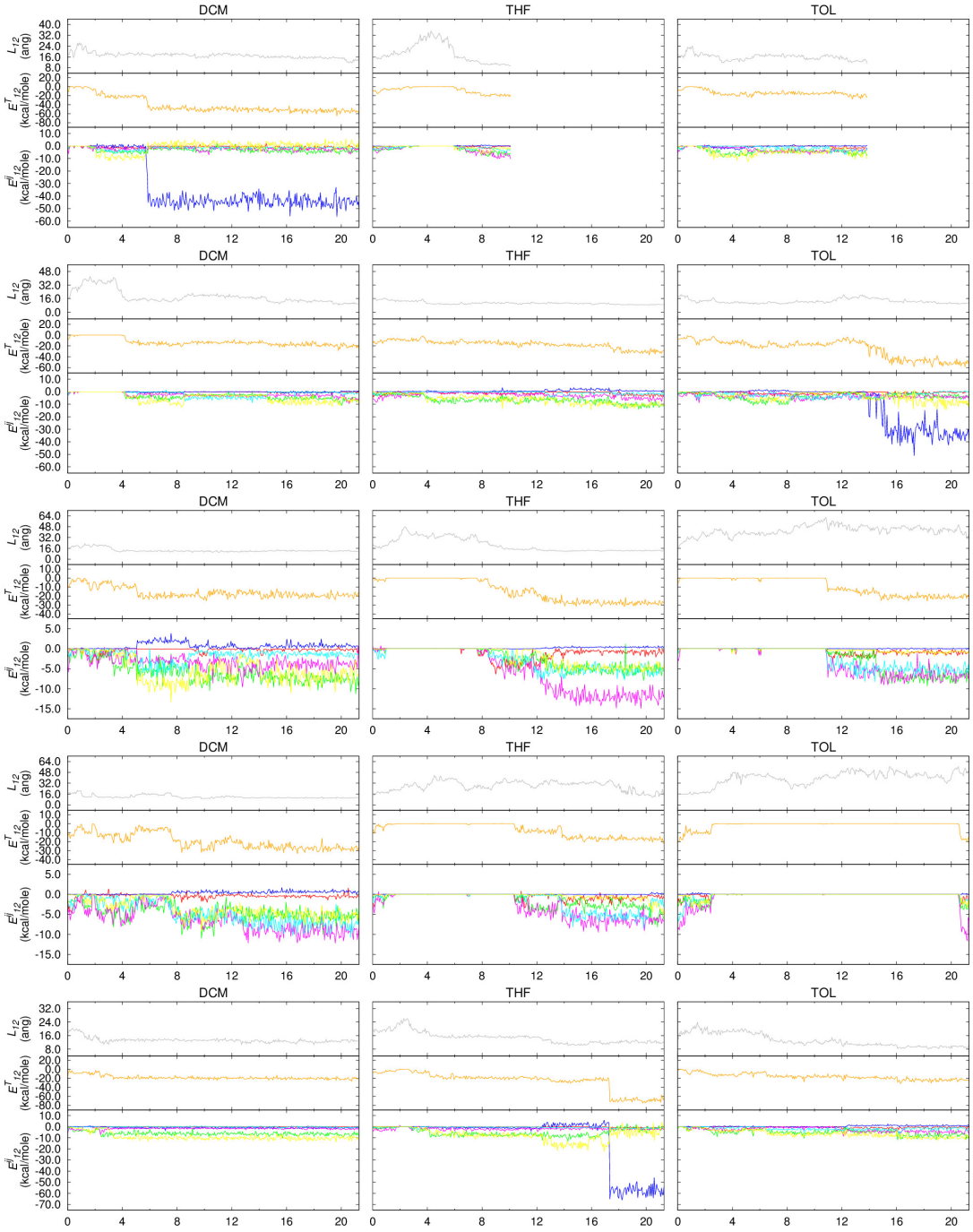

Figure B.8: Variation of complex-to-complex interaction in tetrakis-Schiff zinc-complex pi-pi bonded bi-dimer during solution FEP simulations.

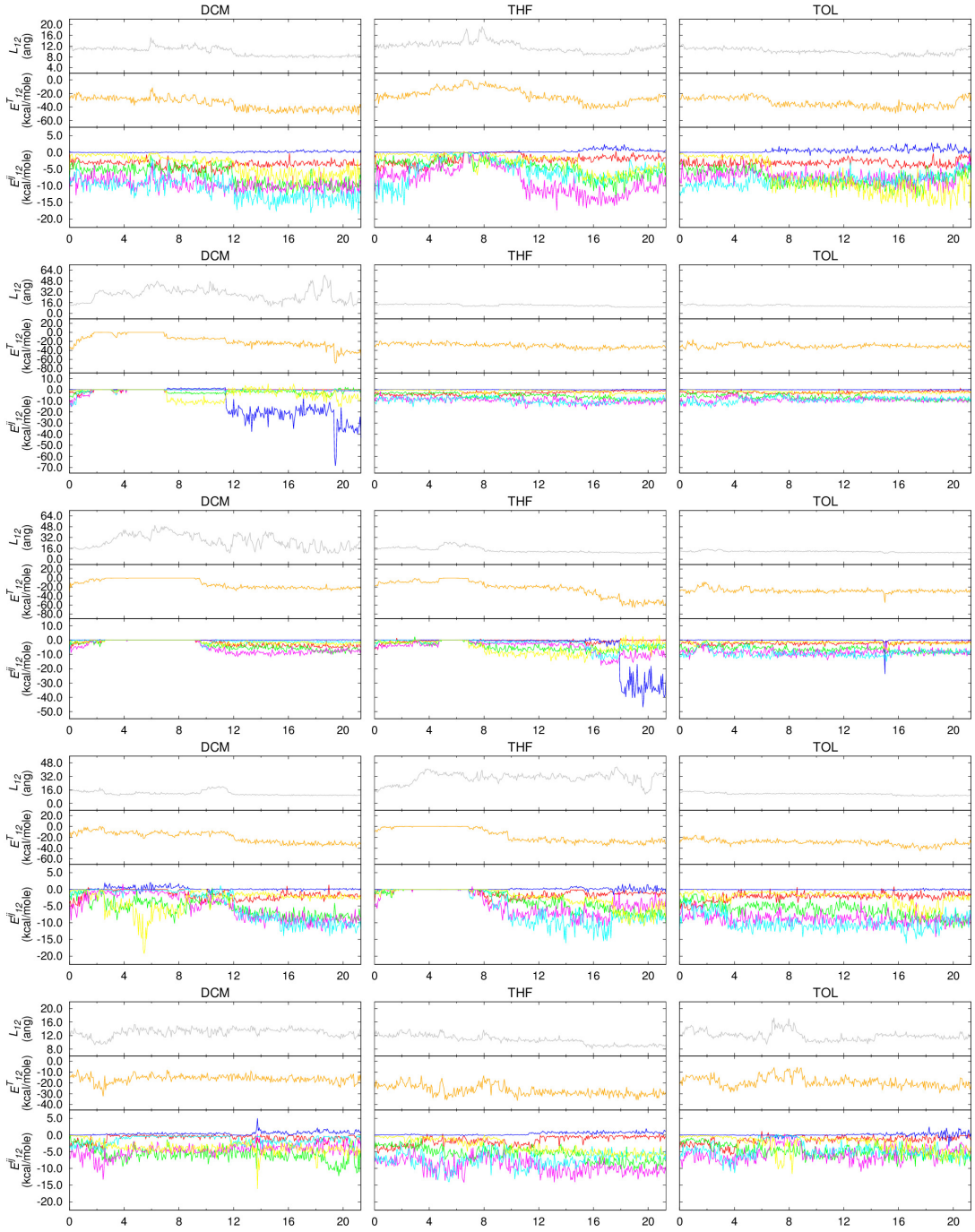

Figure B.9: Variation of complex-to-complex interaction in tetrakis-Schiff zinc-complex sandwitch-like bi-dimer during solution FEP simulations.

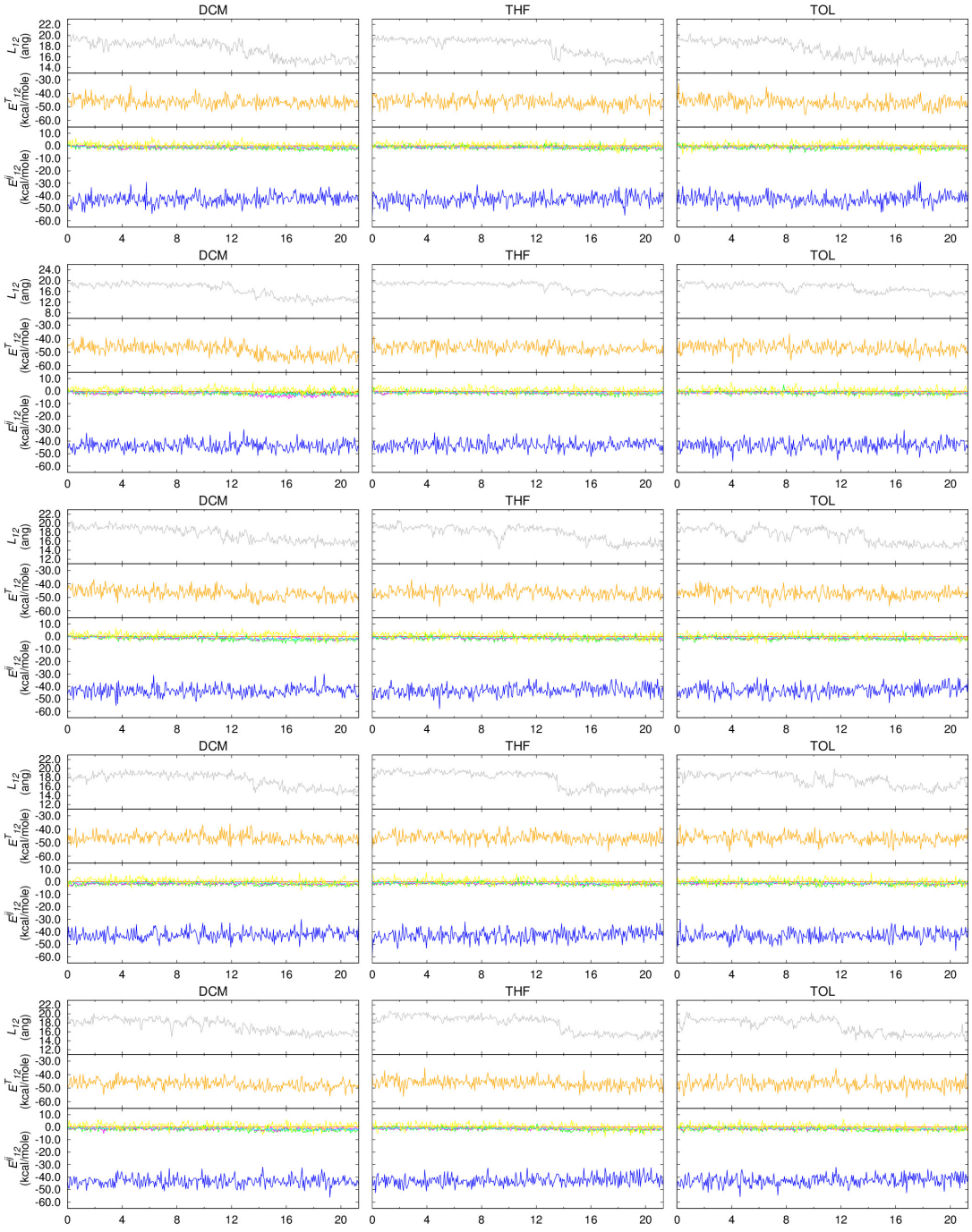

Figure B.10: Variation of complex-to-complex interaction in tetrakis-Schiff zinc-complex chain-like bi-dimer during solution FEP simulations.